Dissertation zur Erlangung des Doktorgrades
der Fakultät für Chemie und Pharmazie
der Ludwig-Maximilians-Universität München

FUNCTIONALIZATION OF COVALENT ORGANIC FRAMEWORKS

Mirjam Elif Dogru

aus

Rosenheim

2012

PREFACE

Erklärung

Diese Dissertation wurde im Sinne von § 7 der Promotionsordnung vom

28. November 2011 von Herrn Prof. Dr. Thomas Bein von der Fakultät für Chemie und Pharmazie betreut.

Eidesstattliche Versicherung

Diese Dissertation wurde eigenständig und ohne unerlaubte Hilfe erarbeitet. München, 02.02.2012

……

Dissertation eingereicht am 02.02.2012

1. Gutachter Prof. Dr. Thomas Bein
2. Gutachter: Prof. Dr. Paul Knochel

Mündliche Prüfung am 27.02.2012

DANKSAGUNG

Als erstes möchte ich meinem Doktorvater Prof Dr. Thomas Bein danken für die herzliche Aufnahme in seinen Arbeitskreis. Damit ermöglichte er mir einen tiefen Einblick in die Welt der kristallinen porösen Materialien zu bekommen. Ich konnte ein neues, interessantes und vielseitiges Forschungsthema bearbeiten, bei dem er mich stets mit vielen Ratschlägen begleitete, zugleich gewährte er mir auch großen wissenschaftlichen Freiraum zur Entwicklung eigener Ideen.

Desweiteren möchte ich mich bei Prof. Dr. Paul Knochel bedanken, der sich nicht nur als Zweitgutachter für meine Arbeit zur Verfügung stellte, sondern uns auch mit vielen verschiedenen organische Linkern versorgte ohne die diese Arbeit nicht möglich gewesen wäre. Vielen Dank für die erfolgreiche Zusammenarbeit über viele Jahre. An dieser Stelle möchte ich mich bei meinen Kooperationspartnern, Dr. Andreij Gavryushin, Dr. Silvia Zimdars, Dr. Thomas Kunz und Veronika Werner, in der Gruppe von Prof. Knochel danken. Vielen Dank für die produktive, konstruktive und sehr nette Zusammenarbeit.

Dr. Dana Medina möchte ich für die „in-group" Kooperation danken aus der das letze Kapitel meiner Arbeit hervorging. Es ist eine schöne Zusammenarbeit und ich hoffe sie begeistert das COF-Feld genauso wie es mich begeisterte.

Matthias Handloser möchte ich für die „in house" Zusammenarbeit danken, der immer eine Antwort auf meine physikalischen Fragen hatte und mir auch half die Herausforderungen physikalischer Messungen zu meistern.

Natürlich danke ich auch den ehemaligen und den neuen Kollegen im AK Bein, die eine tolle Arbeits-und auch Partyatmosphäre schafften. Vielen Dank an die Ex-Akler, Hendrik (danke fürs Empfehlen), Camilla (Teil der Mittagsessensküchen-crew),

Andreas (im AMS Büro), Enrica, Johann I und Johann II, die mich damals so nett aufgenommen haben. Ein besonderes Dankeschön an Monika, die mich während meiner Masterarbeit betreute und für all meine vielen und nervigen Fragen immer ein offenes Ohr hatte. Meinen Bürokollegen Dr. Jörg Schuster und Dr. Axel Schlossbauer (ja ja das „Dreierpack“) danke ich für die angenehme Arbeitsatmosphäre, aber auch für die gelegentlichen sehr willkommen Auszeiten. Besonderen Dank auch an meine sub-group, genauer gesagt das zweite sub-group Mitglied, Florian Hinterholzinger (HiHo). Lange standen wir wie auf verlorenem Posten, was den Zusammenhalt der COF/MOF sub-group gestärkt hat und ich so einen Kollegen gefunden hatte, der mich nicht nur bei freudigen Fortschritten begleitete, sondern mir auch bei Rückschlägen beistand. Auch bei allen anderen Kollegen, Norma, Benni, Basti, Flo Auras, Karin, Dina, Christian, Alex, Hans, Stefan, Fabi, Alesja, Stefan (Woody) und Maria für den großen Spaß in den Kaffepausen, auf den Stammtischen und Konferenzen. Eine große Hilfe manchmal auch eine große Herausforderung waren AMS -oder F-Praktikanten und meine Masterandin: Jürgen, Ellen, Conni, Ruanshang, Janio und Maria. Auch den permanenten AK Mitgliedern möchte ich meinen besonderen Dank aussprechen. Vielen Dank Tina für die zahlreichen Messungen, die stets gut gefüllten und gut sortierten Chemikalien. Danke Steffen für die REM sessions (hier nochmal Dank auch an die REM Nachfolger: Basti, Benni und Flo A.). Danke Markus für die schönen TEM Bilder, trotz der schlonzigen Proben. Herausragenden Dank an Regina, nicht nur für das Erledigen des „Verwaltungskrams“, für einen reibungslosen Ablauf aller Organisatorischer Dinge, sondern auch für ein stets offenes Ohr bei allen freudigen oder auch unfreudigen Angelegenheiten.

Der größte Dank geht aber an meine Eltern und meinen Bruder, ohne deren unerschöpfliche moralische und auch finanzielle Unterstützung all dies nicht möglich gewesen wäre. Vielen Dank für die Ermutigung, dass man alles tun kann, wenn man es nur möchte. Johannes, dir möchte ich auch besonders danken, dass du mich all die Jahre während der Promotion ausgehalten hast. Alle Hochs und Tiefs mitgemacht hast und es immer geschafft hast mich wieder aufzubauen.

ABSTRACT

Covalent Organic Frameworks (COFs) are a novel class of highly stable, purely organic crystalline frameworks made of molecular building blocks. For example, the condensation of boronic acids with appropriate polyols in principle allows the design of precisely controllable structures since their chemical and physical properties can be easily tuned through the selection of the building blocks. The young research field of COFs has attracted scientists due to their extraordinary and versatile properties, however, strategies to control the topology and the properties of the backbone as well as the inner surface are still not well established. With support of Prof. Knochel and his group, who contributed numerous new organic COF linkers, this thesis aims to extend the functionalization strategies for the design of Covalent Organic Frameworks. Investigation of the structural modification and the associated change in physical and chemical properties should lead to progress regarding the applicability of these materials.

Employing the concept of reticular chemistry in combination with High Throughput Synthesis Techniques, the formation of a very large Covalent Organic Framework BTP-COF with 4 nm open pores was successfully carried out. The solvothermal co-condensation of 1,3,5-benzenetris(4-phenylboronic acid) (BTPA) and 2,3,6,7-tetrahydroxy-9,10-dimethyl-anthracene (THDMA) was carried out using microwave irradiation instead of conventional synthesis in an oven, thus synthesis time of BTP-COF was reduced from initially 72 h to 5 min. Extending the open pore diameter of a crystalline material to 4 nm, in combination with the resulting high accessible surface area of 2000 m^2/g offers great potential to exploit organic reactions in the pores and enables the incorporation of large functional guests, such as polymers or dyes.

Bearing these results in mind the scope of functionalization possibilities was expanded from the geometric extension to the chemical modification of the inner surface of COFs. Decorating the organic building blocks with small functional active groups, such as methyl-, -methoxy- and hydroxy- allowed for the successful synthesis of several organic frameworks. Chemical and physical properties of the backbone and the inner surface can be precisely tailored by chemical modification of the building blocks. In order to investigate post-synthetic modification strategies, the methyl- and hydroxy-groups were used as reaction anchor points to covalently attach molecules after framework formation. The co-condensation of benzene-1,3,5-triyltriboronic acid (BTBA) and the 9,10-dimethyl-anthracene-2,3,6,7-tetraol (DMAT) succeeded in the formation of AT-COF-Me. In a radical bromination reaction the methyl groups of an anthracene linker were successfully brominated giving AT-COF-Br without degrading the crystalline framework of AT-COF-Me. The formation of the resulting benzylic bromine was monitored with IR spectroscopy and solid state NMR, respectively. Elemental analysis results correspond to the bromination of half the $-CH_3$ groups. Reaction of (2',5''-dihydroxy-[1,1':4',1''-terphenyl]-4,4''-diyl)diboronic acid (HTDBA) and 2,3,6,7,10,11-hexahydroxytri-phenylene (HHTP) The terphenyl-based hydroxyl substituted T-COF-OH, formed by (2',5''-dihydroxy-[1,1':4',1''-terphenyl]-4,4''-diyl)diboronic acid (HTDBA) and 2,3,6,7,10,11-hexahydroxytri-phenylene (HHTP), was tested in several nucleophilic substitution reactions. Esterification of the –OH group was achieved with either acetylchloride or in a Steglich type reaction with 4-pentynoic acid. X-ray diffraction analysis after the post-synthetic modification shows that the crystallinity of the framework was preserved. This indicates that T-COF-OH is compatible with the reaction conditions. The detection of the newly formed ester moieties in IR and in

solid state NMR spectra proves the successful post-synthetic esterification of the –OH groups.

Another approach to tailor functionality in COFs is to assemble monomers with distinct properties in COF synthesis. Modification of the backbone of the framework was realized with two heterocyclic building blocks. Benzothiadiazole (BTD) and thienothiophene (TT) monomers are known as building blocks of semiconducting polymers. These molecules were equipped with boronic acid or boronate ester moieties in para position. The linkers were then used in co-condensation reactions with HHTP. The synthesis of BTD-COF was carried out in a two step microwave synthesis procedure: first the pinacolboronate 4,7-Bis(4-(4,4,5,5-tetramethyl-1,3,2-dioxaborolan-2-yl)phenyl)benzo[*c*][1,2,5]thiadiazole (BTDA) was cleaved with HCl, in a second step addition of HHTP resulted in the crystalline product in only 60 min. TT-COF was synthesized in a conventional co-condensation reaction of thieno[3,2-b]thiophene-2,5-diyldiboronic acid (TTBA) with HHTP; the black TT-COF showed aborbance over the whole spectrum of the visible light. Upon irradiation with light the system showed significant photoconductivity. The 3 nm pores of the hole-transporting TT-COF offer enough space to incorporate large fullerene-based electron-transporting materials such as PCBM. This inclusion leads to a significant quenching of the luminescence of TT-COF, indicating light-induced charge transfer at the interface of these two materials.

The oriented growth of thin films of porous COF-10, a product of the condensation of 4,4′-biphenyldiboronic acid(BPBA) and HHTP, and TT-COF on self-assembled monomer (SAM)-functionalized gold surfaces is shown. Films grown on boronic acid terminated SAMs result in a parallel orientation of the pores along the substrate. Scanning electron microscopy was used to investigate the morphology of

the films. Homogenous films with thicknesses of around 150 nm and a total coverage of the substrates were obtained.

In summary, several functionalization strategies are shown to control or tune the topology and properties of Covalent Organic Frameworks. Tuning the topology and functionality to large open pore systems or intrinsic semiconductivity allows incorporation of large functional molecules and study the host-guest interactions. The post-synthetic modification of COFs offers a synthetic pathway to integrate organic functionalities, which cannot be synthesized directly by co-condensation. These strategies provide the means necessary for a precise control of the pore environment and design a porous material for specific applications. A facile and rapid method to produce thin oriented COF films will pave the way for this material to fabricate technological devices, such as photovoltaic devices, sensors of OFETs.

TABLE OF CONTENTS

1. Introduction

1.1. Covalent Organic Frameworks- A new class of materials

Porous materials have attracted a great deal of attention due to their exceptional properties and thus their versatile applications. During the last decades nanoporous materials were designed to precisely match their intended applications. Tailoring metrics, composition, chemical and physical properties of these nanostructures can be achieved by exact synthetic control. Nanoporous frameworks such as zeolites, AlPOs or metal-organic frameworks (MOFs) offer great potential for targeted applications, due to their crystalline nature combined with a great structural and compositional variety. Catalysis, separation, sensors or drug delivery applications are among the most prominent examples. Global warming, oil shortage or the recent nuclear explosion in Fukushima illustrate the importance of discovering and developing new materials and technologies in the field of clean or renewable energy, e.g. gas storage, photocatalysis or photovoltaics. For efficient energy storage or conversion, accessible high internal surfaces with well-defined and controllable walls are desirable for ideal charge transfer and transport. The field of organic photovoltaics provides several advantages with respect to conventional inorganic or dye sensitized solar cells. The organic compounds are cost-efficient, producible at large scale and can be easily modified by the versatile tools of organic chemistry. The ability to design the desired material on a molecular basis allows fine tuning of the energy gap and the light absorbance of the semiconductor. In addition, due to high light absorbance already a small amount of the photoactive species can lead to efficient energy conversion. This allows for the fabrication of very thin devices. However, there are still some major drawbacks to overcome, for

example, the devices often exhibit low stability and low efficiency. The latter is mostly caused by low charge transport ability and recombination, due to inefficient stacking of the conducting polymers or due to insufficient and disordered donor-acceptor interfaces. Therefore it would be desirable to have synthetic access to conducting materials with total control over their nanoscale structure and orientation.

Recently a new class of semiconducting materials has been introduced exhibiting high charge carrier mobilities. Covalent Organic Frameworks (COFs) are porous organic frameworks linked, e.g., by boronate ester formation or Schiff base formation. The reversible nature of the condensation reaction of boronic acids with polyols or of amines with aldehydes assures a self-healing process which is necessary to promote crystallization. Aromatic organic building blocks can assemble into conjugated two-dimensional sheets that are held together by π-stacking in the third dimension, resulting in accessible channels in one direction. Depending on the geometry, size and property of the organic building blocks, several new COF structures have been realized. The π-interactions of the eclipsed stacked layers combined with the crystalline nature allow high electronic interlayer interaction, resulting in a defined conduction path along the framework. Properties such as chemical stability, absorbance behavior, conductivity and band gap energies can be tailored by assembling the appropriate building blocks or by post-synthetic chemical modification of the framework. In addition the crystalline framework structure is ideal for creating interpenetrated networks of donor and acceptor systems on the nanoscale. All in all this new class of material offers a great opportunity to overcome long standing challenges in organic semiconductor device fabrication. In the following several important topics will be addressed, including

backbone and inner surface functionalization of COFs. The former includes expansion strategies to create high surface areas and large pore systems, thus enabling host-guest interactions with large functional molecules. The latter includes prior to synthesis and post-synthetic modification strategies to functionalize the inner surface and to promote a desired property. Especially the ability to molecularly engineer building blocks or networks offers, in principle, access to a great variety of tailored materials. Connecting molecules or functional moieties to the crystalline walls in simple reactions without damaging the framework structure has not been intensively studied yet, however, it is viewed as indispensible for future advances of this class of materials.

Many technological devices are based on the preparation of thin films. A precisely controllable thickness and orientation on different solid supports is required for many applications.

After a short review on classical crystalline porous materials a more detailed overview over synthetic approaches and applications of COFs as an emerging class of porous crystalline materials is given.

1.2. Inorganic Crystalline Frameworks: Zeolites and Zeotypes

The commercialization of porous solids in industry has increased significantly. Due to their outstanding properties and wide range of applications as strong and selective adsorber material, as selective ion exchangers or as catalysts these materials were investigated extensively in the last decades. Zeolites are crystalline aluminosilicates, consisting of [TO_4] tetrahedrons (T = Si, Al) connected over all four edges with neighboring tetrahedrons, the general formula for zeolites is

$M^{n+}_{x/n}$ $[(AlO_2)_x(SiO_2)_y]_x \cdot wH_2O$ (M=metal).[1] Their crystal structure exhibits cavities with a regular array of channels and cages in the range of about 3 to 15 Å.[2, 3] Substitution of silicon with aluminum results in a negatively charged framework, which is compensated by insertion of alkali or earth alkali cations into the cavities. Replacement of the silicon atoms with aluminum and phosphorus gives the microporous class of aluminophosphates; ALPOs.[4] The sparsely variable Al to P ratio is the characteristic feature of the $ALPO_n$ composition. Unlike zeolites ALPOs can exhibit not only tetrahedrally coordinated T- atoms, but also octahedral aluminum leading to a neutral framework with even-numbered rings. Introducing bivalent metals, e.g. copper,[5] gallium[6] or zinc[7] leads to the formation of new zeotypic materials exhibiting a negatively charged metal phosphate framework. Due to their high chemical and thermal stability and their low production costs zeolite materials were exploited as water purifiers[8,9] or softeners,[10] as catalysts for petrochemical cracking[11] or as heat storage materials,[12,13] among many other applications.

1.3. Inorganic-Organic Hybrid Crystalline Frameworks

In recent years the field of applications of porous materials has expanded to new concepts such as hydrogen storage, sensor devices, drug delivery and photovoltaic devices. In purely inorganic materials the potential for functionalization is limited.[14, 15] Therefore it was highly desirable to design organic zeolite analogues, as they would offer a more comprehensive control of physical and chemical properties of the pore environment. With the development of a new class of inorganic-organic hybrid materials, the Metal-Organic Frameworks (MOFs) a great variety of

structural flexibility was opened up. MOFs are organic-inorganic hybrids based upon coordination bonds between a transition metal or metal cluster and the heteroatom of an organic building block called ligand or spacer (Figure 1.1).[16]

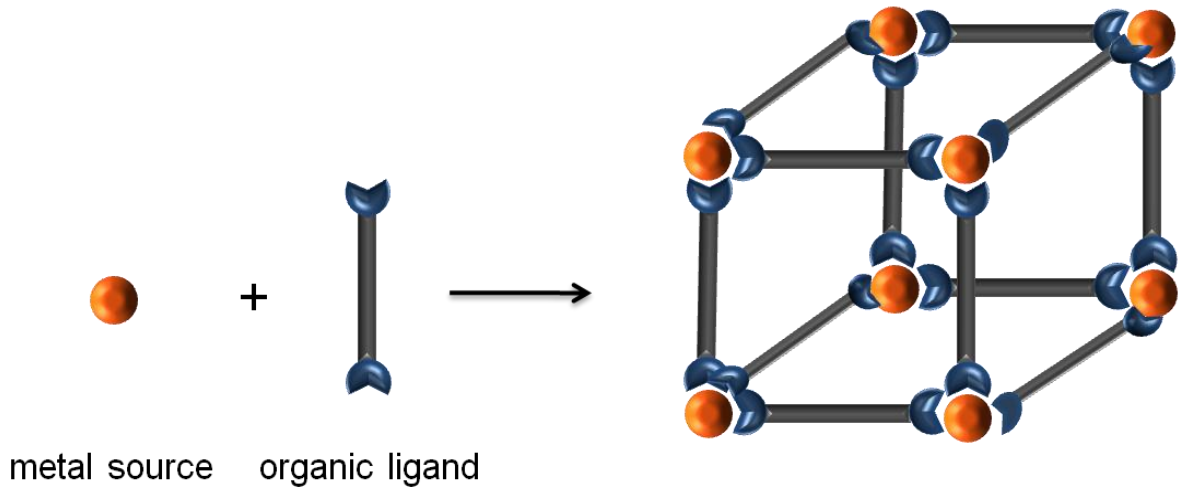

Figure 1.1: General reaction scheme for MOF synthesis: organic ligands with at least two functional groups coordinate a metal ion.

Synthesis of specific networks can be predictable to a certain degree due to the reticular assembly of the appropriate nodes (metal coordination geometries) and organic ligands.[17-19] The great interest in MOFs is based upon the availability of an immense variety of organic linkers and inorganic metal ions or clusters. Beyond that synthetic chemistry permits modification of the organic ligand or the MOF itself. In Figure 1.2 possible geometries and sizes of metal clusters and representative organic linkers are shown.

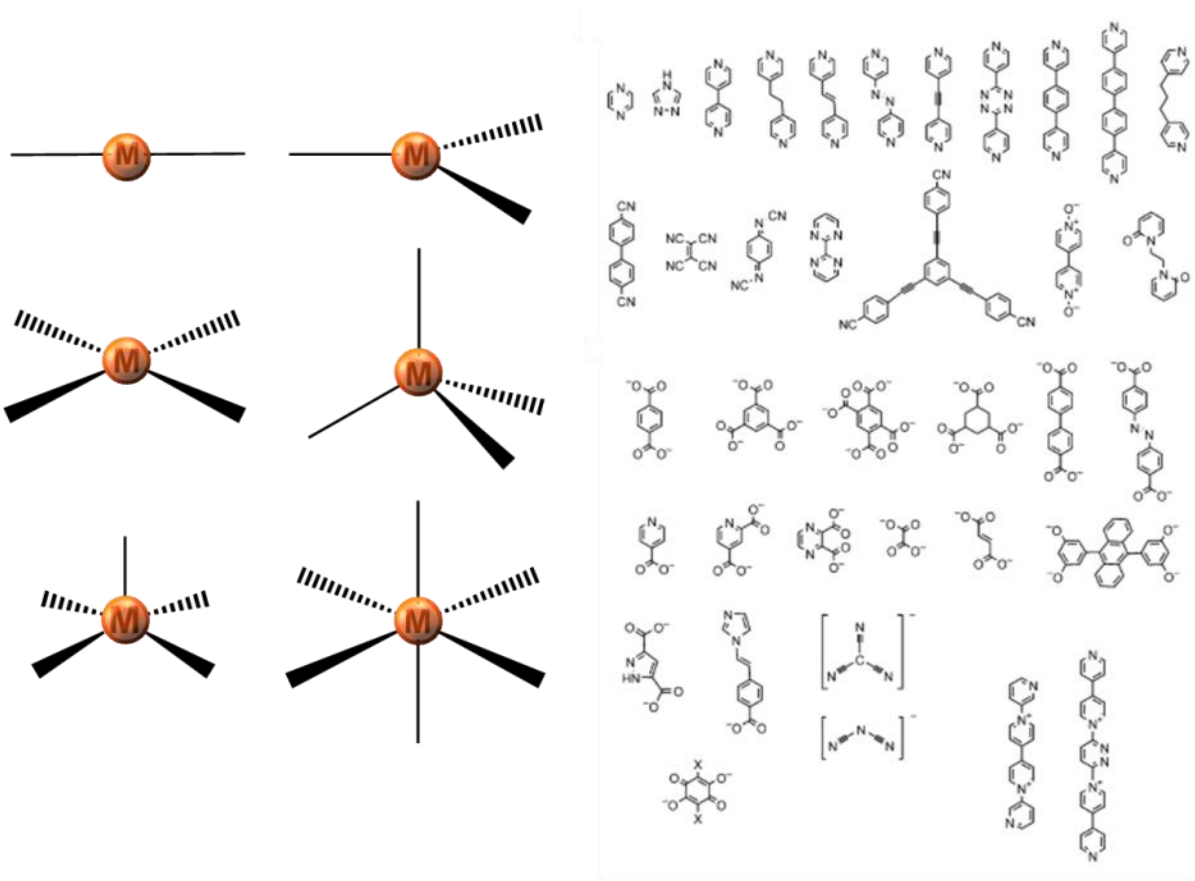

Figure 1.2: Different coordination geometries of metal centers and examples of organic linkers for MOFs.[18]

Thus the chemical and physical properties, such as polarity or dimensions of the pores in MOFs can be fine-tuned. In 2002 Yaghi introduced an isoreticular series of MOF-5 (IRMOF), a zinc terephthalate with a cubic framework. Using 16 different organic linkers, MOFs with precisely predictable metrics and functionalities were designed and realized.[20, 21] An additional approach to introduce functionalities is realized by the post-synthetic modification (PSM) of MOFs.

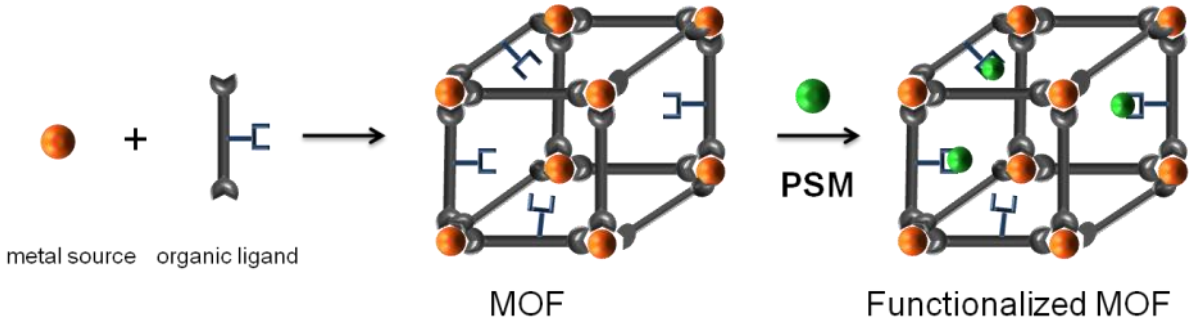

Figure 1.3: Schematic reaction pathway for a MOF and its post-synthetic modification.

Thereby the functionalization of MOFs is achieved by the exploration of organic chemistry inside the pores after the framework synthesis (Figure 1.3).[21-25] However most MOFs have windows in the microporous regime which hinder the interaction with big guest molecules.[26] The recently investigated mesoporous MOFs often lack sufficient chemical and thermal stability[27]

1.4. Organic Crystalline Frameworks

More recently a new class of materials, the Covalent Organic Frameworks (COFs), has attracted the attention of scientists. COFs are organic, crystalline and highly porous materials exclusively made out of light elements like hydrogen, boron, carbon, nitrogen and oxygen. The COF frameworks consist of organic building blocks connected by covalent bonds. Niu *et al.* reported the synthesis of boronate polymers in which the precursors alternately react with each other and degrade in the next step. In a last step the fragments are repaired and the polymeric structure is formed (Figure 1.4). The covalent yet reversible bonding interactions of boronate esters are very favourable for the generation of self-assembled polymeric materials.[28]

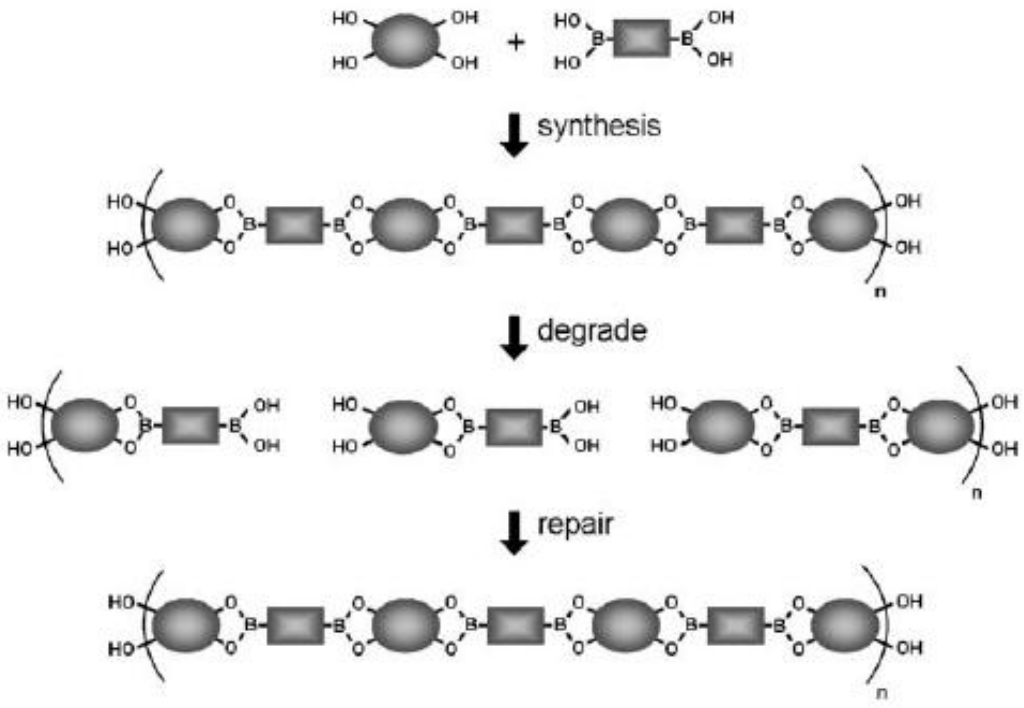

Figure 1.4: Schematic of the synthesis featuring self-repair capabilities of poly(dioxoborolane)s.[29]

Yaghi´s group set out to generate ordered crystalline networks by making use of this reversible boronate ester condensation (Figure 1.5).[30]

The key to assemble a crystalline organic framework is to gain thermodynamic control over the reaction. With this approach it is possible to overcome the long standing "crystallization problem" for covalently linked solids. This is accomplished by striking a balance between the kinetic and thermodynamic factors to induce reversible covalent bond formation, a necessary criterion to crystallize extended structures.[31]

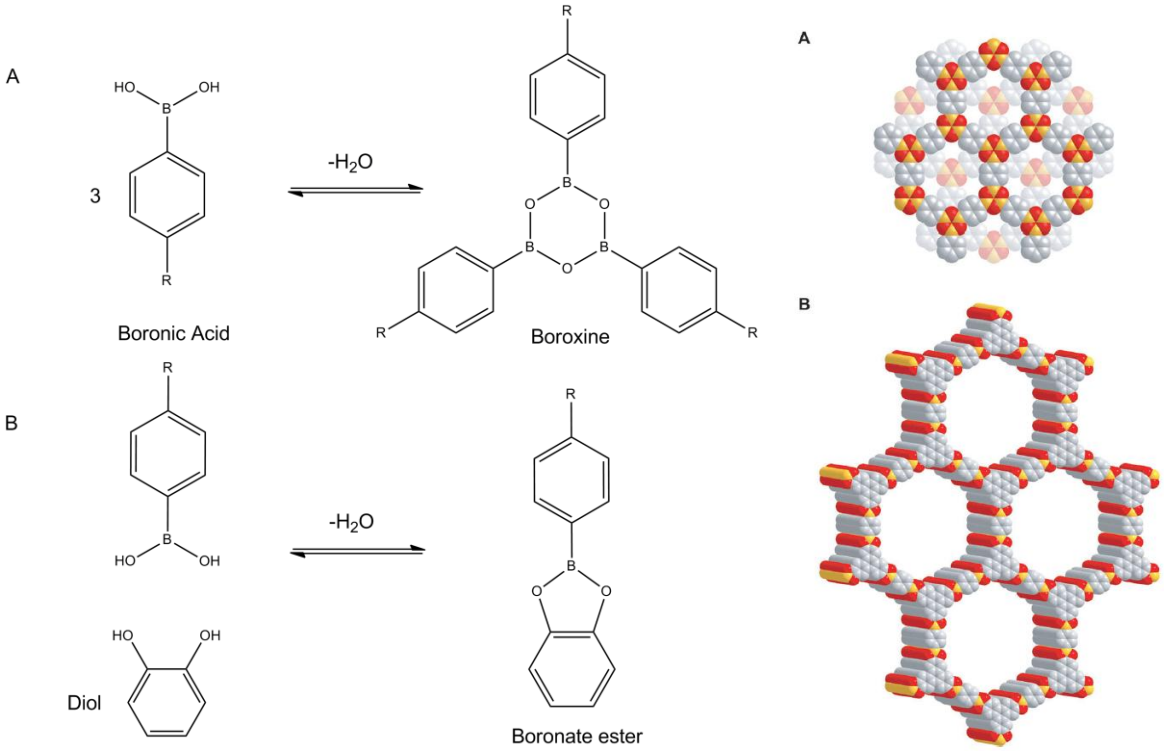

Figure 1.5: Reversible reactions of boronic acids: A) self-condensation forms a boroxine ring and B) co-condensation with a vicinal diol forms a boronate ester.[30]

This chemistry has led to the design and synthesis of new porous materials whose compositions, structures, metrics and functionalities can be systematically varied.[20] The rigid structure exhibits very low density and permanent porosity. Their high surface areas in combination with exceptional thermal stability (up to 600°C) make them suitable candidates for gas storage, separation and catalysis. The following paragraphs discuss the potential and challenges of these materials.

1.4.1. Synthesis Principles

Crystalline COFs containing 2D-layers were synthesized in one-step-condensation reactions of organic building blocks resulting in either hexagonal or tetragonal layers depending on the geometry and connectivity of the linkers. These two-dimensional layered structures are held together by π-stacking in the third dimension. This leads to pores accessible in one direction. The synthesis of COF-1, the first COF introduced by Yaghi in 2005 is based on the dehydration reaction of 1,4-benzenediboronic acid (BDBA) (Figure 1.6). The condensation of the diboronic acid leads to the formation of a planar six-membered ring of B_3O_3 (boroxine) accompanied by the elimination of three water molecules.[32] The formation of the network is entropically favoured, due to liberation of water molecules. Planar 2 D organic sheets are formed, which are stacked in a staggered arrangement.

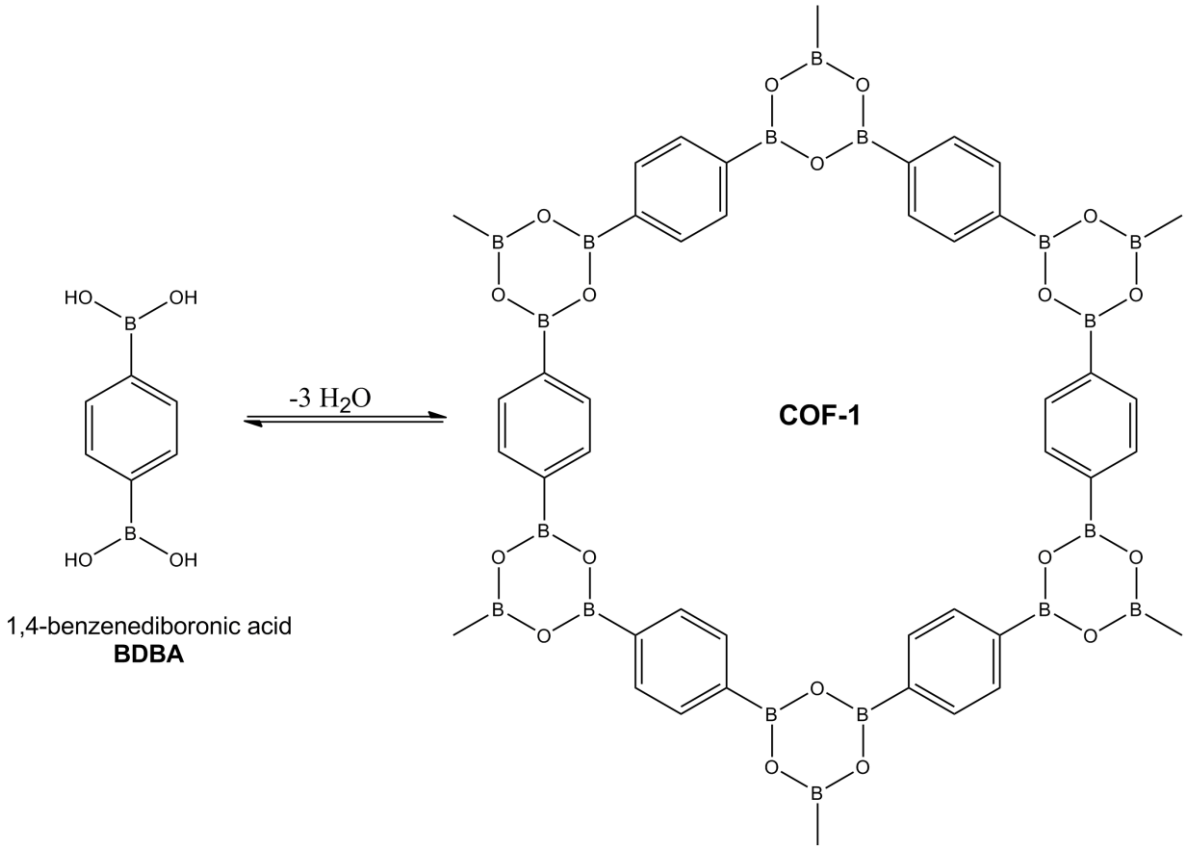

Figure 1.6: Reaction scheme for the self-condensation reaction of COF-1.

Yaghi postulated that the reaction has to be carried out in a closed reaction system with solvents in which diboronic acid is not completely soluble. These conditions allow a slow condensation of BDBA. The sparing solubility of BDBA in this system controls the diffusion of the building blocks into solution and facilitates the nucleation of a crystalline material. The use of a closed reaction system sustains the availability of H_2O for maintaining reversible conditions conducive to crystallite growth. [30] The co-condensation reaction of a diboronic acid with the trigonal building block hexahydroxytriphenylene (HHTP) produces a five-membered BO_2C_2 ring. The so-created structures are discussed in detail in the next section. Recently Yaghi and co-workers expanded the linkage chemistry for COF synthesis. By linking amines and aldehydes imines are formed. The first imine-linked 3D COF was produced by solvothermal synthesis of a tetrahedral tetra-(4-anilyl)methane and

terephthalaldehyde resulting in a diamond topology.[33] A 2D COF, synthesized by Schiff base reaction of a tetraamino porphyrin and terephthalaldehyde was recently reported.[34] Moreover, using the dehydration reaction of 2,5-diethoxyterephthalohydrazide and 1,3,5-triformylbenzene or 1,3,5-tris(4-formylphenyl)benzene, hydrazone linked COFs were successfully produced.[35]

1.4.2. 1D Channels in 2D Structures

In order to build up a 2D COF the organic linkers have to meet certain criteria. Connectivity of the organic building blocks is one criterion. Until now organic ligands with either linear-trigonal, trigonal-trigonal or linear-tetragonal connectivity gave COF structures. Additionally for successful 2D COF synthesis the organic building blocks need to be planar. Using planar aromatic systems enables an interlayer distance of around 3.5 Å, such that π-interactions can occur. Furthermore the linkers should not carry functional groups that interfere with the linkage chemistry of the COF formation.

The first COFs, namely COF-1 and COF-5 were introduced by Yaghi and co-workers in 2005. COF-1, the simplest form of a COF is described in the previous section. COF-5 (Figure 1.7) is formed by co-condensation of the linear benzenediboronic acid (BDBA) with the triangular building block hexahydroxytriphenylene (HHTP).[30]

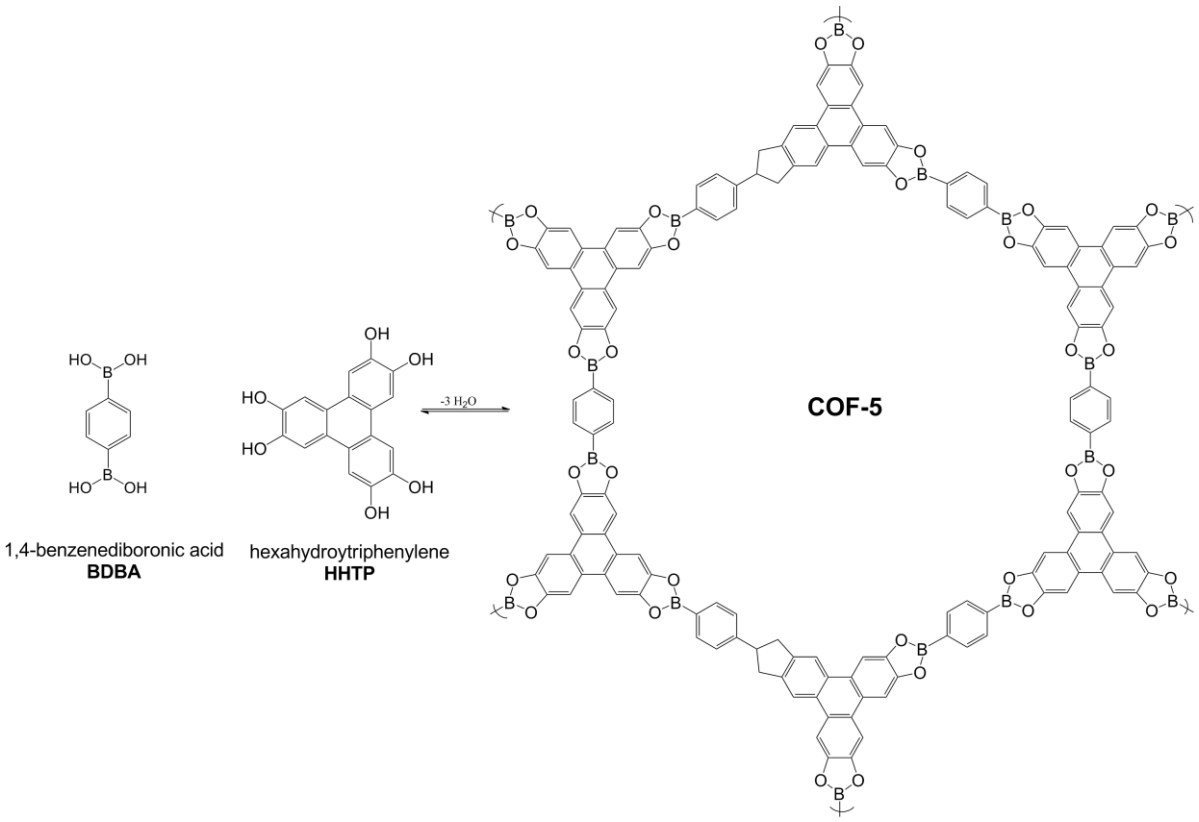

Figure 1.7: Reaction scheme for the co-condensation reaction of COF-5.

Lavigne showed in 2006 a reverse assembly, meaning co-condensation of a linear alcohol (tetraol) with a triangular triboronic acid giving COF- 18Å.[36] In 2007 Yaghi and co-workers extended the scope of 2D hexagonal COFs. COF-6, -8 and 10 (Figure 1.8) were synthesized by linking the trigonal HHTP with trigonal 1,3,5-benzenetriboronic acid (BTBA), trigonal 1,3,5-benzenetris(4-phenylboronic acid) (BTPA) or linear 4,4'-biphenyldiboronic acid (BPDA), respectively.[37] Due to the reticular assembly of planar aromatic building blocks with different extensions, COFs with varying pore sizes from 9 to 32 Å were constructed.

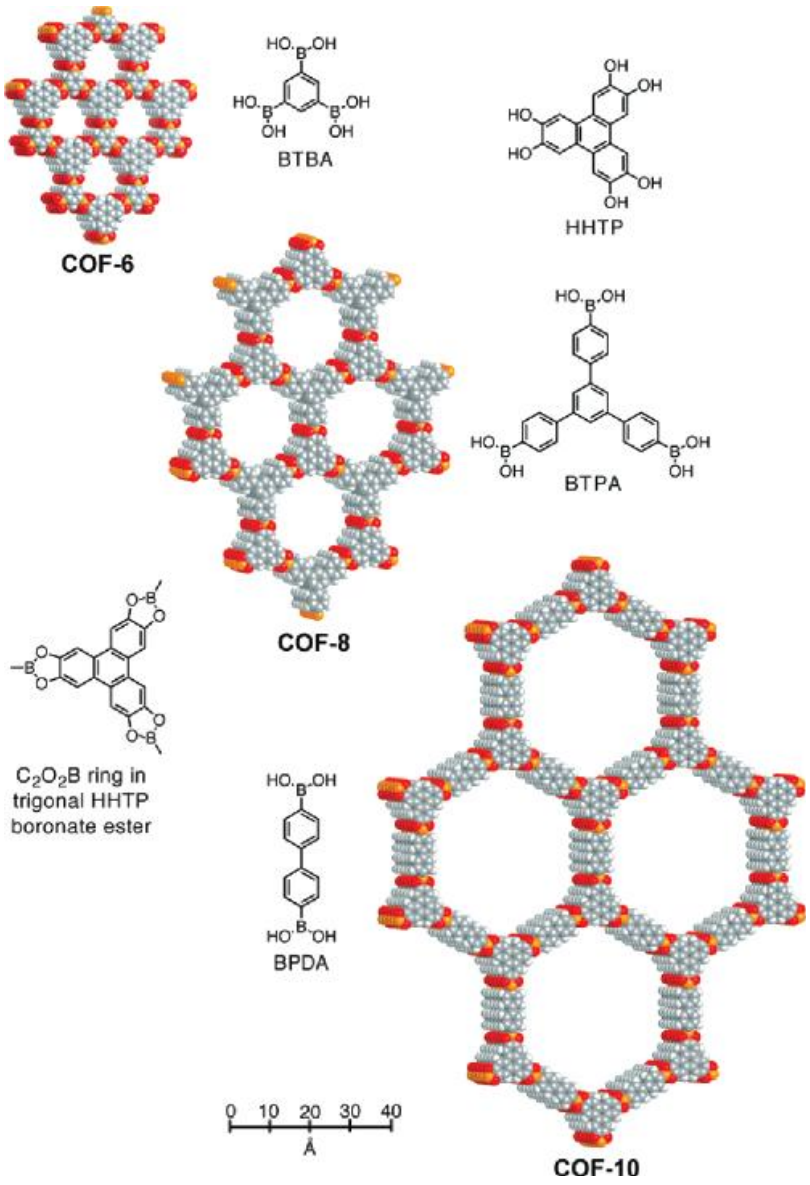

Figure 1.8: Reticular series of co-condensation reactions of boronic acid building blocks (BTBA, BTPA, BPDA) with HHTP to give 2D COFs (COF-6, -8, and -10). Dimensions of COFs see scale bar. Coloring scheme: C, gray; H, white, B, orange, O, red.[37]

By rational pre-selection of the organic linkers, the pore dimension and pore environment can be customized for desired applications. For example, Tilford *et al.* illustrated micropore tailoring of COF-18Å down from 18Å to 11Å. Tetrahydroxybenzene was modified with alkyl side chains of up to three carbon atoms.[38] The authors showed that the incorporated alkyl substituents influence host-guest interactions. On the one hand nitrogen uptake is reduced, but on the other,

the amount of adsorbed hydrogen into the framework increased essentially (Figure 1.9).

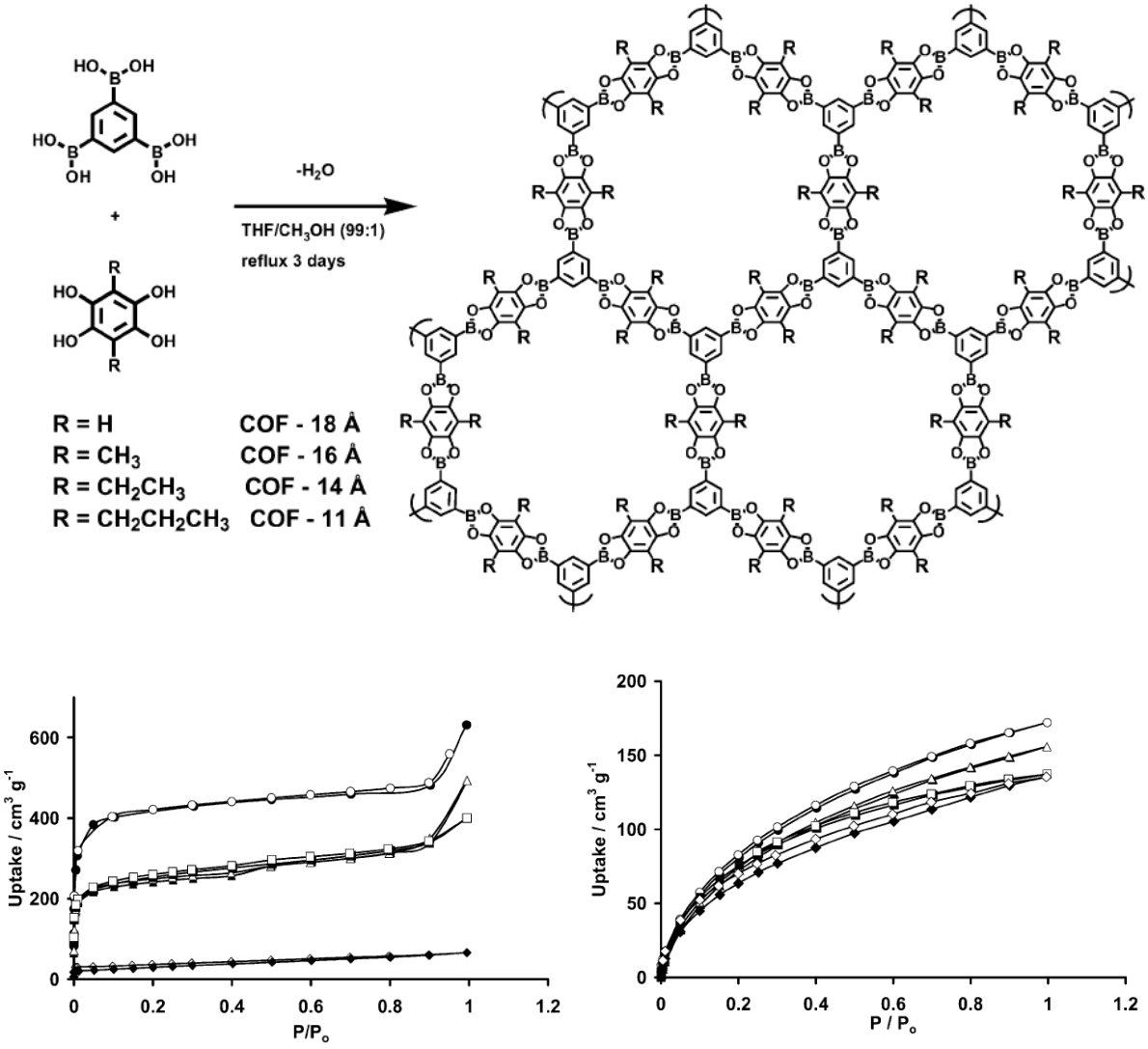

Figure 1.9: top: Co-condensation reaction of triboronic acid and alkyl-functionalized tetraol resulting in COF-18 Å to 11 Å, on the left bottom: Nitrogen sorption isotherms for COF-18Å, 16Å, 14Å and 11Å and bottom right: Hydrogen adsorption isotherms of COF-16Å (Δ/▲), COF-14Å (□/■), COF-11Å (♦/◊)] and unsubstituted [COF-18Å (○/●)].[39]

For host-guest interactions with large molecules, pores with several nm in diameter are desired. Recently we introduced the BTP-COF with fully accessible open pores of 4 nm, synthesized by co-condensation of 1,3,5-benzenetris(4-phenylboronic acid)

(BTPA) and the polyol 2,3,6,7-tetrahydroxy-9,10-dimethylanthracene (THDMA).[40] After degassing the material for 12 h at 150 °C a large surface area of 2000 m^2/g was obtained; this value agrees very well with the calculated Connolly surface. In addition to a hexagonal array of linear and trigonal linkers Spitler *et al.* showed that the composition of a tetragonal octaol, or more precisely a tetragonal phthalocyaninetetra(acetonide) can react with a linear diboronic acid and addition of catalytic amounts of a Lewis acid (BF_3*OEt_2) to form a tetragonal lattice.[41] The concept of a tetragonal COF was extended by Jiang and co-workers, they reported a metallophthalocyanine COF and a porphyrin-based COF.[42, 43] The condensation of the zinc porphyrin tetraboronic acid with tetrahydroxybenzene was investigated with different solvent ratios and reaction times. Due to the solubility of the porphyrin species in dioxane the solvent ratio had to be adjusted to mesitylene : dioxane 9 : 1 (conventional COF synthesis ratio 1 :1) allowing a reversible, self-healing and slow crystallization. After 15 days at 120 °C cubic crystals with 666 ± 72 nm in length and width were observed. Typical characterization techniques, such as XRD, IR, physisorption and NMR confirmed the claimed structure. These examples show the successful crystallization of hexagonal and tetragonal organic frameworks. The great variety of organic building blocks applicable as starting materials offers great potential to design new porous solids.

1.4.3. 2D Channels in 3D Structures.

In 2007 Yaghi extended the idea of linking organic building blocks by covalent bonds from two-dimensional structures to 3D frameworks. This was accomplished by linking tetrahedral and triangular building blocks together (Figure 1.10).

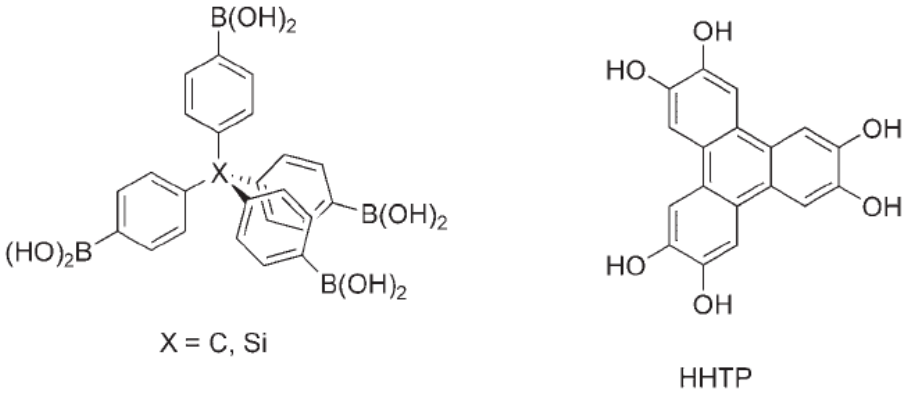

Figure 1.10: Tetrahedral and triangular building blocks for the synthesis of 3D COFs.

Tetra(4-dihydroxyborylphenyl)methane (TBPM), for example, reacts in a self-condensation reaction to form triangular B_3O_3 rings giving the so-called COF-102. This tetrahedral building block TBPM can also undergo a co-condensation reaction with HHTP forming C_2O_2B rings and resulting in the framework structure of COF-105. Using the silane-analog of TBPM, tetra(4-dihydroxyborylphenyl)silane (TBPS) in self- or co-condensation reactions gives COF-103 and COF-108, respectively.[31]

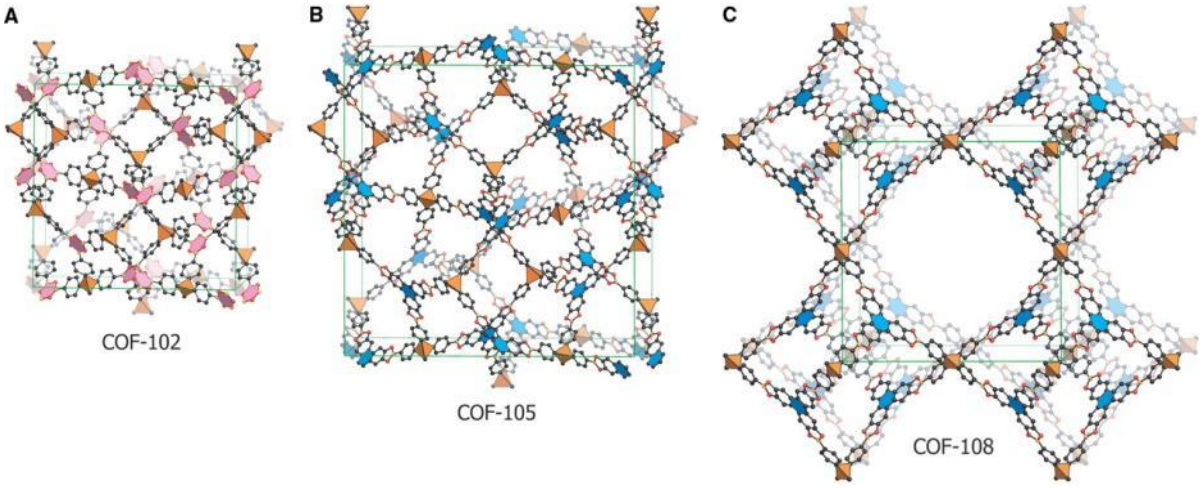

Figure 1.11: Modeled crystalline structure of COF-102 (**A**), COF-105 (**B**), and COF-108 (**C**). Color code: Carbon is grey, boron is illustrated as orange and oxygen atoms are represented as red.[31]

These structures are among the most porous frameworks, exhibiting fully accessible porosity with surface areas as high as 4210 m^2/g (COF-103), comparable to the surface areas of MOFs such as MOF-177 (4500 m^2/g)[44] and MIL-101.[45] Furthermore COF-108 is one of the most porous organic materials with the lowest density (0.17 g/cm^3) reported.[31] Expanding the idea of reticular chemistry Hunt *et al.* employed the condensation of borosilicate clusters, known from the borosilicate glass Pyrex, to build thermally and chemically stable 3D COFs. COF-202 is formed by B-O-Si linkage of *tert*-butylsilane and the tetrahedral tetra(4-dihydroxyboryl-phenyl)methane (Figure 1.12). The *tert*-butyl groups are facing into the pores of the network providing a chemically transformable site with sufficient space for further reactions.[46]

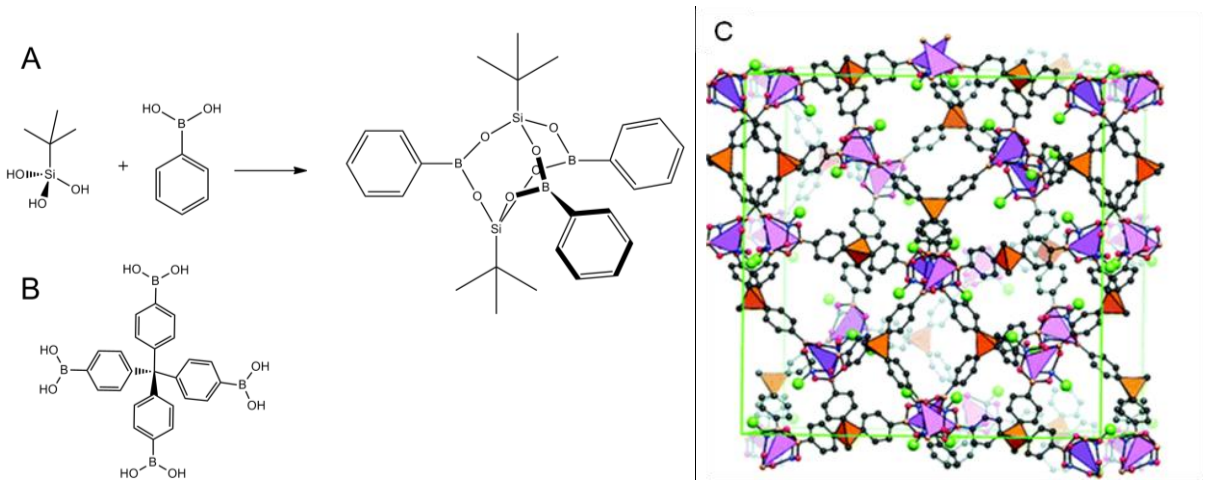

Figure 1.12: A) Condensation of tertbutylsilane triol with a benzeneboronic acid forming a borosilicate cage. B) Using tetra(4-dihydroxyboryl-phenyl)methane as boronic acid reagent gives 3D crystalline framework with the crystalline structure depicted in C).[46]

The above discussed properties combined make 3D COFs promising candidates for gas storage applications.

1.4.4. COFs as Gas Storage Materials

The adsorption of gases is a widely studied property of porous solids. Therefore porous materials have attracted a great deal of attention as possible storage material for gases such as hydrogen, methane or carbon dioxide. Especially recent incidences, such as the nuclear power explosion in Japan or the devastating Deepwater Horizon oil spill in the Gulf of Mexico demonstrate the urgent need for clean and sustainable energy sources. To collect and store greenhouse gases, such as methane and carbon dioxide, the improvement of kown or the invention of new porous solids is being extensively studied. The use of hydrogen as a substitutional energy source requires a secure and efficient storage facility with high capacities at managable conditions.

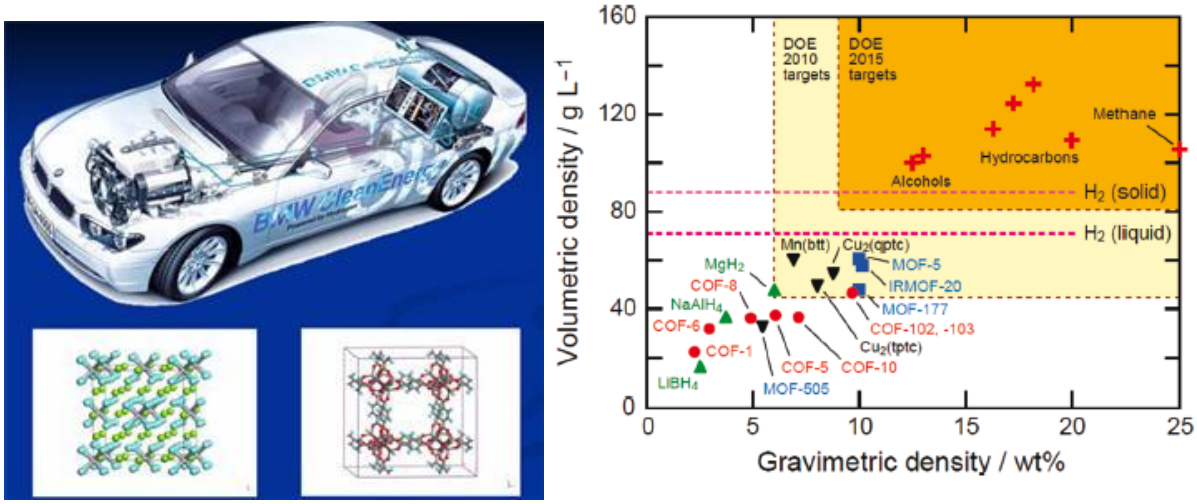

Figure 1.13: Illustration of a car operated with hydrogen fuel, DOE Targets for gas storage compared to the best performances of MOFs and COFs. [47]

The US Department of Energy (DoE) targets a gravimetric capacity of 7.5 wt% H_2 until the year 2015 (corner of orange panel in Figure 1.13).[48] Besides metal hydrides, zeolites and porous carbon materials, MOFs are very promising candidates for this purpose.[18] MOF-177 surpasses the volumetric capacity of 6 wt% targeted by the DoE until 2010 (Figure 1.13).[49] However, the best gas uptake reported for MOFs is at low temperatures such as 77 K. For example, MOF-210, which is a structure composed of octahedral $ZnO_4(CO_2)_6$ with two organic linkers biphenyl-4,4´-dicarboxylate and 4,4′,4″-[benzene-1,3,5-triyl-tris(ethyne-2,1-diyl)]tribenzoate exhibits a total uptake of 15 wt%, exceeding the high values earlier reported for MOF-177 (7.5 wt%) and MOF-5 (7.1 wt%). MOF-210 exhibits a BET surface area of 6240 m^2/g, and the authors claim this to be the highest reported surface area for any solid.[50] Only accessible metal sites in a porous framework are beneficial for the uptake of hydrogen and lead to an enhancement of the storage capacity. Otherwise a reverse effect will occur due to the fact that they add weight to the material .[51] As briefly discussed in the previous section, COFs are also a very promising class of materials for gas storage applications. They combine the benefits

of MOFs, such as high surface areas, high permanent porosity and thermal stability with a framework exclusively made of light elements. This results in a framework with ultra low densities, enabling a higher amount of hydrogen storage.[52] To illustrate the H_2 adsorption of COFs, several groups carried out theoretical studies based on quantum mechanical simulations and force field simulations. Grand Canonical Monte Carlo simulations were carried out by Han *et al.* to predict H_2 adsorption isotherms for several COFs. In order to evaluate the accuracy of the theoretical output the calculated values of COF-5 were compared to the experimentally obtained H_2 adsorption isotherm for COF-5. Due to a good agreement of the simulated value of 3.4 wt% and the experimental value of 3.3 wt% (80 bar, 77 K), the theoretical approach was evaluated as useful.

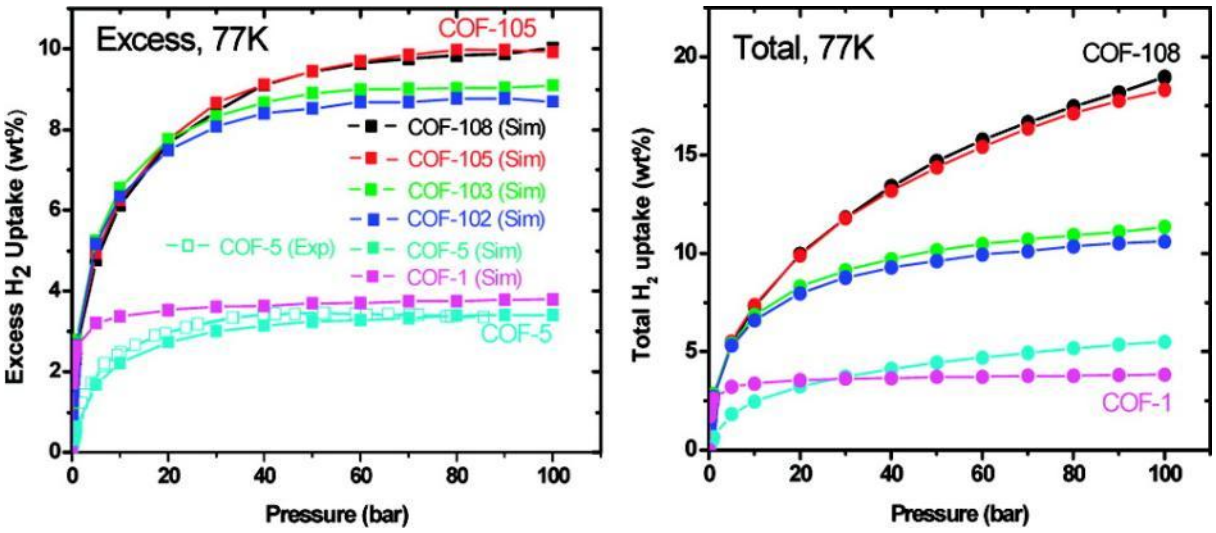

Figure 1.14: On the left: comparison of excess hydrogen uptake of different COFs (open symbols represent experimental results, filled symbols simulated results). On the right: total H_2 adsorption isotherms in gravimetric units (wt %) at 77 K.

Predictions were also made about COF-1, COF-102, COF-103, COF-105 and COF-108 (Figure 1.14). For COF-105 ad COF-108 values of 10 wt% at 77 K are calculated.[53] This would even outshine the best performance of MOF-210 (Figure 1.15).

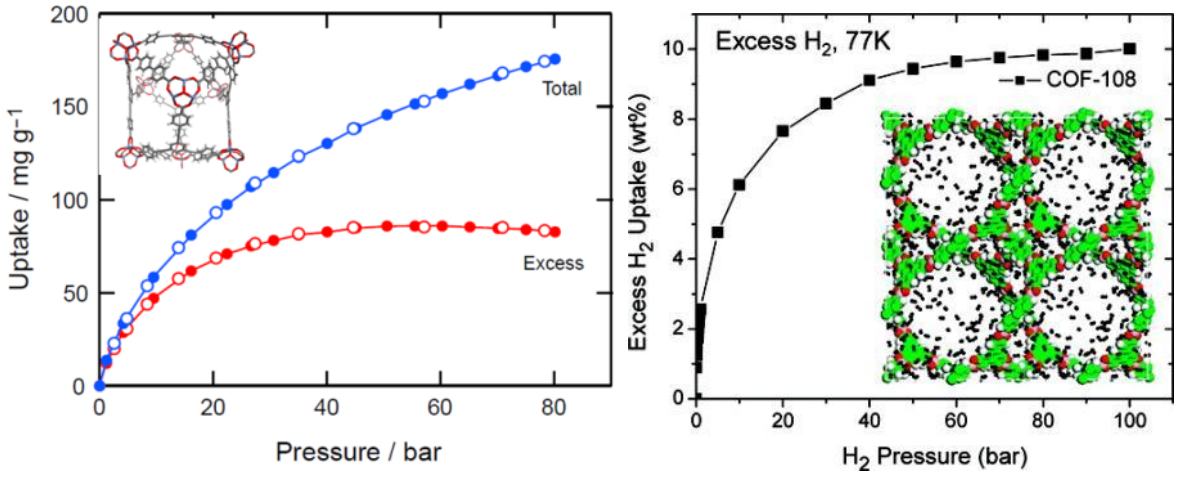

Figure 1.15: Comparison of H_2 uptake of MOF-210 (left curve) and COF-108 at 77 K (right curve)(simulated).

Klontzas *et al.* calculated the gravimetric and volumetric isotherms of hydrogen adsorption for COF-102,- 103, -105 and -108 at 77 K and 300 K. The authors find comparable uptake for COF-102, -103 and IRMOF-14, due to the small pores of the COFs. The volumetric storage capacity is similar, since these structures exhibit similar surface areas and comparable strong binding sites. The large pores of COFs -105 and -108 showed also significantly higher amounts of H_2 uptake compared to MOFs. Moreover, considering the lightweight framework with extremely low density results in a two times bigger gravimetric H_2 uptake in COFs.[51] Further simulations carried out by Smit and co-workers gave similar results. The authors investigated the hydrogen adsorption capacity of COF-102, COF-103, COF-105 and COF-108 at ambient and cryogenic temperatures.[54] Furthermore the effect of doping the frameworks with lithium was simulated. In Figure 1.16 the calculated positions of the lithium are depicted.

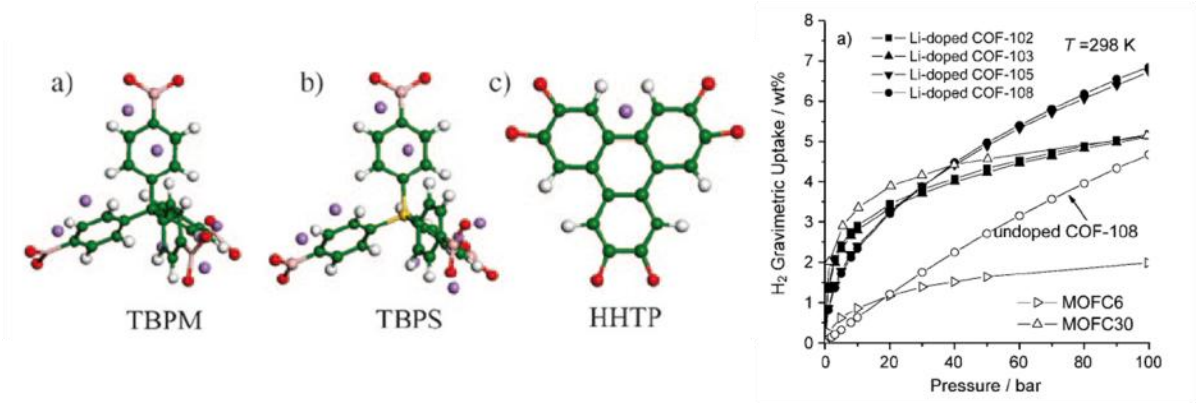

Figure 1.16: Illustration of Li-doped building blocks for COF-102(a),-105(b) and -108 (c), calculation of H_2 adsorption isotherms for COFs in gravimetric units (wt %) at 298 K compared to undoped COF-108 and MOFC6 and MOFC30.[54]

At 77 K COF-105 and COF-108 showed hydrogen adsorption capacities of 18.05 and 17.80 wt%, respectively. These values are very promising compared to the highest values obtained with MOF-177 (10 wt %). At 298 K the simulated H_2 storage capacities of COF-105 and COF-108 reach 4.67 and 4.51 wt%, respectively (Figure 1.16). Furthermore, H_2 storage capacities of newly-designed COFs comprising diphenyl, triphenyl, naphthalene and pyrene building blocks were examined (see linkers and structures in Figure 1.17).

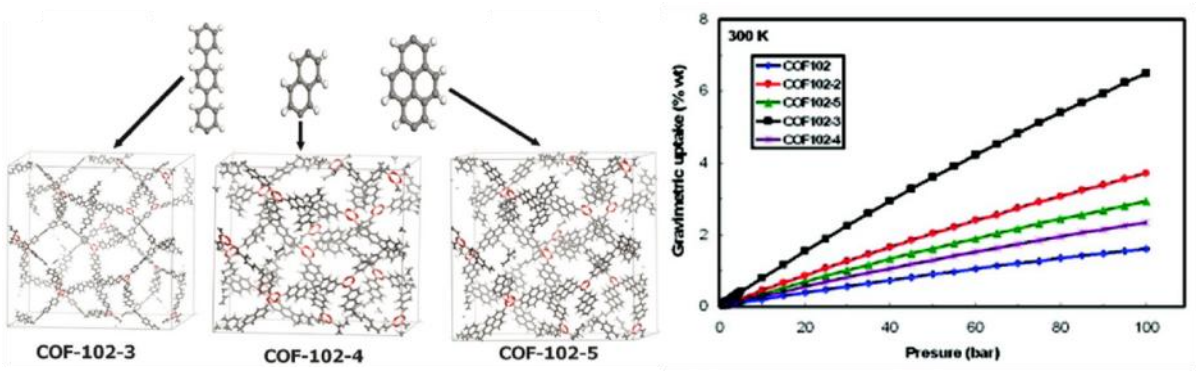

Figure 1.17: Design of theoretical COFs having the same topology as COF-102 with terphenyl, biphenyl and pyrene building blocks, comparison of calculated gravimetric H_2 adsorption isotherms at 300 K of COF-102 (blue) and new

constructed COF-102-2 (red), COF-102-3 (black), COF-102-4 (purple), COF-102-5 (green).[55]

By means of theoretical calculations co-workers of Froudakis claimed that these designed COFs would even be superior to the already realized COF-108. Materials with properties suggested by theoretical calculations might further stimulate synthesis efforts and help to realize potential candidates to fulfill the DoE targets by 2015.[55] First experimental proof was given in studies by Furukawa *et al.* comparing the gas uptake of 3 different groups of COFs (Table 1.1), namely group (1) the microporous materials COF-1 and COF-6, group (2) the mesoporous COFs -5, -8, -10 and group (3) the 3D systems COF-102 and- 103.[56]

Table 1.1: Comparison of porosity and gas uptake of COFs with other porous materials.

material	composition	pore size/ Å	S_{BET} /m^2 g^{-1}	$V_{p,DR}$ /cm^3 g^{-1}	Q_{st} /kJ mol^{-1}	H_2 uptake /mg g^{-1}	CH_4 uptake /mg g^{-1}	CO_2 uptake /mg g^{-1}
COF-1	C_3H_2BO	9	750	0.30	6.2	14.80	40 (44)	230
COF-5	$C_9H_4BO_2$	27	1670	1.07	6.0	35.8	89 (127)	870
COF-6	$C_8H_3BO_2$	9	750	0.32	7.0	22.6	65 (68)	310
COF-8	$C_{14}H_7BO_2$	16	1350	0.69	6.3	35.0	87 (114)	630
COF-10	$C_{12}H_6BO_2$	32	1760	1.44	6.6	39.2	80 (124)	1010
COF-102	$C_{25}H_{24}B_4O_8$	12	3620	1.55	3.9	72.4	187 (243)	1200
COF-103	$C_{24}H_{24}B_4O_8Si$	12	3530	1.54	4.4	70.5	175 (229)	1190
MOF-5	$C_{24}H_{12}O_{13}Zn_4$	12, 15	3800		4.8	76	120 (at 300 K)	970 (40 bar)
MOF-177	$C_{54}H_{30}O_{13}Zn_4$	11, 17	4750		4.4	75.2		1490 (40 bar)
IRMOF-6	$C_{30}H_{18}O_{13}Zn_4$	10, 15	2800			48.5	160	870 (40 bar)
MIL-101(Cr)	$C_{24}H_{12}O_{13}FCr$	29, 34	4230	2.15			160	1760 (50 bar)
zeolites			260−590	0.2−0.36			31−82	220−350
Mesoporous silica			450−107				14−65	

S_{BET} is the BET surface area. $V_{p,DR}$ is the measured total pore volume. D_{bulk}. Q_{st} is the isosteric heat of adsorption for H_2 at zero coverage. H_2 uptake is the saturation H_2 uptake at 77 K. CH_4 and CO_2 uptakes are those at 35 and 55 bar, respectively, and 298 K. The CH_4 uptakes in parentheses are the uptakes at 85 bar and 298 K.[56]

Performing low-pressure H_2 uptake and high-pressure gravimetric adsorption measurements, the authors were able to confirm the high storage capacities already

predicted by theoretical simulations. Among porous solids group (3) materials showed excellent performance. Since similar values were obtained for group (3) COFs and MOFs a structure-independent H_2 capacity was implied (Figure 1.18).

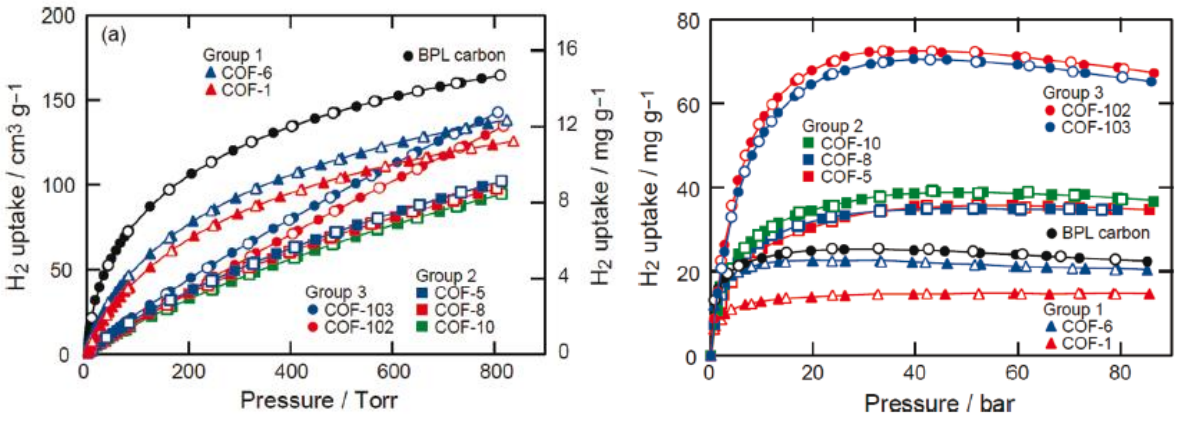

Figure 1.18: left: data for low-pressure H_2 isotherms for group 1 (▲), 2 (■) and 3 (●) COFs. Right: high-pressure H_2 isotherms for group 1 (▲), 2 (■) and 3 (●) COFs. Both measured at 77 K and BPL carbon is added for comparison.[56]

Creating high-affinity sites in COFs by metal doping was simulated and yielded a theoretical increase of H_2 storage capacity at room temperature.[56] Calculations predict that the capacity for hydrogen can be doubled by insertion of metal clusters such as lithium into the pores of the framework. Lithium doping in MOFs almost doubled the hydrogen uptake.[57] Hereby it is important to consider the optimized amount and distribution of positively charged Li ions in the framework. Calculations predict the best performance with COF-105 and COF-108, reaching values of 6.84 wt% and 6.73 wt% respectively, at 100 bar and 298 K.[54] Studies about hydrogen storage capacities of a non-doped and Li-doped borosilicate COF, COF-202 indicated that Li-doped COF-202 has a gravimetric uptake of 4.39 wt% at 298 K and 100 bar.[58] These outstanding results need to be experimentally confirmed, and it should be considered that such metal clusters would also be extremely water sensitive. Other groups suggested substitutional doping to enhance hydrogen

uptake of COFs. In simulation experiments Li *et al.* postulated that replacing boron in the C_2O_2B rings in COF-108 with aluminum and the oxygen with nitrogen or substituting boron with nitrogen and oxygen with magnesium increases the stored amount of H_2 by the factor of two or nearly three, respectively. The calculations were made for room temperature and pressures up to 100 bar.[52] Substitution of aromatic carbon atoms in COF-1 with boron and subsequent doping with metal ions, such as calcium, titanium or scandium is another possibility to enhance hydrogen storage in organic frameworks.[59] However one has to keep in mind that these are only calculations for materials that are not realized yet. On the other hand doping of existing COFs might lead to an efficient increase of sustainable hydrogen storage.

1.4.5. COFs as Electroactive Materials

Recently Jiang and co-workers suggested that charge carriers can be transported along the framework of COFs. They reported highly ordered conjugated pyrene-containing COFs. The co-condensation reaction of the **t**riphenylene HHTP and the **p**yrenediboronic acid (PDBA) results in a hexagonal crystalline framework (TP-COF, see Figure 1.19) with eclipsed arrangement resulting in open pores with a diameter of 3.14 nm and a specific surface area of 868 m^2 g^{-1}.

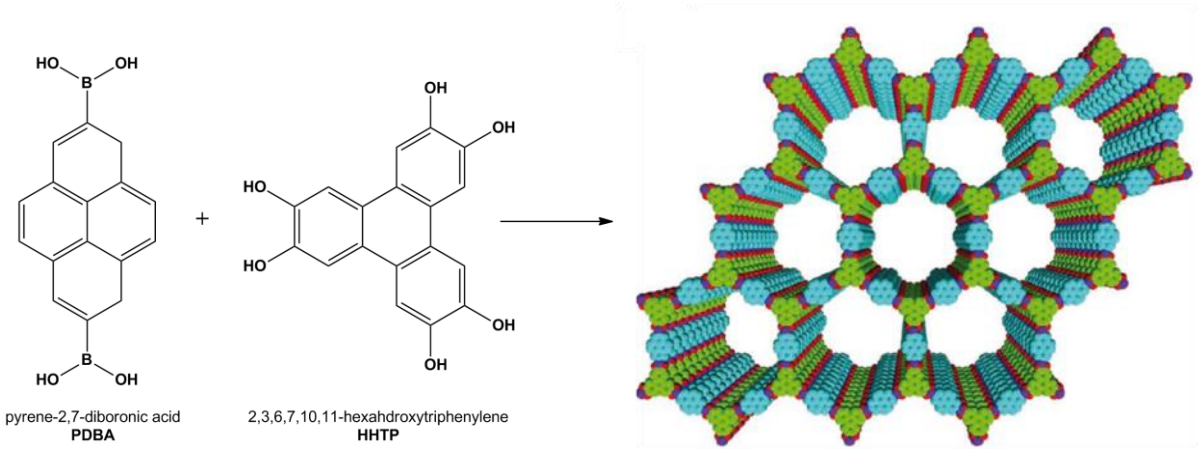

Figure 1.19: Reaction pathway for TP-COF, synthesized by a co-condensation reaction of pyrenediboronic acid and hexahydroxytriphenylene. Schematic structure of TP-COF based on quantum chemical calculations and crystal lattice parameters. Boron in purple, oxygen in red, triphenylene in green and pyrene in blue.[60]

TP-COF exhibits semiconducting properties and blue luminescence.[60] A blue luminescence has been previously reported for polyboronate.[61, 62] Excitation at 376 nm or at 417 nm results in an emission at 474 nm (Figure 1.20 A, dotted curve in Figure 120 B) and excitation at 340 nm resulted in a strong emission at 376 nm from the pyrene units and a negligible weak emission at 402 nm from the triphenylene units (Figure 1.20 B, black curve), a mere mixture of the starting materials however displayed an emission at 402 nm. Furthermore the

electrical conductivity was measured using the two probe method. For semiconducting material a linear I-V curve is expected, this was observed for TP-COF at ambient standard conditions, with a current of 4.3 nA at a bias voltage of 2 V between a 10 µm gap: Upon doping the framework with iodine a significant rise in current up to 20 nA was observed (Figure 1.20 C), confirming the p-type semiconducting character of TP-COF.

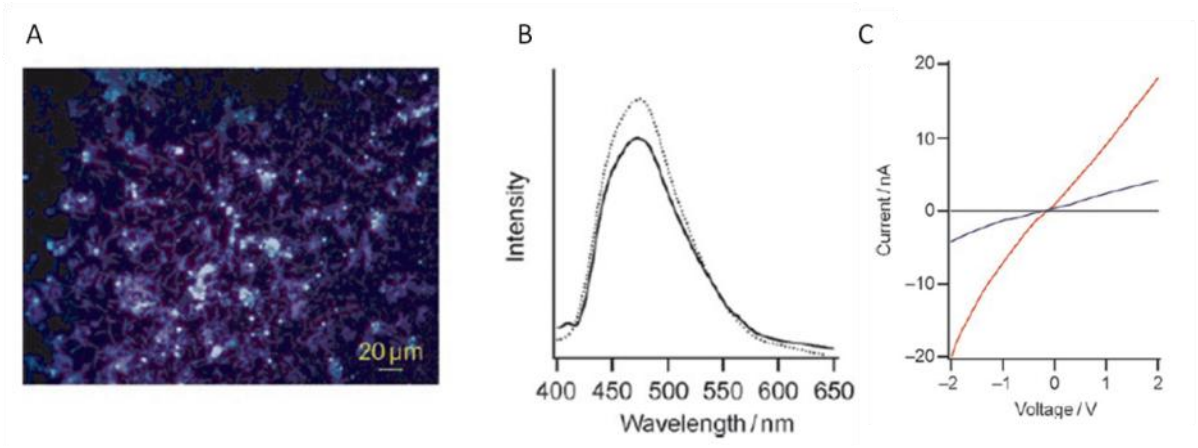

Figure 1.20: A) Fluorescence image of TP-COF; B) Fluorescence spectrum of TP-COF upon excitation at 340 nm (black line) upon excitation at 376 nm (dotted line); C) I-V curves of TP-COF across a 10 µm gap between two Pt electrodes, black line gap without TP-COF, blue with TP-COF and red with iodine-doped TP-COF.[60]

A self-condensation of pyrenediboronic acid (Ppy-COF see Figure 1.21 A) also results in an optoelectronically active framework with a pore size of 1.73 nm and a specific surface area of 923 m^2/g. Ppy-COF generates photocurrent of 5 nA (Figure 1.21 B), due to the defined conduction paths for charge migration provided through the highly ordered structure.[63]

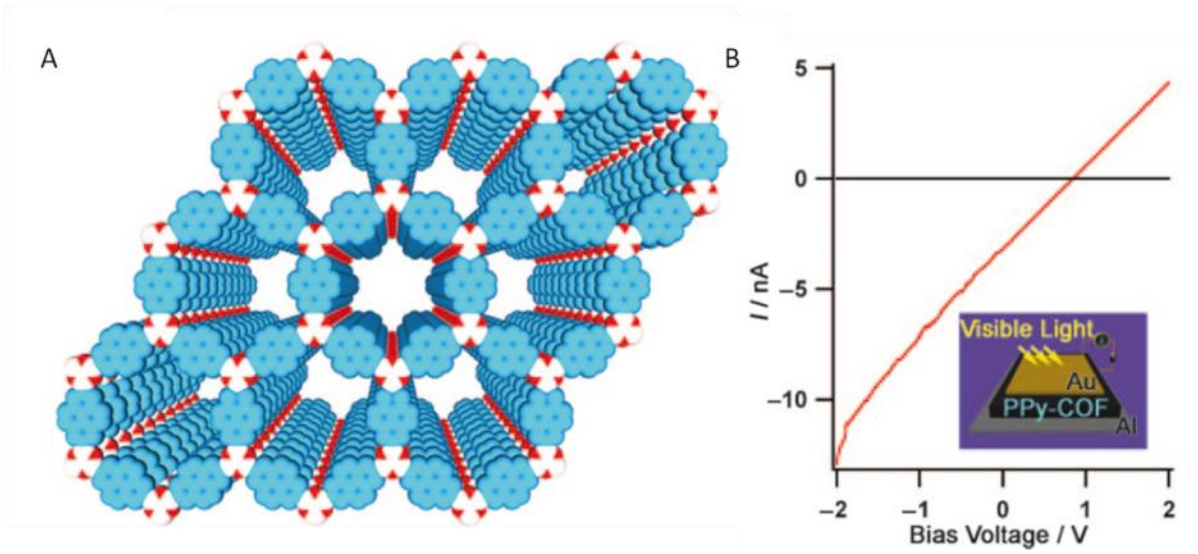

Figure 1.21: A) Top view of hexagonal structure of Ppy-COF based on quantum-chemical calculations and crystal lattice parameters (B white, O red, pyrene blue); I-V curves of Ppy-COF sandwiched between a transparent Au electrode and an Al electrode without irradiation (black line) and upon irradiation with a xenon light > 400 nm (red line).[63]

Another highly photoconductive COF was reported with a tetragonal metallophthalocyanine building block, NiPc–COF (Figure 1.22A), which exhibits high charge carrier mobilities. Incorporating phthalocyanine into the framework broadens the absorption profile of the COF. The eclipsed stacking of the phthalocyanine and arene boronic acid leads to an open framework with a surface area of 624 m^2/g and a micropore diameter of 1.9 nm. Upon irradiation with a xenon lamp the current increased from 20 nA to 3 μA, furthermore panchromatic photoresponse was very fast and reproducible without deterioration.[42]

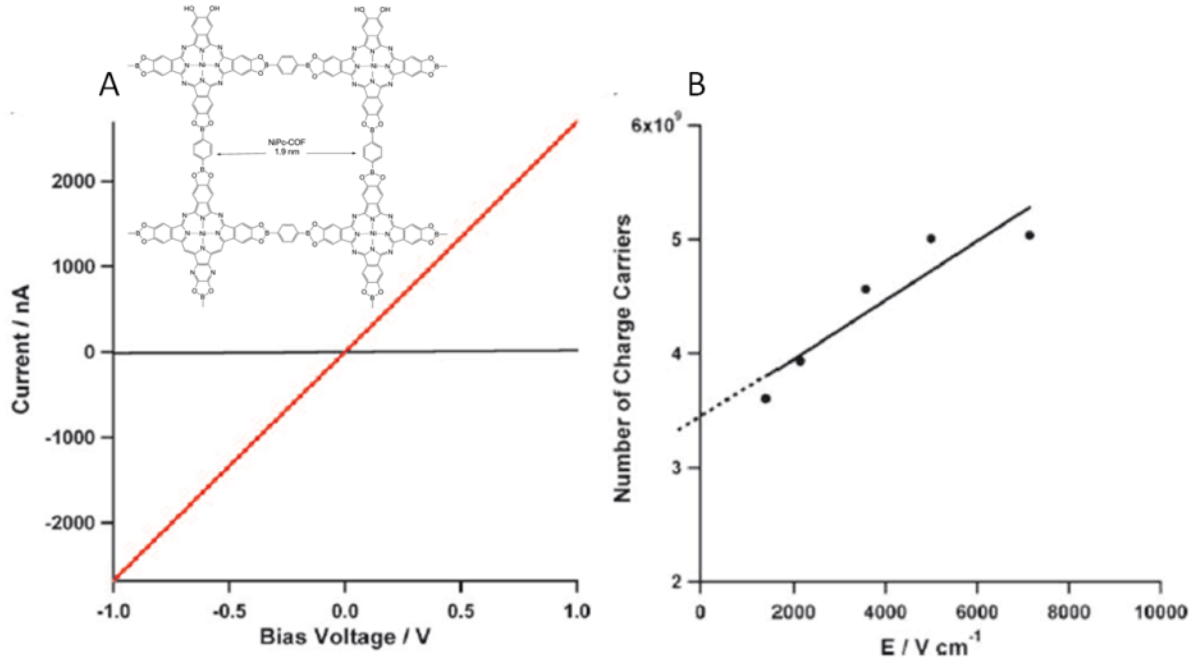

Figure 1.22: A) I-V curves of NiPc-COF without irradiation in black and upon irradiation with a xenon lamp in red; B) Number of charge carriers measured by the time-of-flight transient current integration at different bias voltages, irradiated with a 355 nm pulsed laser at 6.5×10^{-14} photons /cm^2.[64]

Yaghi extended the scope of macrocyclic COFs exhibiting semiconductor properties with two new structures (Figure 1.23) based on condensation reaction of porphyrin (Figure 1.23) by either a boronate ester formation with tetrahydoxyanthracene (COF-66) or imine bond formation with terephthalaldehyde (COF-366).

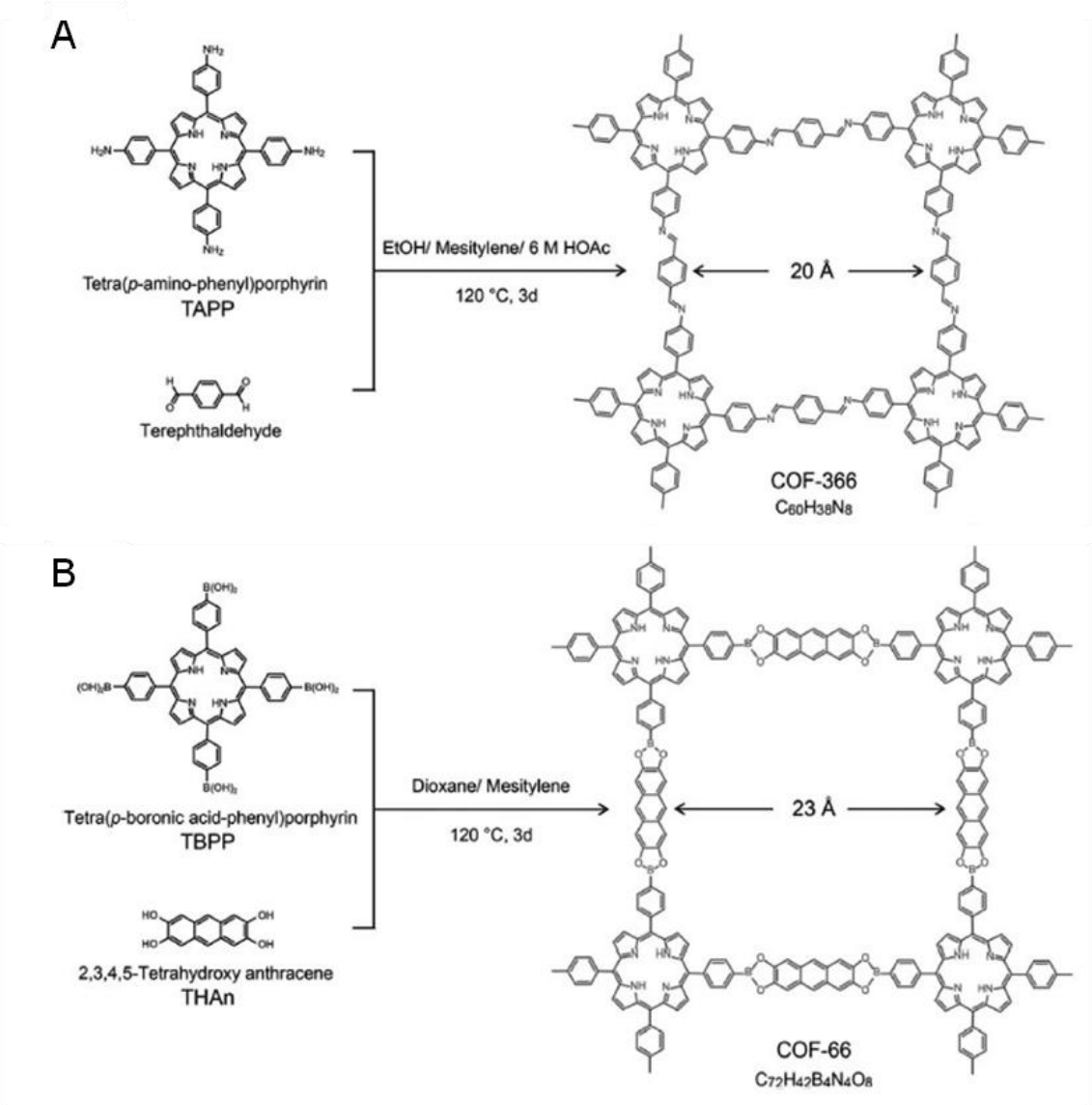

Figure 1.23: Schematic reaction pathway for A) COF-366 synthesized by imine bond formation of terephthalaldehyde and tetraamino porphyrin and B) COF-66 formed by boronate ester formation of tetrahydroxyanthracene and porphyrin tetraboronic acid.[34]

With Time of Flight (ToF) measurements of a 1.5 µm thick COF/ poly(methylmethacrylate) (60 : 40 wt %) film sandwiched between indium tin oxide and aluminum the hole mobilities of COF-66 and COF-366 were determined to be as high as 3.0 cm^2/V s and 8.1 cm^2/V s, respectively.[34]

The first electron-transporting COF was achieved by substituting the benzene groups at the edges of the NiPc-COF with electron-deficient benzothiadiazole (BTDA) building blocks (Figure 1.24). The resulting n-channel NiPc-BTDA COF exhibits the excellent electron mobility of 0.6 cm^2/V s. The absorbance is very broad and ranges up to 1000 nm, resulting in a panchromatic photoresponse with high sensitivity to near-infrared photons. Upon excitation with white light enhanced conductivity from 250 nA to 15 μA was detected.[65]

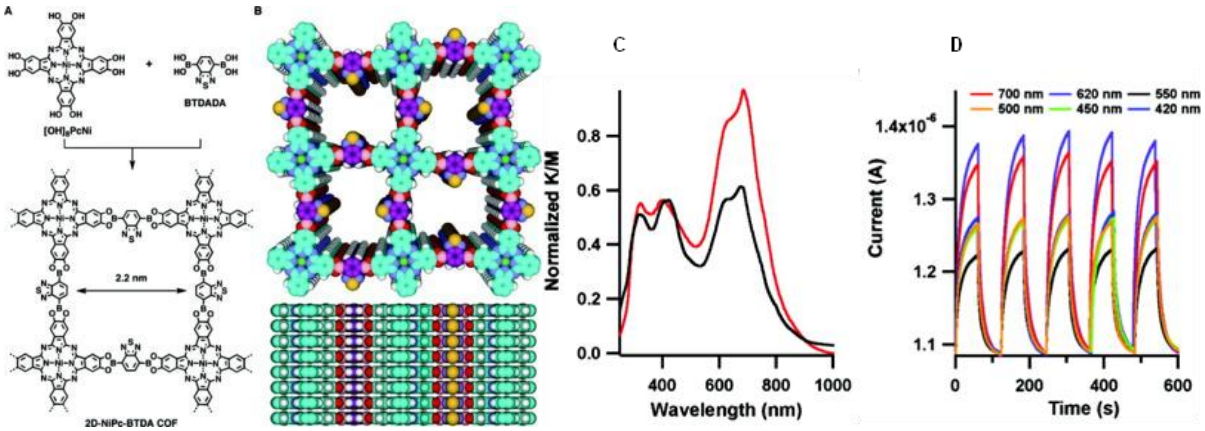

Figure 1.24: A) Schematic reaction pathway for NiPc-BTDA COF and B) top and side view of the framework showing the eclipsed stacking (Pc, sky blue; BTDA, violet; Ni, green; N, blue; S, yellow; O, red; B, orange; and H, white), C) Absorbance spectra of 2D-NiPc-BTDA COFs (red) and $[MeO]_8PcNi$ (black), D) (F) On–off switching of photocurrent of 2D-NiPc-BTDA COFs at the bias voltage of 1.0 V with different wavelengths.[65]

1.5. Self-Assembled Monolayers (SAMs)

Self-Assembled Monolayers are highly ordered layers of long chain hydrocarbons that are adsorbed either from the solution or gas phase onto the surface of a solid support. The adsorbed molecules typically assemble spontaneously with a certain symmetry on the substrate. Molecules used in such a self-assembly process must feature a special structure, comprising a functional head group possessing a strong affinity to a specific substrate. The most extensively investigated SAMs are alkanethiol molecules on gold[66, 67] and silane monolayers on silicon dioxide.[68] The thiol head groups bind very well to gold surfaces, due to the high binding energy of gold and sulfur. The head group is typically connected to the tail group through a long alkane chain (spacer). In Figure 1.25 the assembly of such long chain thiols on gold is shown.

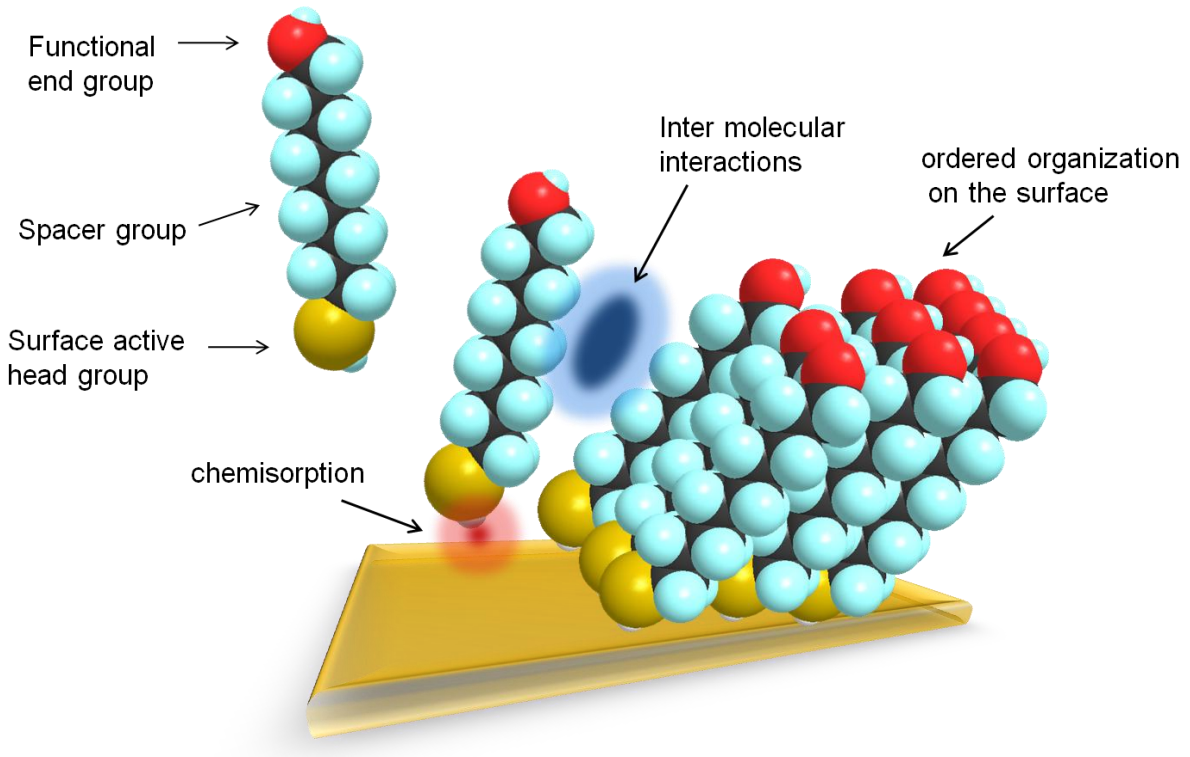

Figure 1.25: Schematic illustration of a Self-Assembled Monolayer on a substrate.

These special surfaces can be designed with different chemical functionalities. Another widely used type of SAM is the covalent bonding of organosilicon compounds on silicon oxide surfaces.[69] A major advantage of silane SAMs compared to thiol SAMs is their significantly higher thermal stability. Thiol monolayers are stable up to not more than 145 °C, whereas silane monolayers typically start to decompose at 250 °C. Perfluorodecyltriethoxysilane (PFDS) is even stable up to 350 °C. However the preparation of thiol SAMs on Au (111) surfaces is rather quick and efficient.[70] Au (111) surfaces are the best choice for thiol anchoring, since the surface roughness is usually low. Furthermore Au (111) surfaces can be readily produced by evaporation of gold on clean and planar surfaces, such as mica, glass or silicon.[71-73] SAM formation is strongly influenced by several synthesis parameters, such as concentration of the reaction solution, immersion time, solvent, water traces and temperature.[74, 75] Thiol SAMs are readily synthesized by immersion of a cleaned gold surface in an ethanolic solution of the desired thiol for about 24 h.[76] Prior to use the substrate has to be cleaned thoroughly either with a strong acid or by plasma cleaning. For silane SAMs this procedure also helps to activate the surface by creating numerous OH-groups on the silicon surface.[77]

A combination of several techniques allows one to fully characterize the monolayer formation. Thickness of the monolayer can be determined by ellipsometry.[78] Polarity, roughness and order of SAM formation can be investigated by contact angle measurements.[79] Information about functional groups and their orientation can be obtained by reflectance absorption infrared spectroscopy (RAIR)[80] and the surface topology at the nanoscale can be investigated by AFM.[81]

On a Au (111) surface the sulfur atoms occupy every sixth hole between three gold atoms and create a (√3x√3)R 30° superlattice with hexagonal structure. The literature suggests that the thiol molecules organize on the surface adopting a secondary ordering of the chains corresponding to a c(4 × 2) superlattice.[82, 83]

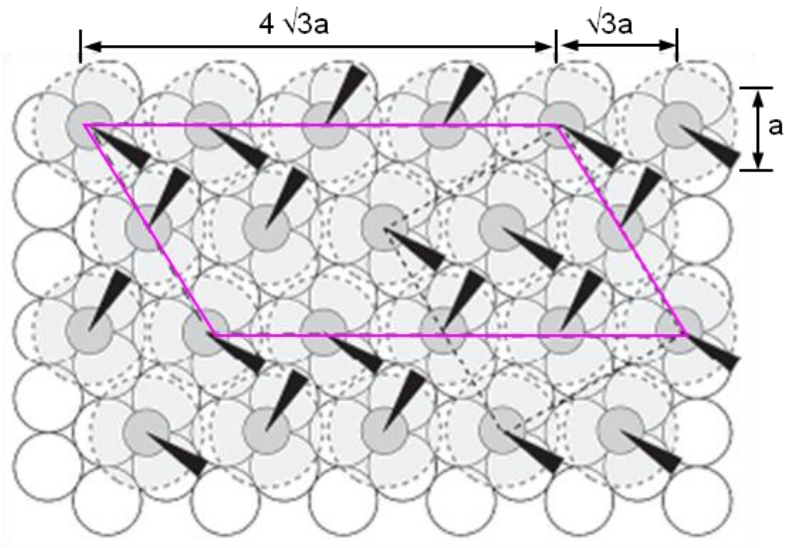

Figure 1.26: Model of the structured adlayer formed by decanethiolates on Au(111) (dark circles: sulfur atoms, white circles: gold atoms and dashed circles: projection of the alkane chain.)

In Figure 1.26 the circles with dashed lines indicate the projection of the alkane chains showing the occupied surface area. The dark wedges indicate the projection of the CCC plane of the alkane chain onto the surface, the alkane chains are tilted in the direction of their next-nearest neighbors. Between each pinning centre a distance of 5.0 Å results due to this geometry, thus for every molecule an area of 21.4 $Å^2$ is available. Due to a van-der-Waals diameter of only 4.6 Å the chains cannot occupy the whole area and tilt forming an angle of approximately 30° with the surface normal.[84]

It has been shown that SAMs with increasing chain length pack with increasing order and coverage (C ≥ 12). The low order and coverage of SAMs with short chain

lengths is explained by weak interchain interactions and by an increasing concentration of gauche defects.[85]

1.6. Growth of Oriented Thin Films of Crystalline Porous Frameworks

1.6.1. Direct Growth Approach

Herein the oriented growth of COFs on gold substrates functionalized with a boronic acid terminated SAM is examined. The concept to align porous solids, e.g. zeolites or MOFs on organic interfaces has been frequently shown in the past decade.[86, 87] The direct growth approach of MOFs was described by Biemmi *et al.* using thiol SAMs with –OH, COOH and -CH_3 end groups to mimic the functional group of the organic linker (benzenetriscarboxylic acid) used for HKUST-1 ($Cu_3(BTC)_{2)}$ synthesis (Figure 1.27).[88]

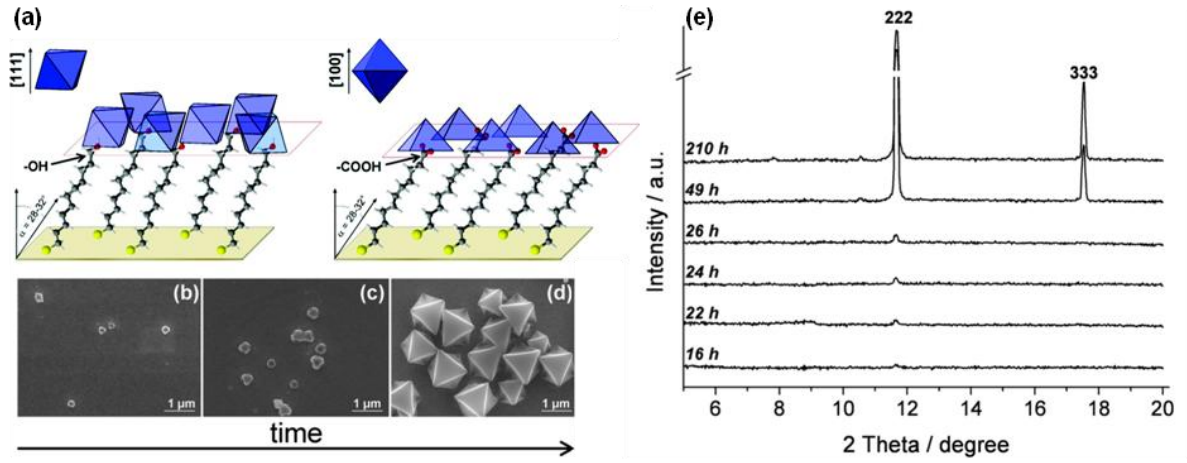

Figure 1.27: (a) Schematic illustration of oriented growth of HKUST-1 nano-crystals on a 11-mercaptoundecanoic acid SAM (left) and on 11-mercaptoundecanol modified gold surfaces (right). (b-d) Scanning electron micrographs of face-down samples after immersion in the crystallization solution for (b) 16, (c) 24, and (d) 45

h. (e) Diffraction patterns of [111]-oriented $Cu_3(BTC)_2$ crystals on OH SAMs collected after immersion times between 16 and 210 h.[88]

Due to the two different coordination sites of HKUST-1 it is possible to achieve differently oriented nucleation on a gold substrate functionalized with either a carboxylic acid or a hydroxyl terminated SAM. Oriented growth of several MOFs by the direct growth approach is well established. Within this thesis the concept of using functionalized organic interfaces to induce oriented growth was adapted to align COFs parallel to the substrate. In Figure 1.28 the concept of direct growth of COFs is illustrated schematically.

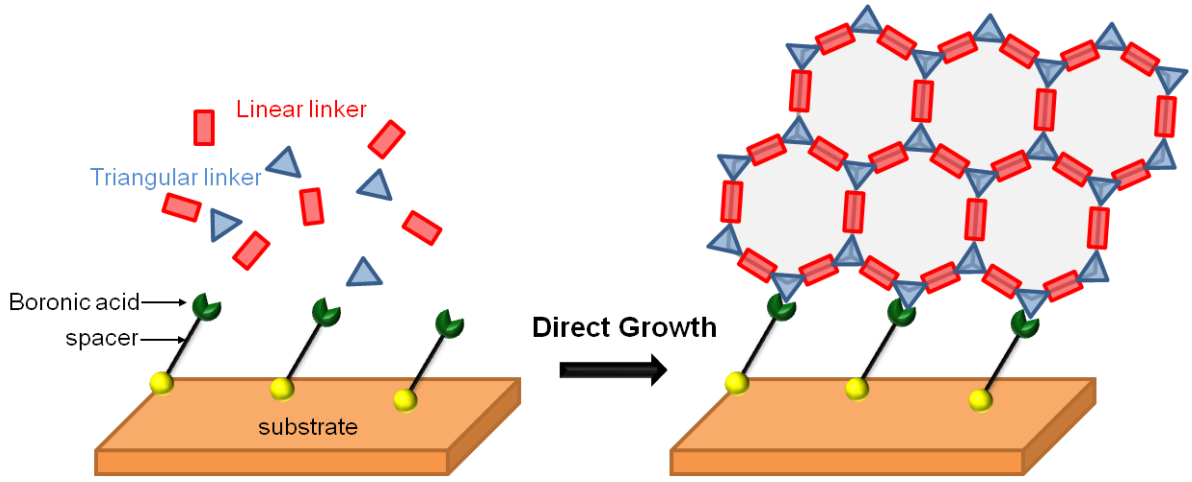

Figure 1.28: Schematic illustration of the concept of direct growth of COFs on SAM functionalized substrates.

The general idea is based on introducing boronic acid end groups on a gold substrate. These substrates can then be incorporated in different COF syntheses. Thereby a preferential directional growth on the gold substrate is encouraged. Functionalizing the gold surface with mercaptophenylboronic acid (Figure 1.29) might lead to a first condensation of the catechols of the polyol to the boronic acid end group of the SAM. This induces further growth of the crystal in one direction with covalent bonding to the surface. The oriented growth of COF-10 and TT-COF

on mercaptophenylboronic acid functionalized gold substrates is presented in Chapter 6.

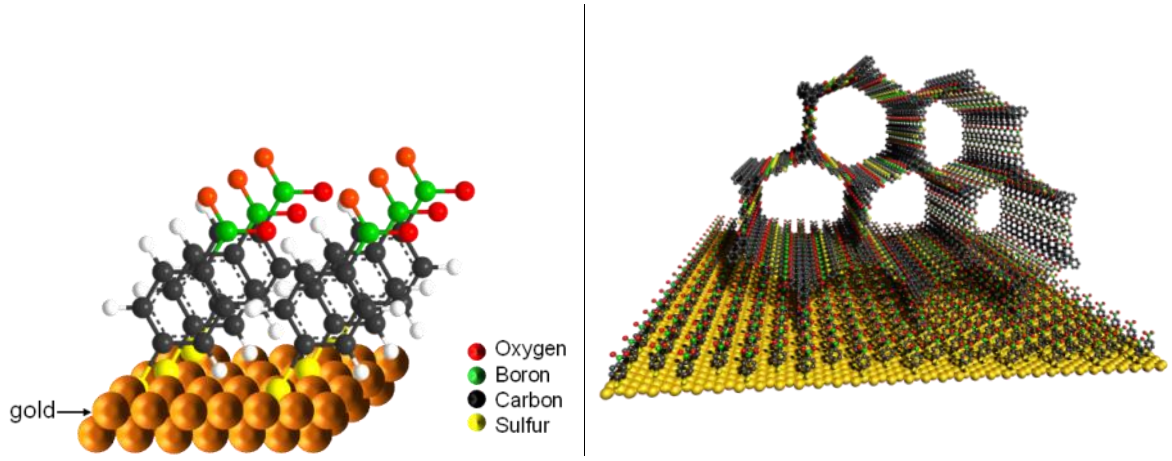

Figure 1.29: Gold surface functionalized with mercaptophenylboronic acid (left). SAM-functionalized surface with COF material grown with preferred orientation (both schematic).

1.6.2. Honeycomb on Graphene

One of the most exciting features of some COFs is a framework made up of π-stacked aromatic building blocks that creates porous networks with electronically coupled 'walls'. The portfolio of the already reported semiconducting and photoconducting COFs is described in detail in section 1.4.5. All of these systems were, however, synthesized as bulk powders, with no control over the orientation of the pore system. As a result, it has not been possible to use COFs in functional devices such as photovoltaic cells or chemical sensors.

Writing in *Science*, William Dichtel and colleagues[89] at Cornell University now report the synthesis of oriented, two-dimensional COF films on single-layer graphene surfaces. In particular, they show that the graphene surfaces, which are supported on various substrates, can act as templates for the growth of COF layers

with accessible pores aligned in the same direction. With this synthetic breakthrough, and the variety of electroactive building blocks accessible through organic chemistry, the design, synthesis and integration of charge-transporting COFs should be possible.

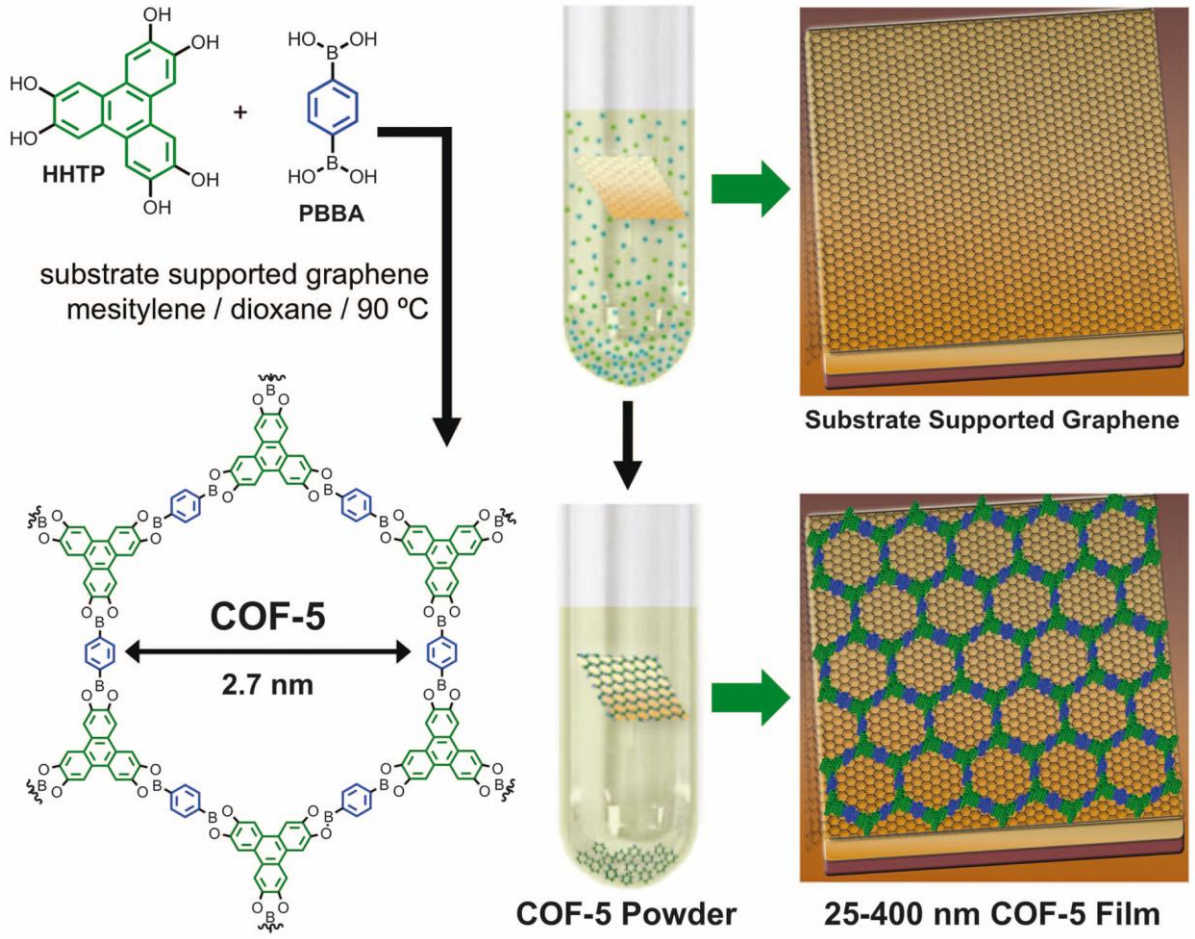

Figure 1.30: The synthesis of a Covalent Organic Framework known as COF-5 on single-layer graphene. COF-5, which has a hexagonal lattice, is prepared using a solvothermal condensation reaction between PBBA (a compound composed of a benzene ring with two boronic acid groups ($R–B(OH)_2$) attached at opposite ends) and HHTP (a flat trigonal building block composed of four fused benzene rings with two OH groups at each corner). By carrying out the reaction in the presence of substrate-supported graphene, a vertically aligned, layered film of COF-5 is formed on the graphene. Bulk powdered material can also be isolated from the bottom of the reaction vessel.[89]

Organic π-conjugated polymers and networks are now being investigated as potential (semi)conducting components in photovoltaic devices and transistors. The use of such species could allow optoelectronic devices with tunable properties to be created in a scalable and cost-effective manner. However, a significant problem with the materials used at present is the lack of control over their nanoscale morphology and orientation. Consequently, unstructured random interphases between donors and acceptors are commonly created. It would, therefore, be desirable to obtain synthetic access to ordered and oriented interpenetrating networks of donor and acceptor phases on the nanoscale. One recent approach uses electroactive organosilane precursors to create covalently bonded frameworks with the help of a surfactant-templated synthesis. With this method, it has been possible to create a porous hole-conducting framework material with a hole mobility of 3×10^{-5} $cm^2/V s$. [90] However, it is difficult to vertically align the channels of these periodic mesoporous organosilica thin films on a solid support.

In the work of Dichtel and colleagues, aligned films of two different hexagonal COFs — namely COF-5 and a pyrene-based COF — are grown using a solvothermal condensation reaction (Figure 1.30). Furthermore, the tetragonal lattice of a nickel phthalocyanine COF, which exhibits high charge-carrier mobilities, was also crystallized on the graphene surface. The team investigated the influence of reaction time and graphene support material on film thickness, crystallinity and orientation of the COFs. Grazing incidence diffraction confirmed the formation of crystalline and aligned films, whereas scanning electron microscopy showed that the films completely cover the graphene surface. Notably, films with thicknesses of around 200 nm could be formed after only 30 min, which is about 100 times faster

than the bulk synthesis, and the film thickness would decrease with longer growth times.

The ability to synthesize vertically aligned open pores, combined with the possibility of preparing single-layer graphene on a variety of substrates, could offer access to a wide range of functionalities. As Dichtel and colleagues point out, the vertical alignment of these materials could be ideal for bulk heterojunctions because anisotropic exciton and charge migration are expected to proceed along the π-stacked layers. Sufficient space for the accommodation of complementary charge conductors may also depend on extending the pore systems into the mesoporous regime.[40]

The ability to create crystalline, aligned, conducting frameworks could at least allow well-defined model systems for nanostructured heterojunctions of electron donors and acceptors to be designed. Moreover, interpenetrating networks with defined paths for charge transport may also lead to higher efficiencies owing to reduced recombination losses. Either way, the future for orientated porous organic solids looks bright.

1.7. References

1. Breck, D. W., *Zeolite molecular sieves: structure, chemistry, and use.* Wiley: New York, 1974.
2. Cundy, C. S.; Cox, P. A., *Chem. Rev.* **2003,** 103 (3), 663-702.
3. Corma, A., *J. Catal.* 216 (1-2), 298-312.
4. Wilson, S. T.; Lok, B. M.; Messina, C. A.; Cannan, T. R.; Flanigen, E. M., *J. Am. Chem. Soc.* **1982,** 104 (4), 1146-1147.
5. Huang, Q.; Ulutagay, M.; Michener, P. A.; Hwu, S.-J., *J. Am. Chem. Soc.* **1999,** 121 (44), 10323-10326.
6. Parise, J. B., *Inorg. Chem.* **1985,** 24 (25), 4312-4316.
7. Gier, T. E.; Stucky, G. D., Nature **1991,** 349 (6309), 508-510.
8. Wingenfelder, U.; Hansen, C.; Furrer, G.; Schulin, R., *Environ. Sci. Technol.* **2005,** 39 (12), 4606-4613.
9. Moreno, N.; Querol, X.; Ayora, C.; Pereira, C. F.; Janssen-Jurkovicová, M., *Environ. Sci. Technol.* **2001,** 35 (17), 3526-3534.
10. Clearfield, A., *Chem. Rev.* **1988,** 88 (1), 125-148.
11. Magee John, S., *Zeolite Cracking Catalysts?an Overview. In Molecular Sieves?*II, American Chemical Society: **1977**; Vol. 40, pp 650-668.
12. TatlIer, M.; Erdem-Senatalar, A., *Applied Thermal Engineering* **1999,** 19 (11), 1157-1172.
13. Fuel and Energy Abstracts **1997,** 38 (5), 348-348.
14. Ferey, G., *Chem. Soc. Rev.* **2008,** 37 (1), 191-214.

15. Budd, P. M., *Science* **2007,** 316 (5822), 210-211.

16. Rowsell, J. L. C.; Yaghi, O. M., *Microp. Mesop. Mat.* **2004,** 73 (1-2), 3-14.

17. Yaghi, O. M.; O'Keeffe, M.; Ockwig, N. W.; Chae, H. K.; Eddaoudi, M.; Kim, J., *Nature* **2003,** 423 (6941), 705-714.

18. Kitagawa, S.; Kitaura, R.; Noro, S.-i., *Angew. Chem., Int. Ed.* **2004,** 43 (18), 2334-2375.

19. Serre, C.; Taulelle, F.; Ferey, G., *Chem. Commun.* **2003,** (22), 2755-2765.

20. Eddaoudi, M.; Kim, J.; Rosi, N.; Vodak, D.; Wachter, J.; O'Keeffe, M.; Yaghi, O. M., *Science* **2002,** 295 (5554), 469-472.

21. Li, H.; Eddaoudi, M.; O'Keeffe, M.; Yaghi, O. M., *Nature* **1999,** 402 (6759), 276-279.

22. Song, Y.-F.; Cronin, L., *Angew. Chem., Int. Ed.* **2008,** 47 (25), 4635-4637.

23. Wang, Z.; Cohen, S. M., *J. Am. Chem. Soc.* **2007,** 129 (41), 12368-12369.

24. Burrows, A. D.; Frost, C. G.; Mahon, M. F.; Richardson, C., *Chem. Commun.* **2009,** (28), 4218-4220.

25. Wang, Z.; Cohen, S. M., *Chem. Soc. Rev.* **2009,** 38 (5), 1315-1329.

26. Ranjan, R.; Tsapatsis, M., *Chem. Mater.* **2009,** 21 (20), 4920-4924.

27. Sonnauer, A.; Hoffmann, F.; Fröba, M.; Kienle, L.; Duppel, V.; Thommes, M.; Serre, C.; Férey, G.; Stock, N., *Angew. Chem.* **2009,** 121 (21), 3849-3852.

28. Lorand, J. P.; Edwards, J. O., *J. Org. Chem.* **1959,** 24 (6), 769-774.

29. Niu, W.; O'Sullivan, C.; Rambo, B. M.; Smith, M. D.; Lavigne, J. J., *Chem. Commun.* **2005,** (34), 4342-4344.

30. Cote, A. P.; Benin, A. I.; Ockwig, N. W.; O'Keeffe, M.; Matzger, A. J.; Yaghi, O. M., *Science* **2005,** 310 (5751), 1166-1170.

31. El-Kaderi, H. M.; Hunt, J. R.; Mendoza-Cortes, J. L.; Cote, A. P.; Taylor, R. E.; O'Keeffe, M.; Yaghi, O. M., *Science* **2007,** 316 (5822), 268-272.

32. Hall, D. G., *Boronic Acids*. Wiley-VCH: Weinheim, **2005**.

33. Uribe-Romo, F. J.; Hunt, J. R.; Furukawa, H.; Klock, C.; O'Keeffe, M.; Yaghi, O. M., *J. Am. Chem. Soc*. **2009,** 131 (13), 4570-4571.

34. ndara, F.; Asano, A.; Furukawa, H.; Saeki, A.; Dey, S. K.; Liao, L.; Ambrogio, M. W.; Botros, Y. Y.; Duan, X.; Seki, S.; Stoddart, J. F.; Yaghi, O. M., *Chem. Mater*. **2011,** 23 (18), 4094-4097.

35. Uribe-Romo, F. J.; Doonan, C. J.; Furukawa, H.; Oisaki, K.; Yaghi, O. M., *J. Am. Chem. Soc*. **2011,** 133 (30), 11478-11481.

36. Tilford, R. W.; Gemmill, W. R.; zur Loye, H.-C.; Lavigne, J. J., *Chem. Mater*. **2006,** 18 (22), 5296-5301.

37. Cote, A. P.; El-Kaderi, H. M.; Furukawa, H.; Hunt, J. R.; Yaghi, O. M., *J. Am. Chem. Soc*. **2007,** 129 (43), 12914-12915.

38. Tilford, R. W.; Mugavero, S. J.; Pellechia, P. J.; Lavigne, J. J., *Adv. Mater*. **2008,** 20 (14), 2741-2746.

39. Tilford, R. W.; Mugavero, S. J., III; Pellechia, P. J.; Lavigne, J. J., *Adv. Mater*. **2008,** 20 (14), 2741-2746.

40. Dogru, M.; Sonnauer, A.; Gavryushin, A.; Knochel, P.; Bein, T., *Chem. Commun.* **2011,** 47 (6), 1707-1709.

41. Spitler, E. L.; Dichtel, W. R., *Nat. Chem*. **2010,** 2 (8), 672-677.

42. Ding, X.; Guo, J.; Feng, X.; Honsho, Y.; Guo, J.; Seki, S.; Maitarad, P.; Saeki, A.; Nagase, S.; Jiang, D., *Angew. Chem., Int. Ed.* **2011,** 50 (6), 1289-1293.

43. Feng, X.; Chen, L.; Dong, Y.; Jiang, D., *Chem. Commun*. **2011,** 47 (7), 1979-1981.

44. Chae, H. K.; Siberio-Perez, D. Y.; Kim, J.; Go, Y.; Eddaoudi, M.; Matzger, A. J.; O'Keeffe, M.; Yaghi, O. M., *Nature* **2004,** 427 (6974), 523-527.

45. Ferey, G.; Mellot-Draznieks, C.; Serre, C.; Millange, F.; Dutour, J.; Surble, S.; Margiolaki, I., *Science* **2005,** 309 (5743), 2040-2042.

46. Hunt Joseph, R.; Doonan Christian, J.; LeVangie James, D.; Cote Adrien, P.; Yaghi Omar, M., *J. Am. Chem. Soc*. **2008,** 130 (36), 11872-3.

47. a)http://www.mobilemag.com/2006/09/08/bmw-to-release-7-series-hydrogen-limousine-in-2007,
b)www.hydrogen.energy.gov/pdfs/review11/st049_yaghi_2011_p.pdf.

48. Yang, J.; Sudik, A.; Wolverton, C.; Siegel, D. J., *Chem. Soc. Rev*. **2010,** 39 (2), 656-675.

49. http://en.wikipedia.org/wiki/Metal-organic_framework.

50. Furukawa, H.; Ko, N.; Go, Y. B.; Aratani, N.; Choi, S. B.; Choi, E.; Yazaydin, A. Ö.; Snurr, R. Q.; O'Keeffe, M.; Kim, J.; Yaghi, O. M., *Science* **2010,** 329 (5990), 424-428.

51. Klontzas, E.; Tylianakis, E.; Froudakis, G. E., *J. Phys. Chem. C* **2008,** 112 (24), 9095-9098.

52. Li, F.; Zhao, J.; Johansson, B.; Sun, L., *Int. J. Hydrogen Energ*. **2010,** 35 (1), 266-271.

53. Han, S. S.; Furukawa, H.; Yaghi, O. M.; Goddard, W. A., III, *J. Am. Chem. Soc*. **2008,** 130 (35), 11580-11581.

54. Cao, D.; Lan, J.; Wang, W.; Smit, B., *Angew. Chem., Int. Ed*. **2009,** 48 (26), 4730-4733, S4730/1-S4730/25.

55. Klontzas, E.; Tylianakis, E.; Froudakis, G. E., *Nano Lett*. **2010,** 10 (2), 452-454.

56. Furukawa, H.; Yaghi, O. M., *J. Am. Chem. Soc*. **2009,** 131 (25), 8875-8883.

57. Mulfort, K. L.; Hupp, J. T., *J. Am. Chem. Soc*. **2007,** 129 (31), 9604-9605.

58. Lan, J.; Cao, D.; Wang, W., *J. Phys. Chem. C* **2010,** 114 (7), 3108-3114.

59. Zou, X.; Zhou, G.; Duan, W.; Choi, K.; Ihm, J., *J. Phys. Chem. C* **2010,** 114 (31), 13402-13407.

60. Wan, S.; Guo, J.; Kim, J.; Ihee, H.; Jiang, D., *Angew. Chem.* **2009,** 121 (18), 3253.

61. Niu, W.; Smith, M. D.; Lavigne, J. J., *J. Am. Chem. Soc.* **2006,** 128 (51), 16466-16467.

62. Li, Y.; Ding, J.; Day, M.; Tao, Y.; Lu, J.; D'Iorio, M., *Chem. Mater.* **2003,** 15 (26), 4936-4943.

63. Wan, S.; Guo, J.; Kim, J.; Ihee, H.; Jiang, D., *Angew. Chem., Int. Ed.* **2009,** 48 (30), 5439-5442.

64. Ding, X.; Guo, J.; Feng, X.; Honsho, Y.; Guo, J.; Seki, S.; Maitarad, P.; Saeki, A.; Nagase, S.; Jiang, D., *Angew. Chem.* **2010**, n/a-n/a.

65. Ding, X.; Chen, L.; Honsho, Y.; Feng, X.; Saengsawang, O.; Guo, J.; Saeki, A.; Seki, S.; Irle, S.; Nagase, S.; Parasuk, V.; Jiang, D., *J. Am. Chem. Soc.* **2011,** 133 (37), 14510-14513.

66. Bain, C. D.; Troughton, E. B.; Tao, Y. T.; Evall, J.; Whitesides, G. M.; Nuzzo, R. G., *J. Am. Chem. Soc.* **1989,** 111 (1), 321-335.

67. Nuzzo, R. G.; Allara, D. L., *J. Am. Chem. Soc.* **1983,** 105 (13), 4481-4483.

68. Maoz, R.; Sagiv, J., *J. Colloid Interface Sci.* **1984,** 100 (2), 465-496.

69. Wasserman, S. R.; Tao, Y. T.; Whitesides, G. M., *Langmuir* **1989,** 5 (4), 1074-1087.

70. Chandekar, A.; Sengupta, S. K.; Whitten, *J. E., Appl. Surf. Sci.* **2010,** 256 (9), 2742-2749.

71. Kang, J.; Rowntree, P. A., *Langmuir* **2006,** 23 (2), 509-516.

72. Semaltianos, N. G.; Wilson, E. G., *Thin Solid Films* **2000,** 366 (1-2), 111-116.

73. Wanunu, M.; Vaskevich, A.; Rubinstein, I., *J. Am. Chem. Soc.* **2004,** 126 (17), 5569-5576.

74. Whitesides, G. M.; Laibinis, P. E., *Langmuir* **1990,** 6 (1), 87-96.

75. Ulman, A., *Chem. Rev.* **1996,** 96 (4), 1533-1554.

76. Barriet, D.; Yam, C. M.; Shmakova, O. E.; Jamison, A. C.; Lee, T. R., *Langmuir* **2007,** 23 (17), 8866-8875.

77. Onclin, S.; Ravoo, B. J.; Reinhoudt, D. N., *Angew. Chem., Int. Ed.* **2005,** 44 (39), 6282-6304.

78. Brunner, H.; Vallant, T.; Mayer, U.; Hoffmann, H., *J. Colloid Interface Sci.* **1999,** 212 (2), 545-552.

79. Ulman, A., *An introduction to ultrathin organic films from Langmuir-Blodgett to self-assembly*. Academic Press: Boston, **1991**.

80. Vickerman, J. C., *Surface analysis: the principal techniques*. Wiley: Chichester, **1997**.

81. Magonov, S. N.; Whangbo, M.-H., Frontmatter. *In Surface Analysis with STM and AFM*, Wiley-VCH Verlag GmbH: **2007**; pp I-XII.

82. Poirier, G. E., *Langmuir* **1997,** 13 (7), 2019-2026.

83. Camillone, N., *J. Chem. Phys.* **1993,** 98 (4), 3503.

84. Love, J. C.; Estroff, L. A.; Kriebel, J. K.; Nuzzo, R. G.; Whitesides, G. M., *Chem. Rev.* **2005,** 105 (4), 1103-1170.

85. Porter, M. D.; Bright, T. B.; Allara, D. L.; Chidsey, C. E. D., *J. Am. Chem. Soc.* **1987,** 109 (12), 3559-3568.

86. Feng, S.; Bein, T., *Nature* **1994,** 368 (6474), 834-836.

87. Hermes, S.; Schröder, F.; Chelmowski, R.; Wöll, C.; Fischer, R. A., *J. Am. Chem. Soc.* **2005,** 127 (40), 13744-13745.

88. Biemmi, E.; Scherb, C.; Bein, T., *J. Am. Chem. Soc*. **2007,** 129 (26), 8054-8055.

89. Colson, J. W.; Woll, A. R.; Mukherjee, A.; Levendorf, M. P.; Spitler, E. L.; Shields, V. B.; Spencer, M. G.; Park, J.; Dichtel, W. R., *Science* **2011,** 332 (6026), 228-231.

90. Mizoshita, N.; Ikai, M.; Tani, T.; Inagaki, S., *J. Am. Chem. Soc*. **2009,** 131 (40), 14225-14227.

2. Preparative and Characterization Methods

2.1. High-Throughput Synthesis Technique for Porous Materials

The High-Throughput (HT) method is a very efficient approach to collect a large amount of experimental data in a short period of time. Important keywords here are parallelization, automation and miniaturization. The goal of the HT method is to perform many reactions simultaneously and to characterize the products without manipulating them individually. Thus it is possible to examine many test parameters, in particular the reaction composition, the concentration or the solvent in a fast and efficient manner. Furthermore costs and resources can be saved due to the low amount of substance used in the HT experiments.[91]

In this research group the High-Throughput method is used in the area of solvothermal synthesis. For this purpose the following working procedure was developed (see Figure 2.1): **(1,2)** The individual Teflon liners with 3 ml volume of a reactor block with a 6 X 4 array are charged with the starting materials. The dosing of the educts and solvents is automated with the SWAVE High-Throughput dispensing system. **(3)** The multiclave setup is closed properly and subsequently heated to the desired temperature in a conventional oven. After solvothermal synthesis a precipitate forms on the bottom of the Teflon liners. **(4)** The solid products are isolated by a 4x6 multi-filtration block. **(5)** The filtrated 4x6 array is transferred to the sample holder of the High-Throughput powder X-ray diffractometer. In the diffractometer each pattern is measured successively. **(6)** The obtained data were analyzed and the products were transferred into 24-well plates for storage (Figure 2.1).

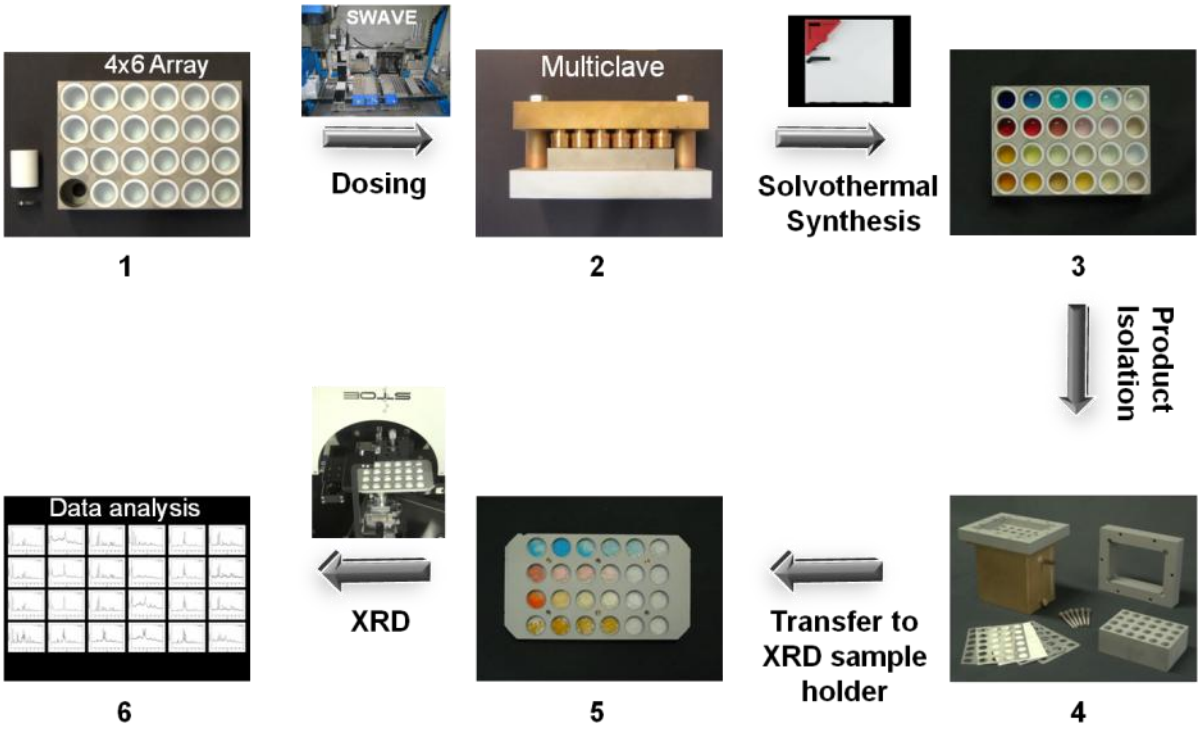

Figure 2.1: High-Throughput working flow.

2.2. X-Ray Diffraction[92-94]

X-Rays are electromagnetic radiation with typical wavelengths of 5 pm up to 100 pm, between UV-light and gamma radiation. They were discovered in 1895 by Wilhelm Conrad Röntgen. Generally X-rays are generated when a cold metal target is bombarded with accelerated, focused electrons. Collision of the electrons with a specimen leads to an emission of a continuous spectrum of X-rays, called Bremsstrahlung. In addition to white radiation characteristic radiation is produced, resulting from X-ray fluorescence. An impinging electron creates a hole in the inner shell of the atom which is filled subsequently by an electron from an outer shell. The energy difference of these two energy states of the transferred electron is emitted as X-ray photon. The wavelength and intensity of the fluorescent X-rays depend on the

target material, since energy differences between the electron shells vary. *Moseley's law* describes the connection between the atomic number Z and the wavelength λ:

$$\frac{1}{\lambda} = \frac{K}{(Z-\sigma)^2}$$

where K and σ are constants for a given spectral line.

To achieve a monochromatic parallel beam, different metal filters and a collimator are applied to selectively isolate an intense part of the spectrum, usually Kα radiation. Incidence of a monochromatic beam of X-ray photons onto a specimen results in three basic phenomena, namely absorption, scattering and reflection.

In 1912 Max von Laue discovered the diffraction of X-rays by crystals, due to the finding that the wavelength of X-rays corresponds to the distance of atoms in a lattice plane. The ordered atomic arrangement in the crystal lattice allows structure determination by monitoring the diffraction maxima caused by constructive interference of scattered X-rays.

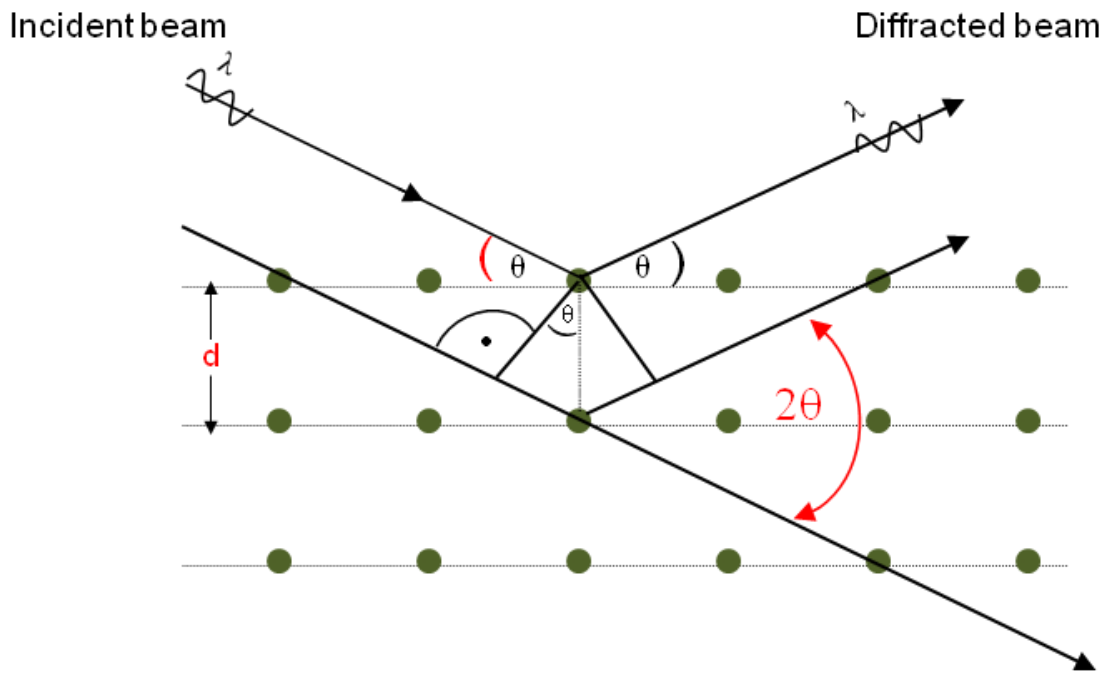

Figure 2.2: Schematic illustration of the Bragg relation, X-rays diffracted at a lattice plane (atoms depicted in green).

For two X-rays hitting the surface the path difference is

$$\Delta S = 2d_{hkl}\sin\theta$$

Where d_{hkl} is the distance between the atomic lattice planes and θ is the angle of incidence.

For constructive interference between these waves, the path difference must be an integral number of wavelengths, which is described by Bragg´s Law:

$$n\,\lambda = 2d\sin\theta$$

λ: X-ray wavelength

n: order of interference

d: lattice plane distance

θ: angle of incidence

Measurement of the diffraction angles at a fixed wavelength allows calculation of the distance of the lattice planes d.

Powder diffraction uses a polycrystalline sample, ideally showing statistical distribution of microcrystal orientations. Reflections of all three spatial directions are projected onto a single dimension. This means that X-rays are diffracted by an angle of 2 θ in concentrical cones (*Debye-Scherrer* cones) around the primary beam.

Obtained diffraction patterns can be compared to sample libraries, thus X-ray diffraction of powders (XRD) is a simple and fast technique to characterize crystalline samples.

Furthermore the domain size D of the crystals can be calculated using the Debye – Scherrer equation:

$$D = \frac{K\,\lambda}{\beta\,sin\theta}$$

D: crystalline domain size

K: Scherrer constant, in general set to 0.9

λ: wavelength

ß: full width at half maximum in radians

θ: angle of incidence

2.3. Electron Microscopy

The minimum distance at which two points can be resolved in imaging depends on the wavelength of the incident light. In a classical optical microscope using visible light the highest achievable resolution is around 0.2 μm. Using electron beams with a much shorter wavelength resolutions down to 0.1 nm are possible. Due to the wave-particle duality electrons can be focused on the specimen with electrical or magnetic fields. In 1931 Ernst Ruska and Max Knoll constructed the first transmission electron microscope (TEM). The beam of electrons is transmitted through the sample forming an image, which can be focused on a photographic film, a fluorescent screen or a CCD camera. In the early 40ies the first commercially available scanning electron microscope (SEM) was produced. The specimen is scanned with an electron beam in a raster scan pattern, imaging the surface.[95]

2.3.1. Scanning Electron Microscopy [96]

The topographic images obtained by Scanning Electron Microscopy exhibit a much better resolution and a sharper depth of focus than light microscopes. The electron beam, which is scanned over the sample, is generated by a field emission gun (FEG) or tungsten filament (electron gun) and accelerated through high voltage. A set of condenser lenses focuses the electrons to a typical spot of a few nm before the beam collides and interacts with the sample. Deflection coils move the electron beam in a grid fashion over the sample. The objective lens focuses the beam on the sample. As the electrons collide with the sample several interactions occur. Backscattered electrons are scattered elastically by the nuclei of the atoms and

provide information about the composition of the specimen. Furthermore inelastic collisions occur that produce secondary electrons with lower energies and X-ray photons. The information can be used either to obtain an image of the sample or to analyze the atomic composition (EDX). A big advantage of the SEM is the facile sample preparation. For most SEMs the sample has to be vacuum compatible because the measurement is carried out in a high vacuum chamber to avoid undesired interactions of the electrons with air molecules. Additionally the sample should be conductive in order to prevent an uncontrolled deflection of the electron beam, due to electrostatic charging. Thus insulating samples are normally coated with a thin film of gold or carbon.

2.3.2. Transmission Electron Microscopy[97]

In contrast to SEM where information about the sample topography is obtained, transmission electron microscopy (TEM) provides information about the internal structure of the specimen. However the illumination systems of both techniques are very similar. Electrons from a field emission gun are accelerated by a high potential difference in the range between 40 to 3000 kV. The electron beam passes a set of condenser lenses where the electron beam is focused before it hits the specimen. The sample thickness should not exceed 100 nm to allow transmission of the electrons. Due to spherical aberration, the quality and resolution of a TEM strongly depends on the quality of the objective lens that generates the first image. This first image is then magnified by the projection lenses and depicted on the fluorescence screen or imaged with a CCD detector.

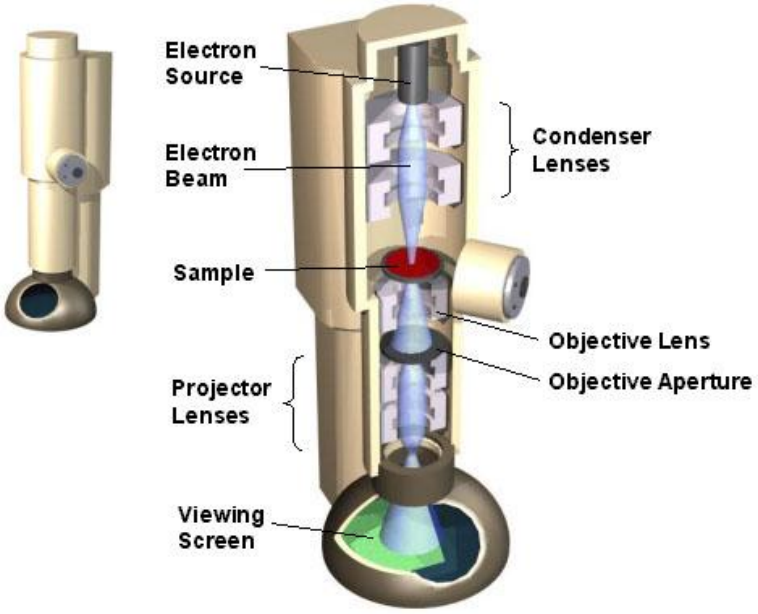

Figure 2.3: TEM model showing the optical pathway and key components.[98]

2.4. Infrared Spectroscopy[99]

When irradiated with infrared light, most molecules absorb specific resonant frequencies, depending on the binding energies and the vibrating masses in the irradiated molecule, thus the position of the absorption bands provides information about functional groups, especially organic moieties. The typical energy range in IR spectroscopy is between 4000 and 400 cm^{-1}. Vibrations of molecules are IR-active if the dipole moment changes during the vibration process.

For powder characterization typically FT-IR spectroscopy is used in transmission or diffuse reflection. In order to investigate thin organic films on reflecting substrates, such as polished silicon wafers or noble metals, a different geometry has to be applied. In Reflectance Absorption IR spectroscopy (RAIR) the IR light is directed onto the film on the reflecting surface at an appropriate angle, thus using the selection rules to enhance sensitivity (Figure 2.4).

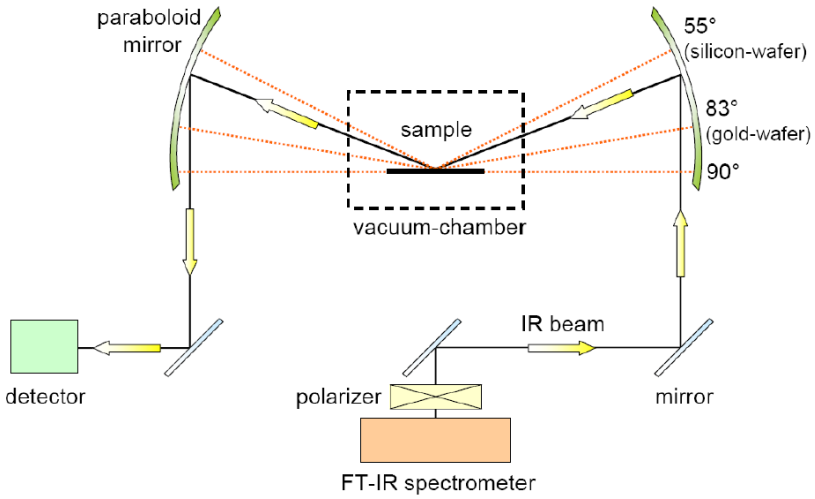

Figure 2.4: Scheme of the reflection absorption IR spectrometer.[100]

The observation of vibrational modes of the organic moieties on metallic substrates is subject to the surface dipole selection rule. Only those vibrations whose transition dipole moments are perpendicular to the surface can be observed as an absorption band. This is because the incident and reflected p-polarized components of the radiation superimpose constructively, enhancing the signal, whereas the s-polarized components cancel each other out, as they undergo a phase change on reflection from the reflection surface.

2.5. Nuclear Magnetic Resonance[101-103]

Nuclear magnetic resonance (NMR) spectroscopy has become an indispensable method for chemical analysis, molecular structure determination, as well as the study of dynamics in organic, inorganic, and biological systems. Nuclei with an odd number of protons, neutrons, or both, will have an intrinsic nuclear spin. This nuclear spin goes along with a magnetic dipole moment. In a magnetic field the

magnetic moments of an atom can only have discrete orientations, the number of possible orientations is given by the spin quantum number I. For each spin quantum number I 2I+1 orientations exist. In an external magnetic field these spin states are not degenerate and split into certain energy levels. The difference in energy between the two states is given by:

γ: gyromagnetic ratio

ħ: reduced Plank constant $\hbar = \frac{h}{2\pi}$

B_0: magnetic field

Resonant absorption between the two states will occur when the employed frequency of the radiation meets the following equation:

$$\nu_0 = \frac{\gamma B_0}{2\pi}$$

Normally radio frequency is used for typical NMR experiments.

The electronic surrounding of each nucleus results in a difference of the applied and local magnetic field, causing a difference in the resonance frequency. Valuable information about the electronic structure and chemical environment can be obtained.

In contrast to liquids where Brownian motion leads to an averaging of anisotropic effects, internuclear dipole-dipole interactions and the anisotropy of the chemical shift result in the broadening of the signal in solids. In order to avoid this effect, the

anisotropic interactions can be eliminated by spinning the sample very quickly at a magic angle of 54°74''(MAS) with respect to the direction of the magnetic field.

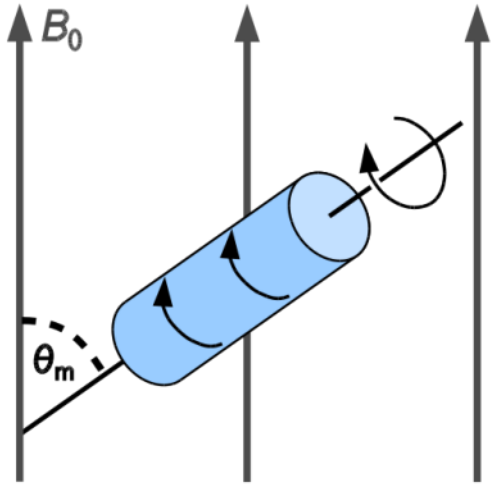

Figure 2.5: Schematic illustration of the "magic angle" which is 54.74 degrees to the magnetic field. [104]

2.6. UV VIS Spectroscopy

In analytical chemistry, spectroscopy based on radiation in the ultraviolet and visible range is often employed to quantitatively determine different compounds. In the Lambert-Beer law the relation between concentration of the absorbing species and the path length as well as the intensity of transmitted light is described:

$$A = -\log \frac{I}{I_0} = \varepsilon \, c \, L$$

A Absorbance

I_0 Intensity of incoming light

I Intensity of transmitted light

ε extinction coefficient

c concentration of absorbing species

L pathway through the absorbing species

To excite an electron from an occupied (HOMO) to an unoccupied (LUMO) orbital the energy of the adsorbed photon has to match the energy difference of the two energy levels.

$$E = h\,f = \frac{h\;c}{\lambda}$$

From this equation it is obvious that the more easily the electrons are excited from the HOMO to the LUMO the longer the wavelength and the lower the band gap of a material, e.g. a semiconductor.

2.7. Fluorescence[93]

Fluorescence is the spontaneous emission of light during the transition of an electronic excited state to a state of lower energy. Due to collisions with other molecules the excited molecule looses energy until it reaches the vibrational ground state of the electronically excited state. Thus the emitted light is typically of lower energy, hence longer wavelength than the absorbed light. Relaxation to the ground state can also occur radiation-less, this process is called fluorescence quenching. When colliding with a second molecule several processes can occur to quench the fluorescence: (1) complex formation (2) internal conversion and (3) energy transfer to the second molecule. In this work fluorescence spectroscopy is used to investigate the properties of conductive p-type Covalent Organic Frameworks. In the

presence of electron accepting molecules, such as the fullerene derivative PCBM, the fluorescence of TT-COF is quenched. This indicates an energy transfer from the p-type framework to the electron accepting PCBM.

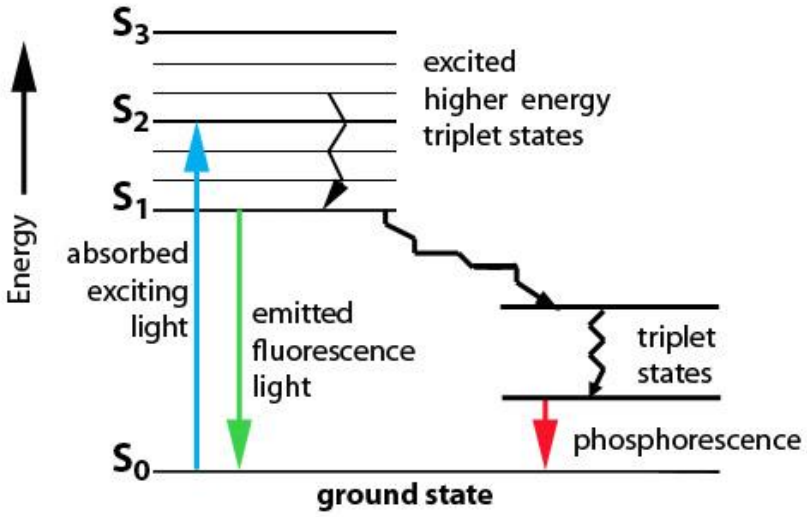

Figure 2.6: Jablonski diagram showing the possible routes for relaxation of an excited molecule.[105]

2.8. Sorption[106, 107]

In physisorption, gaseous adsorptives reversibly bind onto the surface of a material (adsorbent), providing valuable information about structure and porosity of the material. During the measurement the amount of adsorbed gas molecules with increasing partial pressure is determined at constant temperature. From the obtained isotherms information about the surface area, the morphology and size of the pores can be concluded. The most common gas for sorption measurements of porous powder samples is nitrogen (N_2) at 77 K.

In a typical isotherm the relative pressure of the adsorptive is plotted against the amount of adsorbed gas at standard pressure and temperature. According to the IUPAC the isotherms can be categorized in six different types:

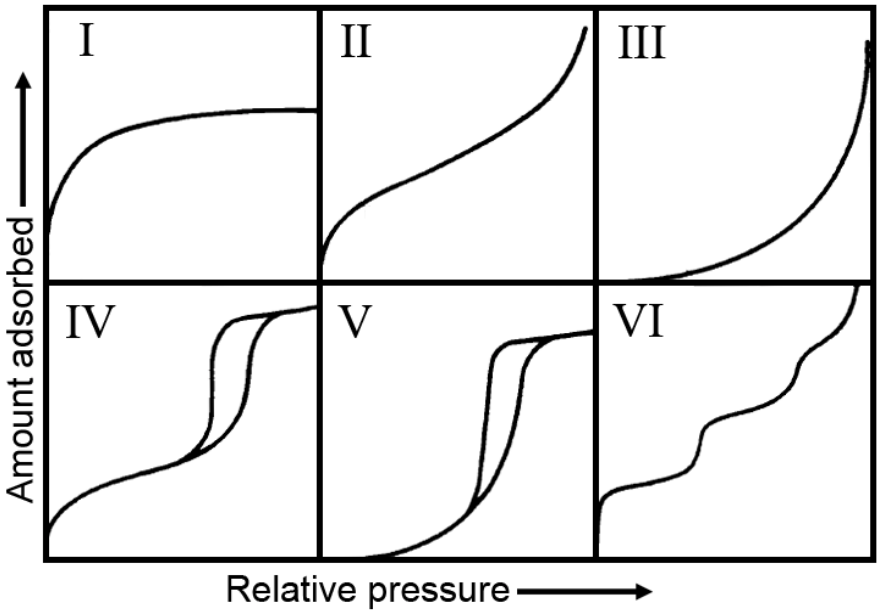

Figure 2.7: IUPAC classification of sorption isotherms, Type I to Type VI.[106]

Type I isotherm is typical for microporous solids and shows a horizontal plateau after filling the micropores. *Type II isotherm* shows physical adsorption of gases by non-porous solids. Monolayer coverage is followed by multilayering at higher relative pressures.

Type III and V isotherms are characteristic for weak adsorbate-adsorbent interactions and are most commonly associated with non-porous and mesoporous adsorbents, respectively.

Type IV isotherm features an absorption step at higher relative pressures and often a hysteresis loop, which is common for mesoporous substances. These materials also exhibit a limited uptake at high relative pressures (plateau). The typical "knee"

at low relative pressures is caused by the progressive formation of mono-and multilayers.

At low relative pressures a monolayer of adsorbed molecules is formed on the surface, followed by multilayer condensation. Filling of the mesopores by capillary condensation leads to a steep slope in the isotherm. After filling the pores a plateau is reached indicating only minor adsorption at the external surface or textural porosity.

Several theories describe and interpret the adsorption isotherms, the most common one is the Brunauer-Emmett-Teller (BET) model. The BET theory extends the Langmuir theory, which covers monolayer molecular adsorption, to multilayer adsorption using two basic assumptions: (1) adsorption enthalpy of all layers with exception of the first monolayer is identical and corresponds to the heat of condensation, and (2) no interaction between each adsorption layer. For low partial pressures ($p/p_0 < 0.3$) the BET equation can be expressed in a linear form:

$$\frac{\frac{p}{p_0}}{n\left(1-\frac{p}{p_0}\right)} = \frac{C-1}{n_m\ C}\ \frac{p}{p_0} + \frac{1}{n_m\ C}$$

n_m : monolayer adsorbed gas quantity

C : BET-constant

p : equilibrium pressure

p_0 : saturation pressure

From experimental results the monolayer adsorbed gas quantity n_m (mol g^{-1}) can be obtained and the specific surface area AS can be calculated according to

$$A_s\ (BET) = n_m\ N_A\ a_m$$

a_m: cross-sectional area of the adsorbate molecule

N_A: Avogadro constant

In order to calculate the pore size from the sorption isotherms different microscopic models, such as molecular dynamics, density functional theory (DFT) or Monte Carlo simulations can be used. These methods lead to realistic results by using quantum mechanical calculations, provided the assumptions made by these models correlate with the material investigated. Therefore these models are not suitable for unknown surfaces. For the evaluation of the pore size distribution of Covalent Organic Frameworks non-local density functional theory (NLDFT) was employed, which is designed specifically for the adsorbent (carbon) and the cylindrical pore geometry.

2.9. Thermogravimetric Analysis

Thermogravimetric analysis (TGA) measures the mass change of a sample as a function of temperature, thus allowing conclusions about structural characteristics, such as removal of crystal water, condensation or decomposition. The sample is heated under a desired atmosphere (e.g. N_2, air or O_2) up to 900°C or higher, typically with a linear heating rate, while a microbalance measures the weight change. In addition the heat flow between the sample and an inert reference at the same surrounding temperature can be measured (differential thermal analysis (DTA). With information about thermodynamic effects, such as exothermic and endothermic processes, phase-transitions can be observed.

2.10. References

91. Akporiaye, D. E.; Dahl, I. M.; Karlsson, A.; Wendelbo, R., *Angew. Chem.* **1998,** *110* (5), 629-631.

92. L. Smart, E. M., *Einführung in die Festkörperchemie*. Vieweg Verlag: **1997**.

93. Atkins, p., *Physikalische Chemie*. 2. Auflage ed.; VCH Weinheim: **1996**.

94. Massa, W., *Kristallstrukturbestimmung*. Teubner: **1996**.

95. http://en.wikipedia.org/wiki/Electron_microscope.

96. P. J. Goodhew, J. H., R. Beanland, Electron microscopy and analysis. 3 rd ed.; London, **1988**.

97. D. B. Williams, C. B. C., *Transmission electron microscopy: a textbook for material science: I: basics*. Plenum: New York, **1996**.

98. (http://barrett-group.mcgill.ca/teaching/nanotechnology/nano02.htm).

99. H. Nauner, W. H., *Untersuchungsmethoden in der Chemie*. Thieme Verlag: Stuttgart, **1997**.

100. Doctoal thesis Camilla Scherb, *Controlling the Surface Growth of Metal-Organic Frameworks*, LMU **2009.**

101. M. Hesse, H. M., B. Zeeh, *Spektroskopische Methoden in der organischen Chemie*. 5. überarb. Auflage ed.; Georg Thieme Verlag: Stuttgart New York, **1995**.

102. Jacobson, N. E., *NMR Spectroscopy Explained*. Wiley Interscience: Hoboken, **2007**.

103. Macomber, R. S., *A Complete Introduction to Modern NMR Spectroscopy*. Wiley Interscience: New York, **1998**.

104. http://en.wikipedia.org/wiki/File:MagicAngleSpinning.svg.

105. http://web.uvic.ca/ail/techniques/epi-fluorescence.html.

106. Sing, K. S. W.; Everett, D. H.; Haul, R. A. W.; Moscou, L.; Pierotti, R. A.; Rouquerol, J.; Siemieniewska, T., *Pure Appl. Chem.* **1985,** *57* (4), 603-19.

107. Condon, J. B., *Surface Area and Porosity Determinatons by Physisorption - Measurements and Theory*. Elsevier: Amsterdam, **2006**.

3. A Covalent Organic Framework with 4 nm Open Pores

This chapter is based on a publication in the RSC Journal "Chemical Communications".

This work results from the cooperation with Dr. Andreij Gavryushin and Prof. Paul Knochel from the Department of Chemistry, University of Munich.

3.1. Introduction

Porous crystalline materials with a well-defined pore size distribution are essential for applications in gas storage,[56] catalysis, separation,[108] optics[109] and chemical sensing.[110] Specifically, large pores reaching several nm diameter permit the design of a multitude of nano-devices interacting with large guest molecules.[45]

To gain maximum control over local structure, chemistry and physics in the pore system, it would be highly desirable to have access to multi-nm pores with molecularly defined walls.[111] For example, Sonnauer *et al.* reported a mesoporous Metal-Organic Framework (MOF) exhibiting giant cages with diameters of up to 4.6 nm, although the windows connecting these cages are much smaller with dimensions of about 2.0 nm.[27] Other mesoporous MOFs with similar pore dimensions have been described.[112, 113] A new class of materials Covalent Organic Frameworks (COFs)[30] purely organic open pore structures exhibit significant stability due to covalent bonding.[36] They feature great structural diversity and also

allow precise geometric control through the design of the molecular building blocks (reticular chemistry).[17] Until now mesoporous COFs with pore sizes larger than 3.4 nm have not been reported.[37, 60, 114]

Here we describe the synthesis and characterization of a new mesoporous Covalent Organic Framework BTP-COF, with fully accessible pores having an open diameter of 4.0 nm. To the best of our knowledge, this is the largest open pore diameter of any crystalline material ever reported.

The new BTP-COF was synthesized under solvothermal conditions by co-condensation of 1,3,5-benzenetris(4-phenylboronic acid) (BTPA) and the polyol 2,3,6,7-tetrahydroxy-9,10-dimethyl-anthracene (THDMA) (Figure 3.1).

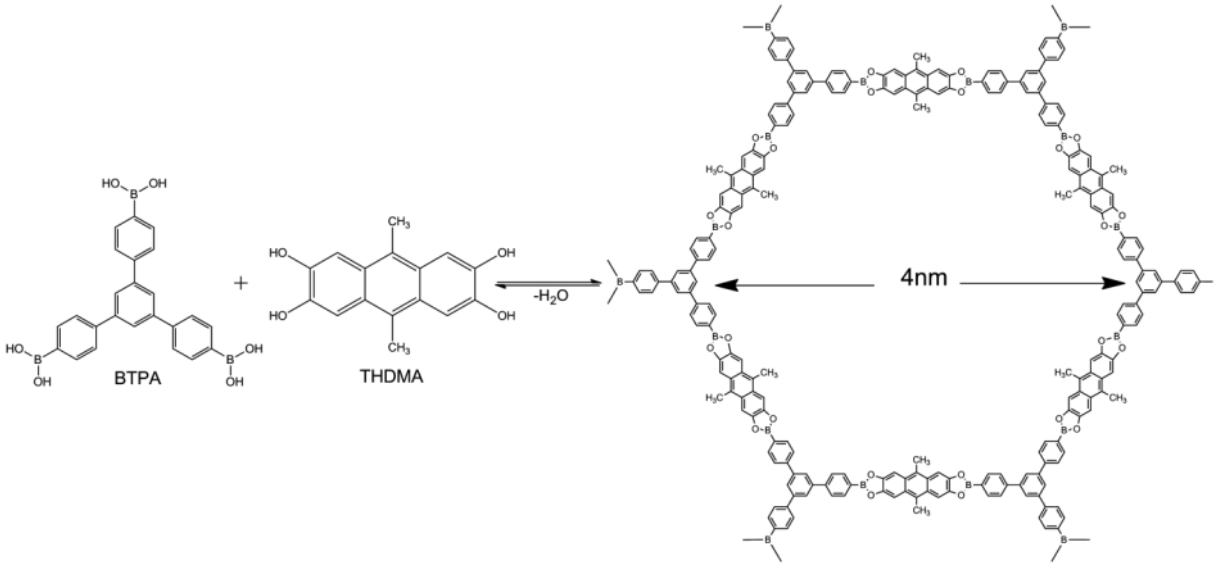

Figure 3.1: Co-condensation reaction for the BTP-COF with 4.0 nm pores.

3.2. Experimental

3.2.1. Materials and Methods

All materials (if not otherwise noted) were purchased from Aldrich or Fluka in the common purities purum and puriss. All materials were used without further purification. The building blocks 9,10-dimethyl-anthracene-2,3,6,7-tetraol (THDMA) and 1,3,5-benzenetris(4-phenylboronic acid) (BTPA) were prepared according to published procedures.[115, 116],[116] All materials were manipulated in air.

X-ray diffraction analysis was carried out in reflection mode using a Bruker D8 Discover with Ni-filtered CuKα-radiation (1.5406 Å) and a position-sensitive detector (Vantec). Fourier-transform infrared spectra of samples were measured with a Bruker Equinox 55 equipped with a PIKE MIRacle ATR-unit at room temperature. The SEM images were recorded with a Jeol 6500F field emission scanning electron microscope with an EDX/WDX detector. For this purpose the samples were put on an adhesive graphite film and sputtered with carbon with a BALTEC MED 020 Coating Sytem. ^{11}B and ^{13}C MAS NMR spectra were recorded on a Bruker DSX Avance 500 with a magnetic field of 11.2 Tesla. A 4 mm MAS triple-resonance sample head was used. The frequency of the rotor was 10 kHz. TG measurements were performed in a stream of synthetic air (25 ml / min) on a Netzsch STA 440 C TG/DSC. The measurements were carried out with a heating rate of 10 K / min and a temperature range from 30 °C to 900 °C. The nitrogen sorption isotherms were recorded on a Nova 4000e at -196°C. Prior to the measurement of the adsorption isotherm the sample was treated as follows. The product was soaked in acetone for 2 days and heated for 24 h at 150°C under oil pump vacuum.

Molecular geometry optimization was performed with Accelrys MS Modeling 4.3 using the universal force field method. The final hexagonal unit cell was calculated with the geometrical parameters from the optimized structure. For the simulation of the PXRD pattern Reflex was used (a software package implemented in MS Modeling 4.3). For this purpose the unit cell parameters were first calculated and then refined from the experimentally observed peak positions in a hexagonal array. As a result we obtained cell parameters of a = b = 43.65 Å and c = 3.52 Å. The simulated PXRD patterns were then compared with the experimentally obtained data. We note that this structure can assemble in two different arrangements, i.e., (i) a staggered AB type with graphite-like packing, and (ii) an eclipsed AA type arrangement with the adjacent sheets lying exactly on top of each other. After optimizing the geometry of each arrangement, the powder patterns were simulated and compared to the experimental patterns. The simulated pattern of the AA arrangement shows very good agreement with our experimental PXRD pattern.

3.2.2. Synthesis Optimization with High-Throughput Methods

High-Throughput methods allowed us to find the optimal reaction conditions for the BTP-COF formation in a fast and efficient manner.[117] In Table 3.1 we present the list of different solvent mixtures and stoichiometric ratios. Successful network formation was only observed with the highlighted solvents anisole and methanol at a ratio 90 to 10. The other solvent mixtures resulted in amorphous material.

Table 3.1: Overview of solvents and solvent ratios investigated for the formation of BTP-COF.

Solvent	Solvent	ratio
Mesitylene	Dioxane	50 : 50
Mesitylene	Methanol	99 : 1/ 98 : 2/95 : 5/90 : 10
Mesitylene	Acetone	99 : 1/ 98 : 2/95 : 5/90 : 10
Anisole	Dioxane	50 : 50
Anisole	Methanol	99 : 1/ 98 : 2/95 : 5/90 : 10/ 80 : 20
Anisole	Acetone	99 : 1/ 98 : 2/95 : 5/90 : 10
Toluene	Dioxane	50 : 50
Toluene	Methanol	99 : 1/ 98 : 2/95 : 5/90 : 10
THF	Dioxane	50 : 50
THF	Methanol	99 : 1/ 98 : 2/95 : 5/90 : 10

The framework only forms with anisole and methanol as solvents; with this knowledge the next steps were to improve crystallinity and yield of the product. Therefore, in the following experiments the ratio of the starting materials (0.1mmol BTPA to 0.2 mmol DMTHA) and the solvent mixture anisole to methanol at the ratio

90:10 were kept constant and reaction time, temperature and concentration were varied (see Table 3.2).

Table 3.2: Overview of volumes, reaction times and reaction temperatures investigated for BTP-COF.

Solvents	**Volume (ml)**	**Time (min)**	**Temperature (°C)**
Anisole:MeOH 90 : 10	1.0 to 2.7 ml / 0.2 steps	5 to 30 min / 5°C steps 45 min and 60 min	80°C to 120°C / 20°C 150°C and 170°C

3.2.3. Optimized Synthesis Parameters

Following optimization in a High Throughput screening approach, the following recipe was established for the synthesis of the new BTP-COF. In a 5 ml Biotage microwave vial the solid mixture of 0.1 mmol (43 mg) 1,3,5-benzentris(4-phenylboronic) acid **BTPA** and 0.2 mmol (63 mg) 9,10-dimethyl-anthracene-2,3,6,7-tetraol **THDMA** was dissolved in 1.5 ml anisole and methanol (9:1 v:v). The cloudy solution in the tightly capped vial was heated to 120°C for 5 min in the Biotage microwave Initiator 2.0. The resulting green powder was isolated by filtration and excessive washing with 50 ml dry acetone (Aldrich). The powder was dried at room temperature, yielding 72% (53 mg) based on BTPA. For gas adsorption measurements the product was soaked in acetone for 2 d and heated at 150 °C under dynamic vacuum for 24 h.

FT-ATR-IR: ν (cm^{-1}) = 3493 (m), 2977 (w), 1605 (m), 1495 (m), 1457 (m), 1386 (m), 1356 (s), 1247 (m), 1210 (s), 1063 (m), 1042 (w), 1016 (m), 889 (m), 822 (m), 755 (m).

3.3. Results and Discussion

The synthesis parameters for the new COF structure were found and optimized in a high throughput screening approach using a robotic dosing system.[117] The investigated reaction parameters were solvents, solvent ratio, concentration, ratio of the starting materials, time and temperature. Thereby it was observed that the solvent mixture is the most important parameter for successful network formation, whereas the latter ones influence the purity (crystallinity and yield) of the system. We can conclude from this that the reversibility of the estercondensation depends strongly on the steric and polarity of the reaction solution. Hence the crystallization is only possible if the right reaction conditions are adapted for every linker system. The COF materials were obtained under microwave synthesis conditions.[118] Results of these experiments were evaluated and depicted in the semi-quantitative Figure 3.2.

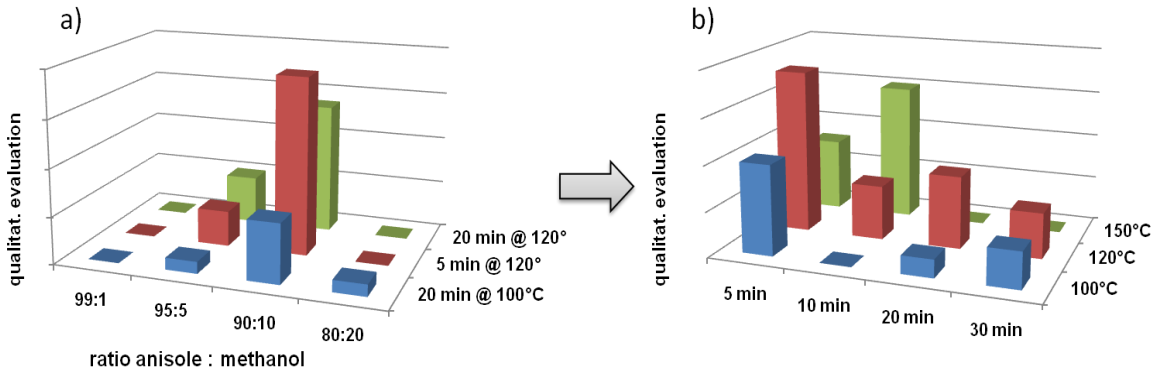

Figure 3.2: Semi-quantitative evaluation of the synthesis optimization; evaluation based on comparable crystallinity and yield of the products.

Powder X-ray diffraction (PXRD) confirms the formation of a highly crystalline Covalent Organic Framework. In order to identify the new phase, possible structures were modelled with MS Studio.[119] Based on the calculated structures, the corresponding powder patterns were simulated and compared to the experimentally obtained data. As reported for previous COF structures, the potential stacking types of the hexagonal planar sheets were calculated.[30] In principle two distinct arrangements are viewed as most likely (Figure 3.3).

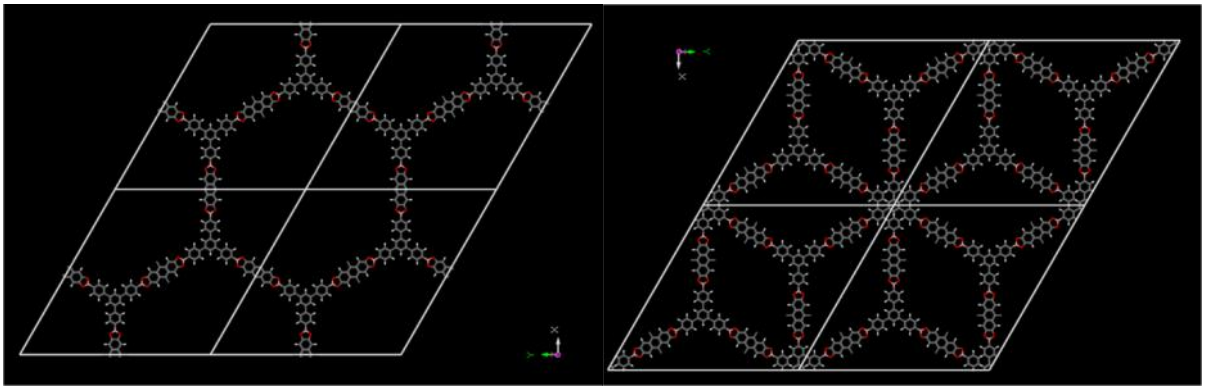

Figure 3.3: left: Simulation of crystal lattice of four unit cells in AB plane calculated in an eclipsed arrangement, right: Simulation of crystal lattice of four unit cells in AB plane calculated in a staggered arrangement (space group P63/mmc).

The adjacent sheets can stack in an eclipsed way (AA type), resulting in accessible pores in one dimension (along the c-axis). Alternatively, the adjacent sheets can form a staggered array (AB type) as in graphite. The experimental PXRD pattern for BTP-COF agrees very well with the simulated pattern for an eclipsed AA arrangement (Figure 3.4). The eclipsed BTP-COF has a hexagonal P6/mmm symmetry. Unit cell parameters determined from the experimental X-ray patterns match very well those obtained from the structure simulations (peak broadening included).

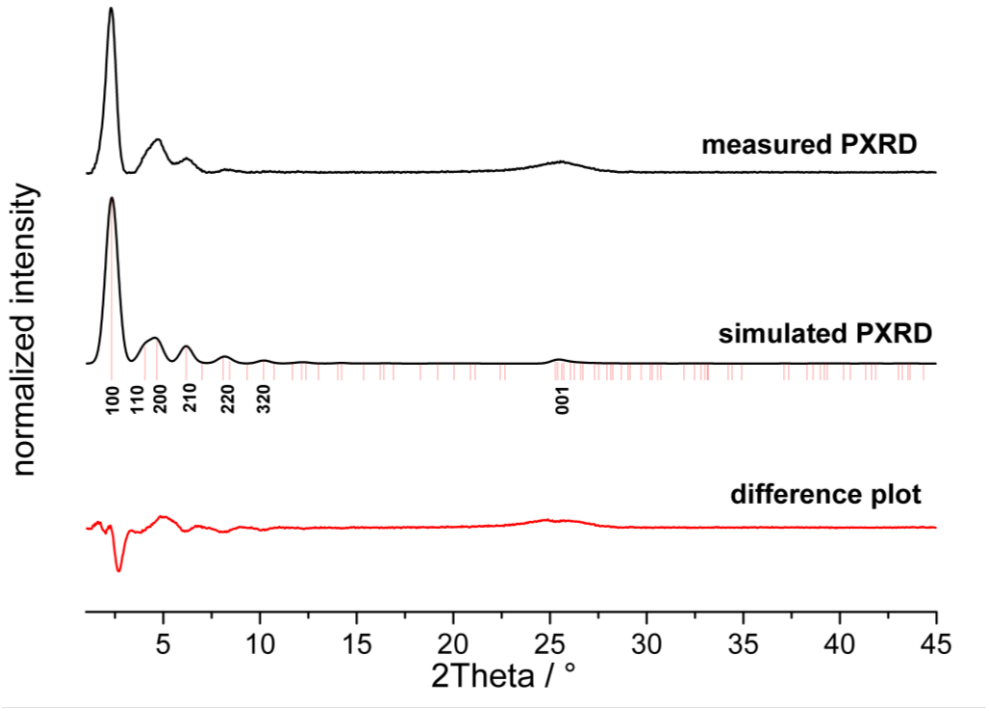

Figure 3.4: The experimentally observed PXRD pattern, after degassing the sample at 150°C for 2 d, the simulated pattern and the difference plot in red.

The (001) reflection is broadened, which can be attributed to disorder in the spacing and/or to a small domain size along this axis. The measured data were compared to several simulated structures. The best fit was obtained for an interlayer distance of 0.352 nm(Figure 3.5), which is larger than the spacing of 0.346 nm in COF-5, 30 a

structure related to that of boron nitride.[120] The slightly larger distance between the sheets along the c-axis can be attributed to the steric requirements of the methyl groups in the pores.

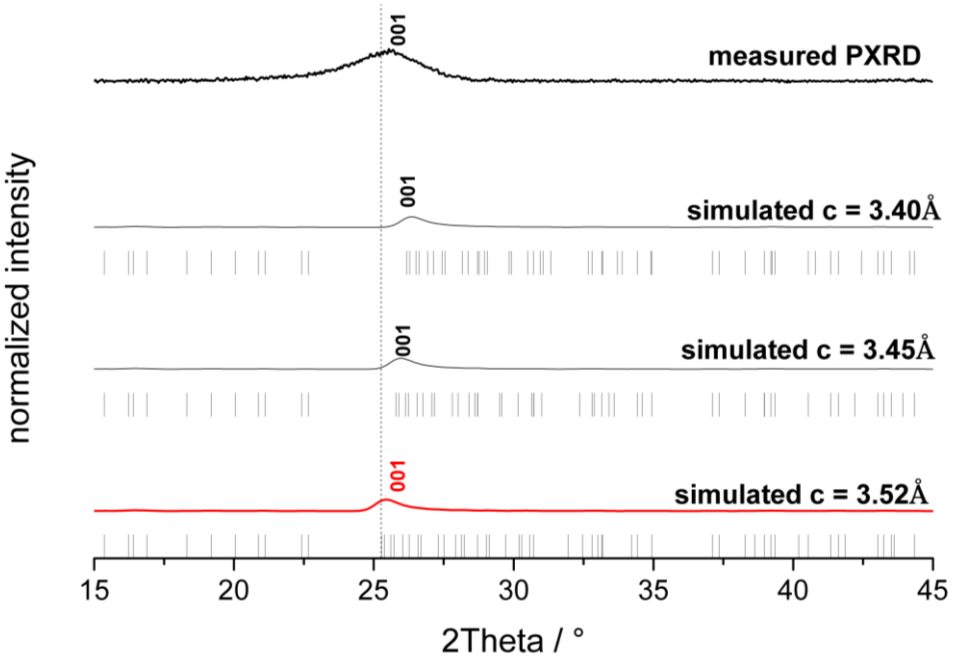

Figure 3.5: Comparison of the 001 reflection of measured PXRD with simulated patterns having different interlayer distances. Best fit was obtained for a distance of 3.52 Å.

The resulting structure of the new Covalent Organic Framework is shown in Figure 3.6. Based on the structure, we can also draw conclusions about the expected pore filling of the framework (see sorption data below).[38]

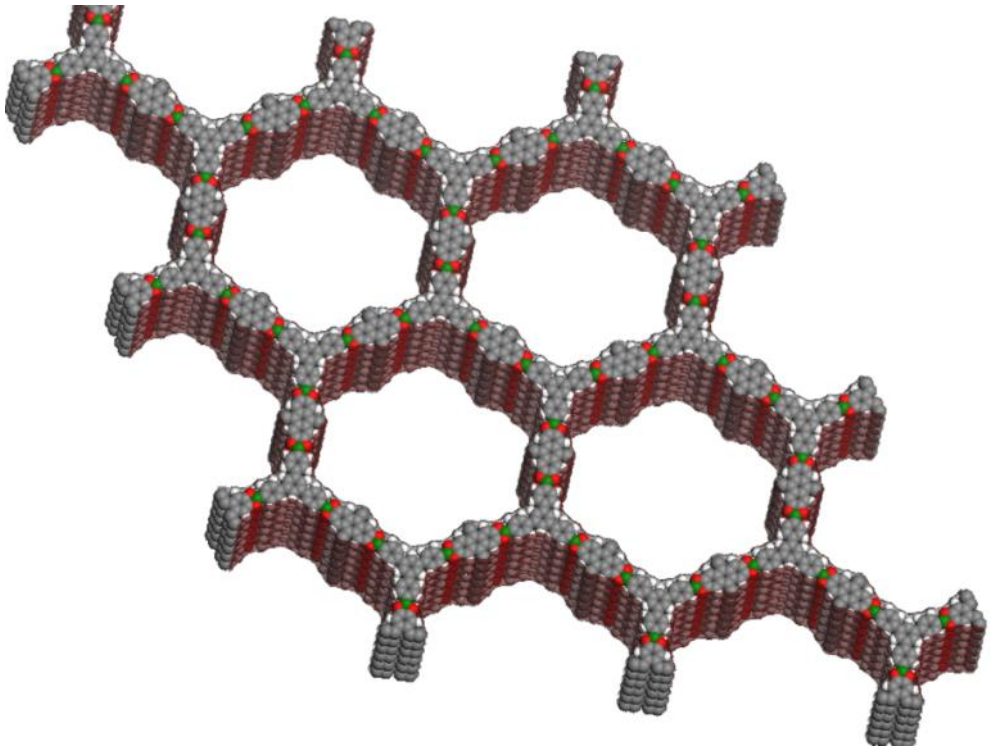

Figure 3.6: Schematic structure of BTP-COF including Connolly surface,based on calculations using the universal force field method and crystal lattice parameters (boron in green, oxygen in red and carbon in grey).

The presence of the building blocks in the assembly was confirmed with FTIR spectroscopy (Figure 3.7). Consistent with previously reported COF-materials, the attenuation of the OH-stretching band indicates esterification of the boronic acids with the polyols. The bands at 1386 cm^{-1} and 1356 cm^{-1} indicate that the expected boronate ester functionality is present.

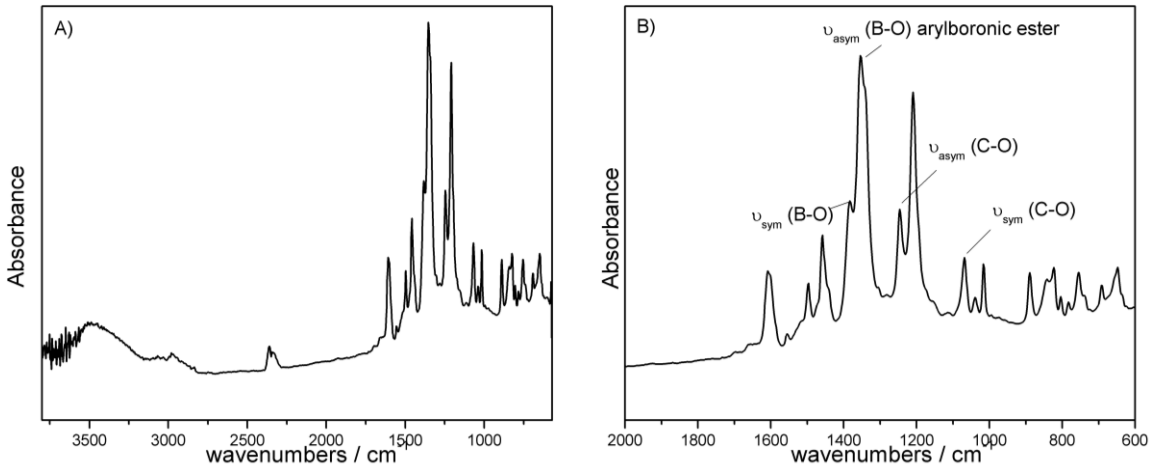

Figure 3.7: A) FT-IR spectrum of the BTP-COF with 4 nm pores, B) FTIR spectrum of BTP-COF, showing the characteristic aryl boronate ester functionality.

Table 3.3.: Assignment of the most important peaks in the infrared spectrum of the BTP-COF.

Peak (cm^{-1})	Assignment
3495 (m)	v_{sym} OH from terminal OH and $B(OH)_2$ groups
2977(w)	v_{asym} Ar-CH_3
2837(w)	Ar-C-H_3
1606(m)	v_{sym} C=C for fused aromatics
1496(m)	v_{sym} C=C for aromatics
1458(m)	v_{sym} C=C for aromatics
1382(s)	v_{sym} B-O
1352(s)	v_{sym} B-O
1245(m)	v_{sym} C-O
1207(s)	C-H in plane bending for p-substituted

1068(m)	benzene
1039(w)	ν_{sym} B-C

The ^{11}B MAS NMR spectrum (Figure 3.8 A) shows the formation of tricoordinated planar boron with a signal at 21 ppm which differs from the starting material, the BTPA (15 ppm).

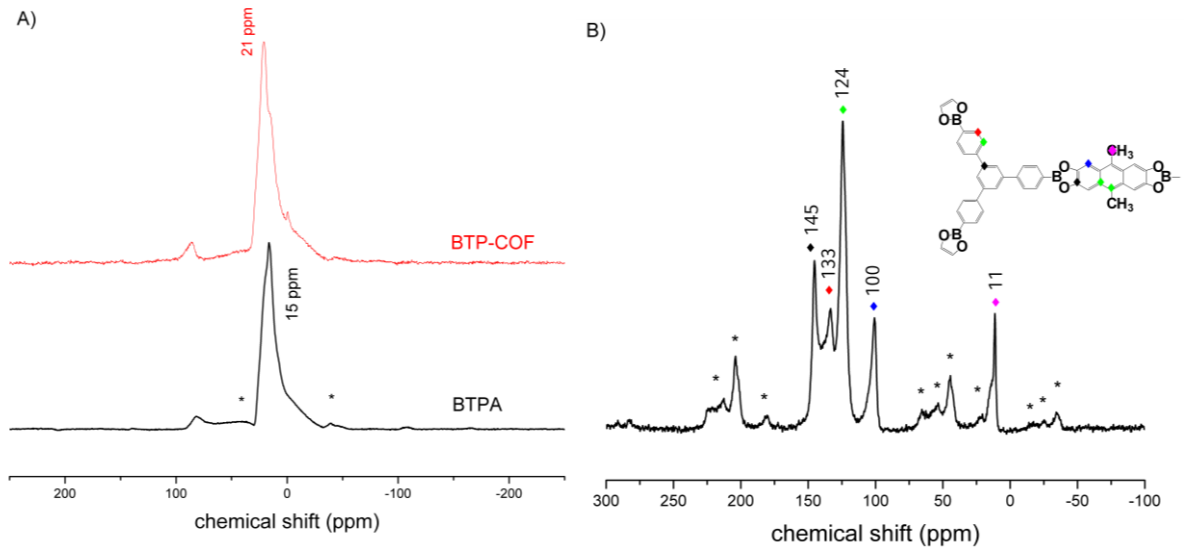

Figure 3.8: A) ^{11}B MAS NMR spectrum of BTP-COF (red) compared to the starting boronic acid BTPA (black), B) The ^{13}C CP-MAS NMR spectrum of BTP-COF indicates that the expected building blocks are present. Asterisks (*) indicate peaks arising from spinning side bands.

Thermogravimetric analysis indicates that BTP-COF is stable up to 400 °C. Heating to 220 °C is accompanied by a mass loss of 12%, which can be attributed to volatile guest molecules in the mesopores. At 600 °C a total weight loss of 61% is reached. The remaining 17% correspond to the stoichiometrically expected amount of B_2O_3.

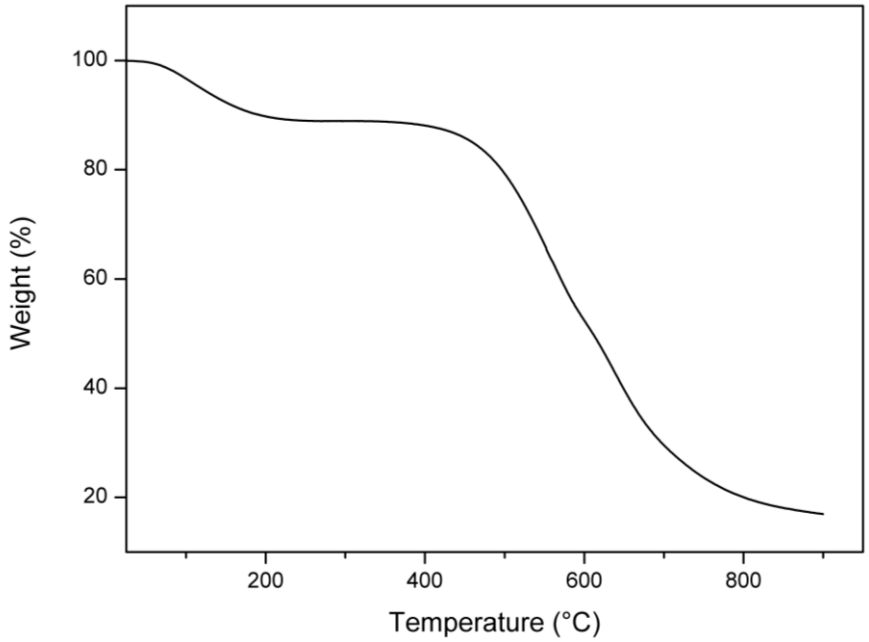

Figure 3.9: Thermogravimetric analysis of the BTP-COF step with a weight loss of 12 % is observed between 50°C and 200°C. The next step with a weight loss of 61 % above 400 °C indicates the degradation of BTP-COF. At a temperature of 700 °C a total weight loss of 17% is reached, which corresponds to a quantity of B2O3 representing 6 boron atoms per unit cell (unit cell formula: $C_{96}H_{60}B_6O_{12}$).

In order to remove guest molecules from the pores, the crude product of BTP-COF was soaked in acetone for 2 d and subsequently dried at 150 °C in vacuum for at least 12 h. As is shown in the powder pattern of BTP-COF after removal of the guest molecules (Figure 3.4), there is no collapse of the crystalline structure and the stacking of the layers is preserved. Furthermore, BTP-COF is stable for several months in air, and it does not degrade in most of the common organic solvents.

The porosity of BTP-COF was confirmed by N_2-sorption measurements after degassing of the sample at elevated temperature. The isotherm was recorded at 77 K. BTP-COF exhibits a type IV isotherm (Figure 3.10 A) characteristic for mesoporous materials,[106] and a very high Brunauer Emmett Teller (BET) surface

area of almost 2000 m^2g^{-1}. The pore size distribution of BTP-COF shows pores with a pore diameter of around 4.0 nm (Figure 3.10 B).

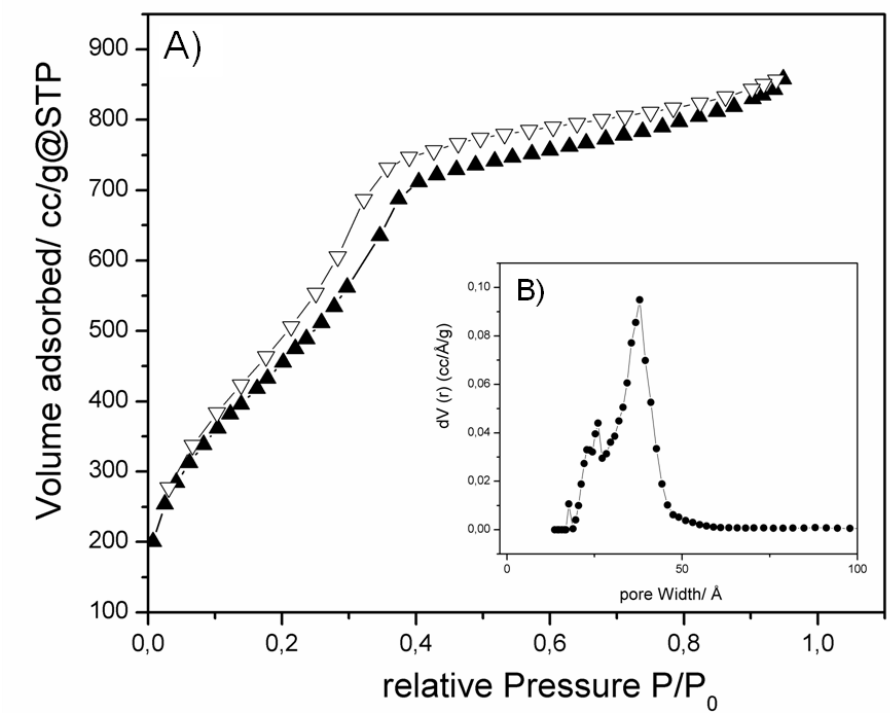

Figure 3.10: A) Nitrogen sorption isotherm of degassed BTP-COF measured at 77 K and (B) pore size distribution.

In order to assess whether the pores in the sample are accessible or blocked by parts of the framework or solvent molecules, the surface area of crystalline materials can be predicted from the crystal structure using geometric methods.[121] The Connolly surface is calculated by simulating a probe molecule (in this case nitrogen) rolling along the surface.[122] Another method to calculate the surface and pore volume is the accessible surface area.[123, 124]

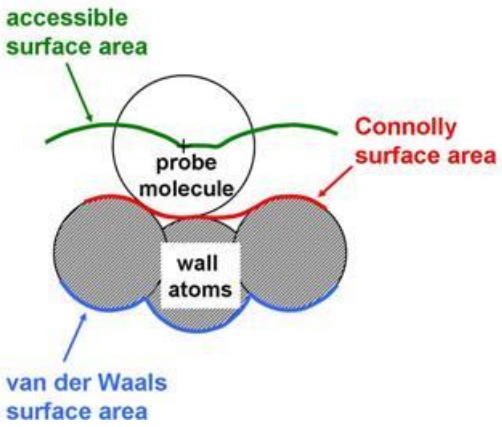

Figure 3.11: Schematic illustration of calculation of Connolly Surface and accessible surface area.

The value for the BET surface area calculated from experimental nitrogen adsorption isotherms is in good accordance with the theoretically calculated values (Table 3.3).

Table 3.3: Theoretical and experimental values for surface area and pore volume of BTP-COF.

	Surface area m^2/g	Volume cm^3/g
Connolly surface	2000	1.63
Access. surface	1764	1.29
Sorption data	1850	1.29

3.4. Conclusion

As shown above, we have synthesized a new mesoporous crystalline material with extremely large permanent pores using the concept of reticular chemistry. For the first time a crystalline open framework structure with accessible 4.0 nm pores is reported. We anticipate this structure and related materials to offer an attractive

platform for the covalent attachment of large molecular functional guests, thus creating a highly controlled environment and well-defined interactions between the crystalline walls of the host and the guest species.

3.5. Notes and references

17. Yaghi, O. M.; O'Keeffe, M.; Ockwig, N. W.; Chae, H. K.; Eddaoudi, M.; Kim, J., *Nature* **2003,** *423* (6941), 705-714.

27. Sonnauer, A.; Hoffmann, F.; Fröba, M.; Kienle, L.; Duppel, V.; Thommes, M.; Serre, C.; Férey, G.; Stock, N., *Angew: Chem:* **2009,** *121* (21), 3849-3852.

30. Cote, A. P.; Benin, A. I.; Ockwig, N. W.; O'Keeffe, M.; Matzger, A. J.; Yaghi, O. M., *Science* **2005,** *310* (5751), 1166-1170.

36. Tilford, R. W.; Gemmill, W. R.; zur Loye, H.-C.; Lavigne, J. J., *Chem: Mater:* **2006,** *18* (22), 5296-5301.

37. Cote, A. P.; El-Kaderi, H. M.; Furukawa, H.; Hunt, J. R.; Yaghi, O. M., *J. Am. Chem. Soc.* **2007,** *129* (43), 12914-12915.

38. Tilford, R. W.; Mugavero, S. J.; Pellechia, P. J.; Lavigne, J. J., *Adv. Mater.* **2008,** *20* (14), 2741-2746.

45. Ferey, G.; Mellot-Draznieks, C.; Serre, C.; Millange, F.; Dutour, J.; Surble, S.; Margiolaki, I., *Science* **2005,** *309* (5743), 2040-2042.

56. Furukawa, H.; Yaghi, O. M., *J. Am. Chem. Soc.* **2009,** *131* (25), 8875-8883.

60. Wan, S.; Guo, J.; Kim, J.; Ihee, H.; Jiang, D., *Angew. Chem.* **2009,** *121* (18), 3253.

106. Sing, K. S. W.; Everett, D. H.; Haul, R. A. W.; Moscou, L.; Pierotti, R. A.; Rouquerol, J.; Siemieniewska, T., *Pure Appl. Chem.* **1985,** *57* (4), 603-19.

108. Seo, J. S.; Whang, D.; Lee, H.; Jun, S. I.; Oh, J.; Jeon, Y. J.; Kim, K., *Nature* **2000,** *404* (6781), 982-986.

109. Kobler, J.; Lotsch, B. V.; Ozin, G. A.; Bein, T., *Acs Nano* **2009,** *3* (7), 1669-1676.

110. Frontmatter. In *Handbook of Porous Solids*, F. Schüth, K. S. W. S., J. Weitkamp, Ed. Wiley- VCH, Weinheim: **2008**.

111. Férey, G.; Serre, C.; Mellot-Draznieks, C.; Millange, F.; Surblé, S.; Dutour, J.; Margiolaki, I., *Angew. Chem.* **2004,** *116* (46), 6456-6461.

112. Klein, N.; Senkovska, I.; Gedrich, K.; Stoeck, U.; Henschel, A.; Mueller, U.; Kaskel, S., *Angew. Chem., Int. Ed.* **2009,** *48* (52), 9954-9957.

113. Y. Park; S.Choi; Kim, H.; Kim, K.; Won, B.; Choi, K.; Choi, J.; Ahn, W.; Won, N.; Kim, S.; Jung, D.; Choi, S. n.; G.Kim; Su.Cha; Jhon, Y.; J.Yang; Kim, J., *Angew. Chem.* **2007,** *119* (43), 8237.

114. Doonan, C. J.; Tranchemontagne, D. J.; Glover, T. G.; Hunt, J. R.; Yaghi, O. M., *Nat Chem* **2010,** *2* (3), 235-238.

115. Chung, Y.; Duerr, B. F.; McKelvey, T. A.; Nanjappan, P.; Czarnik, A. W., *J. Org. Chem.* **1989,** *54* (5), 1018-1032.

116. Huang, W.-H.; Jia, W.-L.; Wang, S., *Can. J. Chem.* **2006,** *84* (4), 477-485.

117. *SWAVE*, Chemspeed Technologies: Augst.

118. Campbell, N. L.; Clowes, R.; Ritchie, L. K.; Cooper, A. I., *Chem. Mater.* **2009,** *21* (2), 204-206.

119. *Accelrys MS Modeling 4.4*, 2008.

120. Sichel, E. K.; Miller, R. E.; Abrahams, M. S.; Buiocchi, C. J., *Phys. Rev. B* **1976,** *13* (Copyright (C) 2009 The American Physical Society), 4607.

121. Leach, A. R., *Molecular Modelling: Principles and Applications*. 2nd ed.; Prentice Hall: Harlow, England, 2001.

122. Connolly, M., *J. Appl. Crystallogr.* **1983,** *16* (5), 548-558.

123. Duren, T.; Millange, F.; Ferey, G.; Walton, K. S.; Snurr, R. Q., *J. Phys. Chem. C* **2007,** *111* (42), 15350-15356.

124. Assfour, B.; Seifert, G., *Microp. Mesop. Mat.* **2010,** *133* (1-3), 59-65.

4. Covalent Functionalization of Covalent Organic Frameworks

4.1. Bromination of a Methyl-Decorated Covalent Organic Framework

4.1.1. Introduction

A great challenge in materials research is the synthesis of crystalline porous materials in which physical and chemical properties and the molecular compositions can be systematically designed. In the past this has been realized for inorganic crystalline materials, such as zeolites and inorganic-organic hybrid metal organic frameworks. Engineering of the zeolitic structures to improve performance and broaden the spectrum of applications has been widely studied.[125] However, due to pore sizes in the microporous range and the absence of organic functional groups modification is limited to cation exchange,[126] preadsorbtion of molecules[127] or internal / external surface modification compatible with silica chemistry.[128] The inorganic-organic hybrid materials; Metal-Organic Frameworks (MOFs), overcame these limitations, due to the possibility to introduce a large variety of chemical functionalities with the organic linkers. For MOFs up to now two different modification approaches have been reported: (1) to use a functionalized organic building block in the self assembly of MOFs (modification prior to MOF synthesis),[129-131] and (2) post-synthetic modification (PSM) of the already existing framework.[23, 108] These modification methods allow to rationally design and fine tune the properties to obtain a functional material. Recently a class of purely organic materials, the Covalent Organic Frameworks (COFs), formed by covalent,

yet reversible condensation reactions of boronic acids with polyols has emerged.[30, 36, 37] The covalent character of the crystalline framework enhances the stability and the use of organic linkers allows for precisely tunable metrics and composition. These materials have gained attention for their hydrogen storage abilities, due to their very high surface areas combined with a very low density and high thermal and chemical stability.[31, 56] Due to a great variety of potential organic linkers many different structures with controllable physical and chemical properties are possible.[60, 63] In principle, as in MOFs, both prior-to-synthesis and post-synthetic modification strategies are conceivable. However, modifying the framework chemically after the synthesis still remains a great challenge.[132] Limiting factors include the compatibility of the anchoring functional group with the COF synthesis (e.g. solvent, reaction temperature), and furthermore the functionality should not decrease the reactivity of the linker nor should it be too demanding sterically). Concerning PSM, the reaction conditions have to be compatible with the COF structure, and the crystalline framework should not degrade during the reaction (e.g. cleavage of boronate ester by base). Regarding the high thermal stability and the large open pore system of COFs, post-synthetic modification grants access to a great variety of covalently attached functionalities. First attempts to tailor pore size and environment were developed by Lavigne and co-workers, using alkyl-functionalized tetraols in the condensation reaction with benzenetrisboronic acid. In this case the framework topology is preserved, but the pore size is altered.[38] The ability to design crystalline porous frameworks with functionalized pores is of great interest, since these materials can find applications in catalysis, separation, and as multifunctional materials with more than one function incorporated in the pore structure. In Figure 4.1 the general modification possibilities are schematically illustrated.

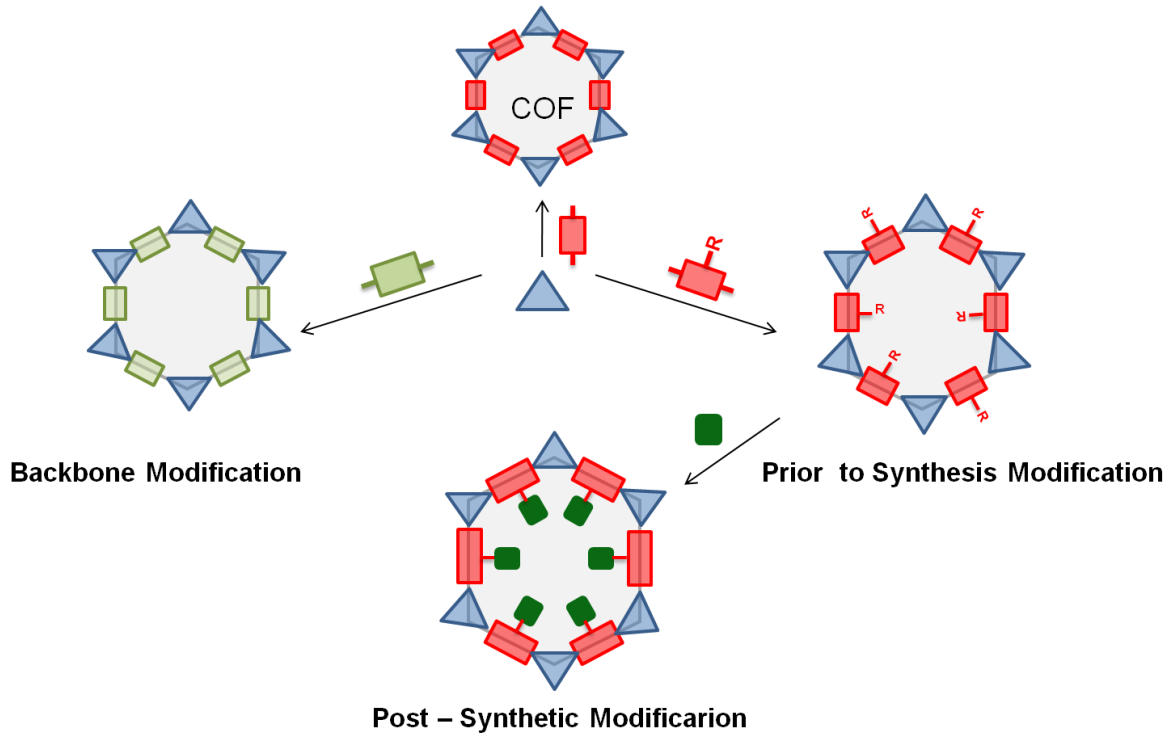

Figure 4.1: Schematic illustration of different modification strategies for COFs.

Here we report the post-synthetic modification of a new mesoporous Covalent Organic Framework. First AT-COF-Me is synthesized by co-condensation of benzene- 1, 3, 5-triboronic acid (BTBA) with 9,10-dimethylanthracene 2, 3, 6, 7-tetraol (DMAT). The methyl groups can be used as anchor points for further reactions; in this work AT-COF-Me was subsequently functionalized with N-bromosuccinimide (NBS) in a radical bromination reaction (Figure 4.2).

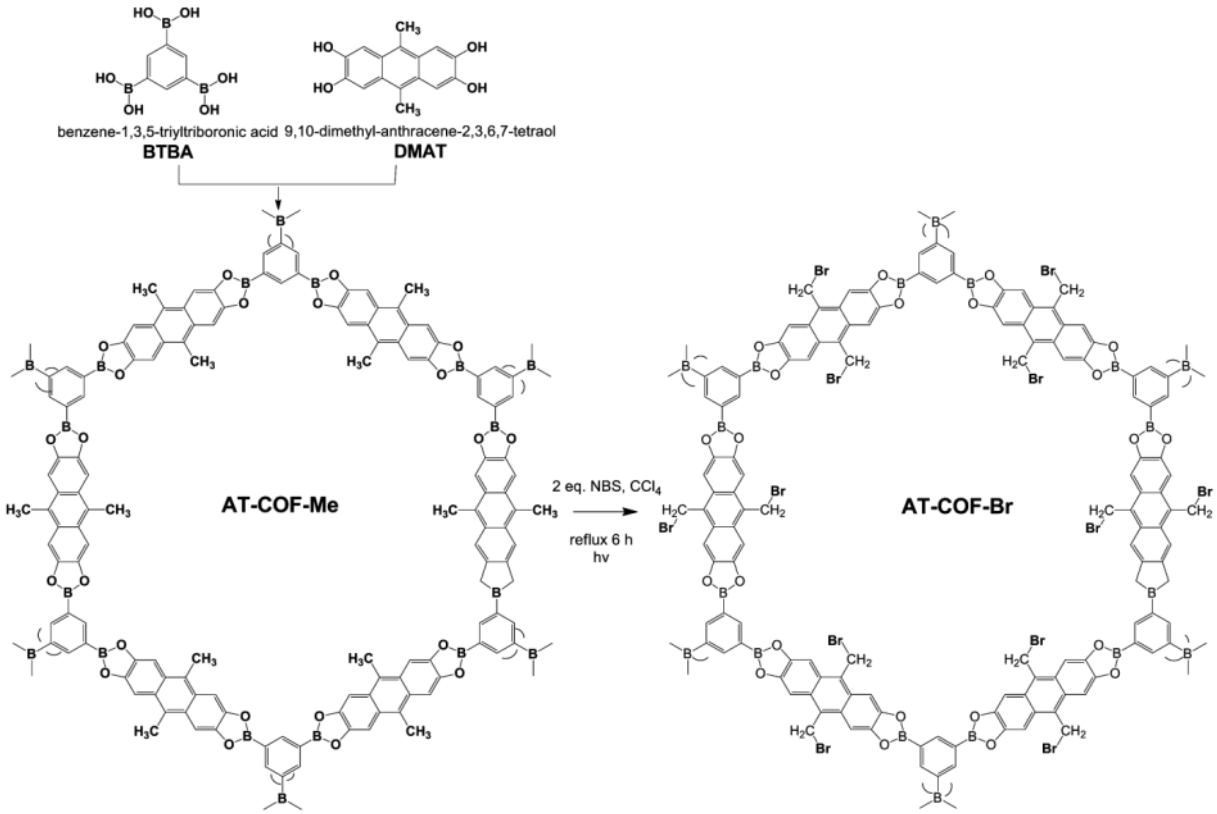

Figure 4.2: Reaction pathway for the synthesis of AT-COF-Me, followed by bromination of AT-COF-Me.

4.1.2. Experimental Section

Materials and Methods

All materials (if not otherwise noted) were purchased from Aldrich or Fluka in the common purities purum and puriss. All materials were used without further purification. The building blocks 9,10-dimethyl-anthracene-2,3,6,7-tetraol (THDMA) and Benzene-1,3,5-triboronic Acid (BTBA) were prepared according to published procedures.[36, 115, 133] All materials were manipulated in air.

X-ray diffraction analysis was carried out on a STOE powder diffractometer in transmission geometry (Cu-Kα1, λ = 1.5406 Å). Fourier-transform infrared spectra of

samples were measured with a Bruker Equinox 55 equipped with a PIKE MIRacle ATR-unit at room temperature. ^{11}B and ^{13}C MAS NMR spectra were recorded on a Bruker DSX Avance 500 with a magnetic field of 11.2 Tesla. A 4 mm MAS triple-resonance sample head was used. The frequency of the rotors was in the case of the ^{13}C-CP-MAS spectrum 10 kHz and for the ^{11}B-MAS spectrum 9 kHz and 20 kHz. TG measurements were performed in a stream of synthetic air (25 ml / min) on a Netzsch STA 440 C TG/DSC. The measurements were carried out with a heating rate of 10 K / min and a temperature range from 30 °C to 900 °C. The nitrogen sorption isotherms were recorded on a Quantachrome Autosorb at 77 K. Prior to the measurement of the adsorption isotherm the sample was heated for 24 h at 150°C under oil pump vacuum. For the evaluation of the surface are the BET model was applied between p/p_0 0.04 and 0.08. The calculation of the pore size distribution was done using the NLDFT model with a carbon kernel for cylindrical pores of the desorption branch.

COF-Me synthesis

For COF-Me synthesis a biotage microwave vial (5 ml) equipped with a magnetic stirring bar was charged with benzene- 1, 3, 5-triboronic acid (0.1 mmol, 26 mg, 1 eq.) and 9,10-dimethylanthracene 2, 3, 6, 7-tetraol (0.2 mmol, 63 mg, 2 eq.). The starting materials were suspended in 1.7 ml of a mixture of anisole and methanol 95 : 5 v : v and heated to 100 °C for 20 min. The green solid product was isolated by filtration and washed with 20 ml dry acetone. After guest removal COF-Me was obtained as green powder (68.5 mg, 0.07 mmol, 71 %).

IR: 3376 (w), 2979 (w), 1701 (w), 1592 (m), 1499 (m), 1458 (s), 1422 (w), 1302 (s), 1247 (m), 1204 (s), 1107 (w), 1041 (m), 900 (s), 841 (m), 764 (m), 753 (w), 701 (m), 632 (m).

^{13}C-CP-MAS NMR (10 kHz): δ = 145 (CO), 125 (Cq), 102 (CH), 13 (CH_3).

^{11}B-NMR (9 kHz): δ = 21 ppm.

Bromination under irradiation

A 50 ml round-bottom flask, equipped with a magnetic stirring bar was charged with COF-Me (50.0 mg, 0.05 mmol, 1 eq.) and NBS (23.1 mg, 0.13 mmol, 2.6 eq.) Subsequently tetrachloromethane CCl_4 (5 ml) was added under a constant N_2 flow. The mixture was heated to reflux for 5 h under irradiation with white light (150 W or 60 W). The precipitate was cooled to room temperature, filtered and washed with acetone. After guest removal at 120 °C in vacuo a black powder was obtained (41.2 mg, 0.03 mmol, 65 %).

IR: 3346 (w), 2961 (w), 2893 (w), 1701 (w), 1592 (m),1505 (w), 1458 (s), 1424 (w), 1304 (s), 1211 (s), 1104 (w), 1066 (w), 943 (m), 900 (w), 873 (w), 848 (w), 812 (w), 787 (w), 701 (m), 635 (m).

^{13}C-CP-MAS NMR (10 kHz): δ = 145 (CO), 125 (Cq), 102 (CH), 26 (CH_2), 12 (CH_3).

^{11}B-NMR (20 kHz): δ = 21 ppm, 16 ppm.

Bromination under AIBN Catalysis

A microwave vial, equipped with a magnetic stirring bar was charged with AT-COF-Me (50 mg, 0.05 mmol, 1 eq), NBS (20 mg, 0.115 mmol, 2.3 eq) and AIBN (14 mg, 0.0005 mmol, 0.01 eq). The reaction mixture was suspended in methyl acetate (3 mL), sealed and heated to 112 °C for 120 min. The precipitate was cooled to room

temperature, filtered and washed with acetone. After guest removal at 120 °C in vacuo a black powder was obtained.

IR: 3346 (w), 2961 (w), 2893 (w), 1701 (w), 1592 (m),1505 (w), 1458 (s), 1424 (w), 1304 (s), 1211 (s), 1104 (w), 1066 (w), 943 (m), 900 (w), 873 (w), 848 (w), 812 (w), 787 (w), 701 (m), 635 (m).

^{13}C-CP-MAS NMR (10 kHz): δ = 145 (CO), 128 (Cq), 124 (Cq), 101 (CH), 29 (CH_2), 11 (CH_3).

^{11}B-NMR (20 kHz): δ = 21 ppm, 16 ppm.

4.1.3. Results and Discussion

Formation and crystallinity of AT-COF-Me was confirmed with powder X-ray diffraction. The expected patterns were simulated with Accelrys software Materials Studio 4.4[119] and compared to the experimentally obtained data. Previously reported 2D COF structures have two possible stacking arrangements of the hexagonal sheets, an eclipsed AA arrangement or a staggered AB stacking.[30, 60] Figure 4.3 shows the PXRD pattern of AT-COF-Me compared to the patterns of the two possible crystal structures. The comparison clearly shows the presence of the eclipsed form.

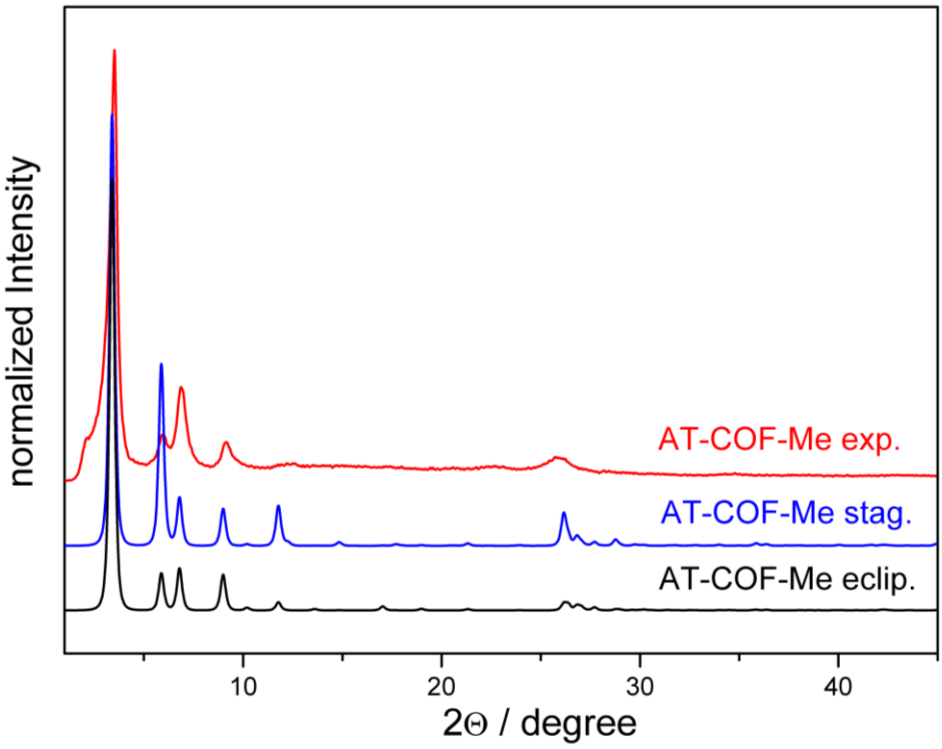

Figure 4.3: Comparison of experimental (red) and calculated staggered (blue) and eclipsed (black) PXRD of AT-COF-Me from the simulated crystal structures.

The connectivity and presence of the desired molecular building blocks was confirmed by ^{11}B and ^{13}C cross polarization magic angle spinning (CP-MAS) NMR spectroscopy and attenuated Total Reflection Infrared (ATR-IR) spectroscopy.

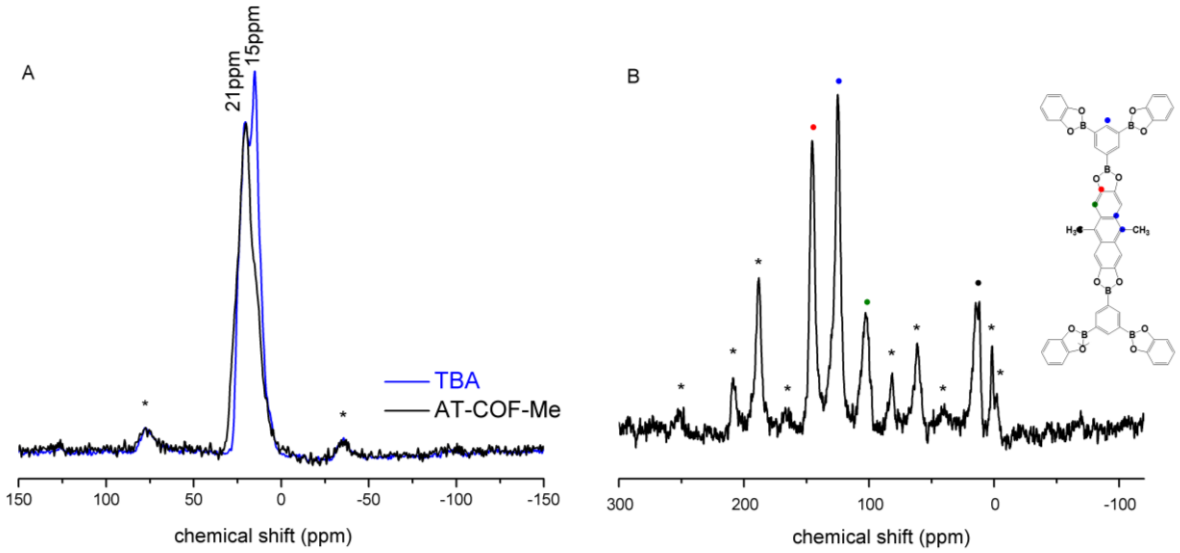

Figure 4.4: A) ^{11}B MAS NMR of starting material TBA (black) and AT-COF-Me (red), B) ^{13}C MAS NMR with assigned carbon atoms. Asterisks (*) indicate peaks arising from spinning side bands.

The esterification of the boronic acid moieties can be confirmed by the shift from 15 ppm of the free boronic acid to 21 ppm of the boronate ester in the ^{11}B NMR spectrum (Figure 4.4 A). The starting material also exhibits a signal at 21 ppm, which is probably caused by initial condensation of boronic acid molecules. In the ^{13}C NMR all signals were assigned to the carbon atoms, confirming the presence of both building blocks in the framework (Figure 4.4 B). Consistent with previously shown COF structures the ATR-IR spectrum (Figure 4.9) indicates the boronate ester formation, due to an attenuated OH stretching band at 3500 cm^{-1}. Further proof is given by the B-O stretching band at 1310 cm^{-1}.

AT-COF-Me exhibits high thermal stability of up to 450 °C as shown by TGA. Permanent porosity of AT-COF-Me was assessed by nitrogen sorption measurements with degassed samples (12 h at 150 °C *in vacuo*). The isotherm was recorded at 77 K. AT-COF-Me shows a type IV isotherm (Figure 4.5) due to the mesoporous character of the material,[106] and a high Brunauer–Emmett–Teller (BET) surface area of 1100 m^2/g. Nitrogen sorption analysis of the material results in anomalous sorption isotherms, which could be reproduced several times. With decreasing relative pressure during desorption, the volume difference between adsorption and desorption at equal relative pressures progressively increases showing a hysteresis-like behavior, most likely due to short equilibration. The pore size distribution of AT-COF-Me was calculated from the desorption branch with NLDFT methods. AT-COF-Me has pores with a pore diameter of around 2.3 nm.

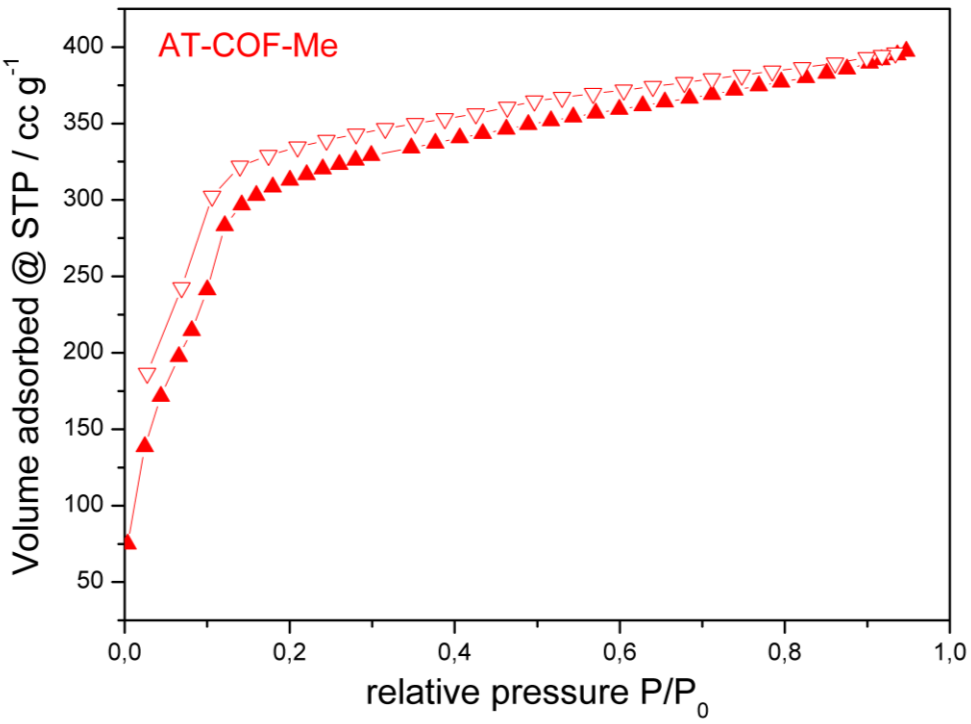

Figure 4.5: N_2 Sorption of AT-COF-Me (▲ adsorption branch and Δ desorption branch)

In order to assess whether the pores in the sample are accessible or blocked by parts of the framework or solvent molecules, the surface area of crystalline materials can be predicted from the crystal structure using geometric methods.121 The Connolly surface is calculated by simulating a probe molecule (in this case nitrogen) rolling along the surface.122 Another method to calculate the surface and pore volume is the accessible surface area.123 The value for the BET surface area calculated from experimental nitrogen adsorption isotherms indicates that almost 70 % of the AT-COF-Me are accessible for solvent molecule. The accessible surface of AT-COF-Me needs to be improved, it emphasizes the significance for an efficient extraction method. (Table 4.1).

Table 4.1: Surface area and pore volume of AT-COF-Me obtained from sorption data and theoretical calculations.

	Surface area m^2/g	Volume cm^3/g
Connolly surface	1970	1.0
Access. surface	1616	0.66
Sorption data	1100	0.45

After successful synthesis and characterization of AT-COF-Me, the material was reacted in a radical Wohl-Ziegler-Bromination reaction with N-Bromoscuccinimide NBS (Figure 4.6). White light (60 W) was used to generate the first radicals by homolytic splitting of the C-Br bond, thus initiating the chain reaction. Both the succinimidyl and bromine radicals can now abstract a hydrogen atom from the tetrahydroxyanthracene-methyl group (THDMA). The resulting primary radical is stabilized by resonance in the anthracene π-system. It abstracts a bromine radical from an additional NBS-molecule, leaving a new succinimidyl radical to continue the chain reaction (Figure 4.6).

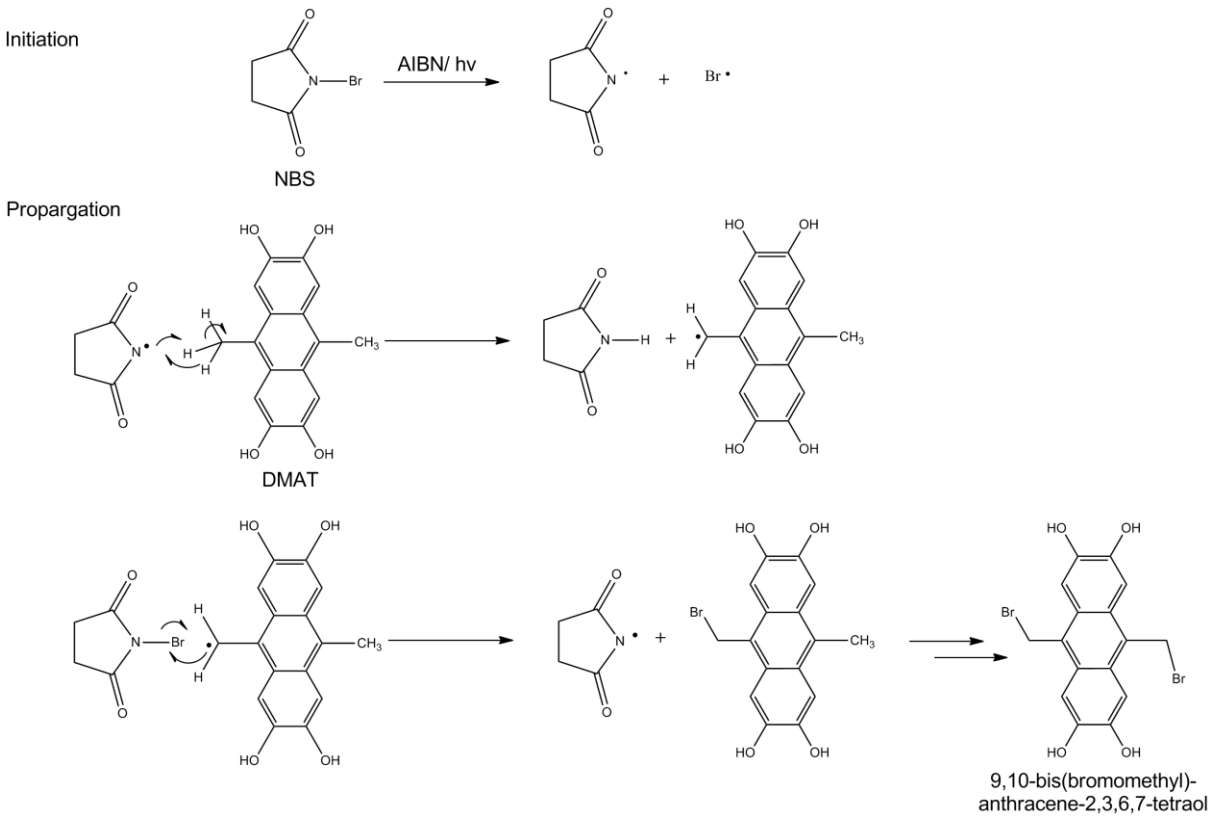

Figure 4.6: Mechanism of the Wohl-Ziegler bromination of DMAT.

As discussed above, the post synthetic modification of crystalline frameworks needs to be conducted with reaction parameters under which the framework stability is maintained. The crystallinity of the framework after the reaction of AT-COF-Me in CCl_4 with NBS as reagent is indicated by PXRD (Figure 4.7). Comparison of the powder patterns of AT-COF-Me and AT-COF-Br shows a decrease in intensity of the 110 reflection, which we attribute to the increase in local electron density in the pores.

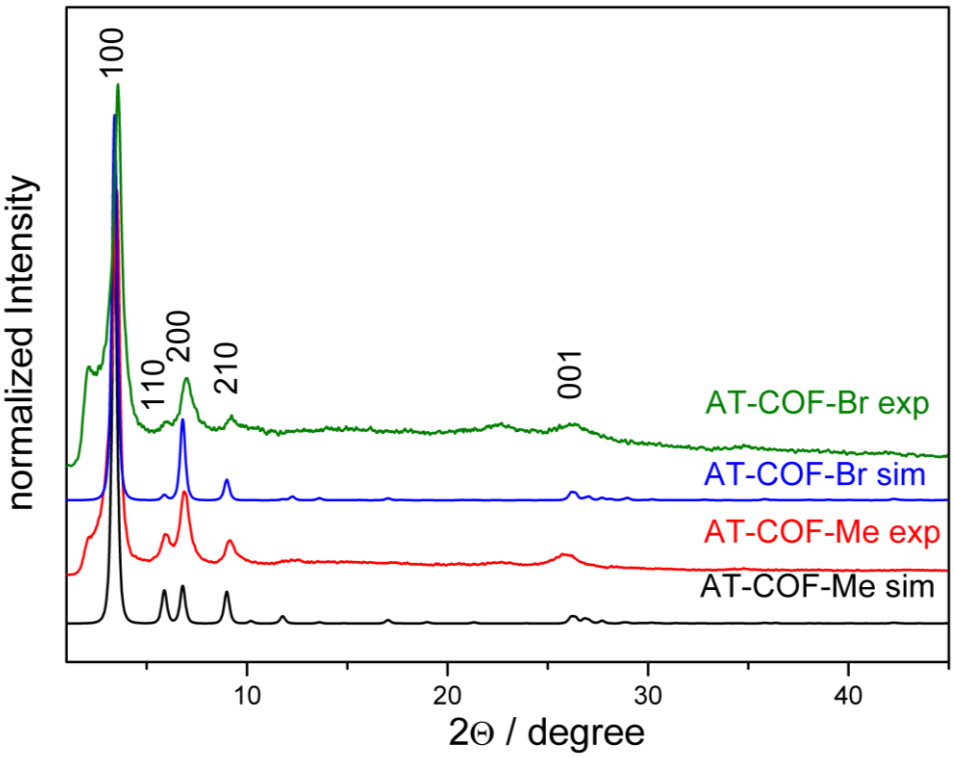

Figure 4.7: PXRD of AT-COF-Me simulated in eclipsed lattice structure (black) and experimentally obtained data (red). The bromination of AT-COF-Me was calculated (grey) and compared to AT-COF-Br experimental data (green).

The bromination was monitored by infrared spectroscopy (ATR-IR) and solid state Nuclear Magnetic Resonance (ss-^{13}C-NMR). As shown in the ^{13}C NMR spectrum (Figure 4.8) of AT-COF-Me the signal at 30 ppm can be clearly attributed to the newly generated methylene group CH_2-Br, which is absent in the original material. However, the signal for -CH_3 is still existent, indicating only a partial bromination of the methyl groups in the framework.

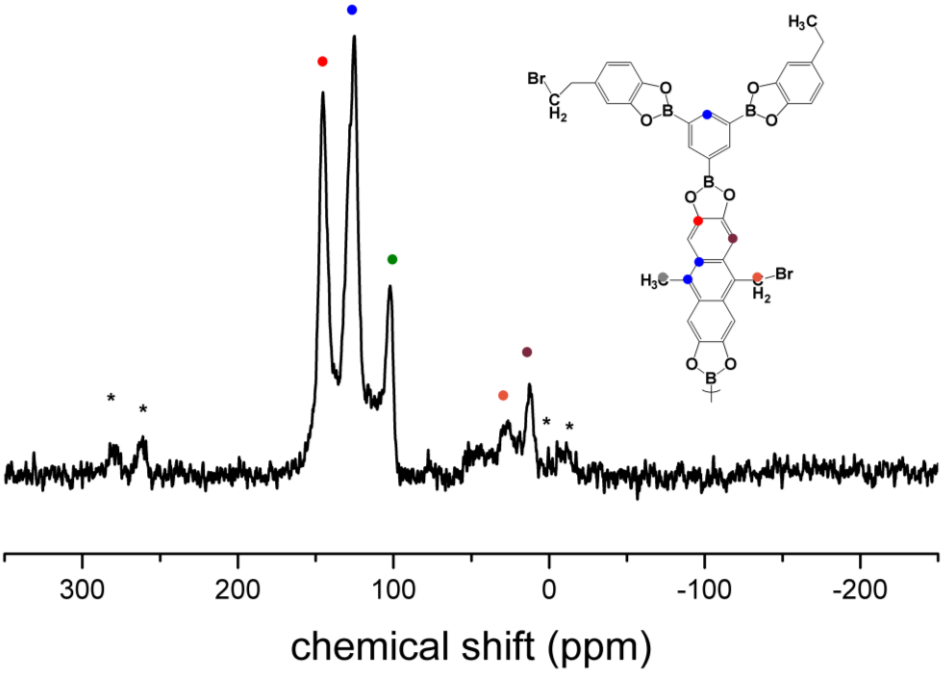

Figure 4.8: ^{13}C NMR spectrum with assigned signals for carbon atoms present in AT-COF-Br. Asterisks (*) indicate peaks arising from spinning side bands.

In the IR spectrum of the products the CH_2 rocking vibration appears at 872 cm^{-1}. The -CH_3 vibrations of the starting material AT-COF-Me seem to be attenuated in the brominated product (Figure 4.9).

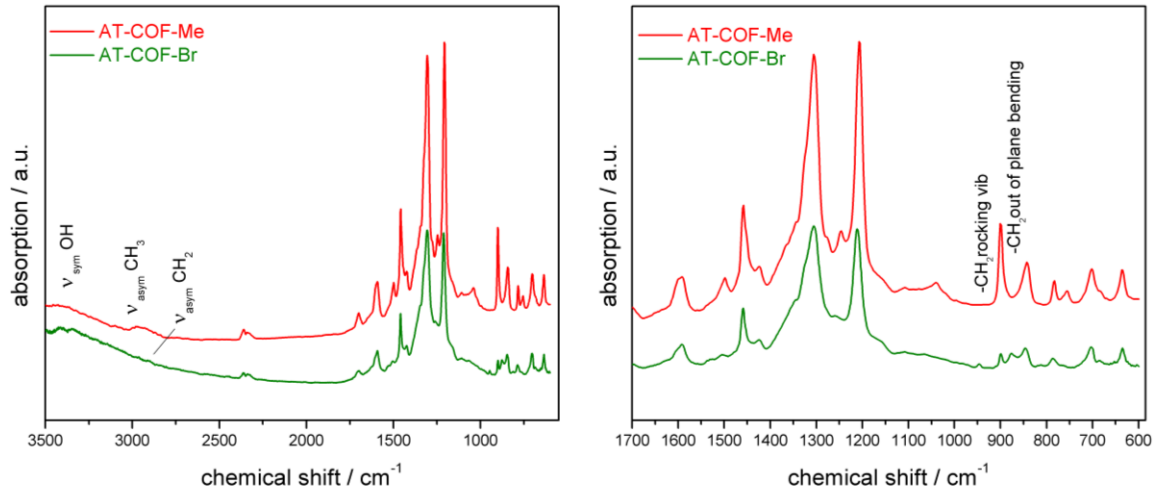

Figure 4.9: ATR-IR spectrum of COF-Me (red) and COF-Br (green).

Table 4.2: Assignment of the most important peaks in the infrared spectrum of AT-COF-Br.

Peak (cm^{-1})	Assignment
3405 (m)	ν_{sym} OH stretch from terminal OH and $B(OH)_2$ groups
2960(w)	ν_{asym} Ar-CH_3
2837(w)	Ar-C-H_3
1699(m)- 1421 (m)	ν_{sym} C=C for fused aromatics
1300(s)	ν_{sym} B-O
1247(s)	$_{sym}$ C-O
1245(m)	ν_{sym} C-O
1207(s)	C-H in plane bending for p-substituted benzene
1068(m)	
1039(w)	ν_{sym} B-C

The percentage of brominated methyl groups was monitored with elemental analysis. Theoretically with complete reaction an amount of 31 wt% bromine is expected. Elemental analysis gives 17 % bromine which corresponds to a bromination of every second -CH_3 group. Furthermore EDX analysis was performed, which also confirms the presence of the bromine. Porosity was confirmed with N_2 sorption measurements at 77 K. The modified material shows a significantly decreased surface area (Figure 4.10). This can be attributed to incompletely emptied pores, probably due to unreacted material or by-products of the reactions.

The pore size distribution is not as homogenous as in AT-COF-Me. This agrees well with the calculated values by comparison of the van der Waals radii of the two materials. The hysteresis-like behavior can be attributed to pore contamination or insufficient equilibrium time as described above. AT-COF-Br exhibits a pore size of about 2.3 nm and the pore size of AT-COF-Br decreases to 1.9 nm. This also explains the typ I isotherm of AT-COF-Br, which is characteristic for microporous materials.

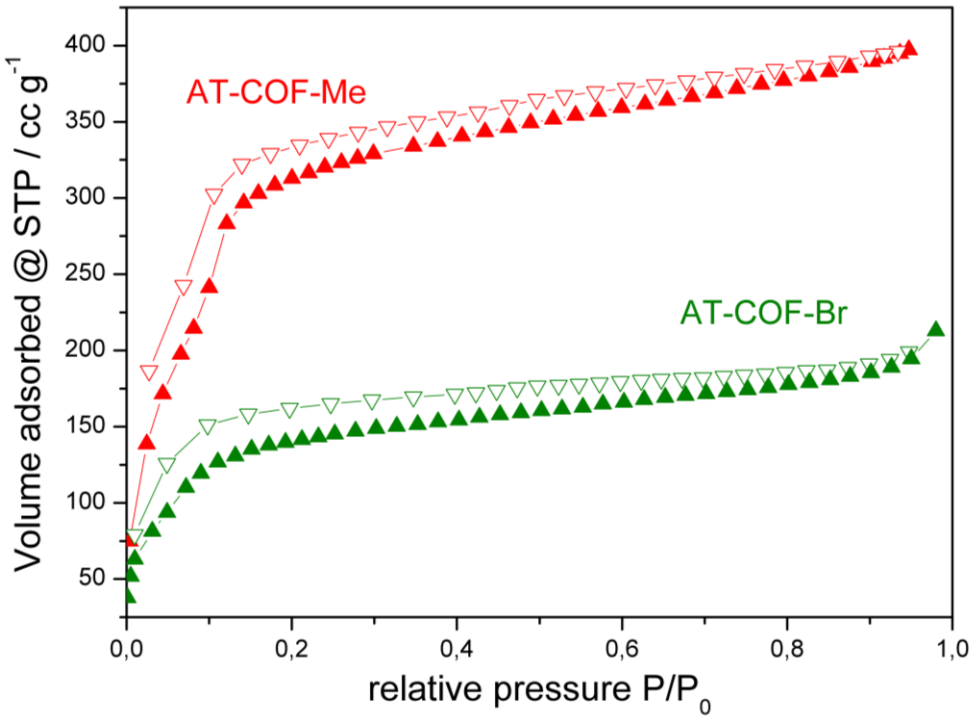

Figure 4.10: Sorption data of mesoporous AT-COF-Me (red) and the microporous brominated species AT-COF-Br (green).

The SEM images show small platelike crystals with sizes of about 100 nm which intergrow to form larger domains (Figure 4.11). No other morphologies were detected.

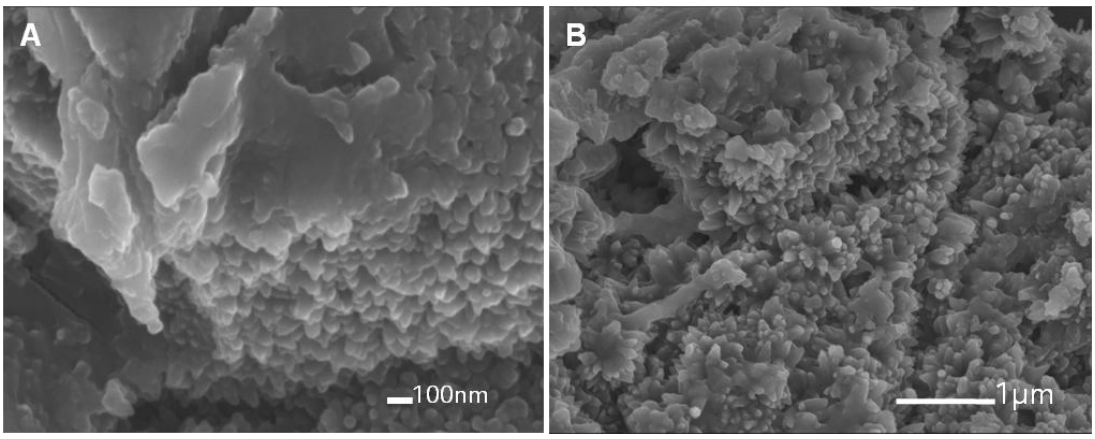

Figure 4.11: SEM micrographs of A) AT-COF-Me and B) AT-COF-Br.

4.2. Esterification of –OH Groups in Terphenyl-based COFs

4.2.1. Introduction

In order to expand the post-synthetic modification strategy to other COF systems a new series of isoreticular COFs based on a terphenyldiboronic acid was investigated. After the successful synthesis of terphenyl-based COF, T-COF-H, by a co-condensation reaction of Terphenyl-4,4''-diboronic acid with HHTP (synthesis described below) a dihydroxy modified terphenyl linker was reacted to form the COF sample T-COF-OH. The ultimate goal of this project is to use the hydroxyl groups in the pores of the framework as anchor points for further reactions. In this thesis several esterification reactions were tested.

First we report the synthesis and characterization of an isoreticular series of terphenyl diboronic acid based COFs: T-COF-H, T-COF-OH and a mixed form T-COF- H/OH. All structures were obtained in a co-condensation reaction with HHTP. The terphenyl based diboronic acids were all synthesized by Pd(II) cross-coupling reaction followed by borylation through boron tribromide. All new ligands were characterized by NMR spectroscopy and mass spectroscopy. Isolated powders were washed extensively with dichloromethane and characterized afterwards with powder X-ray diffraction, solid state MAS NMR, IR spectroscopy, sorption measurements and computer simulations.

The terphenyl-based T-COF series have all the same topology and symmetry as COF-5, however the elongation of the benzene diboronic acid by two more benzene rings leads to greater dimensions. The T-COFs differ slightly in their volume and surface of the pores and significantly in their nature of functional groups decorating

the pores. Pore expansion is also within the scope of this thesis, as illustrated by the structure of BTP-COF (Chapter 3). Using the concept of reticular chemistry it is possible to design new crystalline materials in the mesoporous range with precisely controllable metrics and functionalities in the pores. Combined with the given exceptional attributes of such materials, including their thermal stability, periodicity, and the demonstrated systematic variation in pore size and porosity, it is expected that each member of this series would exhibit unusually rich inclusion chemistry.

Although there have been several new COF structures reported, no examples of a polar functionality in the channels has been shown so far. Here we report for the first time a COF whose pores are decorated with hydroxyl groups (Figure 4.12). After successful synthesis and characterization of T-COF-OH, the hydroxyl groups were esterified with two different reaction strategies: (1) with acetyl chloride and (2) with carboxylic acid followed by a Steglich type reaction. The possibility to exploit small anchoring groups in the pore walls as reaction centers will open up new perspectives for this class of materials.

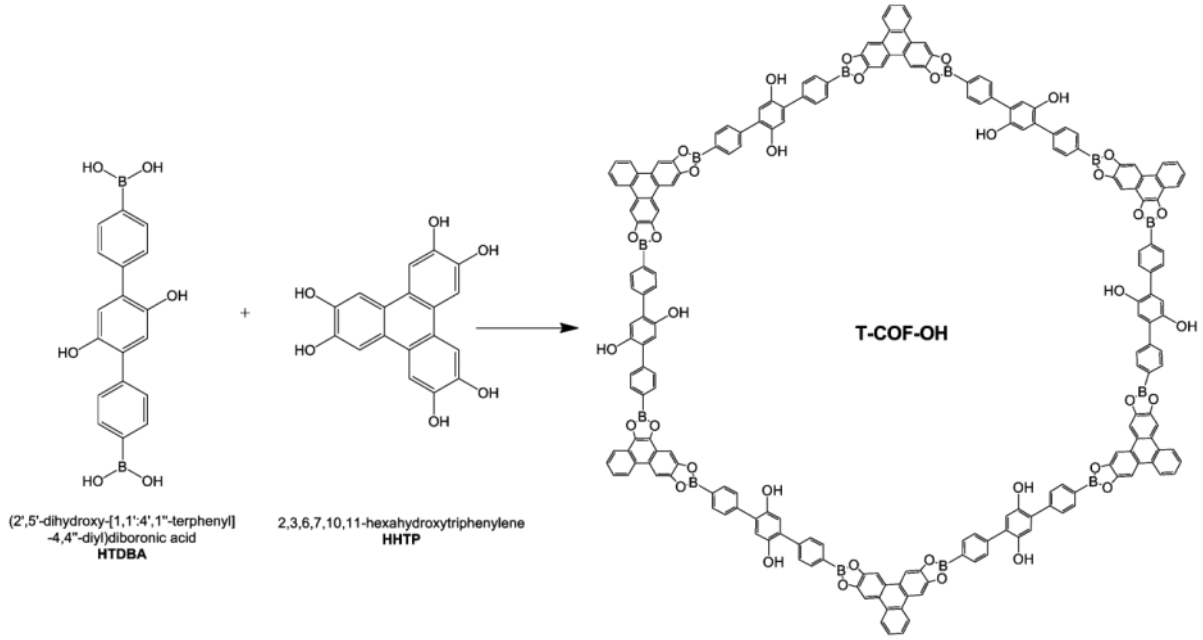

Figure 4.12: Reaction pathway for the synthesis of T- COF-OH.

4.2.2. Experimental Section

Synthesis of [1,1';4',1'']Terphenyl-4,4''-diboronic acid

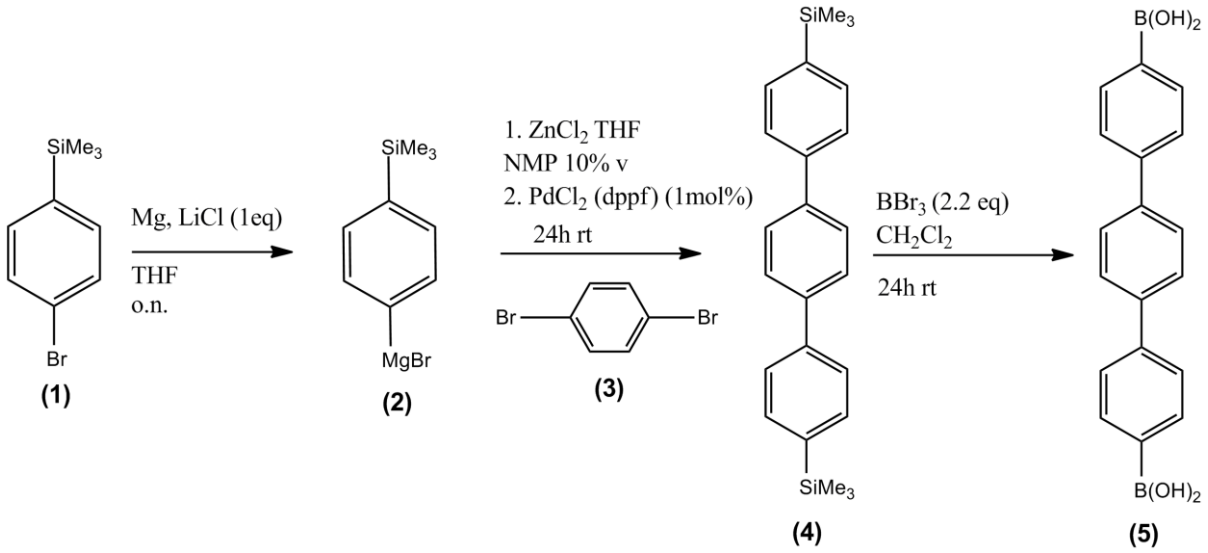

A 250 ml round-bottom flask equipped with a magnetic stirring bar was charged with magnesium turnings (2.15 g, 88.20 mmol, 1.4 equiv.) and lithium chloride

(3.00 g, 63.35 mmol, 90 %, 1.0 equiv). The reactants were dried under vacuum at 250 °C for 20 min. The mixture was cooled under argon atmosphere. Subsequently 50 ml of anhydrous tetrahydrofuran was added. Activation of magnesium was achieved by vigorous stirring of the mixture at room temperature for one hour. Afterwards (4-bromophenyl)trimethylsilane **(1)** (15.21 g, 63.35 mmol, 1.0 equiv) was added dropwise. After 5 minutes, an exothermic reaction set in. The solution was stirred for another hour, and subsequently added dropwise to an ice bath-cooled mixture of zinc (II) chloride (4.36 g, 32.00 mmol, 0.5 equiv.) in 32 ml THF and 3.2 ml (10 %) *N*-Methyl-2-pyrrolidone (NMP).

In a 250 ml round-bottom flask palladium(II) acetate (28.10 mg, 1.13 mmol, 0.50 mol%), 2-dicyclohexylphosphino-2',6'-dimethoxybiphenyl (102.60 mg, 0.25 mmol, 1.0 mol%) and 1, 4- dibromobenzene **(3)** (5.90 g, 25.00 mmol, 0.4 equiv) were dissolved in tetrahydrofuran (20 ml). This mixture was added dropwise to the zinc compound. After a short time the color of the exothermic reaction turned brown and a solid precipitated. The suspension was quenched with 100 ml of a saturated ammonium chloride solution. 60 ml diethyl ether was added and the mixture was extracted four times with 60 ml of water. Successively the grey solid was filtered and dried at 80 °C in an oven for 16 h. Recrystallization in n-heptane yielded the product as a grey solid (5.68 g, 15.5 mmol, 60 %).

[1,1';4',1'']terphenyl-4,4''-di-trimethylsilane **(4)** (5.68 g, 15.5 mmol, 1.0 equiv) was dissolved in 140 ml dichloromethane. Subsequently boron tribromide (9.5 g, 37.9 mmol, 2.2 equiv) was added and the reaction mixture was stirred at room temperature for 24 h. The white suspension was poured on ice (250 g) and stirred until the ice was completely molten. Dichloromethane was removed on the rotary

evaporator and the product was filtered. Recrystallization in water yielded a white powder **(5)** (2.83 g, 8.9 mmol, 57 %)

IR: 3307 (m), 2980 (w), 2963 (w), 2922 (w), 2897 (w), 2867 (w), 1607 (m), 1549 (w), 1421 (m), 1397 (m), 1375 (m), 1346 (m), 1328 (m), 1294 (m), 1274 (w), 1255 (m), 1186 (m), 1113 (m), 1081 (m), 1042 (w), 1026 (w), 1015 (m), 894 (w), 865 (m), 839 (w), 814 (m), 748 (m), 689 (w); 662 (w), 646 (m), 630 (w), 622 (w), 578 (w).

^{13}C-CP-MAS NMR (10 kHz): δ = 138.3 (Cq), 135.8 (Cq), 129.6 (CH), 126.0 (CH), 124.8 (CH) ppm.

^{11}B-NMR (10 kHz): δ = 17.07 ppm.

MS (-p ESI) m/z (%): 353 (100) [M^-+Cl], 352 (40) [M^-+Cl-H].

Synthesis of 2',5''-Dihydroxy-[1,1';4',1'']terphenyl-4,4''-diboronic acid

A 250 ml round-bottom flask, equipped with a magnetic stirring bar was charged with magnesium turnings (2.15 g, 88.20 mmol, 1.4 equiv.) and lithium chloride (3.00 g, 63.35 mmol, 90 %, 1.0 equiv). The reactants were dried under vacuum at 250 °C for 20 min. After cooling to room temperature under argon atmosphere, 50 ml of anhydrous tetrahydrofuran was added. The reaction solution was stirred for another hour. Afterwards (4-bromophenyl)trimethylsilane (15.21 g, 63.35 mmol, 1.0 equiv) was added dropwise. After 5 minutes, an exothermic reaction set in. The solution was stirred for another hour and added dropwise to an ice bath-cooled solution of zinc (II) chloride (32 ml, 1M in tetrahydrofuran) and 3.2 ml (10 %) *N*-methyl-2-pyrrolidone (NMP).

In a 250 ml round-bottom flask, bis(di-tertbutyl)4-dimethylaminophenyl)-phosphine)dichloropalladium (II) (45.00 mg, 0.063 mmol, 1 mol%) and 1, 4-dibromo 2,5-dimethoxybenzene (7,5 g, 25.00 mmol, 0.4 equiv) were dissolved in tetrahydrofuran (20 ml). The mixture was added dropwise to zinc (II) chloride (4.36 g, 32.00 mmol, 0.5 equiv.) in 32 ml THF and 3.2 ml (10 %) *N*-Methyl-2-pyrrolidone (NMP). The suspension was quenched with 100 ml of a saturated ammonium chloride solution. 60 ml diethyl ether were added and the mixture was extracted four times with 60 ml of water. Subsequently the solution was dried over magnesium sulfate and filtered. The solvent was removed by rotary evaporation. Recrystallization in n-heptane yielded the product as a white powder (7.13 g, 16.4 mmol, 66 %).

2',5''-dihydroxy- [1,1';4',1'']terphenyl-4,4''-di-trimethylsilane (7.13 g, 16.4 mmol, 1.0 equiv) was dissolved in 60 ml dichloromethane. Boron tribromide (27.9 g, 111.52 mmol, 6.8 equiv) was added and the reaction mixture was stirred at room temperature for 24 h. The white suspension was poured on ice (500 g) and stirred until the ice was completely molten. Dichloromethane was removed on the rotary evaporator and the product was filtered. The crude product was dissolved in acetone (80 ml), and subsequently reduced to half volume. Then 1,4-dioxane (30 ml) were added and again reduced to half volume. Recrystallization from n-heptane yielded a white powder (5.3 g, 15.1 mmol, 93 %)

IR: 3347 (s), 1606 (m), 1556 (w), 1537 (w), 1423 (m), 1395 (m), 1376 (m), 1338 (s), 1290 (w), 1271 (w), 1256 (w), 1202 (w), 1154 (m), 1094 (m), 1024 (m), 1001 (m), 813 (m), 794 (m), 737 (m), 643 (w), 627 (m).

^{13}C-CP-MAS NMR (10 kHz): δ = 146.5 (CO), 139.6 (Cq), 133.2 (CH), 129.0 (Cq), 127.2 (CH), 115.7 (CH) ppm.

^{11}B-NMR (10 kHz): δ = 17.44 ppm.

^{1}H-NMR (270 MHz, Methanol-D4, 27 °C, TMS): δ = 7.78 (d, *J* = 7.7 Hz, 1H), 7.69 – 7.53 (m, 5H), 6.95 (s, 1H), 6.90 (d, *J* = 3.6 Hz, 1H), 6.86 (s, 1H), 3.65 (s, 2H).

^{13}C NMR (150 MHz, Methanol-D4, 27 °C, TMS): *δ = 133.0 (CH), 133.2 (CH), 128.2 (Cq), 128.1 (CH), 117.5 (CH) ppm.*

MS (-p ESI) m/z (%):385 (100) [*M*$^-$+Cl], 384 (64) [*M*$^-$+Cl-H], 341 (29) [*M*$^-$+Cl-HO_2B].

Synthesis of T-COF-H

A stainless steel autoclave (20 ml) was charged with [1,1';4',1''']terphenyl-4,4'''-diboronic acid (66.7 mg, 0.21 mmol, 2.3 equiv) and 2,3,6,7,10,11-hexahydroxytriphenylene (30.0 mg, 0.09 mmol, 1.0 equiv). 2 ml of a mixture of toluene : methanol 85 : 15 v : v were added. The reaction mixture was heated to 150 °C for 72 h. The grey solid product was isolated by filtration and washed with 20 ml dry DCM. After guest removal T-COF-H was obtained as grey powder (45.5 mg, 34.0 µmol, 48 %).

IR: 3330 (w), 3033 (w), 1696 (w), 1609 (m), 1530 (m), 1493 (m), 1440 (m), 1354 (s), 1276 (m), 1241 (m), 1160 (m), 1070 (m), 1018 (w), 1002 (w), 856 (w), 835 (w), 812 (m), 736 (w), 648 (w), 612 (w).

Synthesis of T-COF-OH/H

A stainless steel autoclave (20 ml) was charged with 2',5'-dihydroxy-[1,1';4',1''']terphenyl-4,4'''-diboronic acid (36.5 mg, 0.10 mmol, 1.1 equiv),

[1,1';4',1''']terphenyl-4,4'''-diboronic acid (32.1 mg, 0.10 mmol, 1.1 equiv) and 2,3,6,7,10,11-hexahydroxytriphenylene (30.0 mg 0.09 mmol, 1.0 equiv). 2 ml of a 9 : 1 v : v mixture of toluene : methanol were added. The reaction mixture was heated at 150 °C for 72 h. The grey precipitate was filtrated and washed with 20 ml DCM. After guest removal T-COF-OH/H was obtained as grey powder (20.0 mg, 14.0 µmol, 43 %).

IR: 3352 (w), 3045 (w), 1609 (m), 1535 (m), 1510 (m), 1493 (m), 1440 (m),1358 (s), 1274 (m), 1243 (s), 1169 (s), 1125 (m), 1070 (m), 1039 (w), 1018 (w), 1002 (w), 994 (w), 987 (w), 854 (m), 812 (m), 804 (w), 735 (w), 674 (w), 649 (m), 621 (w), 610 (w).

Synthesis of T-COF-OH

A stainless steel autoclave (20 ml) was charged with 2',5'-dihydroxy-[1,1';4',1''']terphenyl-4,4'''-diboronic acid (73.0 mg, 0.21 mmol, 2.1 equiv) and 2,3,6,7,10,11-hexahydroxytriphenylene (30.0 mg 0.09 mmol, 1.0 equiv). 2 ml of a 1 : 1 v : v mixture of mesitylene : 1,4–dioxane were added. The reaction mixture was heated at 150 °C for 72 h. The brown solid was isolated by filtration and washed with dry 20 ml acetone. After guest removal T-COF-OH was obtained as grey powder (16.0 mg, 11.1 µmol, 16 %).

IR: 3307 (w), 1609 (m), 1526 (m), 1491 (m), 1440 (m), 1392 (m), 1353 (s), 1278 (m), 1243 (s), 1164 (m), 1111 (w), 1070 (m), 1039 (w), 1015 (m), 999 (w), 854 (m), 838 (m), 804 (w), 768 (w), 748 (w), 727 (w), 705 (w), 679 (w), 653 (w), 613 (w).

Esterification of T-COF-OH with acetyl chloride

In a dried and argon-flushed 10 ml Schlenk flask, equipped with a septum and a magnetic stirring bar T-COF-OH (71.7 mg, 0.05 mmol, 1.0 equiv) was suspended in dichloromethane (6 ml) for 10 min. Acetyl chloride (19.4 µl, 0.36 mmol, 1.20 equiv) was added to the reaction solution and stirring was continued at room temperature for 16 h. The grey solid was filtrated and washed with dry acetone (20 ml) and DCM (5 ml). Acetylated T-COF-OH, namely T-COF-OAc was obtained as grey powder.

IR: 3307 (w), 1741 (w), 1609 (m), 1526 (m), 1491 (m), 1440 (m), 1392 (m), 1353 (s), 1278 (m), 1243 (s), 1164 (m), 1111 (w), 1070 (m), 1039 (w), 1015 (m), 999 (w), 854 (m), 838 (m), 804 (w), 768 (w), 748 (w), 727 (w), 705 (w), 679 (w), 653 (w), 613 (w).

^{13}C-CP-MAS NMR (10 kHz): δ = 171.2 (CO), 145.5 (Cq), 139.5 (Cq), 133.2 (Cq), 127.4 (CH), 123.5 (Cq), 103.2 (CH), 20.0 (CH_3).

^{11}B-NMR (20 kHz): δ = 21.90 ppm.

Steglich Esterification of T-COF-OH

In a 25 ml round-bottom flask equipped with a magnetic stirring bar T-COF-OH (75.0 mg, 0.05 mmol, 1.0 equiv) was suspended in dichloromethane (5 ml). The suspension was allowed to stand for 10 min without stirring. Subsequently a pre-mixed solution of 4-pentynoic acid (9.81 mg, 0.1 mmol, 2.0 equiv), *N,N'*-diisopropylcarbodiimide (12.6 mg, 0.1 mmol, 2.0 equiv) and 4-dimethylaminopyridine (DMAP) (5.0 mg, 0.04 mmol, 10 mol %) in dichloromethane (2 ml) was added dropwise to the T-COF-OH suspension. The reaction mixture was

stirred at 22 °C for 72 h. The solid was filtered of and washed with acetone (20 ml) and dichloromethane (5 ml).

IR: 3271 (w), 2987 (w), 2941 (w), 1735 (m), 1648 (s), 1610 (m), 1546 (m), 1492 (s), 1439 (m), 1392 (m), 1356 (s), 1249 (s), 1214 (m), 1160 (m), 1069 (w), 1040 (m), 1017 (w), 995 (w), 942 (m), 839 (w), 806 (m), 748 (w), 724 (w), 681 (w), 648 (w)

^{13}C-CP-MAS NMR (10 kHz): δ = 185.8 (CO), 170.7 (CO), 145.3 (Cq), 133.4 (Cq), 127.7(Cq), 122.8(CH), 116.8 (Cq), 103.4 (CH), 82.3 (C_q), 68.9 (CH), 38.1 (CH_2) 13.4 (CH_3).

^{11}B-NMR (20 kHz): δ = 22.30 ppm

4.2.3. Results and Discussion

Terphenyl-based COFs

Synthesis and characterization of the isoreticular series of T-COFs were successfully carried out during this work. The respective diboronic acids were reacted in a solvothermal synthesis with the trigonal polyol HHTP. The optimized synthesis conditions for each system, e.g. solvents, solvent ratio, concentration and educt ratio were obtained by parameter screening in High-Throughput experiments (see appendix). The optimized reaction time and temperature of the isoreticular series of T-COFs was found to be 72 h and 150 °C. The isolated powders were characterized by powder X-ray diffraction. Starting with the possible arrangement of the building blocks, the crystalline structure was modeled. Based on the geometry-optimized structure, diffraction patterns were calculated using the module reflex in the Materials Studio program.[119] The simulated powder patterns were compared to the experimental patterns (Figure 4.13). In all cases the hexagonal sheets are aligned by π-stacking in an eclipsed conformation resulting in 1D channels along the c-axis. The additional peaks arise most probably to due to residues of the terphenyl boronic acid, which isn't removed in the washing procedure, due to its low solubility.

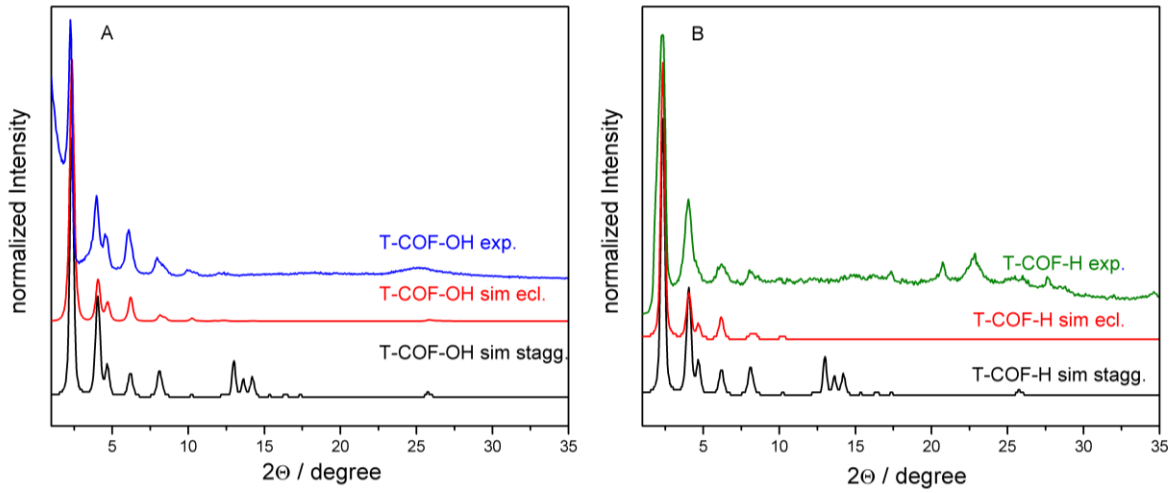

Figure 4.13: In A) the experimentally obtained powder pattern of T-COF-OH (blue), and in B) T-COF-H (green) respectively, is compared to the calculated diffraction patterns of the two possible arrangements of the molecular building blocks, eclipsed (red) stacking and staggered (black) packing of the hexagonal sheets.

The porosity of the IRCOF series was confirmed with N_2 sorption measurements at 77 K. The obtained isotherms are depicted in Figure 4.14, showing in all cases type IV isotherms, typical for mesoporous materials. Porosity calculations using the NLDFT kernel gives pores of around 4.2 nm (Figure 4.15). To evaluate these data, porosity was calculated with the solvent accessible surface tool of MS studio and compared to the experimentally obtained data. As shown in Table 4, the IRCOF series should be highly porous with pore sizes of 4 nm and surface areas of more than 2000 m^2/g. However, the N_2 sorption measurements show only modest porosity, with the exception of T-COF-OH. The pores of T-COF-H are not free, since only 10 % of the surface area is accessible, 40 % of T-COF-H/ OH and 70 % T-COF-OH are accessible. This discrepancy very likely results from the insufficient extraction of the frameworks. During synthesis solvents and single molecules or oligomers of the starting materials are probably enclosed in the pores of the

framework. Prior to sorption measurements the crude product was treated with dichloromethane for 24 h, followed by outgassing for 12 h at 150°C.

Table 4.3: Surface area and pore sizes of T-COFs obtained from sorption data and theoretical calculations.

T-COF-	H	OH	H / OH
Pore size calc. [nm]	4.1	4.1	4.1
Pore size exp. [nm]	-	4.2	4.2
$S_{solv.\ acces.}$ [m^2/g]	1980	1830	1910
$S_{Connolly}$ [m^2/g]	2190	2020	2100
S_{BET} [m^2/g]	190	1400	850

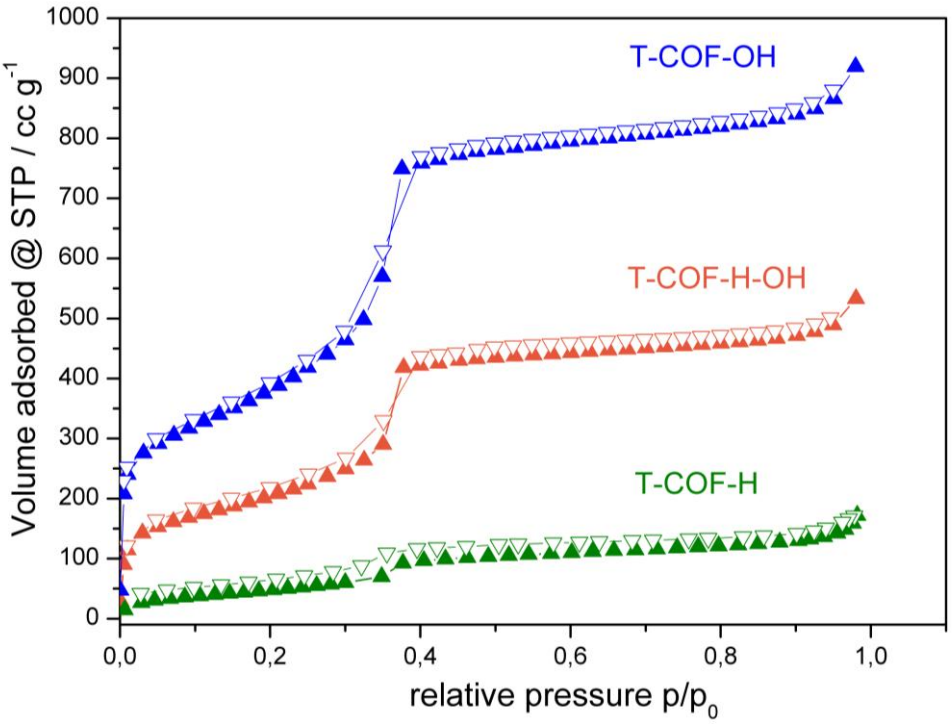

Figure 4.14: N_2 Sorption of isoreticular series of T-COFs.

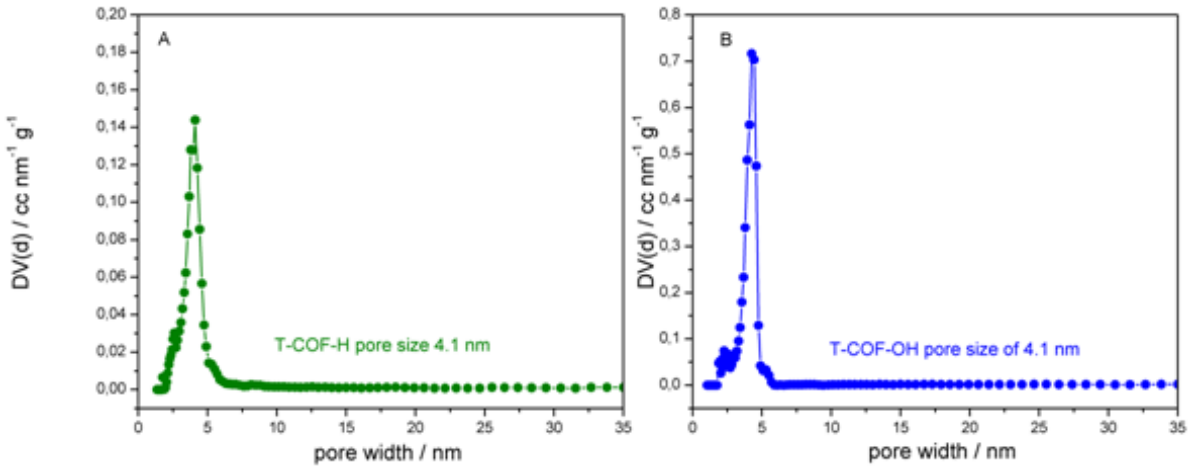

Figure 4.15: Pore size distribution of T-COF-H (green) and T-COF-OH (blue).

Thermal stability was monitored with thermogravimetric analysis under ambient conditions. All terphenyl COFs are thermally stable up to 450 °C (Figure 4.16). For T-COF-H two small steps are observed, thus likely in the first step up to 150 °C solvent removal is achieved and in the second step up to 200 °C unreacted starting material and small oligomers are combusted. This second step agrees with the impurities in the PXRD pattern and the clogged pores of the T-COF-H shown by nitrogen sorption. The amount of remaining B_2O_3 corresponds approximately to the expected boron content. The shape of the TGA trace of T-COF-OH suggests that the pore system is already degassed at about 150 °C, which corresponds to the much greater surface area compared to T-COF-H determined in the nitrogen sorption experiments.

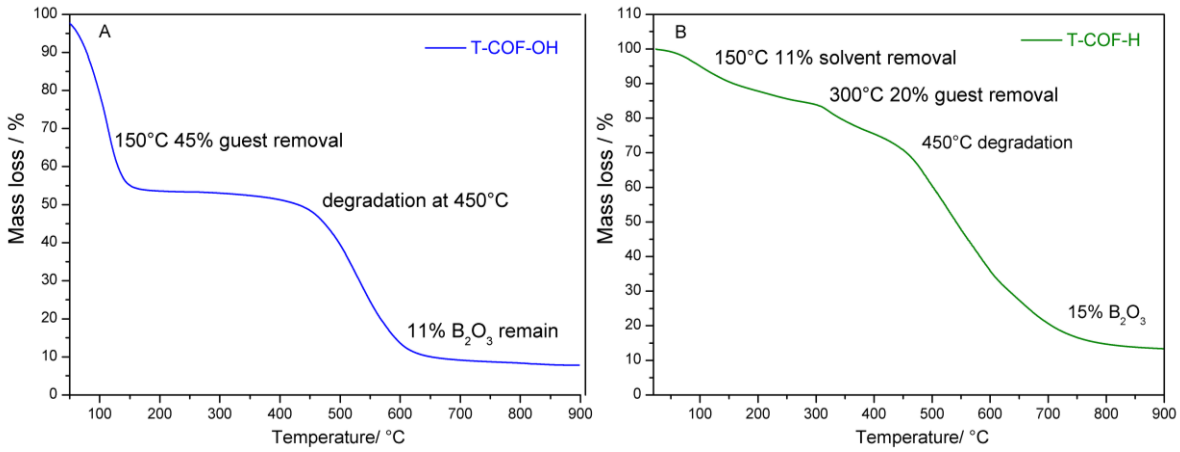

Figure 4.16: TGA data of isoreticular series of terphenyl-based COFs.

After successful synthesis and characterization of the new series of terphenyl COFs, different esterification reactions of T-COF-OH were investigated.

Esterification with acid halides

The acetylation of alcohols with acetyl halides gives the desired ester. Acetyl halides, e. g. acyl chloride are very reactive reagents.

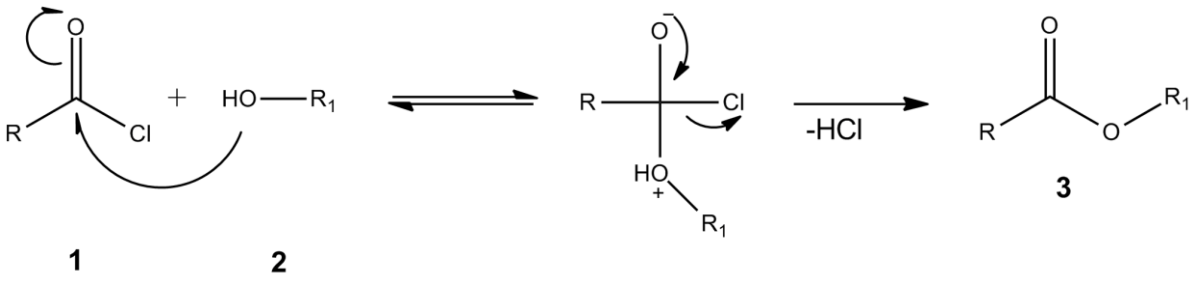

Figure 4.17: Mechanism of esterification of an alcohol with an acetylchloride derivative.

The chloride group is an excellent leaving group enabling the nucleophilic acyl substitution. Addition of a base is desirable to neutralize the hydrochloric acid byproduct. However, during this work the esterification reactions were performed

without a base, due to the basic ester of the boronate ester in the COF framework. During this work R_1 represents the terphenyl linker of the COF framework.

In order to examine the stability and crystallinity of the framework after the modification reactions, X-ray diffraction was performed. The powder pattern of acetylated T-COF-OAc is in good accordance with the as-synthesized pattern of T-COF-OH (Figure 4.18), leading to the conclusion that the framework is intact after post-modification. However an increase of the background can be detected implying an increase of amorphous material, suggesting a partial degradation of the framework, probably caused by the hydrochloric acid generated during reaction. Alternatively, this reduction in signal-to-noise could also result from filling of the pores with reaction products, thus reducing the X-ray contrast. After thermal treatment at 150 °C for 12 h in vacuo, the amorphous background decreases again, presumably due to removal of reaction products, such as monomers or oligomers in the pores.

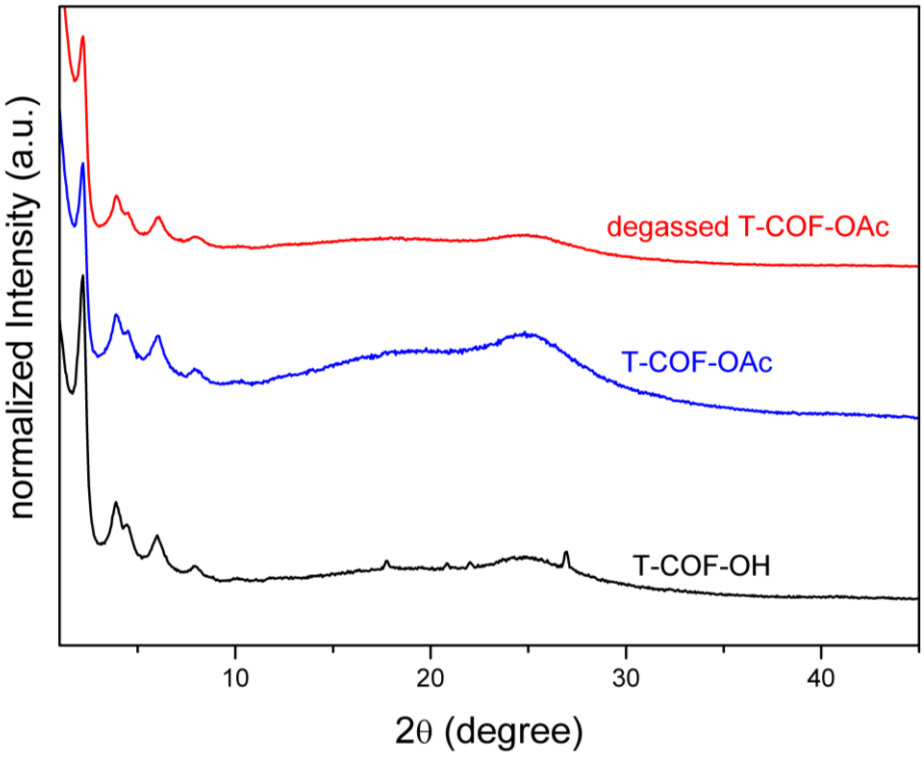

Figure 4.18: PXRD of T-COF-OH (black) compared to T-COF-OAc before degassing (blue) and after degassing (red).

Formation of the acetyl bond was followed by ATR-IR spectroscopy. The presence of the C=O stretching vibration of acyl ester at 1741 cm^{-1} confirms the successful esterification of T-COF-OH. C=O bands of starting material (acetyl chloride 1802 cm^{-1}) and possible by-products (acetic acid 1711 cm^{-1}) can be clearly distinguished from the ester formed in the COF. Peak broadening arises, probably due to guest interactions in the pores with the ester.

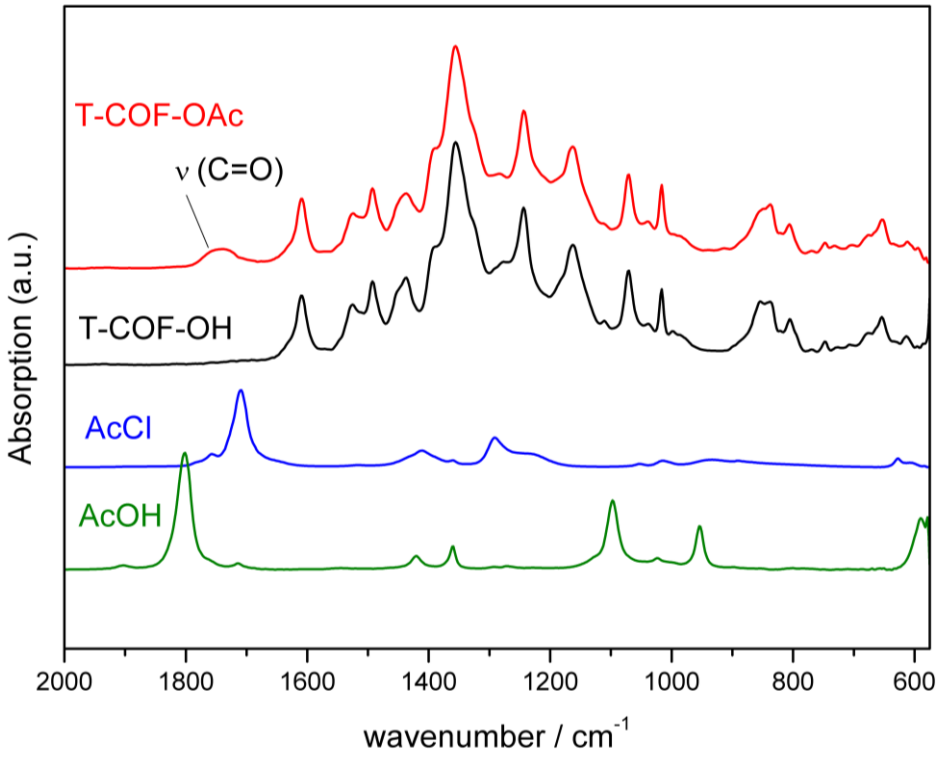

Figure 4.19: ATR-IR spectrum of T-COF- OH (black) as synthesized, T-COF-OAc (red), acetyl chloride (green) and acetic acid (blue).

Further proof for the ester formation can be provided by ^{13}C CP-MAS NMR spectroscopy (Figure 4.20). The signal at 171 ppm can be clearly assigned to the sp^2 carbon atom of the ester moiety and the signal at 20 ppm to the sp^3 carbon of the methyl group, indicating a successful acetylation of the hydroxyl groups, since both signals are absent in the ^{13}C-MAS-NMR spectrum of T-COF-OH (see Appendix Figure 8.10).

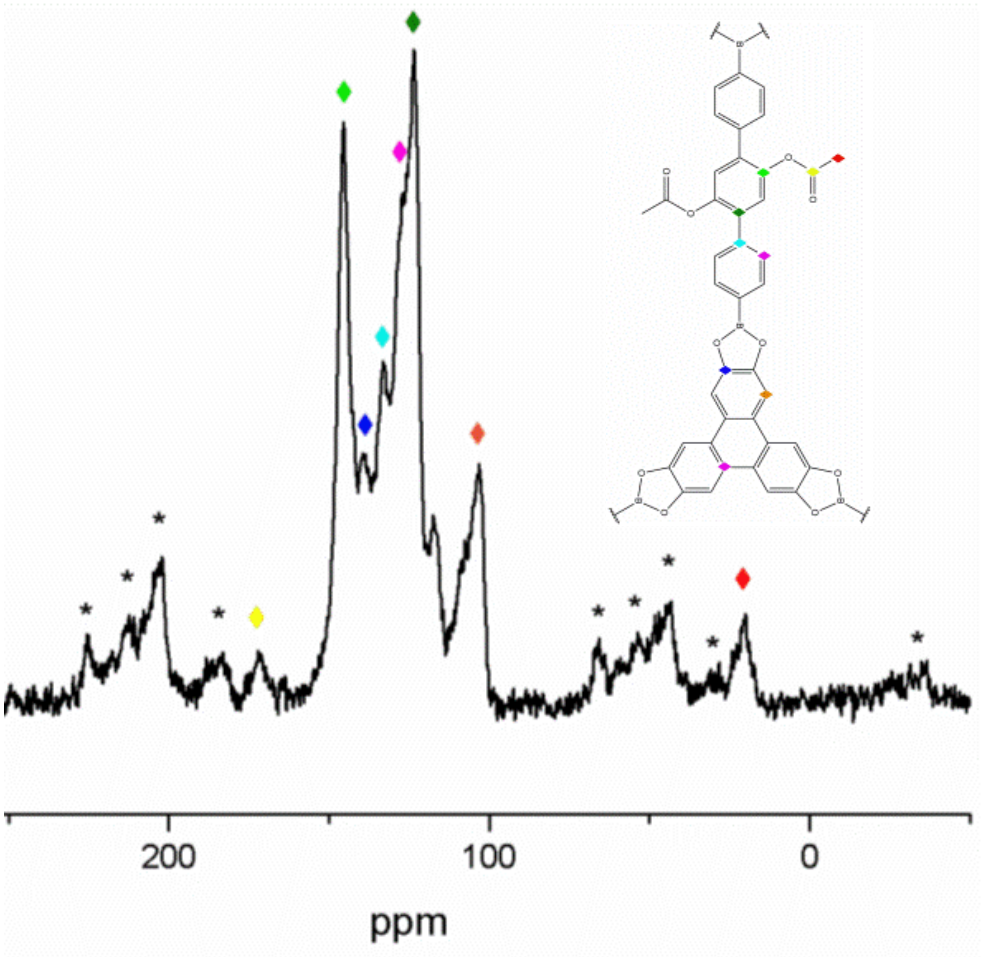

Figure 4.20: ^{13}C NMR spectrum of T-COF-OAc with assigned signals for present carbon atoms. Asterisks (*) indicate peaks arising from spinning side bands.

The pore system of T-COF-OAc, investigated with N_2 sorption at 77 K, shows a typical type IV isotherm. However the BET surface area of 128 m^2/g is significantly lower than the surface area of T-COF-OH (see above). Theoretical calculations of the solvent accessible surface area predict an internal surface that is 17 times higher (see Table 4.3). Reasons for this significant difference of surface areas can be partial filling with reaction products and hence incomplete extraction of the pores, or partial degradation of the framework. Both conclusions would also be consistent with the higher amorphous background obtained in the powder pattern. Conclusions about a successful reaction at the hydroxyl groups of the T-COF-OH framework are therefore not possible, since also degraded parts, such as mono- or

oligomers, react in the same manner. Further proof is needed, to ascertain modification at the desired framework hydroxyl groups. The powder patterns of the COF before and after the post-synthetic modification should be without impurities or amorphous background, indicating a clean and perfectly crystalline structure, in addition with an agreement of the calculated and measured surface areas the presence of any other material can be excluded indicating that the modification only took place at the framework walls.

Thermal stability was investigated by thermogravimetric analysis. Figure 4.21 shows a first weight loss of 8 % until 160 °C, indicating removal of guest molecules, such as the solvents mesitylene and dioxane. Degradation of the T-COF-OH framework starts at 400 °C and the remaining amount of 9 % corresponds to B_2O_3 and some impurities.

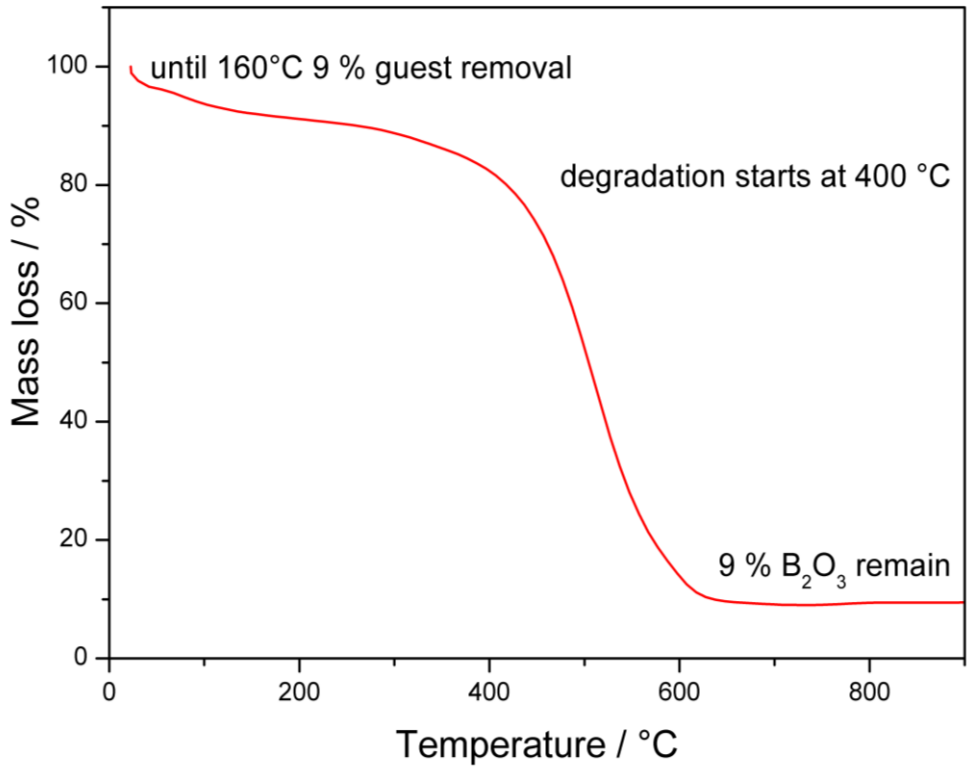

Figure 4.21: TGA of T-COF-OAc.

Steglich Esterification of T-COF-OH

The esterification of the hydroxyl groups of T-COF-OH was carried out using a slightly modified version of the Steglich esterification.[134]

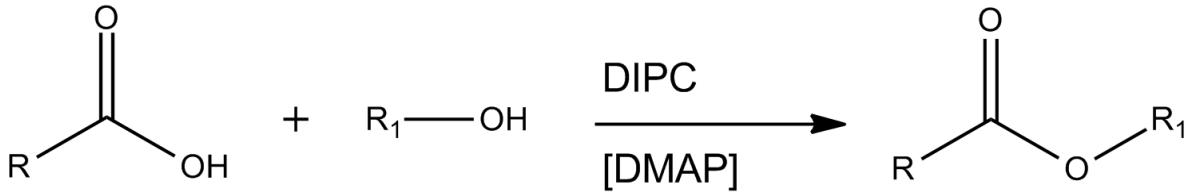

Figure 4.22: Reaction scheme for Steglich esterification of a carboxylic acid and an alcohol.

In a first step the acidic proton is abstracted from the acid by a nitrogen lone pair of the *N,N'*-diisopropycarbodiimide (DIPC) (**2**). The carboxylate ion can then attack the central diimide carbon atom in an SN_2 reaction to yield an *O*-acyl isourea intermediate, which can be viewed as a carboxylic ester with an activated leaving group. 4-*N,N'*-dimethylaminopyridine (DMAP) subsequently attacks as a nucleophile in a second SN_2 reaction the intermediate (**3**), forming a reactive amide by substitution of diisopropylurea (DIPU). In (**3**) the electron density at the carboxylic carbon atom is further reduced and therefore allows the alcohol to act as a nucleophile.

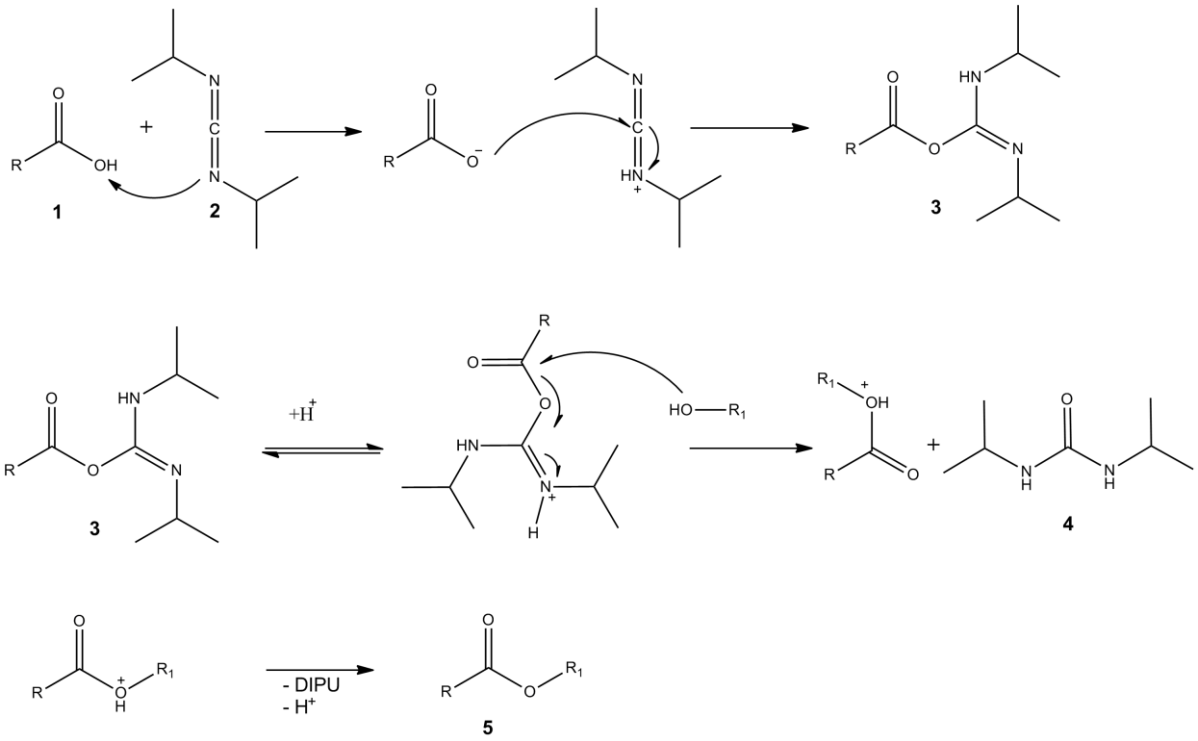

Figure 4.23: Mechanism of a Steglich esterification reaction.

After subtraction of a proton, DMAP is restored to enter a new catalytic circle and the desired ester is formed. Instead of traditionally used *N*,*N*'-dicyclohexyl carbodiimide (DCC), the more readily soluble *N*,*N*'-diisopropy carbodiimide (DIPC) was used to prevent clogging of the COF's pores by the urea byproduct.

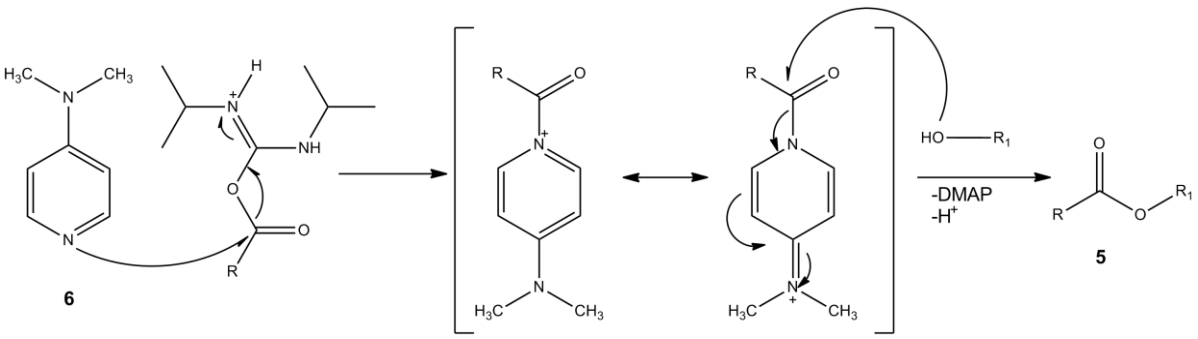

Figure 4.24: Mechanism of the suppression of the rearrangement of the urea byproduct by catalytic amounts of DMAP.

After the esterification reaction the stability of the T-COF-OH framework was monitored with powder X-ray diffraction.

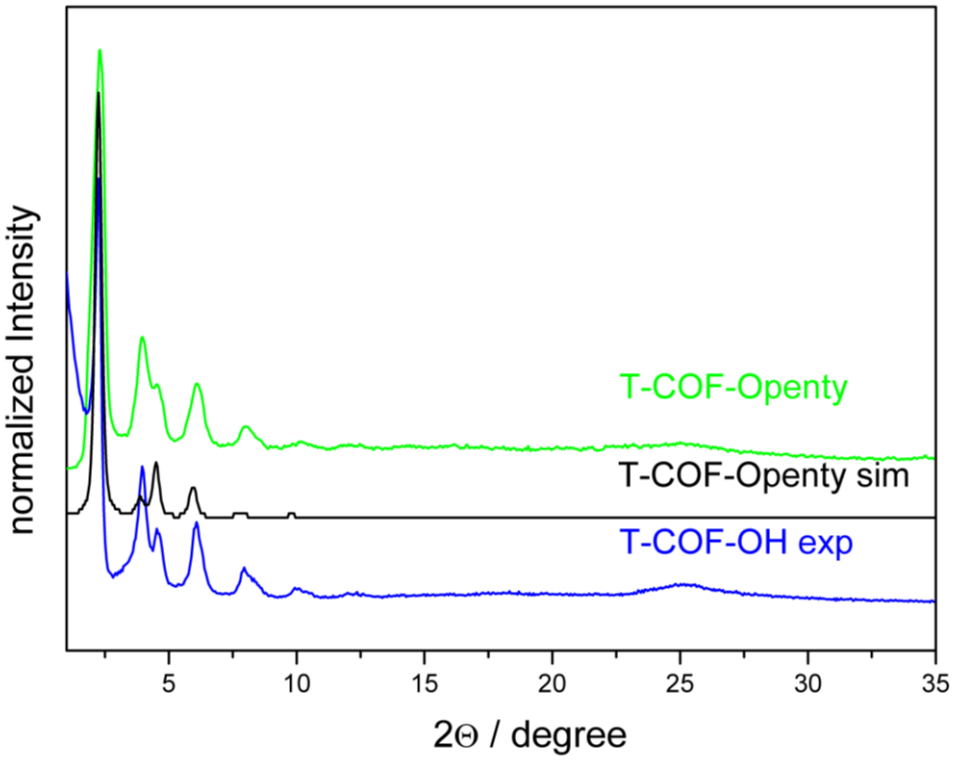

Figure 4.25: PXRD pattern of T-COF-OH (black) in comparison to the structures functionalized with pentynoic acid after Steglich esterification calculated (blue) and as synthesized T-COF-Openty (green).

As indicated by the presence of the reflections indexed as 100, 110, 200, 210 and 001 in Figure 4.25 the framework is compatible with the reaction conditions of the Steglich reaction. Furthermore the crystallinity is conserved. However the intensities of the 110 and 200 reflections differ from the calculated powder patterns. A reasonable explanation therefore might be that in the simulated data every single hydroxyl group is acetylated, which is probably not the case for the experimental data.

To verify the presence of the acetyl groups ATR-IR spectroscopy was performed, showing a weak C=O stretching band at 1750 cm^{-1} (Figure 4.26). Furthermore, the presence of the acetylene group is confirmed at 1216 cm^{-1} and at 1015 cm^{-1}.

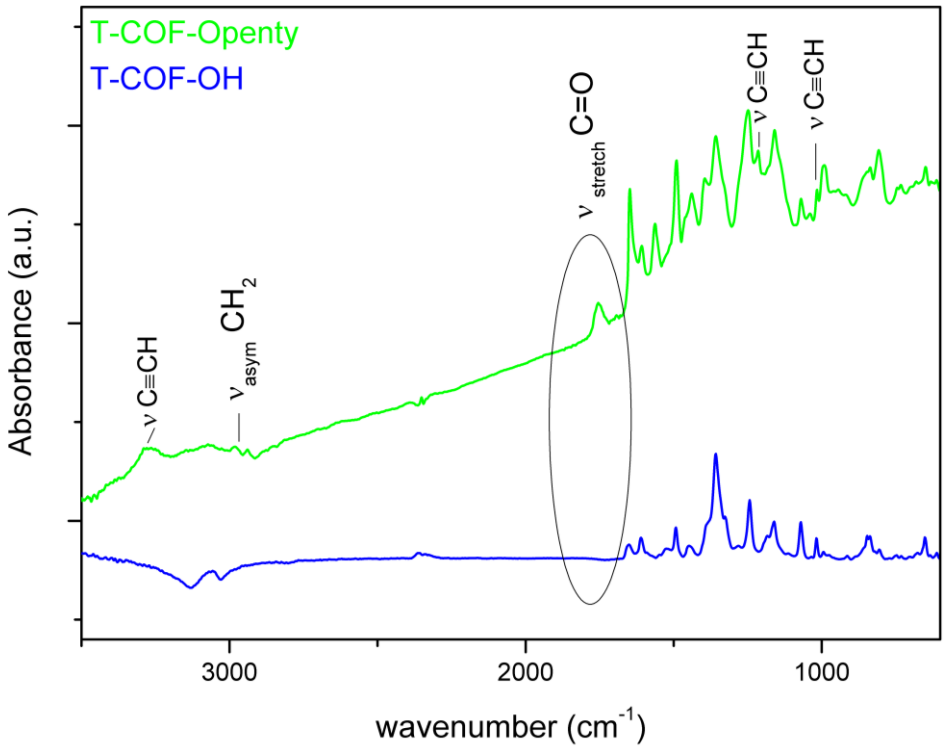

Figure 4.26: ATR-IR spectrum of T-COF-OH (red) and T-COF-Openty (green).

Further proof was given by the arising additional carbon atoms of the carboxyl and acetylene groups in the ^{13}C CP-MAS NMR spectrum. As shown in Figure 4.27 a precise assignment of the sp^2 (68 ppm) and sp carbon (82 ppm) atoms of the ester species is possible. In the spectrum of T-COF-OH these signals are absent, which leads to the conclusion that the hydroxyl groups of T-COF-OH were successfully esterified using the Steglich method.

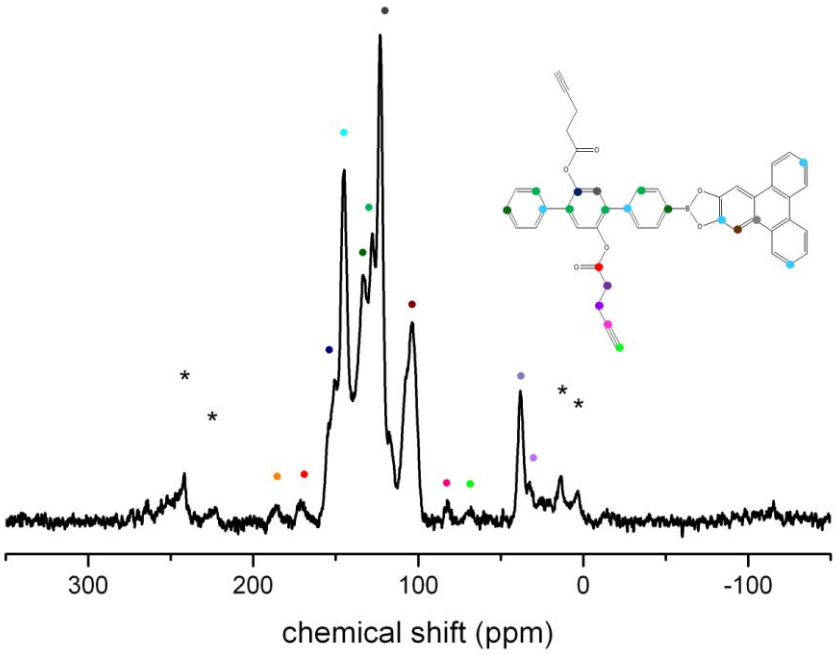

Figure 4.27: ^{13}C CP MAS NMR spectrum of T-COF-OH (left) and T-COF-Openty (right) after outgassing at 150°C for 24 h.

However, as already observed in the esterification reaction with acetyl chloride, the surface area of T-COF-OH after the Steglich esterification has significantly decreased.

4.2.4. Conclusions

The above results demonstrate that by means of reticular chemistry, the design and synthesis of an isoreticular series of Covalent Organic Frameworks is feasible. It was possible to incorporate small functional groups into the framework by using a modified linker in the condensation reactions. This prior-to-synthesis modification allows for pore tailoring on a completely new level in this research field. The chemical and physical properties can be adjusted for the later use of the porous

material. Furthermore we demonstrated that the incorporated organic groups can act as anchor points to covalently attach a desired molecule. The bromination of the methyl groups of the anthracene linker of AT-COF-Me was carried out successfully. Thus an "unreactive" methyl group can be transformed into reactive benzylic bromide, which is considered to be a very good leaving group in nucleophilic substitution reactions. The great advantage of this post-synthetic modification of the methyl groups of AT-COF-Me is the unhindered synthesis of the framework. Substituents on the aromatic core of the organic linkers can not be chosen freely. The size and the electronic surrounding of the organic moiety plays a great role in framework formation, since the functionalities should neither be too big to hinder the π-stacking nor should they decrease the reactivity of the alcohol groups or the boronic acid moiety. Therefore the possibility to transform "innocent" groups into synthetically valuable groups is anticipated to offer access to a large variety of new functional materials. In order to expand this post-synthetic modification approach to other systems, the hydroxyl containing COF, T-COF-OH, was studied in two different esterification reactions: (1) with acetyl chloride and (2) in a Steglich type reaction with carboxylic acid. Although the framework was compatible with the reaction conditions of the esterification and the formation of the ester was spectroscopically detected, the porosity of the esterified COFs decreased significantly. Therefore distinct conclusions about modifications at the framework walls are not feasible.

The results described in this chapter represent a "proof of concept", namely that introducing small functional groups in the framework by prior-to-synthesis modification can be successful. Furthermore the use of these functionalities for PSM was demonstrated; hence it is possible to connect any molecule to the functional

groups of the linkers by exploiting appropriate organic chemistry. However, further work is needed to localize the modified groups and to exclude side reactions as far as possible. The chemical reactions performed with COFs represent a great opportunity to link functional molecules to the internal pore surfaces, thus we anticipate that not only the pore properties, such as polarity or size of the pore, but properties such as luminescence, conductivity or catalytic centers of the material can be tailored. This will increase the use of Covalent Organic Frameworks as high performance tailor-made crystalline materials.

4.3. References

23. Wang, Z.; Cohen, S. M., *J. Am. Chem. Soc.* **2007,** *129* (41), 12368-12369.

30. Cote, A. P.; Benin, A. I.; Ockwig, N. W.; O'Keeffe, M.; Matzger, A. J.; Yaghi, O. M., *Science* **2005,** *310* (5751), 1166-1170.

31. El-Kaderi, H. M.; Hunt, J. R.; Mendoza-Cortes, J. L.; Cote, A. P.; Taylor, R. E.; O'Keeffe, M.; Yaghi, O. M., *Science* **2007,** *316* (5822), 268-272.

36. Tilford, R. W.; Gemmill, W. R.; zur Loye, H.-C.; Lavigne, J. J., *Chem. Mater.* **2006,** *18* (22), 5296-5301.

37. Cote, A. P.; El-Kaderi, H. M.; Furukawa, H.; Hunt, J. R.; Yaghi, O. M., *J. Am. Chem. Soc.* **2007,** *129* (43), 12914-12915.

38. Tilford, R. W.; Mugavero, S. J.; Pellechia, P. J.; Lavigne, J. J., *Adv. Mater.* **2008,** *20* (14), 2741-2746.

56. Furukawa, H.; Yaghi, O. M., *J. Am. Chem. Soc.* **2009,** *131* (25), 8875-8883.

60. Wan, S.; Guo, J.; Kim, J.; Ihee, H.; Jiang, D., *Angew. Chem.* **2009,** *121* (18), 3253.

63. Wan, S.; Guo, J.; Kim, J.; Ihee, H.; Jiang, D., *Angew. Chem., Int. Ed.* **2009,** *48* (30), 5439-5442.

106. Sing, K. S. W.; Everett, D. H.; Haul, R. A. W.; Moscou, L.; Pierotti, R. A.; Rouquerol, J.; Siemieniewska, T., *Pure Appl. Chem.* **1985,** *57* (4), 603-19.

108. Seo, J. S.; Whang, D.; Lee, H.; Jun, S. I.; Oh, J.; Jeon, Y. J.; Kim, K., *Nature* **2000,** *404* (6781), 982-986.

115. Chung, Y.; Duerr, B. F.; McKelvey, T. A.; Nanjappan, P.; Czarnik, A. W., *The J. Org. Chem.* **1989,** *54* (5), 1018-1032.

119. *Accelrys MS Modeling 4.4*, **2008**.

121. Leach, A. R., *Molecular Modelling: Principles and Applications*. 2nd ed.; Prentice Hall: Harlow, England, **2001**.

122. Connolly, M., *J. Appl. Crystallogr.* **1983,** *16* (5), 548-558.

123. Duren, T.; Millange, F.; Ferey, G.; Walton, K. S.; Snurr, R. Q., *J. Phys. Chem. C* **2007,** *111* (42), 15350-15356.

125. E. F. Vansant, P. V. d. V., K.C. Vrancken, *Characterization and Chemical Modification of the Silica Surface*. Elsevier Science B. V.: Amsterdam, **1995**.

126. Yan, Y.; Bein, T., *J. Am. Chem. Soc.* **1995,** *117* (40), 9990-9994.

127. Wada, Y.; Otsuka, K.; Morikawa, A., *J. Catal.* **1980,** *64* (2), 417-425.

128. Thijs, A.; Peeters, S.; Vansant, E. F.; Peeters, G.; Verhaert, I., *Journal of the Chemical Society, Faraday Transactions 1: Physical Chemistry in Condensed Phases* **1986,** *82* (3), 963-975.

129. Kitaura, R.; Onoyama, G.; Sakamoto, H.; Matsuda, R.; Noro, S.-i.; Kitagawa, S., *Angew. Chem., Int. Ed.* **2004,** *43* (20), 2684-2687.

130. Kiang, Y. H.; Gardner, G. B.; Lee, S.; Xu, Z.; Lobkovsky, E. B., *J. Am. Chem. Soc.* **1999,** *121* (36), 8204-8215.

131. Ma, L.; Falkowski, J. M.; Abney, C.; Lin, W., *Nat Chem* **2010,** *2* (10), 838-846.

132. Wang, Z.; Cohen, Seth M., *Angew. Chem., Int. Ed.* **2008,** *47* (25), 4699-4702.

133. Yamakawa, T.; Kagechika, H.; Kawachi, E.; Hashimoto, Y.; Shudo, K., *J. Med. Chem.* **1990,** *33* (5), 1430-1437.

134. Neises, B.; Steglich, W., *Angew. Chem. Int.Ed.* **1978,** *17* (7), 522-524.

5. Backbone-Modification of COFs – Electroactive Heterocyclic COFs

5.1. Benzothiadiazole Containing COF

This work results from the cooperation with Dr. Andreas Sonnauer from our group and Silvia Zimdars from the group of Prof. Knochel.

5.1.1. Introduction

Covalent Organic Frameworks (COFs) are a novel class of highly stable, purely organic crystalline frameworks. The reversible nature of the covalent bonding of boronic acids with polyols allows the formation of ordered layers that crystallize upon stacking.[30, 31, 37] In the past years COFs were mainly emphasized as gas storage materials due to their lightweight framework with high surfaces for gas uptake.[53] More recently Jiang and co-workers suggested that charge carriers could be transported along the framework; they reported pyrene-containing COFs exhibiting photoconductivity and semiconductor properties.[60, 63] Further evidence for high carrier mobilities was given with the hole conducting tetragonal metallophthalocyanine COF, NiPc –COF and porphyrin based COFs, COF-66 and COF-366.[34, 42] Using these electroactive macrocycles as backbone building blocks shows that it is possible to transfer properties of the monomers to the framework. Jiang and co-workers recently reported an n-channel COF by exchanging the benzene unit at the edges of NiPc-COF with the electron-poor benzothiadiazole (BTDA) heterocyclic group. However, the resulting 2D-NiPc-BTDA-COF exhibits rather small pores with a diameter of 2.2 nm, in comparison with the molecular size

of potential complementary functional guest materials. Large pores are beneficial for controlled host-guest interactions of donor-acceptor systems.[65]

Here we report the synthesis and characterization of a new mesoporous Covalent Organic Framework, BTD-COF (Figure 5.1), based on a benzothiadiazole-decorated linear diboronic acid. The electron deficient benzothiadiazole unit incorporated into the framework might lead to the formation of a n-type conducting framework with open pores, 3.6 nm in size.

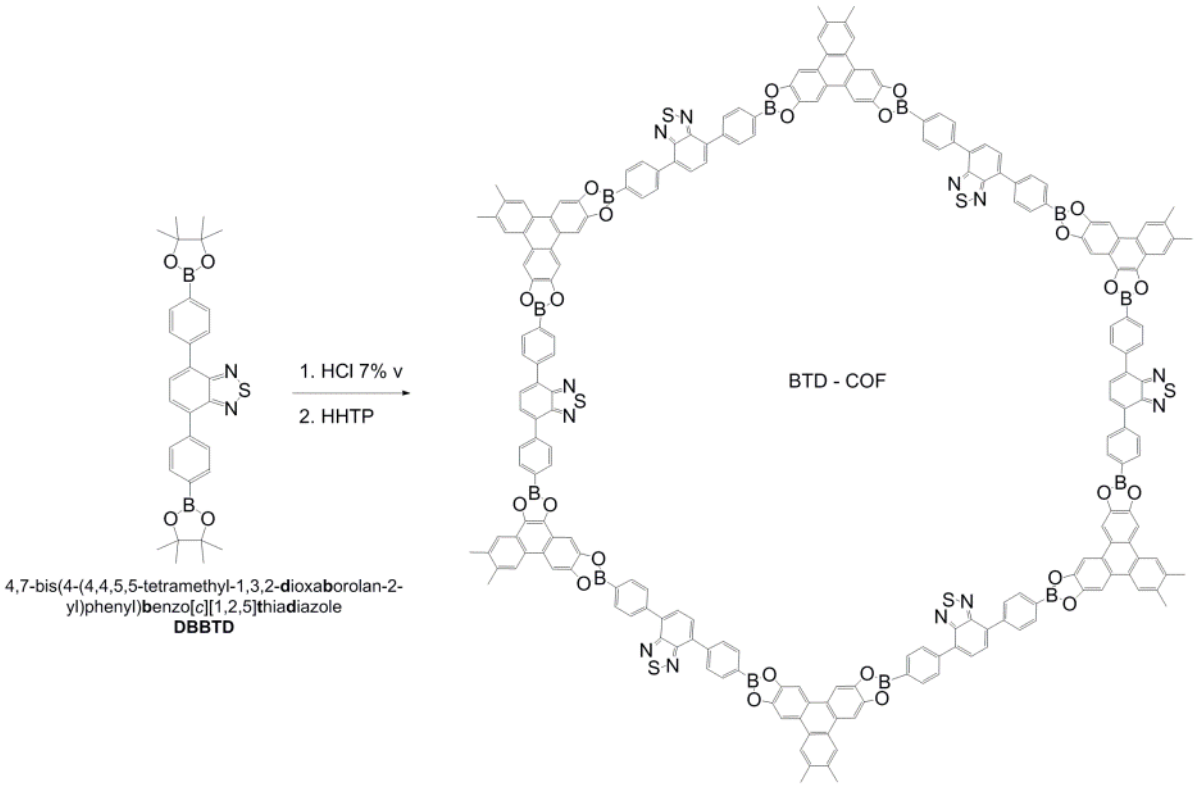

Figure 5.1: Illustration of the reaction pathway of BTD-COF.

5.1.2. Experimental

Materials and Methods

All materials (if not otherwise noted) were purchased from Aldrich or Fluka in the common purities purum and puriss. All materials were used without further purification. The building block 4,7-bis(4-(4,4,5,5-tetramethyl-1,3,2-dioxaborolan-2-yl)phenyl)benzo[*c*][1,2,5]thiadiazole (BTMDBP-BTD) was prepared by Sylvia Zimdars in the group of Prof. Knochel.

X-ray diffraction analysis was carried out in reflection mode using a Bruker D8 Discover with Ni-filtered CuKα-radiation (1.5406 Å) and a position-sensitive detector (Vantec). Fourier-transform infrared spectra of samples were measured with a Bruker Equinox 55 equipped with a PIKE MIRacle ATR-unit at room temperature. The SEM images were recorded with a Jeol 6500F field emission scanning electron microscope with an EDX/WDX detector. For this purpose the samples were put on an adhesive graphite film and sputtered with carbon with a BALTEC MED 020 Coating Sytem. ^{11}B and ^{13}C MAS NMR spectra were recorded on a Bruker DSX Avance 500 with a magnetic field of 11.2 Tesla. A 4 mm MAS triple-resonance sample head was used. The frequency of the rotors was 10 kHz. ((Give NMR details)) TG measurements were performed in a stream of synthetic air (25 ml / min) on a Netzsch STA 440 C TG/DSC. The measurements were carried out with a heating rate of 10 K / min and a temperature range from 30 °C to 900 °C. The nitrogen sorption isotherms were recorded on a Nova 4000e at 77 K. Prior to the measurement of the adsorption isotherm the sample was treated as follows. The product was soaked in dichloromethane for 12 h and heated for 12 h at 150°C under oil pump vacuum.

Molecular geometry optimization was performed with Accelrys MS Modeling 4.4 using the universal force field method. The final hexagonal unit cell was calculated with the geometrical parameters from the optimized structure. For the simulation of the PXRD pattern Reflex was used (a software package implemented in MS Modeling 4.4). For this purpose the unit cell parameters were first calculated and then refined from the experimentally observed peak positions in a hexagonal array. As a result we obtained cell parameters of a = b = 32.84 Å and c = 3.47 Å. The simulated PXRD patterns were then compared with the experimentally obtained data. We note that this structure can assemble in two different arrangements, i.e., (i) a staggered AB type with graphite-like packing, and (ii) an eclipsed AA type arrangement with the adjacent sheets lying exactly on top of each other. After optimizing the geometry of each arrangement, the powder patterns were simulated and compared to the experimental patterns. The simulated pattern of the AA arrangement shows very good agreement with our experimental PXRD pattern.

Synthesis of 4,7-Bis(4-(trimethylsilyl)phenyl)benzo[c][1,2,5]thia-diazole

The starting materials benzo[c][1,2,5]thiadiazole and dibromobenzo[c][1,2,5]thiadiazole were synthesized following published procedures.[135, 136]

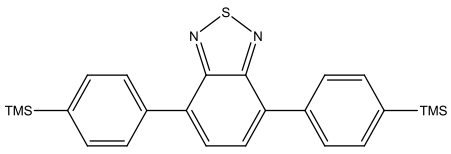

In a 250 mL Schlenk-flask equipped with a stirring bar under argon atmosphere bis(di-*tert*-butyl(4-dimethylaminophenyl)phosphine)dichloropalladium(II) (28 mg,

0.04 mmol) and 4,7-dibromobenzo[c][1,2,5]thiadiazole (1.47 g, 5 mmol) were added successively to a solution of (4-(trimethylsilyl)phenyl)zinc(II) chloride (36.4 mL of a 0.55 M solution in THF, 20 mmol) and the resulting greenish reaction mixture was stirred at 50 °C for 3 h. After addition of 100 mL saturated NH_4Cl solution the aqueous layer was extracted with CH_2Cl_2 (3 times 200 mL). The combined organic layers were dried with $MgSO_4$ and the solvents evaporated in vacuo. Purification via column separation (silicagel, pentane) yielded 4,7-bis(4-(trimethylsilyl)phenyl)benzo[*c*][1,2,5]thiadiazole (1.6 g ,75 %) as a bright yellow solid.

mp (°C): 151.1–152.8.

IR (ATR) $\tilde{\nu}$ (cm^{-1}): 3016 (w), 2952 (w), 2894 (w), 1554 (w), 1480 (w), 1400 (w), 1247 (m), 1095 (w), 837 (vs), 818 (s), 813 (s), 757 (m), 721 (m), 691 (w).

^{1}H-NMR (300 MHz, $CDCl_3$): δ = 7.96–7.92 (m, 4H), 7.79 (s, 2H), 7.73–7.70 (m, 4H), 0.34 ppm (s, 18H).

^{13}C-NMR (75 MHz, $CDCl_3$): δ = 154.2, 140.8, 137.8, 133.7, 133.5, 128.5, 128.1, −1.1 ppm.

MS (70 eV, EI): m/z (%) = 434 (10), 433 (32), 432 (79), 419 (17), 418 (40), 417 (100), 202 (14), 201 (35), 73 (18), 57 (10).

HRMS (EI): m/z calc. for [$C_{24}H_{28}N_2SSi_2$] 432.1512; found: 432.1509.

Synthesis of 4,7-Bis(4-iodophenyl)benzo[c][1,2,5]thiadiazole

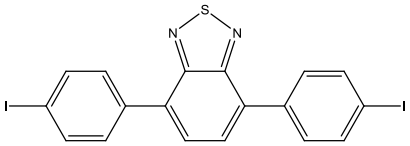

In a 500 mL round bottom flask 4,7-Bis(4-(trimethylsilyl)phenyl)benzo[*c*][1,2,5]thiadiazole (10 g, 23 mmol) was dissolved in 200 mL CH_2Cl_2 and cooled to 0 °C. ICl (2 mL, excess) was added dropwise and the reaction mixture stirred at 0 °C for 10 min, slowly warmed up to 20 °C and stirred for further 2 h. Filtration yielded 4,7-bis(4-iodophenyl)benzo[*c*][1,2,5]thiadiazole (11.6 g, 93 %) as a yellow solid.

mp (°C): 214.0–217.8.

IR (ATR) $\tilde{\nu}$ (cm^{-1}): 2920 (w), 2851 (w), 1586 (w), 1552 (w), 1472 (m), 1402 (w), 1116 (w), 1102 (w), 1060 (w), 1006 (m), 972 (w), 943 (w), 886 (w), 849 (w), 806 (vs), 710 (w).

^{1}H-NMR (300 MHz, $CDCl_3$): δ = 7.90–7.85 (m, 4H), 7.76 (s, 2H), 7.73–7.68 ppm (m, 4H).

^{13}C-NMR (75 MHz, $CDCl_3$): δ = 153.8, 137.8, 136.7, 132.6, 131.0, 127.9, 94.6 ppm.

MS (70 eV, EI): m/z (%) = 542 (6), 541 (21), 540 (100), 288 (11), 286 (9), 143 (6).

HRMS (EI): m/z calc. for [$C_{18}H_{10}I_2N_2S$] 539.8654; found: 539.8650.

Synthesis of 4,7-Bis(4-(4,4,5,5-tetramethyl-1,3,2-dioxaborolan-2-yl)phenyl)-benzo[c][1,2,5]thiadiazole

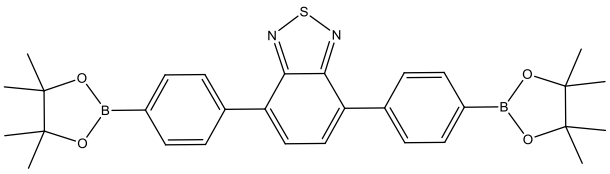

In a 250 mL Schlenk-flask equipped with a stirring bar KOAc (4.9 g, 50 mmol) was dried under 10^{-5} bar at 100 °C. After addition of 100 mL 1,4-dioxane, 4,7-bis(4-iodophenyl)benzo[*c*][1,2,5]thiadiazole (5.4 g, 10 mmol), 4,4,4',4',5,5,5',5'-octamethyl-2,2'-bi(1,3,2-dioxaborolane) (10.2 g, 40 mmol) the reaction mixture was degassed. $Pd(OAc)_2$ (90 mg, 0.4 mmol) and tricyclohexylphosphine (220 mg, 0.8 mmol) were added successively and the resulting greenish reaction mixture stirred at 80 °C for 24 h. After addition of 100 mL saturated $NaHCO_3$ solution the aqueous layer was extracted with Et_2O (4 times 200 mL). The combined organic layers were dried with $MgSO_4$ and the solvents evaporated in vacuo. Recrystallization from Et_2O yielded 4,7-Bis(4-(4,4,5,5-tetramethyl-1,3,2-dioxaborolan-2-yl)phenyl)benzo[*c*][1,2,5]thiadiazole (4.1 g ,74 %) as a bright yellow solid.

mp (°C): 184.0–186.2.

IR (ATR) $\tilde{\nu}$ (cm^{-1}): 2975 (w), 1609 (w), 1550 (w), 1519 (w), 1396 (m), 1356 (vs), 1320 (m), 1294 (m), 1214 (w), 1143 (s), 1122 (m), 1105 (m), 1084 (m), 1020 (w), 961 (w), 890 (w), 856 (m), 821 (s), 744 (w), 657 (m).

^{1}H-NMR (600 MHz, $CDCl_3$): δ = 8.00–7.95 (m, 8H), 7.80 (s, 2H), 1.37 ppm (s, 24H).

^{13}C-NMR (150 MHz, $CDCl_3$): δ = 154.0, 140.0, 135.0, 133.5, 128.5, 128.2, 83.9, 24.9 ppm.

MS (70 eV, EI): m/z (%) = 542 (10), 541 (34), 540 (100), 539 (44), 441 (14), 440 (11), 341 (24), 340 (22), 339 (9).

HRMS (EI): m/z calc. for [$C_{30}H_{34}B_2N_2O_4S$] 540.2425; found: 540.2419.

Synthesis of BTD-COF

BTD-COF was synthesized starting from 4,7-bis[4-(4,4,5,5)-tetramethyl-[1,3,2]dioxaborolan-2-yl)-phenyl]-benzo[1,2,5]thiadiazole (BTMDBP-BTD) and 2,3,6,7,10,11-hexahydroxyphenylene (HHTP) in a two step synthesis by microwave heating. The syntheses were performed in special microwave vials 0.5-2 ml from Biotage. In step 1 BTMDBP-BTD (32.4 mg, 0.06 mmol) was solved in a mixture of 1,4-dixoane/mesitylene (375 µL / 375 µL) and concentrated HCl (37 wt-%, 105 µL) was added. The mixture was heated up to 180 °C for 10 minutes under continuous stirring (600 rpm). A phase mixture of a yellow precipitate and solvents is obtained, which is necessary for reaction step 2. HHTP (13.0 mg, 0.04 mmol) and a mixture of 1,4-dixoane/mesitylene (375 µL / 375 µL) was further added. The mixture was then heated for 30 minutes und continuous stirring at 160 °C to finally obtain a green powder (BTD-COF) with yield based on BTMDBP-BTD about 75 %. Reference one-pot investigations for direct transesterification of BTMDBP-BTD with HHTP were performed with microwave and conventional heating, but led not to the requested BTD-COF. The yellow precipitate after step 1 was also characterized by X-ray powder diffraction and revealed a crystalline phase, which could not be clearly identified, presumably a precondensated oligomer. Without this crystalline precursor no BTD-COF is formed during the reaction step 2.

The optimum reaction time and temperature for each of the two-steps were optimized by systematic parameter screening (Figure 5.2). The evaluation based on crystallinity and yield of obtained BTD-COF.

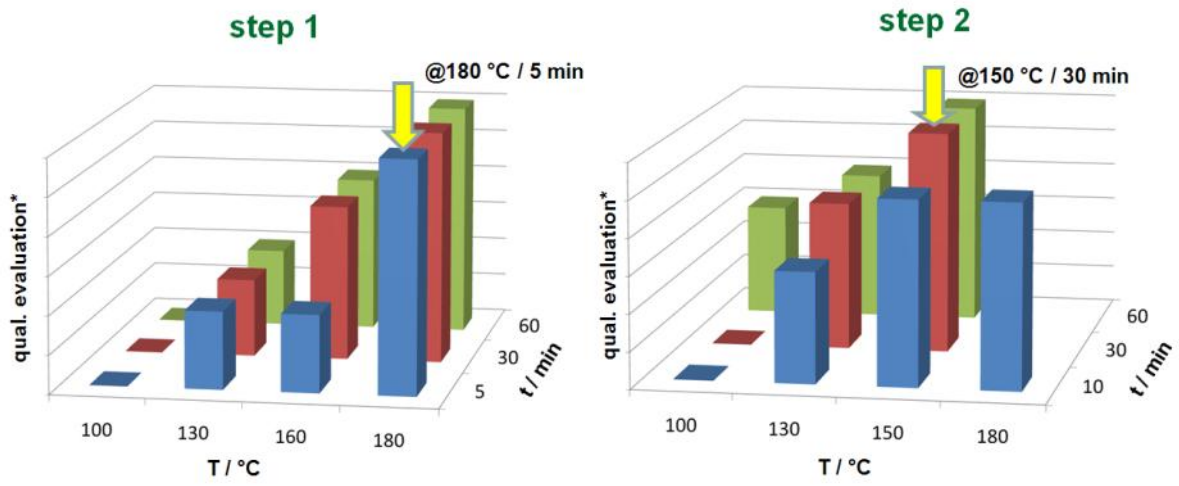

Figure 5.2: Optimization of step 1 (left) and step 2 (right). *Evaluation based on comparable crystallinity and yield of the products.

5.1.3. Results and Discussion

Based on the functional groups and geometry of the used precursor molecules the final structure can be predicted and then compared to the experimental powder X-ray diffraction pattern (PXRD). As expected from the geometry and connectivity of the precursor molecules, a two-dimensional layered structure with hexagonal symmetry should be obtained. In principle a staggered and an elliptical arrangement of the hexagonal sheets is possible. Calculations and geometry optimizations of both crystal structures based on Universal Force Field methods are

shown in Figure 5.3.

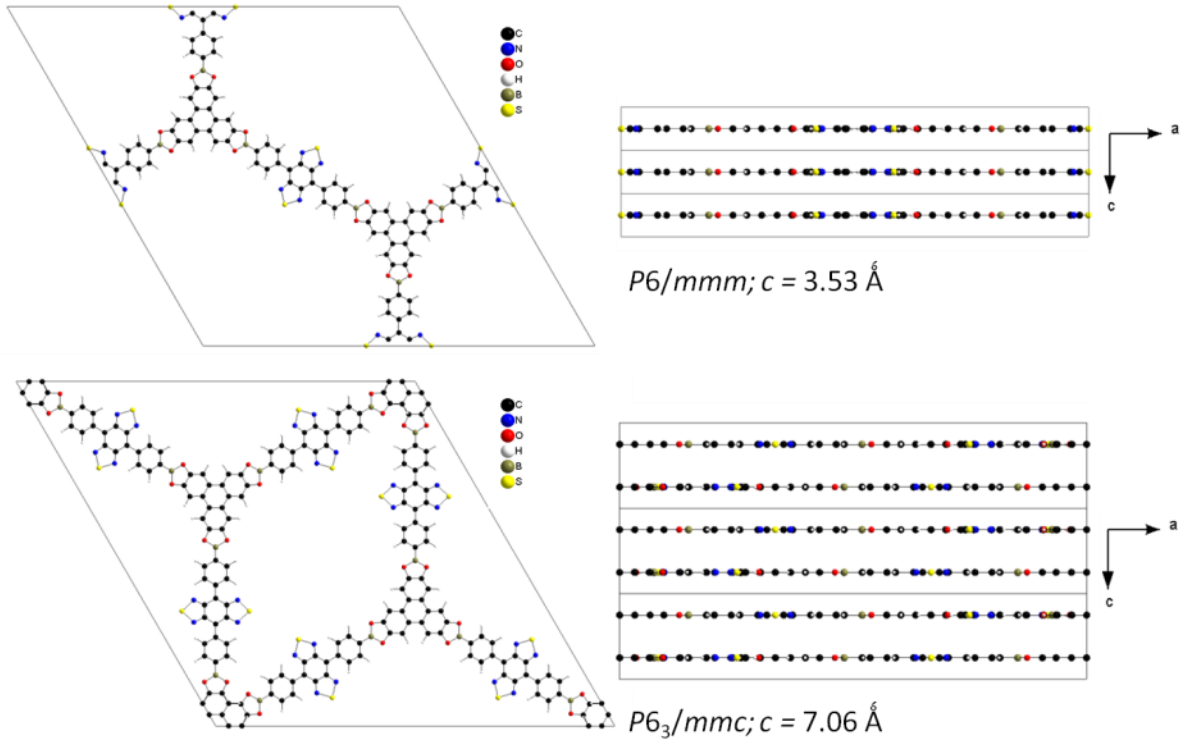

.

Figure 5.3: Eclipsed (upper) and staggered (lower) lattice packing of BTD-COF, with the benzothiadiazole group placed on both sides of the corresponding aromatic ring with 50 % occupancy for a statistical arrangement.

Based on the crystal structure the diffraction patterns for both arrangements are simulated. In Figure 5.4 the simulated PXRD-patterns are compared to the experimentally obtained data, indicating an eclipsed arrangement, due to the disagreement with the staggered conformation and a good agreement with the eclipsed lattice packing.

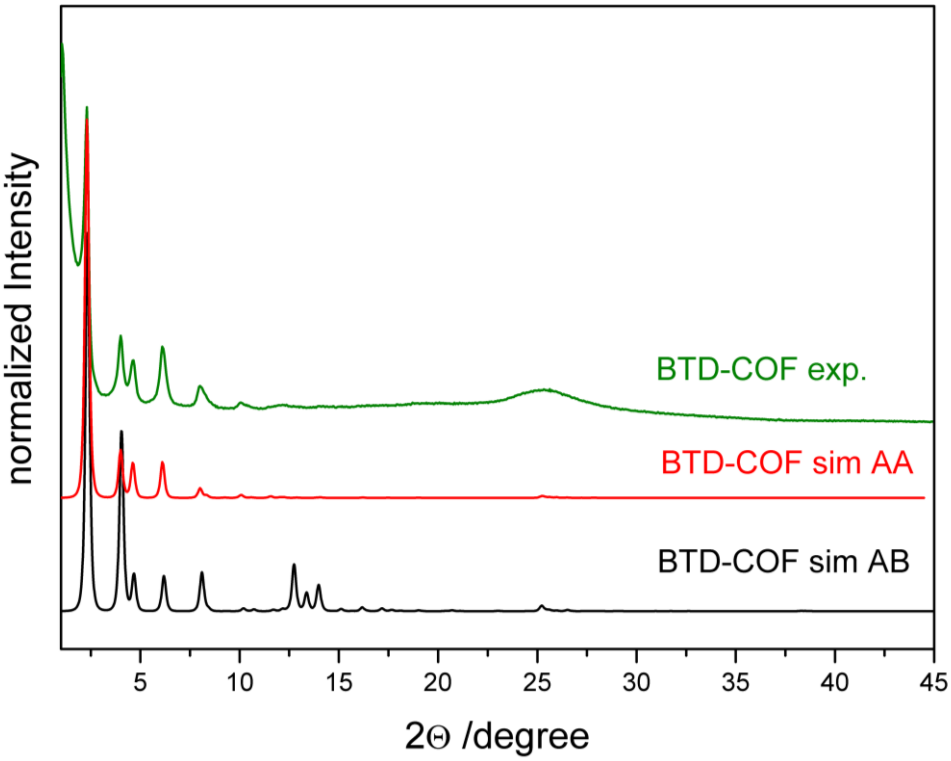

Figure 5.4: PXRD pattern of as synthesized BTD-COF (green), compared to the simulated PXRD pattern in AA arrangement (red) and AB arrangement (black).

Transmission electron microscopy shows a crystalline material with domains of about 100 nm in size. In Figure 5.5 A, the TEM image shows the periodic hexagonal structure with unit cell parameters of 3.6 nm; the crystal structure parameters obtained from PXRD and calculations (3.5 nm) agree very well with the data obtained by TEM. In Figure 5.5 B a view along the pores is given, indicating long and free channels in the structure.

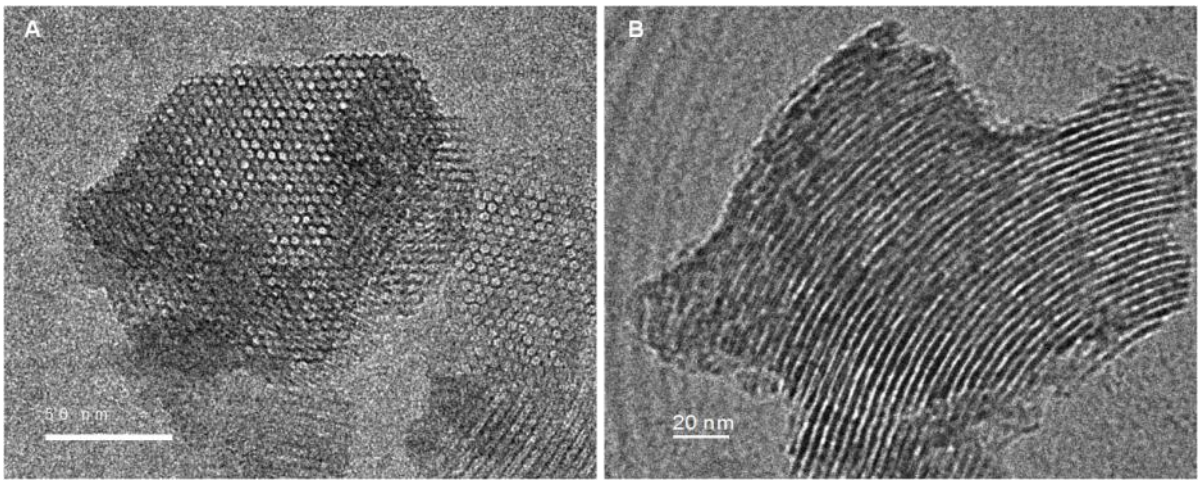

Figure 5.5: Transmission electron micrograph of BTD-COF A) top view showing hexagonal structure with 3.6 nm open pores and B) image of a tilted crystal with side view along the pores.

FT-IR spectroscopy confirmed the presence of the boronate ester functionality of BTD-COF (Figure 5.6).

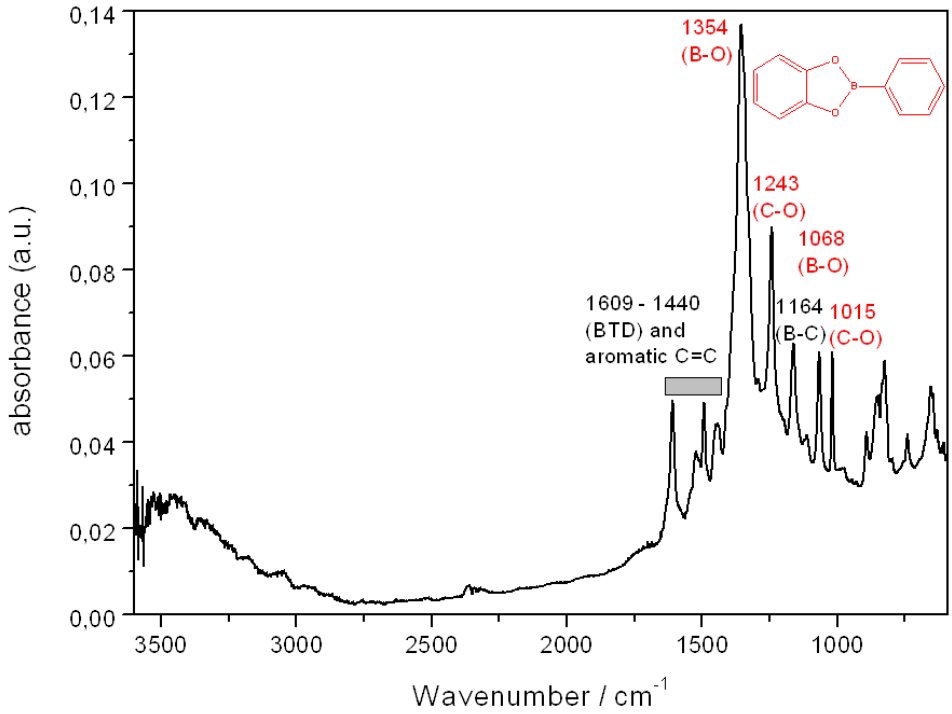

Figure 5.6: IR spectrum of BTD-COF with indication of the most important signals.

Comparison of the ^{11}B MAS NMR spectra (Figure 5.7) of the starting material BTDA with BTD-COF shows almost identical chemical shifts. BTDA is an aliphatic boronate ester with a chemical shift of 23.7 ppm, and the aromatic boronate ester BTD-COF occurs at 22.2 ppm.

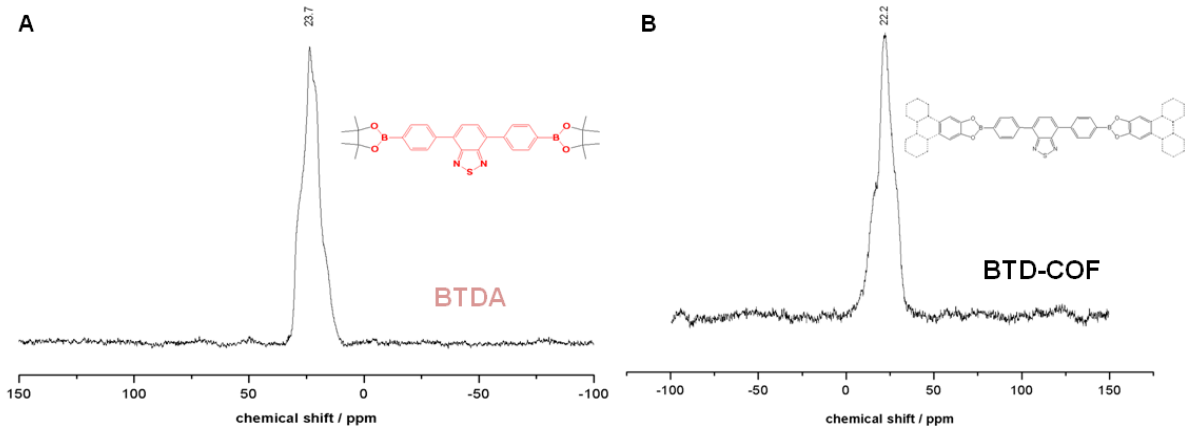

Figure 5.7: ^{11}B MAS-NMR spectrum of A) the starting material BTDA compared to B) BTD-COF.

^{13}C CP-MAS-NMR confirmed the transesterification reaction during the framework synthesis, due to the absence of the signals of the methyl groups of the starting pinacolester. Furthermore signals from both building blocks are present and can be assigned to the carbon atoms (Figure 5.8).

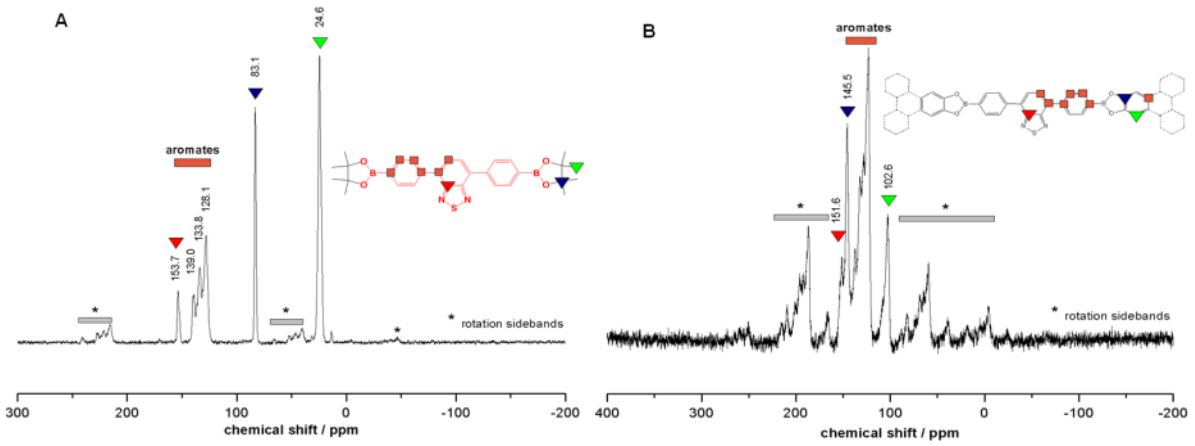

Figure 5.8: ^{13}C MAS-NMR of A) starting compound 4,7-bis[4-(4,4,5,5)-tetramethyl-[1,3,2]dioxaborolan-2-yl)-phenyl]-benzo[1,2,5]thiadiazole (BTMDBP-BTD) compared to B) BTD-COF.

Nitrogen sorption measurements revealed the porosity of the BTD framework after degassing the sample at 200 °C for 12 h. The adsorption isotherm was recorded at 77 K. BTD-COF exhibits a type IV isotherm (Figure 5.9 A) typical for mesoporous materials,[18] and a Brunauer Emmett Teller (BET) surface area of almost 1000 m^2/g. The pore size distribution of BTD-COF shows a pore size of around 3.2 nm (Figure 5.9 B).

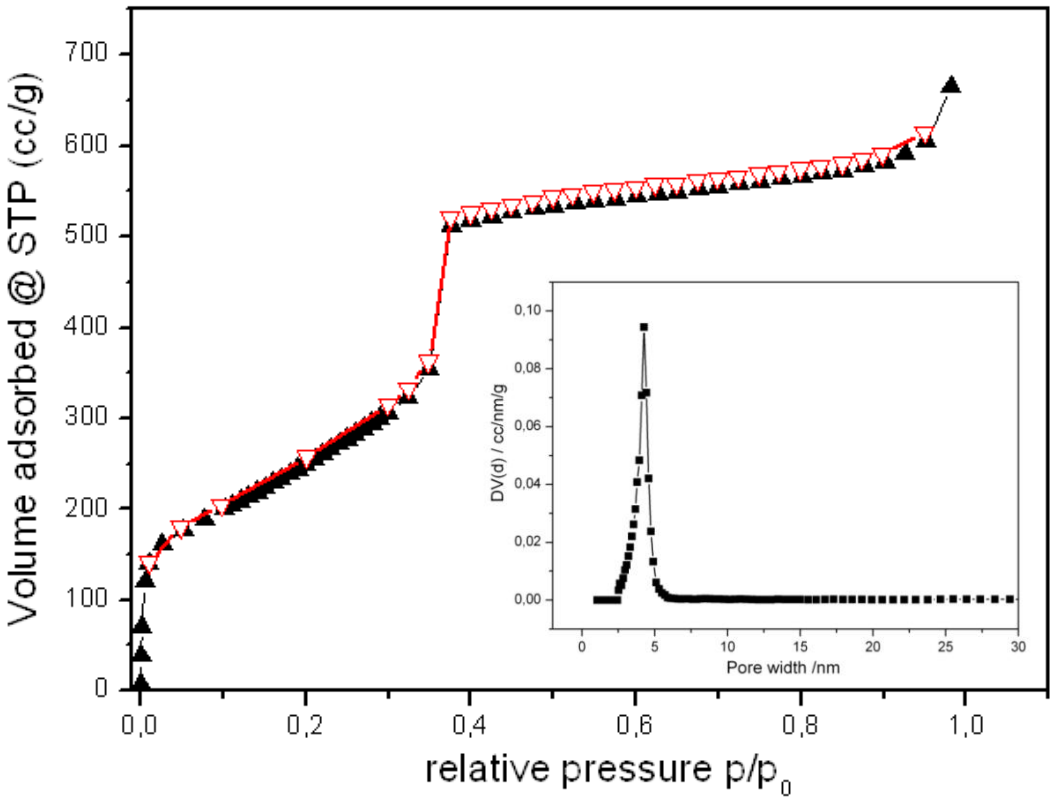

Figure 5.9: (A) Nitrogen sorption isotherm of degassed BTD-COF measured at 77 K and (B) pore size distribution with a mean pore size of about 31.7 Å.

The experimental data from the sorption experiment are not in good agreement with the theoretical calculated surface area and volume (Table 5.1.), moreover, the experimental pore size of 3.6 nm is slightly smaller than theoretically predicted one of 3.8 nm. We conclude that there is still some unreacted material or oligomers formed from the starting materials present in the pores.

Table 5.1: Theoretical and experimental values for surface area and pore volume of BTD-COF.

	Surface area m^2/g	Volume cm^3/g
Connolly surface	2114	1.83
Access. surface	1891	1.46
Sorption data	1000	0.92

Thermogravimetric analysis (Figure 5.10) indicates that BTD-COF is stable up to 450 °C. Heating to 200 °C is accompanied by a mass loss of 10%, which can be attributed to volatile guest molecules in the mesopores. At 700 °C a total weight loss of 78% is reached. The remaining 12% correspond to the stoichiometrically expected amount of B_2O_3.

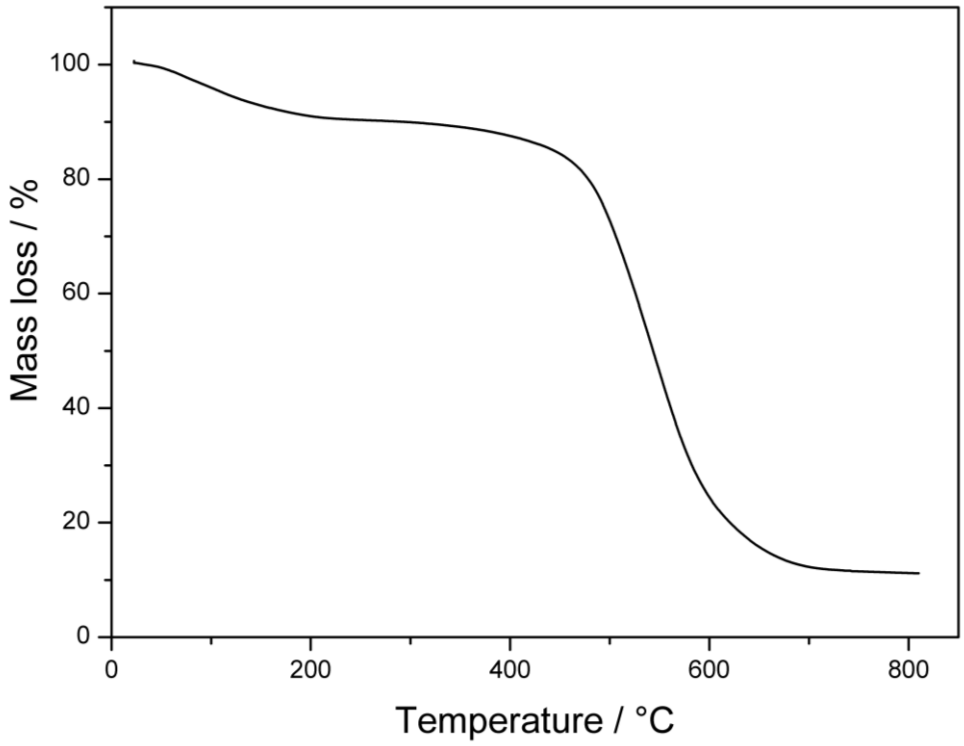

Figure 5.10: TG data for BTD-COF.

The absorbance spectrum (Figure 5.11) of the BTD-COF shows a broad absorbance between 250 nm and 500 nm, with two maxima at 300 nm and 400 nm.

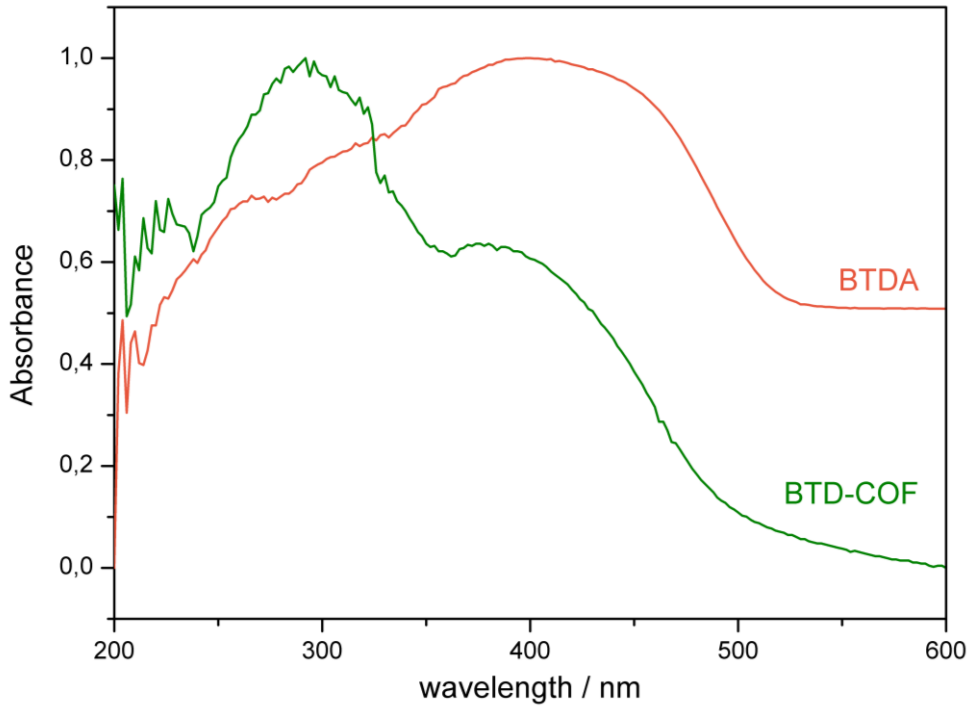

Figure 5.11: UV VIS absorbance spectrum of BTD-COF (green) and the starting pinacol ester (orange).

Upon excitation at 330 nm, the BTD-COF showed fluorescence emission at 484 nm (Figure 5.12). Compared to the starting material, however, the fluorescence intensity was significantly lower.

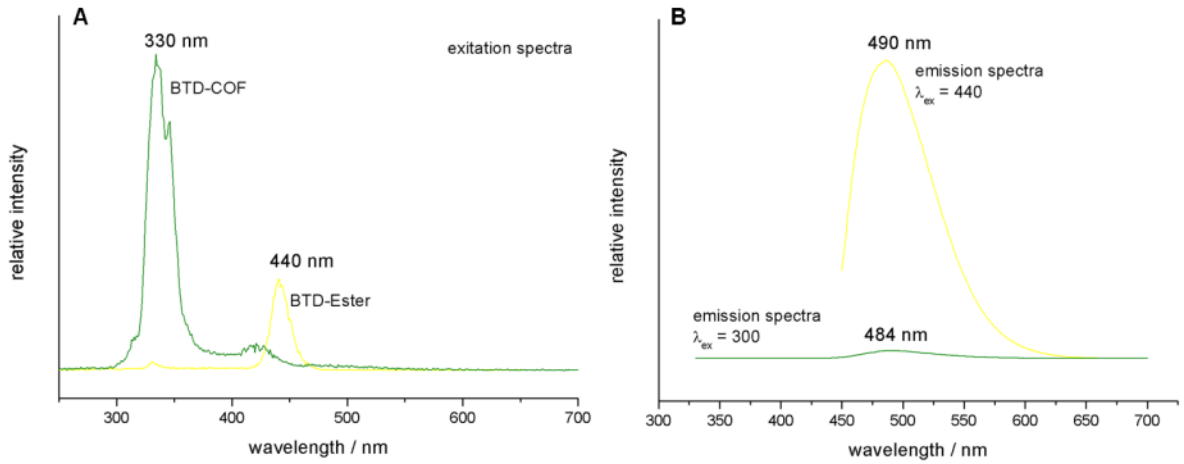

Figure 5.12: Fluorescence excitation (A) and emission (B) profiles of the starting pinacolboronate (yellow) and the BT-COF (green).

5.1.4. Conclusion

Condensation of a benzothiadiazole-decorated terphenyl diboronic acid with HHTP gives a crystalline framework with large accessible pores. Structural investigation with TEM confirms the lattice characteristics obtained with theoretical simulations and X-ray diffraction. BTD-COF is a highly thermally and chemically stable material, which can be handled under ambient conditions and is resistant against most common organic solvents.

5.2. A Photoconductive Thienothiophene-Based COF Showing Charge Transfer Towards PCBM

This work results from the cooperation with Dr. Thomas Kunz and Prof. Paul Knochel and Matthias Handloser and Prof. Achim Hartschuh from the Department of Chemistry, University of Munich.

5.2.1. Introduction

Covalent Organic Frameworks (COFs) are a novel class of highly stable, purely organic crystalline frameworks. The condensation of boronic acids with appropriate polyols allows the design of precisely controllable structures since their chemical and physical properties can be easily tuned through rational selection of the building blocks.[30-34] The stacked layers of 2D-COFs are of great interest for charge migration along the framework.[60] Several structures exhibiting semiconducting properties[60,63] and high carrier mobilities[65] have already been reported. Recently Spitler *et al.* showed lattice expansions of phthalocyanine COFs to the mesoporous regime, pointing out the need to have electroactive structures large enough for fullerene acceptors.[138] Here we report for the first time a thieno[2,3-b]thiophene-based Covalent Organic Framework, TT-COF, with high surface area and a 3 nm open pore system. This open framework can take up the electron-accepting fullerene derivative PCBM, thus forming a novel structurally odered donor-acceptor network. Spectroscopic and photoconductivity results demonstrate light-induced charge-transfer from the TT-COF donor network to the encapsulated PCBM phase in the pore system. The organization of the molecular building blocks into a crystalline

framework with defined conduction paths can be used as a model system to study ordered/interpenetrated networks of donor-acceptor systems at the nanoscale.

The most prominent hole-conducting material used in organic solar cells is P3HT, a thiophene-containing polymer with high charge carrier mobilities. The soluble fullerene derivative PCBM is often used as electron acceptor in organic photovoltaics.[139] However, due to the lack of structural order in the respective bulk-heterojunctions it is very difficult to assess the impact of molecular building blocks, bonding motifs and energy levels on the microscopic processes involving light-induced exciton formation, charge separation and transport in such systems. The creation of nanostructured or ordered nanophases with long range order of the D-A complex seems to be ideal to enhance efficiency of photovoltaic devices.[141] Hence crystalline charge-transporting frameworks with large open pores and high surface areas are of great interest to understand the mechanistic details of the light-induced processes and ultimately to obtain design rules for the creation of efficient and stable organic photovoltaic devices.

The new TT-COF was synthesized under solvothermal conditions by co-condensation of thieno[3,2-b]thiophene-2,5-diyldiboronic acid (TTBA) and the polyol 2,3,6,7,10,11-hexahydroxytriphenylene (HHTP) (Figure 5.13). Reaction parameters are described in the Supporting Information. As described in the following, the thienothiophene-based COF forms stacks in an AA arrangement, as confirmed by N_2 sorption and powder X-ray diffraction. Upon mixing TT-COF with $PCBM_{60}$, the photoconductive behavior as well as the luminescence of TT-COF demonstrates electronic interaction of the COF with the electron acceptor $PCBM_{60}$.

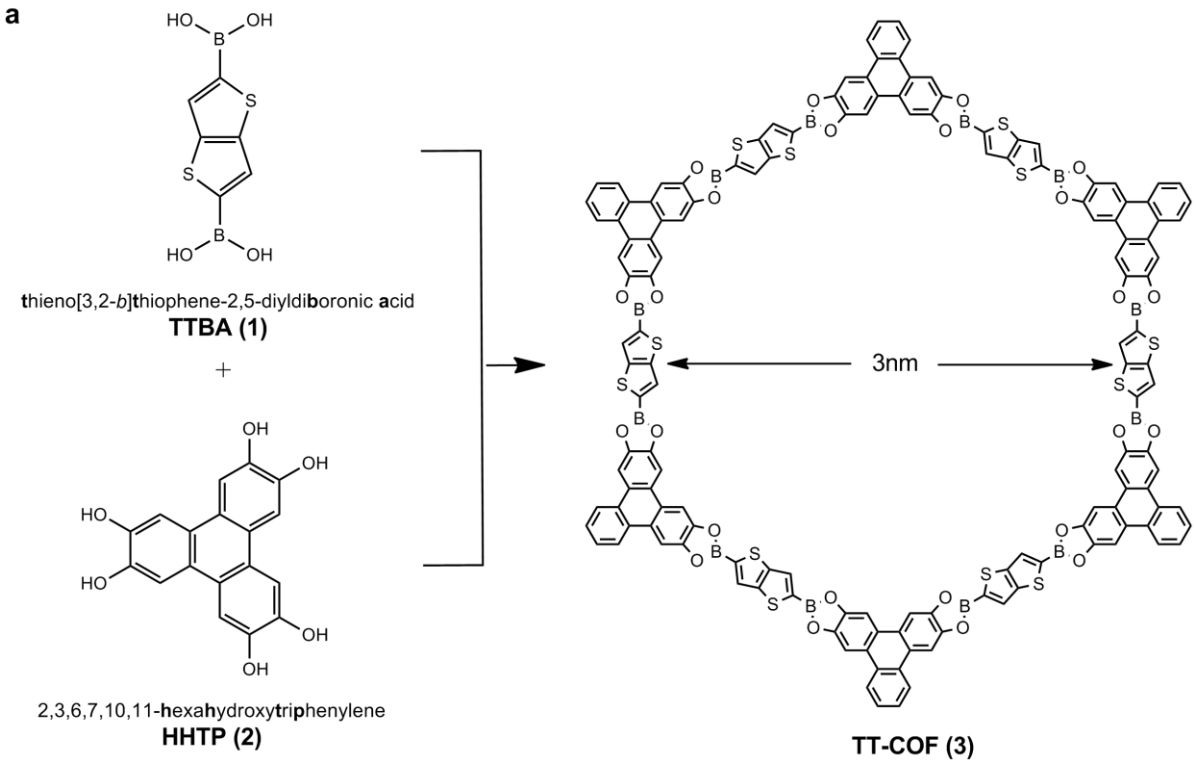

Figure 5.13: Reaction scheme for the co-condensation of TT-COF.

5.2.2. Experimental

Materials and Methods

All materials (if not otherwise noted) were purchased from Aldrich or Fluka in the common purities purum and puriss. 2,3,6,7,10,11-hexahydroxytriphenylene (HHTP) was purchased from TCI Europe. All materials were used without further purification. The building block 2,5-bis(4,4,5,5-tetramethyl-1,3,2-dioxaborolan-2-yl)thieno[3,2-b]thiophene was prepared in the group of Prof. Knochel by Thomas Kunze. Thieno[3,2-*b*]thiophene and 3-bromothieno[3,2-*b*]thiophene were prepared according to a method described by Matzger *et al*. Analytical data were found to match literature data. The COF materials were manipulated in air.

For the synthesis of 2,5-bis(4,4,5,5-tetramethyl-1,3,2-dioxaborolan-2-yl)thieno[3,2-b]thiophene all reactions were carried out under an argon atmosphere in flame-dried glassware. Syringes used to transfer anhydrous solvents or reagents were purged with argon prior to use. THF was continuously refluxed and freshly distilled from sodium benzophenone ketyl under nitrogen. Yields refer to isolated yields of compounds estimated to be >95% pure as determined by ^{1}H-NMR (25 °C) and capillary GC. NMR spectra were recorded in solutions in $CDCl_3$ or C_6D_6 with residual solvent reference ($CDCl_3$: δ = 7.26 ppm for ^{1}H-NMR and δ = 77.1 ppm for ^{13}C-NMR, D_2O: δ = 4.79 ppm for ^{1}H-NMR). Abbreviations for signal couplings are as follows: s, singlet; d, doublet; t, triplet; q, quartet; m, multiplet; br, broad. Column chromatography was performed using SiO_2 (0.040 – 0.063 mm, 230 – 400 mesh ASTM) from Merck. All reagents were obtained from commercial sources. TMPH, liquid aldehydes and acid chlorides were distilled prior to use. Magnesium turnings (> 99.5%) were obtained from Riedel-de Haën. CuCN, $ZnCl_2$ and LiCl were obtained from Merck. The given Watt-values refer to the maximum magnetron power output of the microwave oven.

X-ray diffraction analysis was carried out in reflection mode using a Bruker D8 Discover with Ni-filtered CuKα-radiation (1.5406 Å) and a position-sensitive detector (Vantec). Fourier-transform infrared spectra of samples were measured with a Bruker Equinox 55 equipped with a PIKE MIRacle ATR-unit at room temperature. The SEM images were recorded with a Jeol 6500F field emission scanning electron microscope with an EDX/WDX detector. For this purpose the samples were put on an adhesive graphite pad. Transmissoon electron microscopy data were obtained with a FEI TITAN 80-300 microscope at an acceleration voltage of 80 kV. ^{11}B and ^{13}C MAS NMR spectra were recorded on a Bruker DSX Avance 500 with a magnetic

field of 11.2 Tesla. A 4 mm MAS triple-resonance sample head was used. The frequency of the rotors was 10 kHz. 11B-NMr spectra were recorded with single puls program with 90 scans and a delay time of 1 sec. For the 13 cross polarization NMR 1808 scans were performed and a delay time of 2 sec. TG measurements were performed in a stream of synthetic air (25 ml / min) on a Netzsch STA 440 C TG/DSC. The measurements were carried out with a heating rate of 10 K / min and a temperature range from 30 °C to 900 °C. The nitrogen sorption isotherms were recorded on a Quantachrome Autosorb-1. Prior to the measurement of the adsorption isotherm the sample was treated as follows. The product was soaked in dichloromethane for 12 h, separated by filtration and heated for 12 h at 150 °C under oil pump vacuum. The calculation of the pore size distribution was done using the NLDFT model with a carbon kernel for cylindrical pores of the desorption branch. Molecular geometry optimization was performed with Accelrys MS Modeling 4.4 using the universal force field method. The final hexagonal unit cell was calculated with the geometric parameters from the optimized structure. For the simulation of the PXRD patterns the Reflex module was used (a software package implemented in MS Modeling 4.4). For this purpose the unit cell parameters were first calculated and then refined from the experimentally observed peak positions in a hexagonal array. As a result we obtained cell parameters of a = b = 32.84 Å and c = 3.47 Å. The simulated PXRD patterns were then compared with the experimentally obtained data. We note that this structure can assemble in two different arrangements, i.e., (i) a staggered AB type with graphite-like packing, and (ii) an eclipsed AA type arrangement with the adjacent sheets lying exactly on top of each other. After optimizing the geometry of each arrangement, the powder patterns were simulated and compared to the experimental patterns. The simulated

pattern of the AA arrangement shows very good agreement with our experimental PXRD pattern.

Current- voltage curves were performed of drop-cast films of TT-COF (10 mg/mL in DCM), TT-COF / $PCBM_{60}$ (1 : 1 weight ratio) and $PCBM_{60}$ (3 mg/mL in dichlorobenzene) between parallel Au electrodes separated by a 10 μm gap by a two probe method using a Keitheley 2010.

Time-correlated single photon counting (TCSPC) was used in combination with confocal microscopy for time-resolved PL measurements. In the studied materials PL results from radiative exciton recombination and its intensity is proportional to the product of absorbed fluence and PL quantum yield. Laser excitation was provided by a Ti:sapphire oscillator operating at a photon energy of 1.55 eV (800 nm), a repetition rate of 76 MHz and a pulse duration of 150 fs. The sample signal was detected at higher photon energies corresponding to two-photon excitation. The inverted confocal microscope used in epi detection combined with a high numerical aperture objective (NA = 1.3) provided a diffraction limited excitation spot of about 400 nm. A fast avalanche photo diode (APD) was used to acquire PL transients and intensities. The instrument response function (IRF) of the system was independently measured by detecting the scattered pump laser light from the sample and had a full width at half maximum (FWHM) of 27 ps. Due to the high signal-to-noise ratio achieved in our experiments and the reproducibility of the IRF the time resolution of the setup is about 3 ps, close to 10 % of the FWHM of the IRF.

*Synthesis of 2,5-dibromothieno[3,2-b]thiophene (**4**):*

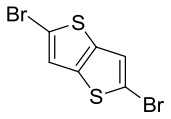

Thieno[3,2-*b*]thiophene[i] (1.4 g, 10 mmol) was dissolved in DMF (20 mL) at 0 °C. N-Bromosuccinimide (3.56 g, 20 mmol) was added and the reaction mixture stirred for 3 h. Water (500 mL) was added and the mixture extracted three times with ether. The organic phase was washed 4 times with water, dried ($MgSO_4$) and concentrated *in vacuo*. Flash column chromatographic purification on silica gel (pentane) afforded **4** (5.84 g, 98%) as a white solid.

mp. : 116.8-118.5 °C.

^{1}H-NMR (300 MHz, $CDCl_3$) : δ 6.31 (s, 2H).

^{13}C-NMR (75 MHz, $CDCl_3$) : δ 138.5, 122.1, 113.7.

IR (Diamond ATR, neat) : $\tilde{\nu}$ = 3088 (w), 1618 (w), 1445 (vs), 1325 (m), 1156 (s), 1001 (s), 840 (s), 803 (vs).

MS (EI, 70 eV) : *m/z* = 298 (100) [M^+], 217 (20), 138 (31), 93 (13), 69 (28), 60 (12).

HR-MS : ($C_6H_2{}^{79}Br_2{}^{32}S_2$) calculated: 295.7965 found: 295.7955.

*Synthesis of thieno[3,2-b]thiophene-2,5-diyldiboronic acid (**5**):*

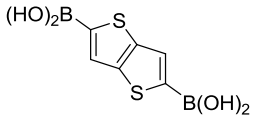

2,5-dibromothienothiophene **4** (1.49 g, 5.0 mmol) was dissolved in THF (40 mL) and cooled to -30 °C. Then *n*-BuLi (4.90 mL, 2.55 m in hexane, 12.5 mmol) was added and the reaction mixture stirred for 45 min at that temperature. triisopropyl borate (2.82 g, 15.0 mmol) was added dropwise at -80 C and the mixture was allowed to warm to room temperature over 4 h. The reaction was quenched with half concentrated aqueous NH_4Cl solution and the phases were separated. The aqueous phase was adjusted to pH 7 with 2 M HCl and extracted with ethyl acetate (3x 25 mL). The combined organic phases were washed with brine, dried (MgSO4) and concentrated *in vacuo*. The resulting solid was washed with pentane and dried to afford a green-gray powder (638 mg, 56%) sufficiently pure for further manipulation.

mp. : > 400 °C.

^{1}H-NMR (300 MHz, D_2O/NaOD) : δ 6.99 (s, 2H)

^{13}C-NMR (75 MHz, D_2O/NaOD) : δ 141.9, 118.9.

IR (Diamond ATR, neat) : $\tilde{\nu}$ = 3194 (s), 3185 (s), 1466 (s), 1461 (s), 1438 (s), 1359 (vs), 1247 (s), 1192 (s), 1170 (s), 698 (s),

HR-MS (ESI): calculated for ($C_6H_6O_4S_2B_2 + HCO_2^-$): 272.9876 found: 272.9886

*Synthesis of TT-COF (**3**)*

A conventional stainless steel autoclave equipped with a 3 ml teflon inlay was charged with **(1)** (11.6 mg, 0.051 mmol) and **(2)** (11.0 mg, 0.034 mmol). The reaction mixture was suspended in 1 ml of a 1 : 1 v : v solution of mesitylene :

dioxane and heated for 72 h at 150 °C. The dark grey precipitate was isolated by filtration and washed with dry acetone (30 ml).

For gas adsorption measurements the product was soaked in dichloromethane for 12 d and heated at 150 °C under dynamic vacuum for 12 h.

FT-ATR-IR: ν (cm-1) = 3493 (m), 2977 (w), 1561 (m), 1487 (s), 1437 (m), 1395 (m), 1353 (s), 1299 (m), 1279 (s), 1235 (m), 1212 (m), 1195 (m), 1162 (m), 1020 (m), 852 (m), 831 (m), 801 (m), 777 (w), 754 (w), 724 (w), 650 (w)

TT-COF/PCBM preparation

TT-COF (**3**) (20 mg, 0.01 mmol, 1 eq.) was added to a solution of PCBM (10 mg, 0.01 mmol, 1 eq.) in 5 ml dichlorobenzene and stirred for 24 h. The mixture was centrifuged and the underlying solid was collected.

5.2.3. Results and Discussion

Powder X-ray diffraction (PXRD) confirms the formation of a highly crystalline Covalent Organic Framework. Identification of the new structure was conducted by comparison of structures modeled with MS Studio.[119] Corresponding powder patterns were simulated and compared to the experimentally obtained data. For previous COF structures different stacking types of the hexagonal planar sheets were reported.[30] Hence calculations were carried out simulating an eclipsed AA arrangement and a staggered AB arrangement. The experimental PXRD pattern for TT-COF agrees very well with the simulated pattern for an eclipsed AA arrangement (Figure 5.14 and Figure 5.15) with a hexagonal P6/m symmetry. Unit cell

parameters determined from the experimental X-ray patterns match very well with those obtained from the structure simulations (peak broadening included

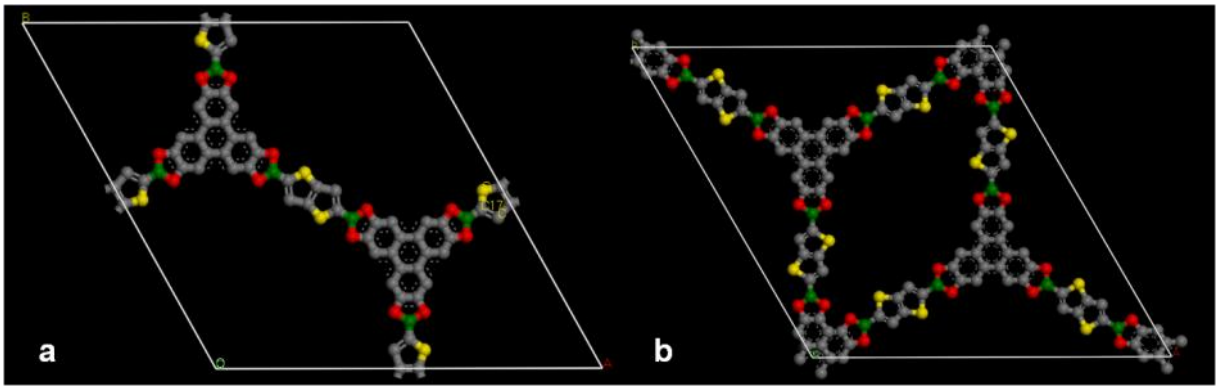

Figure 5.14: Simulation of the crystal lattice of the unit cell calculated in an eclipsed arrangement: **a**, top view on AB plane. **b**, Simulation of crystal lattice of the unit cell calculated in a staggered arrangement (space group P63. top view on AB plane, the pore size and the internal surface is significantly smaller than the experimental data

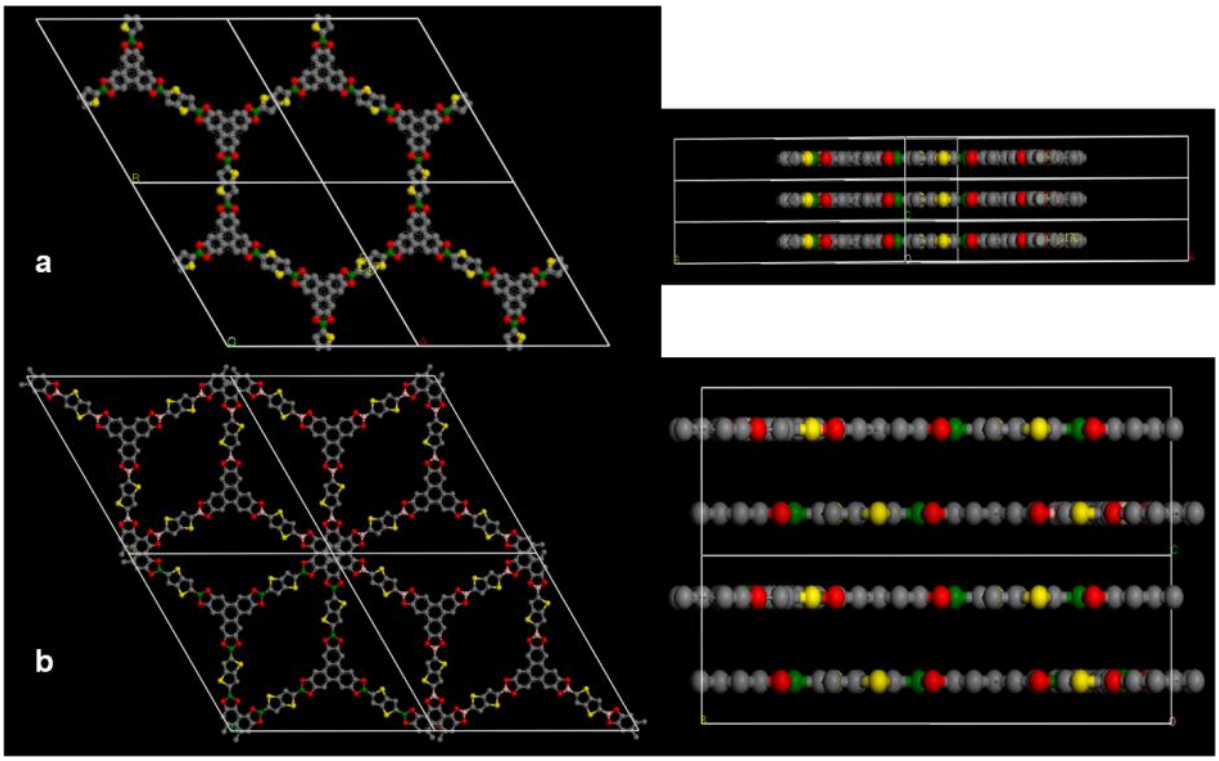

Figure 5.15: a, Crystal structure of 4 unit cells in an eclipsed arrangement and view along c-axis with an interlayer distance of 3.45 Å. **b**, Crystal structure of four unit cells in AB plane of the staggered arrangement and view along c-axis: doubling of

the sheets leads to a larger interlayer distance, this would result a much smaller 2 theta value for the 001.

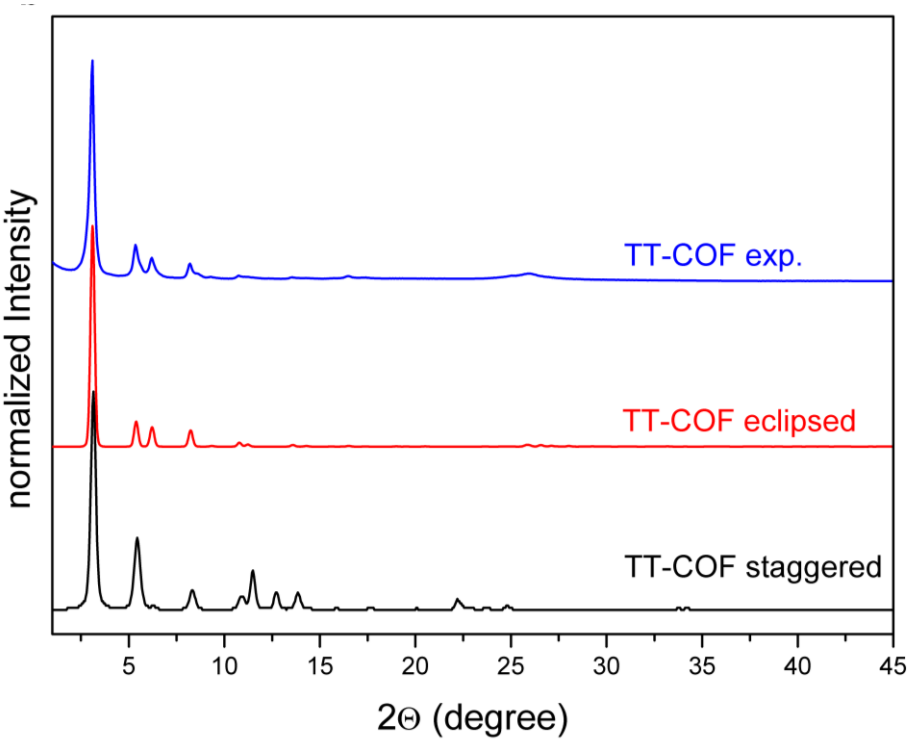

Figure 5.16: Comparison of the experimentally observed PXRD pattern (blue) with the simulated patterns using the Reflex Module of MS Studio in an AA arrangement (red) and AB arrangement (black).

Transmission electron microscopy (TEM) images show the nanoscale morphology of the crystals. A slightly tilted side view offers a view into the long ordered channels with distinct pore sizes. (Figure 5.17).

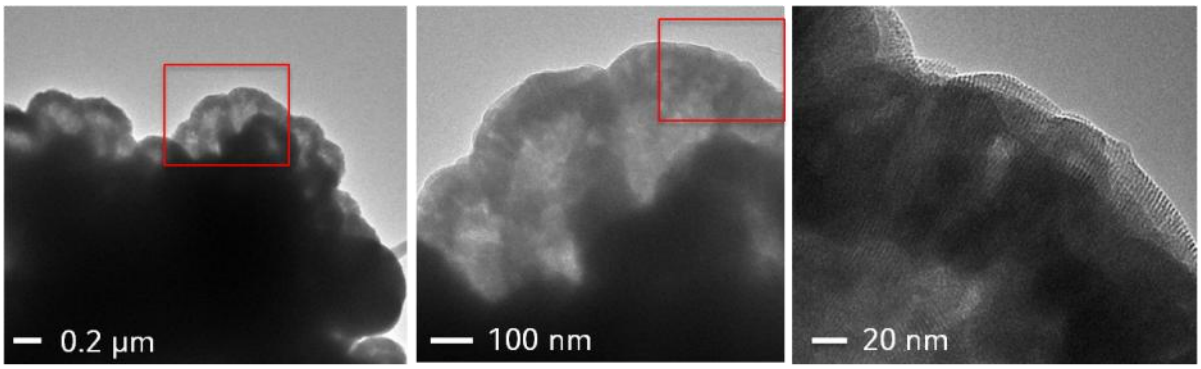

Figure 5.17: TEM micrographs with different magnifications.

A top view of certain crystals (along the c-axis) shows hexagonal structures with a pore-to-pore distance of 2.9 nm (Figure 5.18 a). The morphology identified by TEM can be ascertained by Scanning Electron Microscopy (SEM). The SEM image shows small crystals with sizes of about 100 nm that appear to intergrow into larger arrangements (Figure 5.16 b). Based on peak broadening of the PXRD patterns we obtain a domain size of about 30 nm.

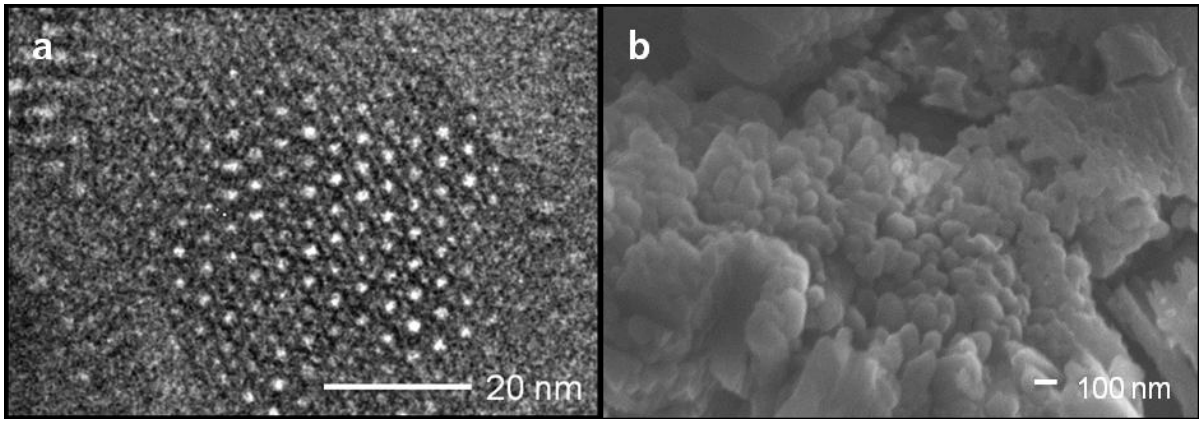

Figure 5.18: **a**, TEM micrograph (top view) along the c-axis showing the hexagonal structure of TT-COF. **b**, SEM micrograph of TT-COF showing some intergrowth of the small crystals. **c,** Nitrogen sorption isotherm of degassed TT-COF measured at 77 K. **d**, pore size distribution with a mean pore size of about 30.05 Å

FT-IR spectroscopy was performed to confirm the presence of the building blocks and the newly-formed boronate ester functionality. As previously reported, the attenuation of the OH stretching band due to ester formation is apparent, furthermore the most characteristic modes of the C-B and C-O functionalities can be assigned to the bands at 1395 cm-1 and 1353 cm-1 (Figure 5.19).[36]

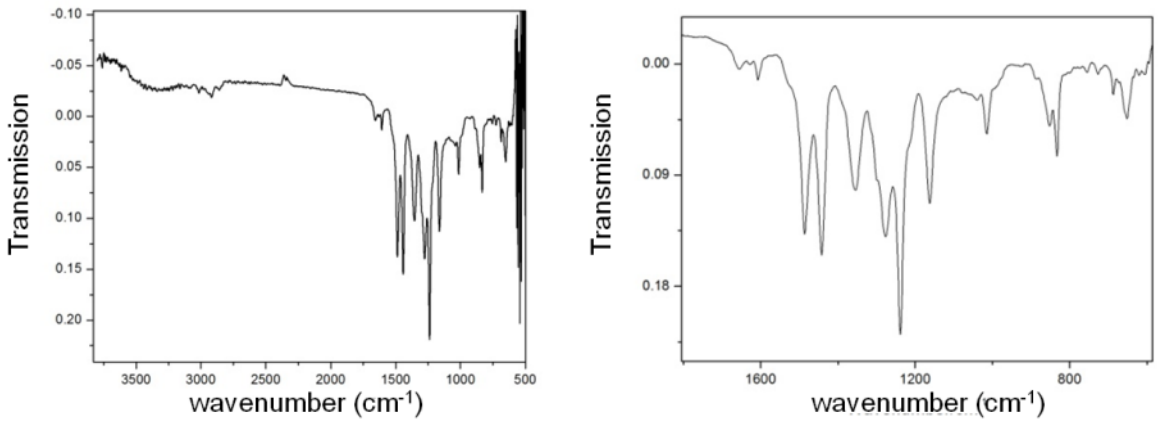

Figure 5.19: IR spectrum of TT-COF.

Table 5.2: Assignment of the most important bands.

Peak (cm^{-1})	Assignment
3495 (m)	ν_{sym} OH from terminal OH and $B(OH)_2$ groups
1561(m)	ν_{sym} C=C for fused aromatics
1487(m)	ν_{sym} C=C for aromatics
1437(m)	ν_{sym} C=C for aromatics
1395(s)	ν_{sym} B-O
1353(s)	ν_{sym} B-O
1235(m)	ν_{sym} C-O
1020(w)	ν_{sym} B-C

^{11}B MAS NMR spectrum (Figure 5.20 a) shows a trigonal planar Boron atom with a chemical shift of 21 ppm, which can be distinguished from the starting material (TTBA 15 ppm). The presence of the building blocks can be confirmed with ^{13}C CP-MAS-NMR (Figure 5.20 b). All signals can be assigned to the carbon atoms in the structure.

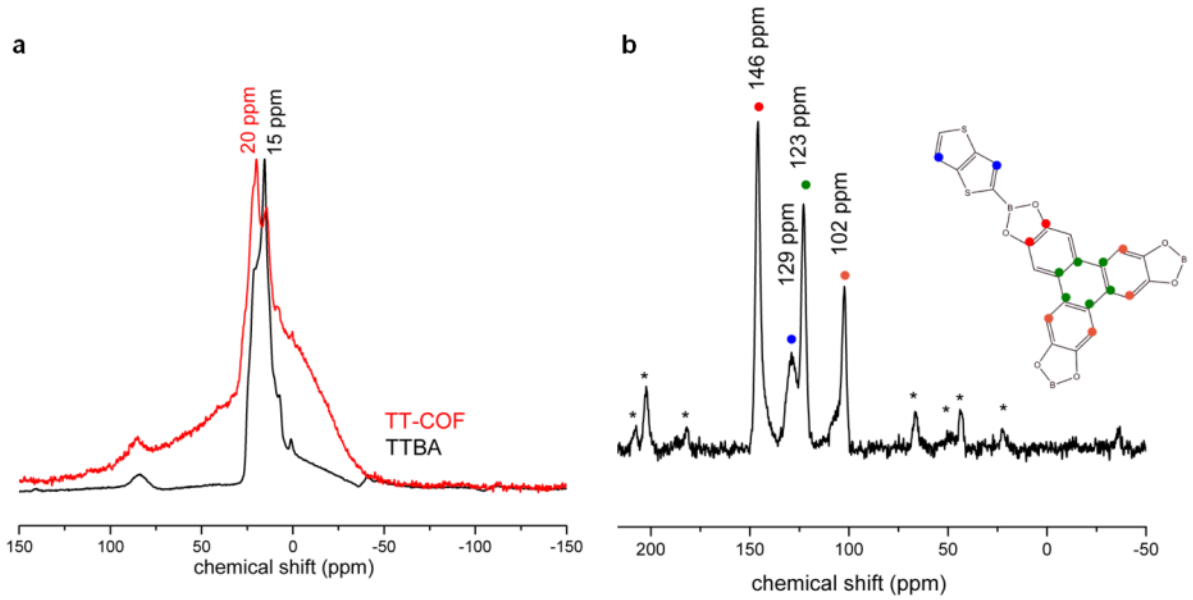

Figure 5.20: a, ^{11}B MAS NMR of TT-COF indicating an esterification of the free boronic acid (peak at 20 ppm). The peak at 15 ppm can result from free boronic acid at the edges of the crystals, or from oligomeric byproducts., the additional broadend intensities can not be assigned at this point **b**, ^{13}C CP-MAS-NMR spectrum of TT-COF indicates that all building blocks are present. The asterisks (*) indicate rotation side bands.

The porosity of TT-COF was confirmed with N_2 sorption measurements at 77 K. The obtained type IV isotherm is characteristic for mesoporous materials (Figure 5.21 a). and shows a very well-defined jump in the uptake as a result of the well-defined mesoporous pore system. Evaluation of the isotherm using the NLDFT-based kernel gives a pore size of 3 nm (Figure 5.21 b). The experimentally obtained surface area and pore volumes from the sorption data were compared to theoretical values obtained with the Connolly method. In crystalline materials these values can be predicted using geometric methods. [121,122] Based on these results we can conclude that the pores of TT-COF are not blocked by solvent molecules or by fragments of the framework

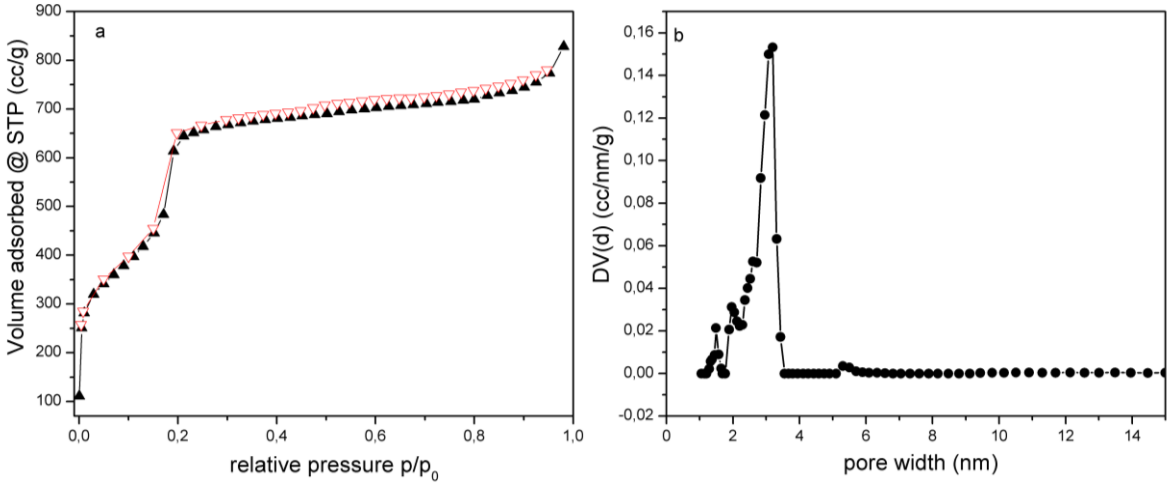

Figure 5.21: a, Nitrogen sorption isotherm of degassed TT-COF measured at 77 K. **b,** pore size distribution with a mean pore size of about 3.0 nm.

Table 5.3: Theoretical and experimental values for surface area, pore size and pore volume of TT-COF.

	Connolly surface	**Sorption data**
Surface area m^2/g	1813	1812
Volume cm^3/g	1.17	1.19
Pore size nm	3.0	3.0

The thermal stability was examined by thermogravimetric analysis (Figure 5.22). The first step corresponds to a weight loss of 9 % between 25 °C and 225 °C. The TT-COF starts to degrade at a temperature of 400°C. At 600°C a total weight loss of 16 % representing 6 Boron atoms (B_2O_3) per unit cell $C_{54}H_{18}S_6B_6O_{12}$.

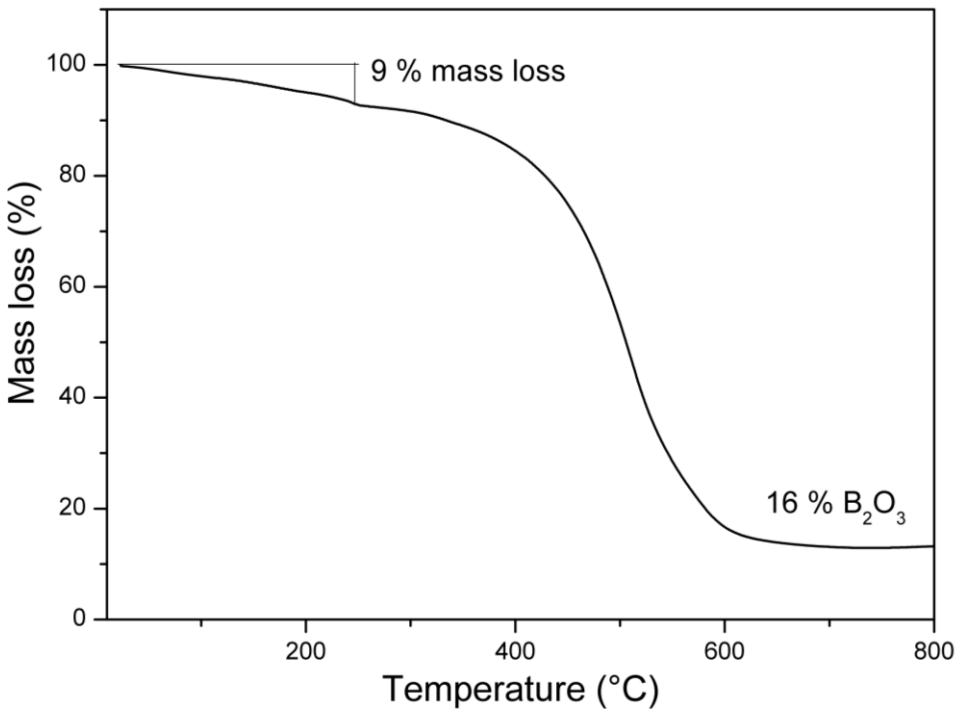

Figure 5.22: Thermogravimetric analysis of TT-COF.

All these results demonstrate that TT-COF is a well-defined mesoporous crystalline material with highly organized sheets resulting in high surface areas. Polymers based on the thieno[2,3-b]thiophene building block are known; these polymers exhibit high charge carrier mobilities and are stable under ambient conditions.[140]. Sariciftci *et al.* reported photoinduced electron transfer from the conducting polymer MEH-PPV to the C_{60}.[141] Moreover, photoinduced charge transfer from polymerized thienothiophene derivatives to fullerene-based acceptor molecules is known.[142] This prompted us to study the electronic interactions between TT-COF and PCBM. The large pores of TT-COF allows for the uptake of such large fullerene molecules, and thus for the investigation of the resulting host-guest interactions.

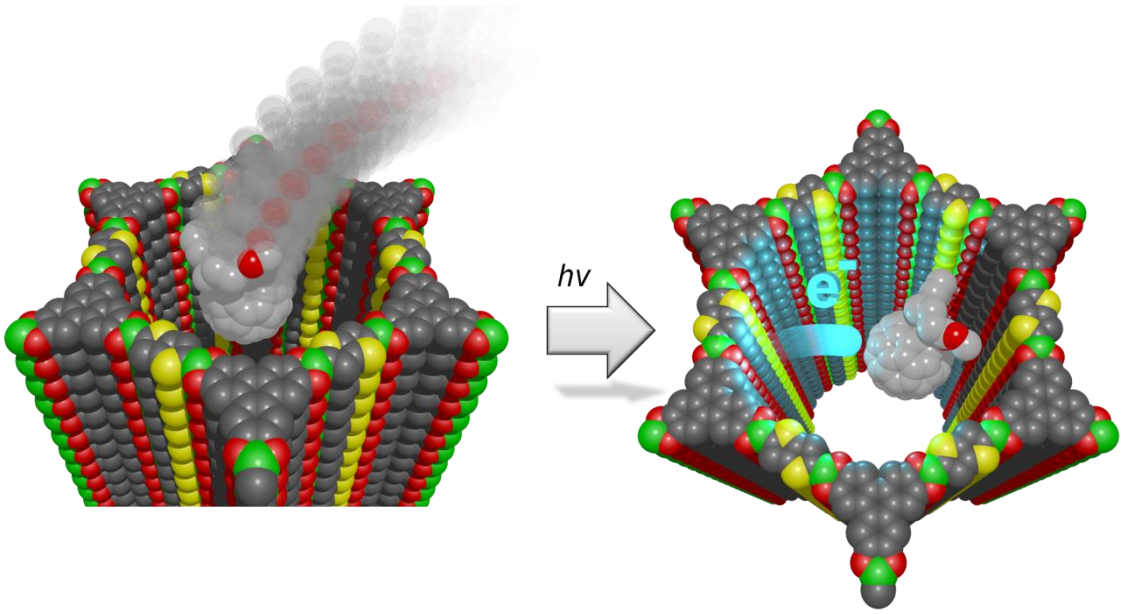

Figure 5.23: Schematic representation of the host-guest complex of TT-COF and a $PCBM_{60}$ molecule to scale; carbon is black, oxygen is red, boron is green and sulfur is yellow). For clarity only one PCBM molecule is shown, while in the experiments described below the COF channels are fully loaded with the PCBM phase

Figure 5.24 shows the absorption spectrum of pure TT-COF thin film, pure $PCBM_{60}$ thin film and a mixture of both materials. The pure TT-COF exhibits a broad absorbance over the whole spectrum of the visible range with small maxima at 400 nm, 550 nm, 680 nm and 800nm. The mixture of TT-COF and $PCBM_{60}$ is a superposition of these two components. The dark-grey color of TT-COF is tentatively attributed due to light scattering from subwavelength nanostructures like described elsewhere. For this scattering process every incident wavelength corresponds to a certain scattering angle.

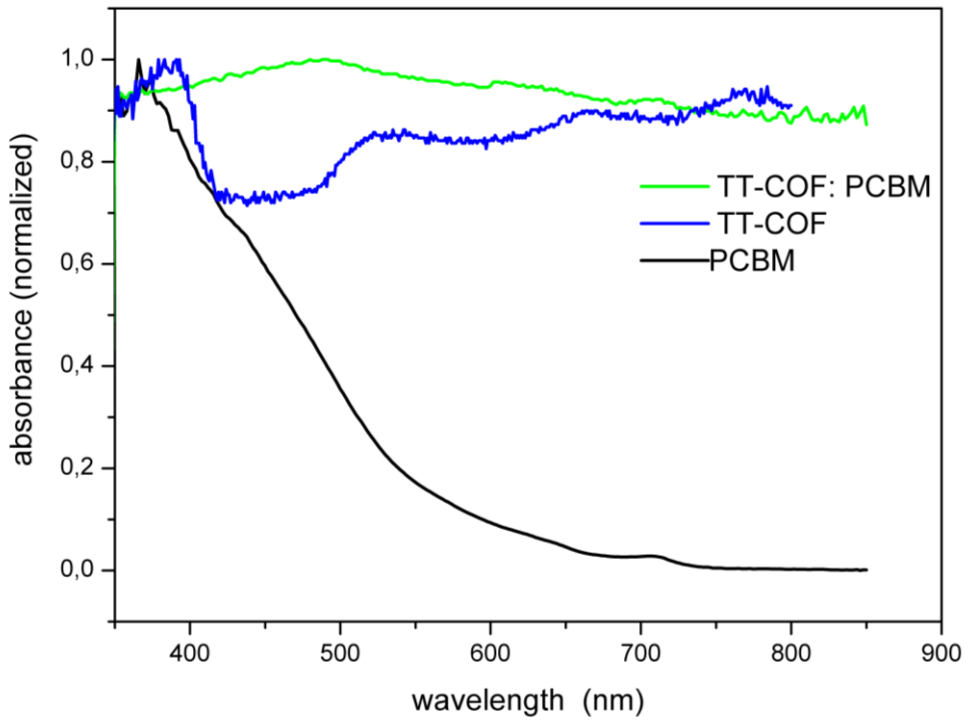

Figure 5.24: UV–Vis absorption spectrum for TT-COF measured from film (black) and $PCBM_{60}$ films (red) and thin films of TT-COF / $PCBM_{60}$ (blue) with 50 : 50 molar ration of TT-COF and $PCBM_{60}$.

Upon irradiation with a 633 nm laser, the TT-COF thin film becomes photoconductive, and the illumination of the 10 µm gap of the sample results in a significant current increase to 120 nA (Figure 5.25). Until now the I-V curve of the mixed system cannot be provided, due to photobleaching of PCBM.

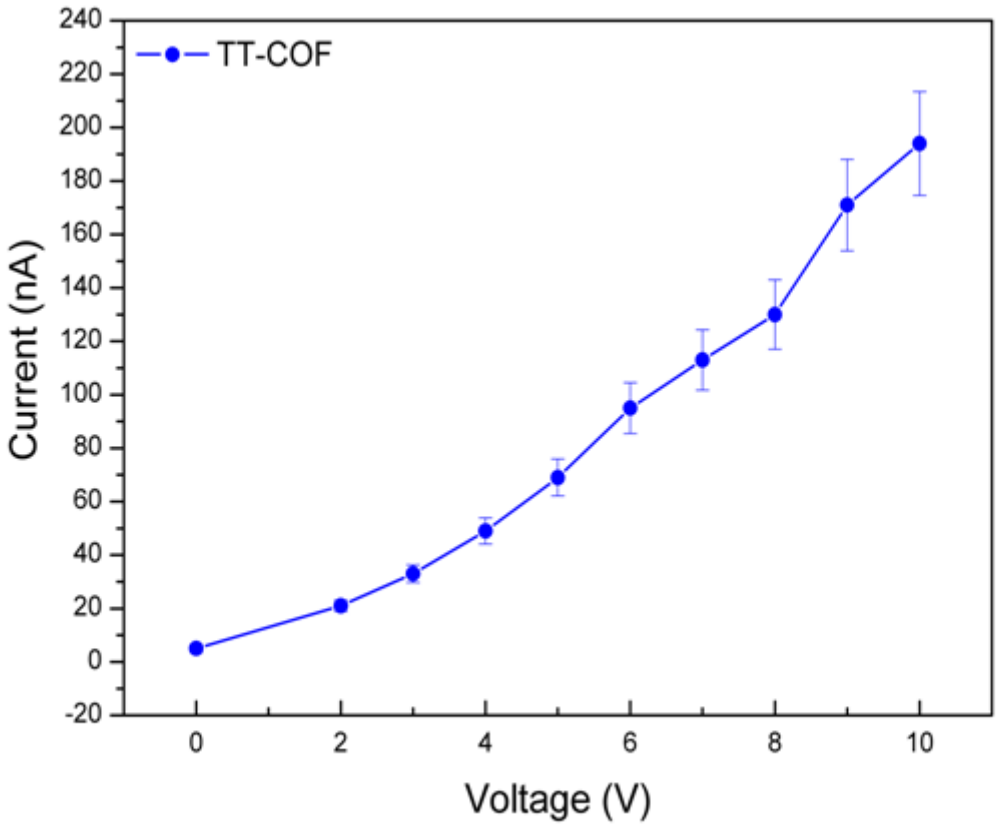

Figure 5.25: a) Current-voltage characteristics of TT-COF (blue ■) and illuminated TT-COF/ $PCBM_{60}$ composite (green ●) measured between a 10 µm gold electrode gap with an irradiation wavelength of 633 nm.

The PL transients and their respective fit-functions of $PCBM_{60}$ and TT-COF loaded with $PCBM_{60}$ are shown in Figure 5.26. In the bulk, $PCBM_{60}$ shows bi-exponential PL decay at the nanosecond time scale, while TT-COF decays tri-exponentially with

an average lifetime of 117 ps (see Table 5.4). When included in the channels of TT-COF, the $PCBM_{60}$ contribution can be modelled by a single exponential decay component of 1070 ps that is close to the intensity weighted average lifetime of 1206 ps of the bulk material. Importantly, the decay of TT-COF with a lifetime below 50 ps (48 and 18 ps) is substantially faster than the average decay in the bulk indicating an efficient additional relaxation channel in agreement with the quenching observed in the PL-spectra (Figure 5.27).

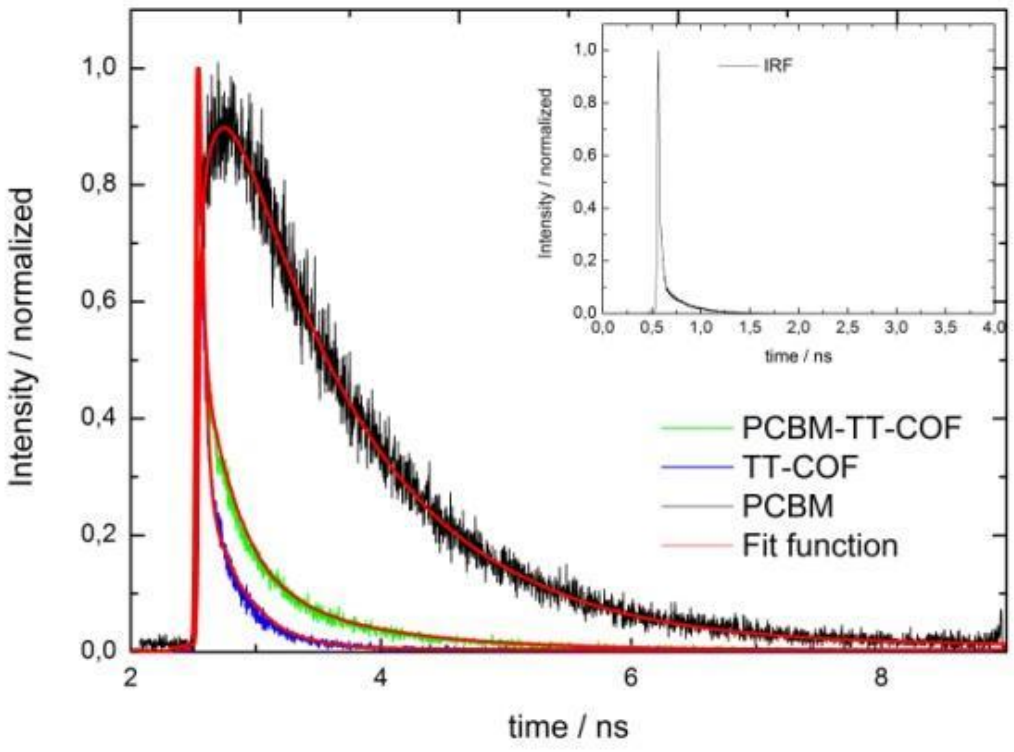

Figure 5.26: PL-lifetime transients of $PCBM_{60}$ (red symbols), TT-COF (blue symbols) and $PCBM_{60}$/TT-COF (green symbols) thin films using a TCSPC technique under femtosecond pulsed excitation at 800 nm.

Table 5.4: PL- lifetimes of the decay of PCBM, PCBM-TT-COF and TT-COF. For PCBM-TT-COF the lifetimes for the slow and fast decay of PCBM were kept fixed for comparison.

	Average lifetime (intensity weighted)	Lifetime exp.1	Lifetime exp.2	Lifetime exp.3	PL-decay
TT-COF	103ps	276ps (31%)	25ps (69%)		Bi-exp.
PCBM TT-COF	466ps	1406ps (2%)	794ps (52%)	60ps (46%)	Tri-exp.
PCBM	1206ps	1406ps (76%)	794ps (24%)		Bi-exp.

In the literature, very fast light-induced electron transfer within the order of femtoseconds has already been reported for $PCBM_{60}$ / P3HT blends.[143] From the observation of the photocurrent, we conclude that electron transfer also occurs for the present system. The photoinduced charges can dissociate at the nanostructured interface between TT-COF and $PCBM_{60}$. In bulk heterojunctions, short diffusion pathways at the order of 10-20 nm are necessary to reach the electron acceptor $PCBM_{60}$ within the lifetime of the photoinduced charges.[143,144] Given the ordered nanochannels of the donor material TT-COF with about 3 nm channel diameter, such short diffusion pathways are clearly available in the interpenetrating system TT-COF-$PCBM_{60}$. Therefore the observation of PL-quenching confirms the interpenetrated structure of TT-COF and $PCBM_{60}$.

The combination of PL intensity and lifetime measurements thus provides access to changes in the excited state relaxation and helps distinguishing radiative and non-radiative rate modifications.

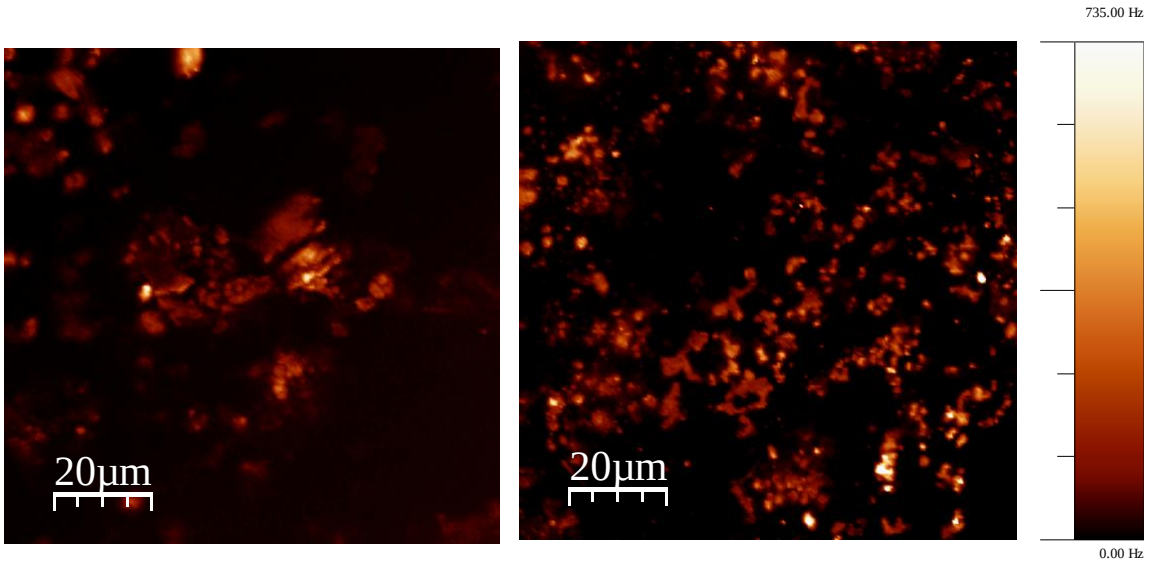

Figure 5.27: PL images after femtosecond laser excitation at 800nm detected at higher energies of TT-COF (left side) and TT-COF with PCBM (right side). For the PCBM TT-COF system the only dot like rests of the bright areas (left side) can be detected (see text), while the overall PL-intensity for PCBM TT-COF is decreased by a factor of 100.

The fluorescence emission spectrum of TT-COF shows that the framework has a blue emission upon excitation at 380 nm. Blue-emissive polymers based on boronate ester condensation have been reported by Lavigne et. al and recently the blue-emissive TP-COF has been reported.[60, 61] In case of introduction of an electron acceptor, e.g. $PCBM_{60}$ into the TT-COF in a weight ratio TT-COF : PCBM 1:1 the emission band at 487 nm is completely quenched (Figure 5.28).

Assuming no internal filter effects, since the concentrations were in the order of millimolars, this is the first evidence indicating separation of exciton for the system under study, since luminescence quenching is used as indication for charge

transfer.[141] The excited state has a lifetime in the order of nanoseconds, therefore an ultrafast process is occurring in this system. Electron transfer in the order of femtoseconds has already been reported for similar P3HT/PCBM blends.[143]

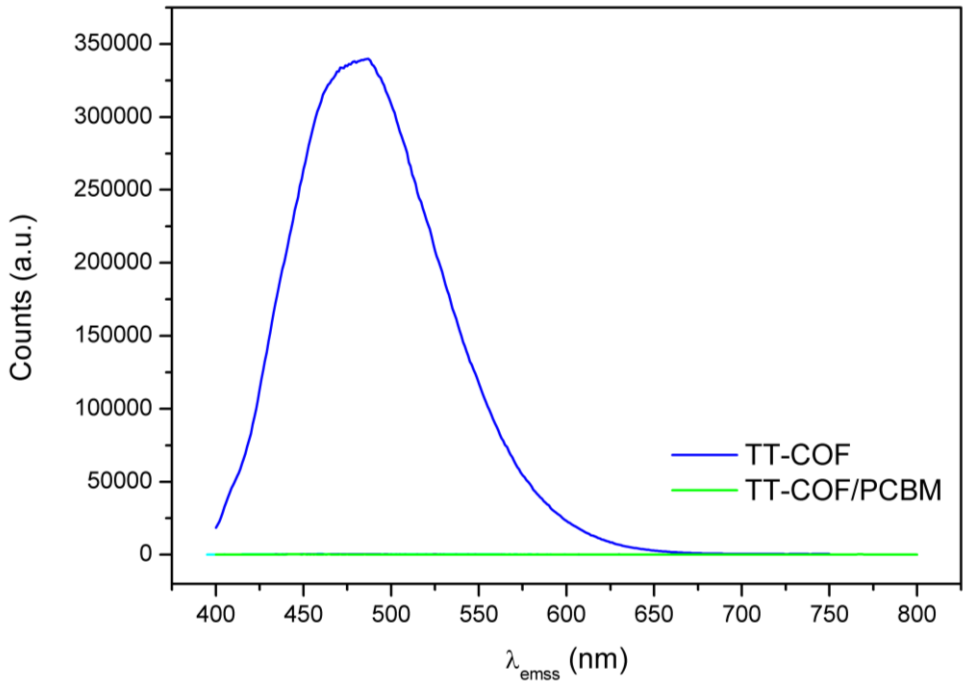

Figure 5.28: Fluorescence quenching of TT-COF (blue) and TT-COF filled with PCBM (green).

5.2.4. Conclusion

Structural disorder of the donor and the acceptor phases can limit charge carrier mobility in organic semiconductors and hence can decrease the performance of organic solar cells. The creation of a crystalline semiconducting framework, e.g, a hole transporter whose pores can be filled with the respective acceptor is ultimately expected to overcome these limitations. The novel thienothiophene-based Covalent Organic Framework TT-COF described here exhibits a significant photoresponse.

Furthermore the TT-COF structure is thermally stable and can be operated under ambient conditions. To increase the efficiency of organic solar cells it would be desirable to overcome the disadvantage of the very short exciton diffusion lengths in organic polymers like PCBM, P3HT or MDMO-PPV. The novel interpenetrated TT-COF/PCBM structure presented here (where the distance between the donor network and the acceptor phase is around 3 nm) supports efficient charge transfer within the lifetime of the excitons. Hence we propose that interpenetrated networks of crystalline porous semiconducting COFs with electron acceptor phases such as $PCBM_{60}$ present a promising model architecture for the development of efficient photovoltaic devices.

5.3. References

30. Cote, A. P.; Benin, A. I.; Ockwig, N. W.; O'Keeffe, M.; Matzger, A. J.; Yaghi, O. M., *Science* **2005,** *310* (5751), 1166-1170.

31. El-Kaderi, H. M.; Hunt, J. R.; Mendoza-Cortes, J. L.; Cote, A. P.; Taylor, R. E.; O'Keeffe, M.; Yaghi, O. M., *Science* **2007,** *316* (5822), 268-272.

34. ndara, F.; Asano, A.; Furukawa, H.; Saeki, A.; Dey, S. K.; Liao, L.; Ambrogio, M. W.; Botros, Y. Y.; Duan, X.; Seki, S.; Stoddart, J. F.; Yaghi, O. M., *Chem. Mater.* **2011,** *23* (18), 4094-4097.

36. Tilford, R. W.; Gemmill, W. R.; zur Loye, H.-C.; Lavigne, J. J., *Chem. Mater.* **2006,** *18* (22), 5296-5301.

37. Cote, A. P.; El-Kaderi, H. M.; Furukawa, H.; Hunt, J. R.; Yaghi, O. M., *J. Am. Chem. Soc.* **2007,** *129* (43), 12914-12915.

41. Spitler, E. L.; Dichtel, W. R., *Nat Chem* **2010,** *2* (8), 672-677.

42. Ding, X.; Guo, J.; Feng, X.; Honsho, Y.; Guo, J.; Seki, S.; Maitarad, P.; Saeki, A.; Nagase, S.; Jiang, D., *Angew. Chem., Int. Ed.* **2011,** *50* (6), 1289-1293.

53. Han, S. S.; Furukawa, H.; Yaghi, O. M.; Goddard, W. A., III, *J. Am. Chem. Soc.* **2008,** *130* (35), 11580-11581.

60. Wan, S.; Guo, J.; Kim, J.; Ihee, H.; Jiang, D., *Angew. Chem.* **2009,** *121* (18), 3253.

61. Niu, W.; Smith, M. D.; Lavigne, J. J., *J. Am. Chem. Soc.* **2006,** *128* (51), 16466-16467.

63. Wan, S.; Guo, J.; Kim, J.; Ihee, H.; Jiang, D., *Angew. Chem., Int. Ed.* **2009,** *48* (30), 5439-5442.

65. Ding, X.; Chen, L.; Honsho, Y.; Feng, X.; Saengsawang, O.; Guo, J.; Saeki, A.; Seki, S.; Irle, S.; Nagase, S.; Parasuk, V.; Jiang, D., *J. Am. Chem. Soc.* **2011,** *133* (37), 14510-14513.

119. *Accelrys MS Modeling 4.4*, **2008**.

121. Leach, A. R., *Molecular Modelling: Principles and Applications*. 2nd ed.; Prentice Hall: Harlow, England, *2001*.

122. Connolly, M., *J. Appl. Crystallogr.* **1983,** *16* (5), 548-558.

135. Tsubata, Y.; Suzuki, T.; Miyashi, T.; Yamashita, Y., *J. Org. Chem.* **1992,** *57* (25), 6749-6755.

136. Pilgram, K.; Zupan, M.; Skiles, R., *J. Heterocycl. Chem.* **1970,** *7* (3), 629-633.

137. Yaghi, O. M.; Cote, A. P.; El-Kaderi, H. M.; Hunt, J. R. Crystalline 3d- and 2d-covalent organic frameworks. 2008-US518592008091976, 20080124., 2008.

138. Spitler, E. L.; Colson, J. W.; Uribe-Romo, F. J.; Woll, A. R.; Giovino, M. R.; Saldivar, A.; Dichtel, W. R., *Angew. Chem.* **2012**, n/a-n/a.

139. Dennler, G.; Scharber, M. C.; Brabec, C. J., *Adv. Mater.* **2009,** *21* (13), 1323-1338.

140. Heeney, M.; Bailey, C.; Genevicius, K.; Shkunov, M.; Sparrowe, D.; Tierney, S.; McCulloch, I., *J. Am. Chem. Soc.* **2005,** *127* (4), 1078-1079.

141. Sariciftci, N. S.; Smilowitz, L.; Heeger, A. J.; Wudl, F., *Science* **1992,** *258* (5087), 1474-1476.

142. Savenije, T. J.; Grzegorczyk, W. J.; Heeney, M.; Tierney, S.; McCulloch, I.; Siebbeles, L. D. A., *J. Phys. Chem. C* **2010,** *114* (35), 15116-15120.

143. Xie, Q.; Perez-Cordero, E.; Echegoyen, L., *J. Am. Chem. Soc.* **1992,** *114* (10), 3978-3980.

144. Duche, D.*, et al. Sol. En. Mat* **2011**.95*, 18–25.*

145. McCulloch, I.; Heeney, M.; Bailey, C.; Genevicius, K.; MacDonald, I.; Shkunov, M.; Sparrowe, D.; Tierney, S.; Wagner, R.; Zhang, W.; Chabinyc, M. L.; Kline, R. J.; McGehee, M. D.; Toney, M. F., *Nat Mater* **2006,** *5* (4), 328-333.

6. Oriented Growth of COFs

6.1. Introduction

In Nature the control over crystal growth of biominerals is mainly achieved by specific interactions between crystallization templates and the crystalline phase; this process is known as biomineralization.[146, 147,148] Additive-controlled crystallization is an attempt to mimic biomineralization processes under laboratory conditions. A major effort in this research is dedicated to the design and production of soluble and insoluble crystallization templates.[149] A prominent and well-studied insoluble type of template is represented by surfaces functionalized with Self Assembled Monolayers (SAMs). [84, 150, 151] For example, it has been demonstrated that surface functionalization with SAMs promotes an oriented crystal growth of dense calcium carbonate or zinc oxide.[152-154] The oriented growth of inorganic crystalline porous materials using SAMs as organic interface has also been demonstrated for different zeolites.[86] Moreover, this concept was extended to inorganic-organic hybrid materials. Metal-Organic Frameworks (MOFs) were successfully grown with a specific orientation on surfaces functionalized with SAMs. It was also illustrated that nucleation processes can be controlled with SAMs.[87, 88, 155]

In 2005 Yaghi introduced a class of organic crystalline frameworks, known as Covalent Organic Frameworks (COFs), which are formed by a reversible boronate ester condensation reaction of a boronic acid and a polyol.[30] Due to their interesting properties such as permanent porosity with very high surface area, combined with low density and high thermal stability, applications in gas storage are likely.[53] More recently semiconducting and photoconducting properties of 2D COFs have been

intensively investigated; e.g., phthalocyanine- and porphyrin-based COFs were reported to exhibit very high charge carrier mobilities, the latter even has the highest mobility ever reported for organic materials.[34, 64] However, these materials have been synthesized mostly as bulk materials with no control over orientation. To achieve total control over the alignment of the channels of porous materials is a great challenge in materials chemistry and is of great interest for many technological devices, e.g. OLEDs or photovoltaic cells.[156, 157] A first effort has been reported by Dichtel and co-workers showing a perpendicular orientation of the pores of 2D COFs on single layer graphene (SLG) coated substrates.[89] The SLG acts as template for the growth of hexagonal and even tetragonal COFs. The crystallinity, thickness and orientation of the grown film is influenced by reaction time and SLG support. The ability to control the orientation of the pore system in conducting COF films could open the way to a great number of functionalities, for example for bulk heterojunction solar cells.

Here we report the oriented growth of Covalent Organic Frameworks on SAM functionalized gold surfaces, resulting in a channel system parallel to the substrate.

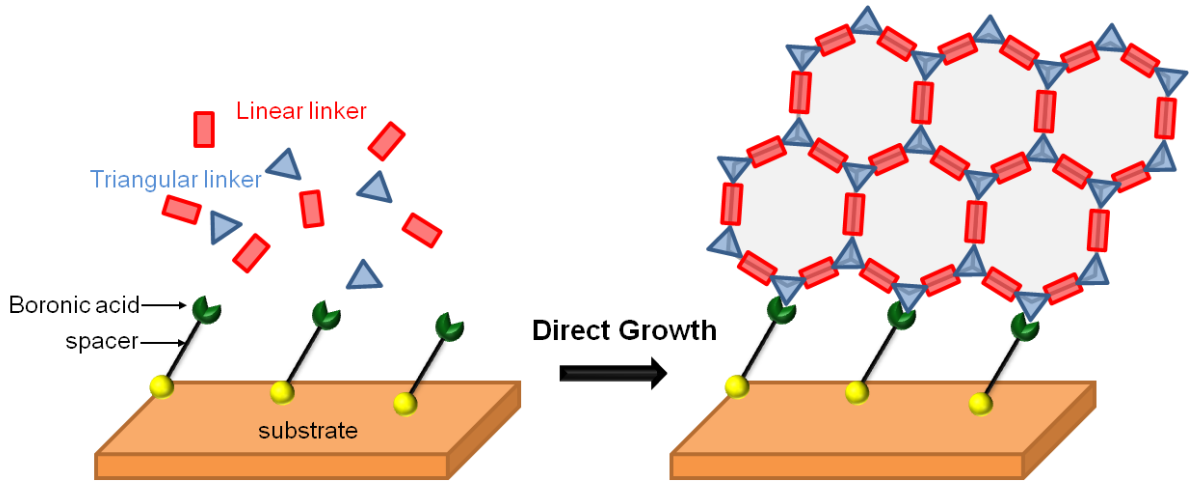

Figure 6.1: Schematic illustration of oriented growth of COF crystals on a SAM functionalized gold surface.

For a first proof of concept two COFs were grown on mercaptophenylboronic acid functionalized gold surfaces. COF-1037 and TT-COF were successfully prepared as thin films. The photoconductive TT-COF is an interesting candidate for the parallel orientation on a substrate. Due to alignment of the π-conjugated aromatic rings, anisotropic charge migration along the π-system is expected to be enhanced. Charge transport parallel to the substrate is ideal for thin film transistors, such as

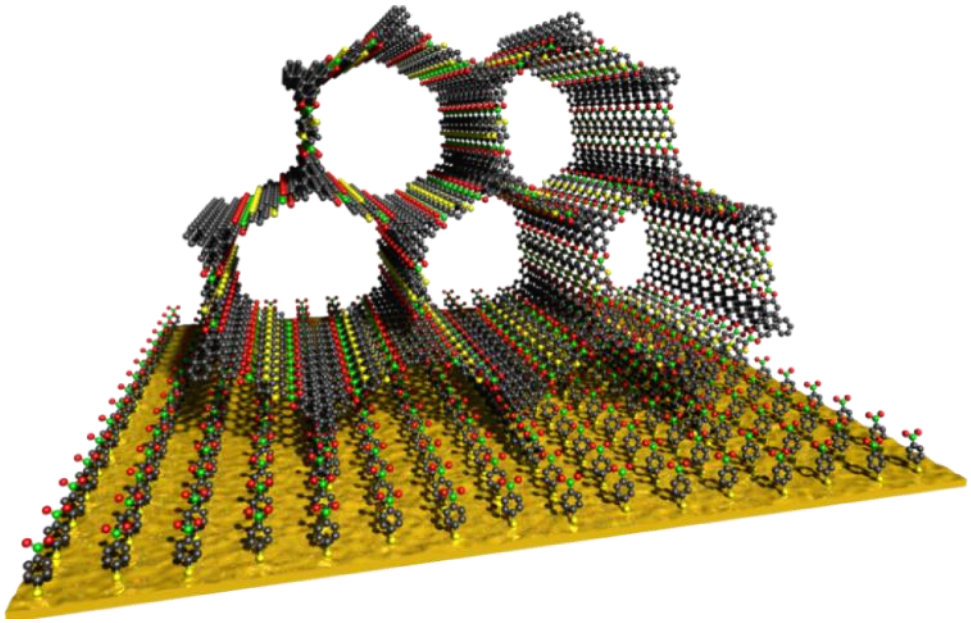

Figure 6.2: Schematic illustration of oriented growth of TT-COF on a mercaptophenylboronic acid SAM functionalized gold surface.

OFETs. The functionalization of gold with mercaptoboronic acids was examined in connection with the molecular recognition of sugars or sugar-carrying proteins (ovalbumin).[158] The affinity of boronic acids to bind 1,2-diols is well known.[32] The boronic acid groups mimic the diboronic acid linkers and thus we might anticipate that the condensation reactions of the COF structure are initiated or facilitated on the surface. The gold substrates were functionalized with mercaptophenylboronic acid following a published procedure.[76] After SAM formation the slides were immersed into the reaction solution of COF-10 and TT-COF in a vertical manner.

6.2. Experimental Section

6.2.1. Materials and Methods

All materials (if not otherwise noted) were purchased from Aldrich or Fluka in the common purities purum and puriss. All materials were used without further purification. The building block hexahydroxytriphenylene was purchased from TCI Europe. The building block 2,5-bis(4,4,5,5-tetramethyl-1,3,2-dioxaborolan-2-yl)thieno[3,2-b]thiophene was prepared in the group of Prof. Knochel by Thomas Kunz. The building block 4,4'-biphenyldiboronic acid was synthesized according to published procedures.[159, 160] All materials were manipulated in air.

X-ray diffraction analysis was carried out in reflection mode using a Bruker D8 Discover with Ni-filtered CuKα-radiation (1.5406 Å) and a position-sensitive detector (Vantec). Characterization of the self-assembled monolayers was performed by RAIR spectroscopy, using a Bruker IFS 66v FTIR spectrometer. The sample chamber containing a high performance variable angle reflection accessory (A-513) is maintained at 2 mbar during the entire measurement by means of an Edwards rotary-pump. In a typical measurement for gold surfaces, an incidence angle of 83° to the surface normal was used. Furthermore, a cleaned gold slide was measured as background prior to the measurements. The SEM images were recorded with a Jeol 6500F field emission scanning electron microscope with an EDX/WDX detector.

Self-Assembled Monolayers on Gold

The gold-coated slides (glass slides (76 × 26 mm^2), coated with 10 nm Ti and 100 nm gold by electron-beam evaporation, were cut in smaller pieces (10 × 13 mm^2) and then cleaned in an ultrasonic bath for 15 min in ethanol and then treated in an oxygen plasma for 15 min. The cleaned gold slides were immersed in a 1 mM ethanolic solution (6 pieces in 20 mL) of the desired mercaptophenylboronic acid, and left at RT for 24 h. The SAM-functionalized gold slides were repeatedly washed with ethanol, and stored under inert nitrogen atmosphere.

COF Film Synthesis

TT-COF: Film synthesis was performed by inserting the functionalized gold slide into the TT-COF bulk synthesis mixture described in Chapter 5. After the reaction the slides were washed extensively with dichloromethane and dried under nitrogen.

COF-10*:* The MPBA functionalized gold substrates were placed face-down in Teflon®-supports in 5 ml of a suspension of the bulk reaction mixture of COF-10. The autoclave was heated to 100 °C for 72 h. After the reaction was completed the slides were washed with copious amounts of dry acetone and dried under nitrogen.

6.3. Results and Discussion

The formation of the SAM was followed by RAIR, as shown in Figure 6.2. The characteristic absorption bands indicating the presence of the MPBA on the surface were detected. The boronic acid moiety B-OH results in an OH stretch at 3245 cm^{-1} and a mode at 1015 $cm^{-1.}$ Further indication is given by the B-O stretching vibration at 1353 cm^{-1}. The aromatic C=C stretch at 1590 cm^{-1} and the band resulting from 1,4-disubstitued benzenes confirms the presence of the functionality on the surface. The band at 586 cm^{-1} can be assigned to the stretching vibration of the C-S bond. (According to the selection rule for absorption reflection IR the presence of the bands are an indication for upright orientation of the SAM molecule.

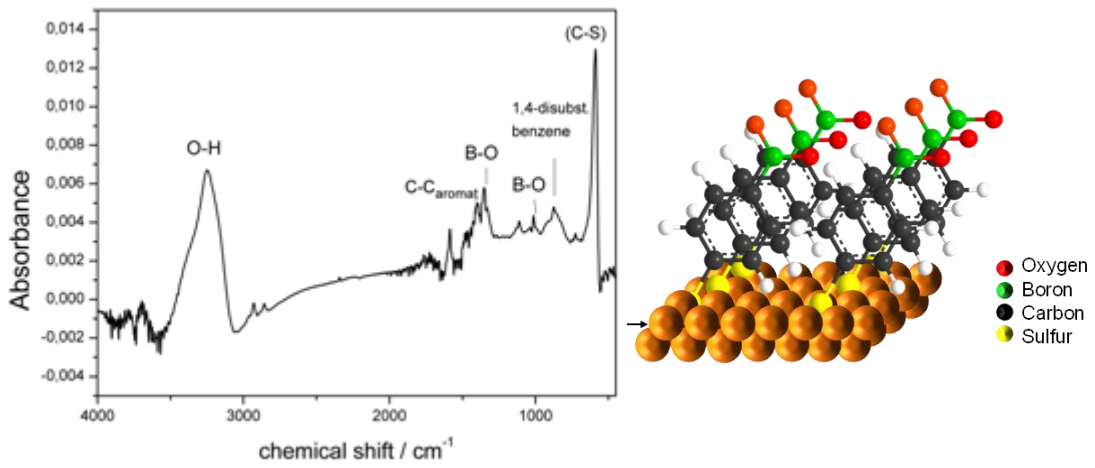

Figure 6.3: RAIR spectrum of MPBA SAM on gold substrate.

The synthesis of oriented thin films of COF-10 and TT-COF, as described in section 6.3, was studied with X-ray diffraction. Strikingly, the TT-COF film grown on the SAM-functionalized gold surface shows preferred orientation in the AB plane, since the 001 reflection is significantly decreased (Figure 6.4).

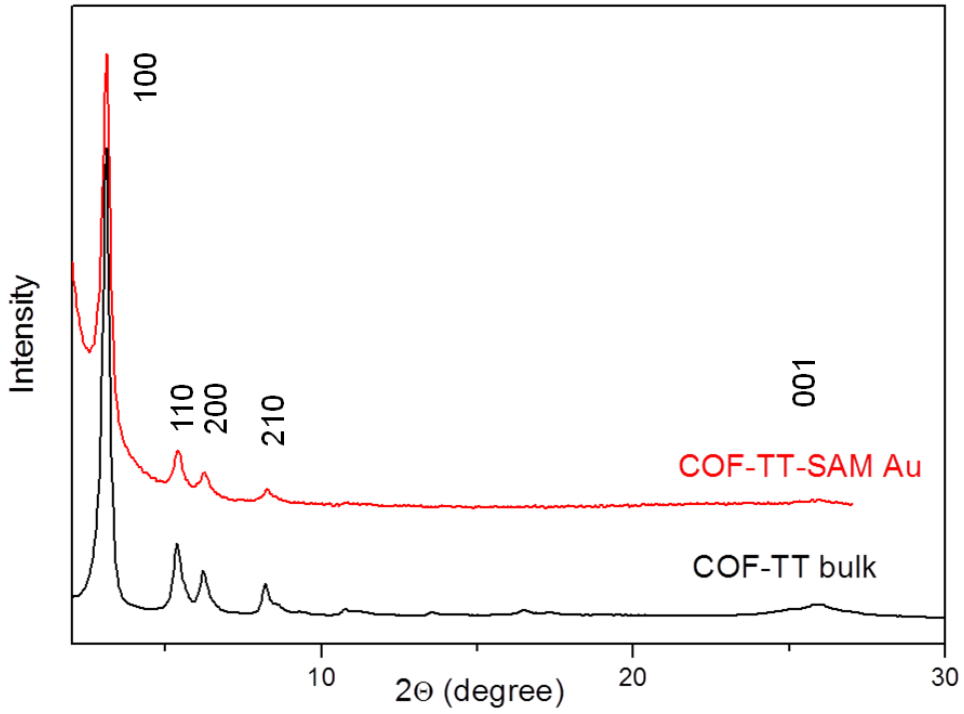

Figure 6.4: PXRD pattern of TT-COF bulk (black) and oriented TT-COF on SAM functionalized gold surface (red).

The same effect was observed with COF-10, synthesized on MPBA-functionalized gold surfaces (Figure 6.4).

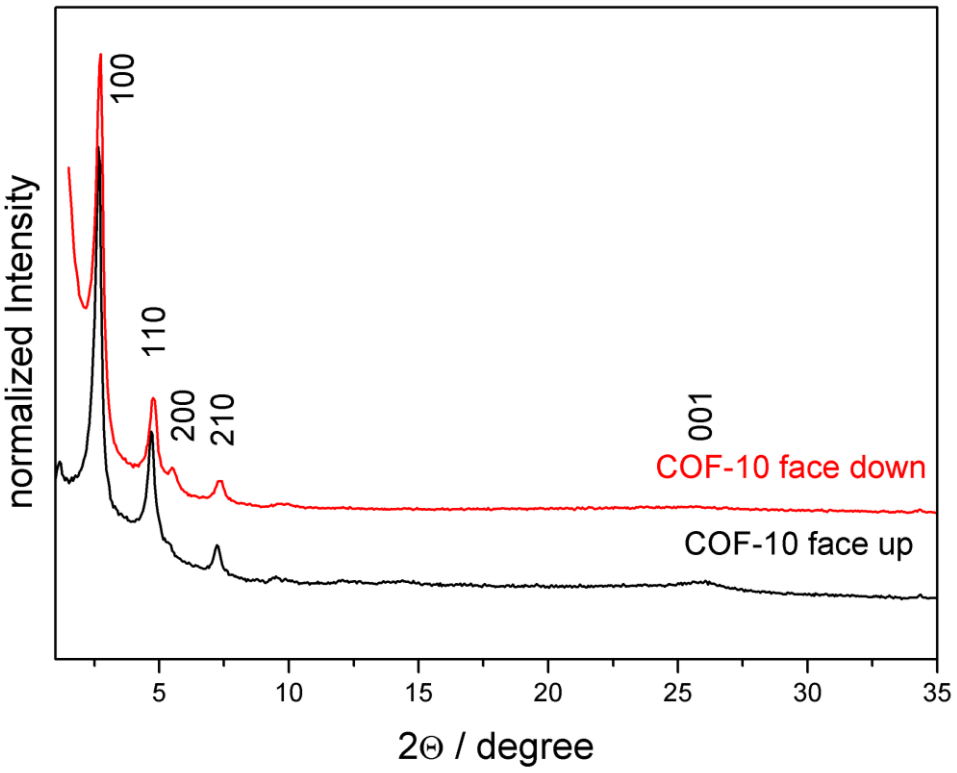

Figure 6.5: PXRD pattern of COF-10 face up (black) without preferred orientation and face down (red) with preferred alignment, indicated by the decrease of the 001 reflection..

A SEM top view of the TT-COF film, synthesized at 100 °C for 4 h and shown in Figure 6.6 A, indicates a very good coverage of the substrate and a very smooth surface of the film. The cross sectional view (Figure 6.6 B, C) shows a 150 nm ± 15 nm film with a uniform thickness.

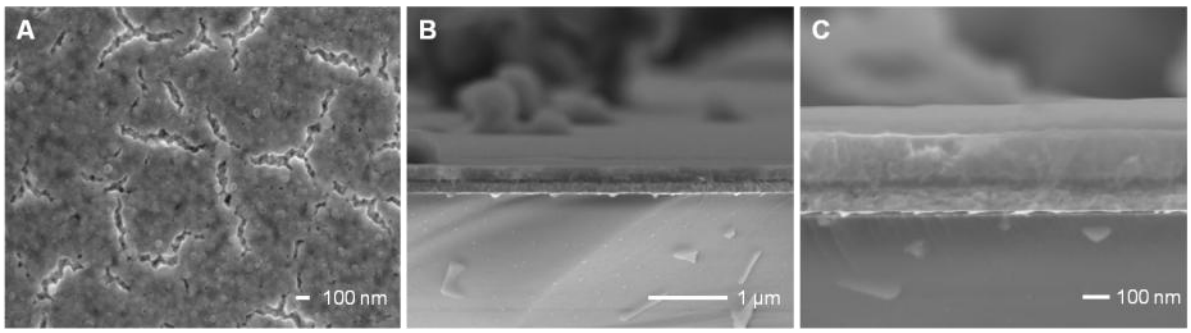

Figure 6.6: SEM micrographs of TT-COF on functionalized gold A) top view and B) and C) cross section with two different magnifications.

The SEM top view image of COF-10 (Figure 6.7 A) also shows a total coverage of the substrate with COF material. In the cross sectional view (Figure 6.7 B) a smooth film with a thickness of around 120 nm was observed.

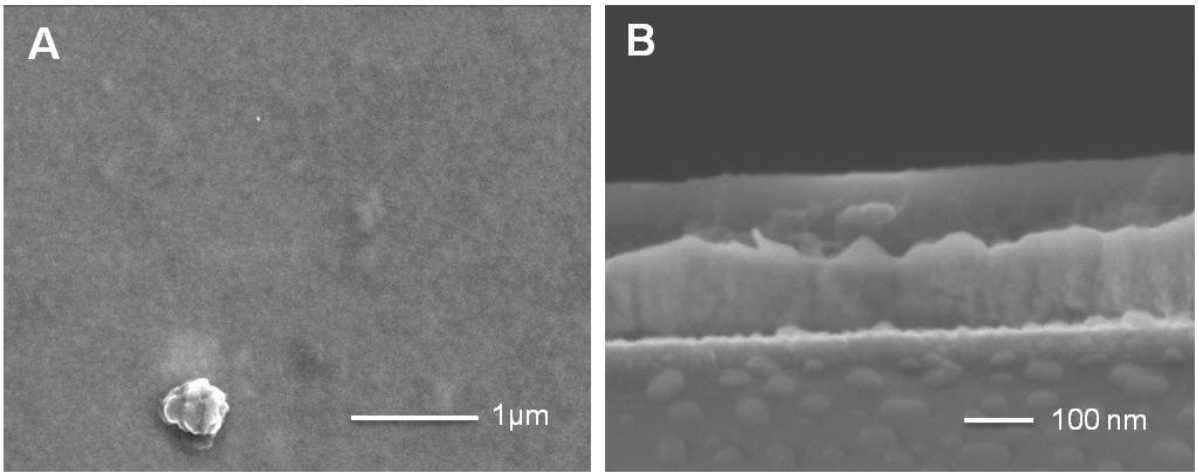

Figure 6.7: SEM micrograph of COF-10 on MPBA-functionalized gold A) top view and B) cross sectional view COF-10 film is represented by the boundry in the background.

6.4. Conclusions

In this chapter we illustrate the control of pore alignment of Covalent Organic Frameworks parallel to a surface. For the first time a possible parallel orientation of COFs was investigated using SAMs to promote oriented crystal growth. The preliminary results demonstrated for COF-10 and TT-COF show that a preferred growth direction of COFs is very likely induced by a boronic acid functionalized surface. Decrease of the 001 reflection is presumably caused by a parallel orientation of COF-10 and TT-COF. The SEM images illustrate that this approach results in smooth films with uniform thicknesses around 150 nm and homogeneous substrate coverage. Further characterization is underway to prove orientation of these systems on the surface. This new approach for oriented film growth potentially provides a general method for applications in optoelectronic devices, such as OFETS.

6.5. References

30. Cote, A. P.; Benin, A. I.; Ockwig, N. W.; O'Keeffe, M.; Matzger, A. J.; Yaghi, O. M., *Science* **2005,** *310* (5751), 1166-1170.

32. Hall, D. G., *Boronic Acids*. Wiley-VCH: Weinheim, **2005**.

34. ndara, F.; Asano, A.; Furukawa, H.; Saeki, A.; Dey, S. K.; Liao, L.; Ambrogio, M. W.; Botros, Y. Y.; Duan, X.; Seki, S.; Stoddart, J. F.; Yaghi, O. M., *Chem. Mater.* **2011,** *23* (18), 4094-4097.

37. Cote, A. P.; El-Kaderi, H. M.; Furukawa, H.; Hunt, J. R.; Yaghi, O. M., *J. Am. Chem. Soc.* **2007,** *129* (43), 12914-12915.

53. Han, S. S.; Furukawa, H.; Yaghi, O. M.; Goddard, W. A., III, *J. Am. Chem. Soc.* **2008,** *130* (35), 11580-11581.

64. Ding, X.; Guo, J.; Feng, X.; Honsho, Y.; Guo, J.; Seki, S.; Maitarad, P.; Saeki, A.; Nagase, S.; Jiang, D., *Angew. Chem., Int. Ed.* ***2011,*** *50 (6), 1289-1293.*

76. Barriet, D.; Yam, C. M.; Shmakova, O. E.; Jamison, A. C.; Lee, T. R., *Langmuir* **2007,** *23* (17), 8866-8875.

84. Love, J. C.; Estroff, L. A.; Kriebel, J. K.; Nuzzo, R. G.; Whitesides, G. M., *Chem. Rev.* **2005,** *105* (4), 1103-1170.

86. Feng, S.; Bein, T., *Nature* **1994,** *368* (6474), 834-836.

87. Hermes, S.; Schröder, F.; Chelmowski, R.; Wöll, C.; Fischer, R. A., *J. Am. Chem. Soc.* **2005,** *127* (40), 13744-13745.

88. Biemmi, E.; Scherb, C.; Bein, T., *J. Am. Chem. Soc.* **2007,** *129* (26), 8054-8055.

89. Colson, J. W.; Woll, A. R.; Mukherjee, A.; Levendorf, M. P.; Spitler, E. L.; Shields, V. B.; Spencer, M. G.; Park, J.; Dichtel, W. R., *Science* **2011,** *332* (6026), 228-231.

146. Mann, S., *Nature* **1993,** *365* (6446), 499-505.

147. Addadi, L.; Weiner, S., *Angew.e Chem.* **1992,** *104* (2), 159-176.

148. Heinz Adolf Lowenstam, S. W., On biomineralization. Oxford University Press: **1989**.

149. Song, R.-Q.; Colfen, H., *CrystEngComm* **2011,** *13* (5), 1249-1276.

150. Aizenberg, J., *Adv. Mater.* **2004,** *16* (15), 1295-1302.

151. Allara, D. L.; Nuzzo, R. G., *Langmuir* **1985,** *1* (1), 52-66.

152. Aizenberg, J.; Black, A. J.; Whitesides, G. M., *J. Am. Chem. Soc.* **1999,** *121* (18), 4500-4509.

153. Hsu, J. W. P.; Tian, Z. R.; Simmons, N. C.; Matzke, C. M.; Voigt, J. A.; Liu, J., *Nano Lett.* **2004,** *5* (1), 83-86.

154. Addadi, L.; Raz, S.; Weiner, S., *Adv. Mater.* **2003,** *15* (12), 959-970.

155. Zacher, D.; Baunemann, A.; Hermes, S.; Fischer, R. A., *J. Mater. Chem.* **2007,** *17* (27), 2785-2792.

156. Kitagawa, S.; Matsuda, R., *Coord. Chem. Rev.* **2007,** *251* (21-24), 2490-2509.

157. Otero, R.; Gallego, J. M.; de Parga, A. L. V.; Martín, N.; Miranda, R., *Adv. Mater.* **2011**, n/a-n/a.

158. Kanayama, N.; Kitano, H., *Langmuir* **1999,** *16* (2), 577-583.

159. Morgan, A. B.; Jurs, J. L.; Tour, J. M., *J. Appl. Polym. Sci.* **2000,** *76* (8), 1257-1268.

160. Coutts, I. G. C.; Goldschmid, H. R.; Musgrave, O. C., *J. Chem.l Soc. C: Organic* **1970,** (3), 488-493.

7. Summary and Outlook

In this thesis project several synthetic strategies to functionalize Covalent Organic Frameworks have been investigated. Pore size tailoring, functionalization of the inner surface prior to synthesis and post-synthetically, and backbone modification aimed at assembling heterocyclic monomers of conducting polymers into a crystalline framework. Moreover, thin films of COFs were prepared by using organic functionalized surfaces that could induce direct growth parallel to the surface.

Developing controllable pathways for the precise functionalization of COFs, the concept of reticular chemistry was employed to expand the metrics of COFs to crystalline structures exhibiting extremely large pores. In chapter 3 a crystalline material with 4 nm open pores is described. Using microwave irradiation, the synthesis time was reduced from originally 72 h to 5 min. The very high surface areas of about 2000 m^2/g combined with the 4 nm open channels provide an ideal model system for further investigation of organic reactions inside the pores or host guest interactions, particularly with large molecules such as dyes or electroactive polymers.

These results prompted us to investigate further modification possibilities, particularly of the inner surface of the COFs. By assembling slightly modified organic linkers, the incorporation of small functionalities such as -methyl, -methoxy and -hydroxyl was possible. The introduction of a “small” organic moiety can not only change the framework properties (stability, hydrophobicity, pore size, catalysis, gas sorption) but also opens the way to post-synthetically connect a desired

molecule to the walls of the framework with precise control over amount and position of the functionality.

In chapter 4 we could demonstrate that the methyl groups of AT-COF-Me can be attacked with *N*-bromosuccinimide (NBS) in a radical bromination reaction without destroying the framework. The newly formed benzylic bromide in the pores might serve as a good leaving group in nucleophilic substitution reactions. This result is a proof of concept that post-synthetic modification reactions in COFs are possible. To extend this approach a series of isoreticular COFs based on a terphenyl diboronic acid (T-COF-H and T-COF-OH) with open pores of about 4 nm were successfully synthesized. T-COF-OH with hydroxyl-decorated large pores is an ideal platform for studying different esterification reactions aimed at attaching organic molecules with different sizes and functionalities to the framework. It was demonstrated that the crystalline structure of the COF is compatible with the reaction conditions for acetyl chloride based esterification reactions and for a 4-(dimethylamino)pyridine-catalyzed Steglich esterification reaction. The carboxylic ester bond formation was detected spectroscopically, however the porosity of the respective COFs decreased significantly upon functionalization. This observation is attributed to the presence of oligomers or other byproducts that were still present in the mesopores of the COF structure. Improved extraction methods are therefore required to fully recreate the inner surface of the functionalized materials.

In order to extend the backbone modification strategy, two monomers of well known semiconducting polymers, benzothiadiazole and thienothiophene, were equipped with diboronic acid moieties and successfully incorporated into COF framework structures. Assembling optoelectronically or electronically active organic linkers into COFs offers the possibility to create frameworks with attractive

properties already known from the building blocks. In chapter 5 the synthesis of a possible electron transporting benzothiadiazole COF (BTD-COF) is described, based on a two-step microwave synthesis procedure. First a pinacolboronate ester was cleaved and in a second step co-condensation with HHTP resulted in the crystalline product in only 60 min. Reacting a thienothiophene diboronic acid with HHTP led to the formation of a photoactive COF, namely TT-COF with a high surface area of 1800 m^2/g, 3 nm pore diameter and very high thermal stability. TT-COF exhibits a very broad optical absorption covering the whole visible spectrum and a fluorescence emission at 497 nm. The defined mesoporous structure offers enough space for the inclusion of an electron acceptor phase. It was shown that the electron accepting fullerene derivative $PCBM_{60}$ leads to a complete quenching of the fluorescence of TT-COF, indicating an electron transfer at the TT-COF/PCBM interface. Due to the broad light absorption and the significant photoconductivity TT-COF might be a suitable candidate for a hole-conducting framework in bulk heterojunction solar cells, OFETs or OLEDs. The performance of such devices is strongly dependent on the ordering of the organic crystals on a solid surface.

In the last chapter the concept of oriented direct growth of COF crystals on SAM functionalized substrates was demonstrated. Functionalizing a gold surface with mercaptophenylboronic acid induces the growth of TT-COF and COF-10 with pores parallel to the surface. The boronic acid end group covalently attached to the surface can interact with the polyols and thus initiate the growth of the framework in one orientation. These results open the door for aligning COF structures on different substrates customized for various applications. Not only the substrate can be varied, but also the length of the spacer of the SAM can be adjusted. In the future, the scope of substrates could be extended to silica or glass substrates using

silane SAMs, additionally enabling solvothermal reactions at temperatures above 100 °C, due to the high thermal stability of the silane SAMs. Additionally this concept to orient electroactive COFs with silane SAMs on silicon subsrates can be transferred to silicon based OFETs. The parallel alignment with the pi-system along the substrate can be beneficial for determination of charge carrier mobilities in thin film transistor measurements.

8. Appendix

8.1. Expansion to an open pore system of 5 nm: QP-COF

8.1.1. Introduction

Applying the idea of reticular chemistry in the COF synthesis to design and synthesize large open pore system would enable the creation of tunable nano-reactors for host-guest interactions with large molecules. Choosing organic aromatic linkers with large extensions in order to create large open pore systems could often result in very poor solubility, which creates difficult synthetic challenges.

Here we report the synthesis and characterization of a new mesoporous Covalent Organic Framework QP-COF, with pores having an open diameter of 5.0 nm. To the best of our knowledge, this is the largest open pore diameter of any crystalline material ever reported. The new QP-COF was synthesized under solvothermal conditions by co-condensation of quaterphenyldiboronic acid (QPBA) and the polyol HHTP (Figure 8.1).

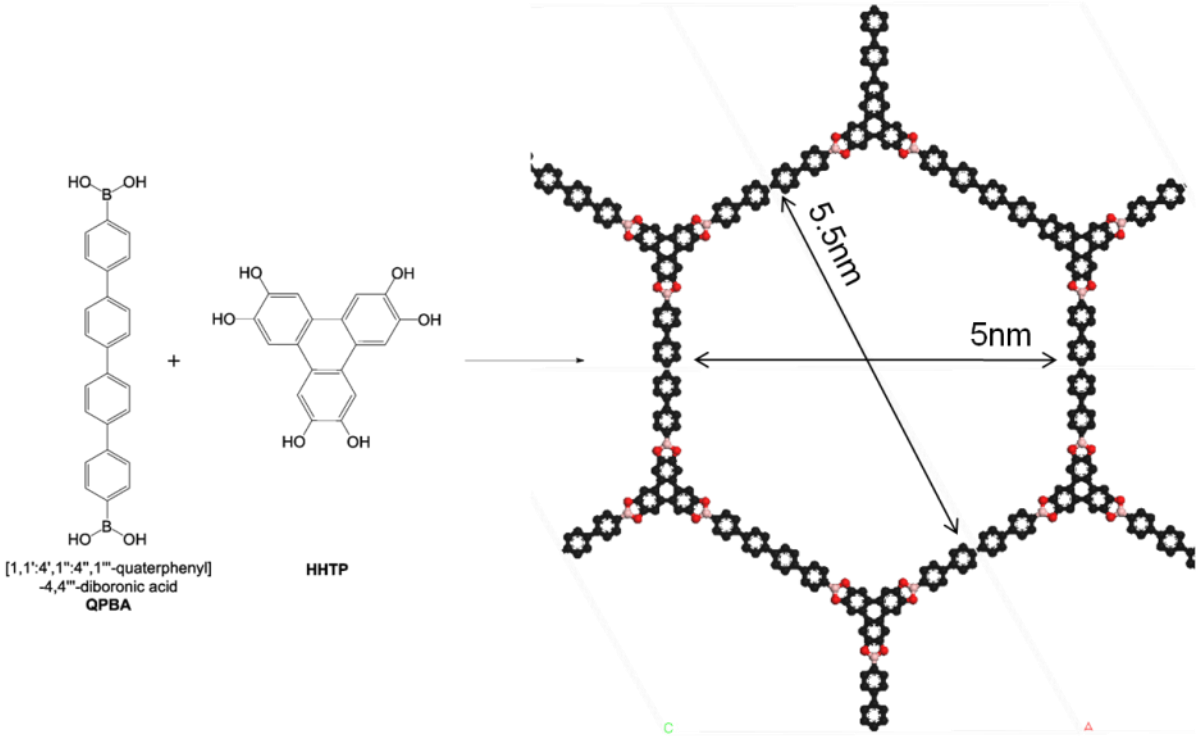

Figure 8.1: Reaction pathway for the synthesis of QP-COF with large open pores of around 5 nm.

8.1.2. Experimental

Materials and Methods

All materials (if not otherwise noted) were purchased from Aldrich or Fluka in the common purities purum and puriss. All materials were used without further purification. The building block hexahydroxytriphenylene was purchased from TCI Europe and the building block quaterphenyldiboronic acid was prepared in the group of Prof. Knochel.

X-ray diffraction analysis was carried out in reflection mode using a Bruker D8 Discover with Ni-filtered CuKα-radiation (1.5406 Å) and a position-sensitive detector (Vantec).

Synthesis of QPBA

A 250 ml round-bottom flask, equipped with a magnetic stirring bar was charged with magnesium turnings (0.12 g, 5.0 mmol, 1.0 equiv.) and lithium chloride (0.21 g, 5.0 mmol, 90 %, 1.0 equiv). The reactants were dried under vacuum at 250 °C for 20 min. The mixture was cooled under argon atmosphere. Subsequently 5 ml of anhydrous tetrahydrofuran was added. Activation of magnesium was achieved by vigorous stirring of the mixture at room temperature for one hour. Afterwards (4-bromophenyl)trimethylsilane (1.25 g, 5.48 mmol, 1.0 equiv) was added dropwise. After 5 minutes, an exothermic reaction set in. The solution was stirred for another hour and added dropwise to a ice bath-cooled 1M solution of zinc (II) chloride (2.5 ml, 0.5 equiv.) and 0.25 ml (10 %) *N*-methyl-2-pyrrolidone (NMP).

In a 250 ml round-bottomed flask bis(di-*tert*-butyl(4-dimethylaminophenyl)phosphine)dichloropalladium(II) (5 mg, 0.007 mmol) and 1, 4-dibromobenzene (0.624 g, 2.0 mmol, 0.4 equiv.) were dissolved in tetrahydrofuran (20 ml). This mixture was added dropwise to the zinc compound. The suspension was quenched with 50 ml of a saturated ammonium chloride solution. 30 ml diethyl ether was added and the mixture was extracted four times with 30 ml of water. Subsequently the white solid was filtered and dried *in vacuuo* for 16 h (0.56 g, 1.3 mmol, 65 %).

[1,1';4',1'']terphenyl-4,4''-di-trimethylsilane (0.56 g, 1.3 mmol, 1.0 equiv) was dissolved in 25 ml dichloromethane. Subsequently boron tribromide (0.715 g, 2.86 mmol, 2.2 equiv) was added and the reaction mixture was stirred at room temperature for 24 h. The white suspension was poured on ice (250 g) and stirred until the ice was completely molten. Dichloromethane was removed on the rotary evaporator and the product was filtered. Recrystallization in water yielded a white powder (0.38 g, 0.96 mmol, 74 %)

Synthesis optimization with High-Throughput Methods

High-Throughput methods allowed us to find the optimal reaction conditions for the QP-COF formation in a fast and efficient manner.[117] In Table 1 we present the list of different solvent mixtures and stoichiometric ratios. Successful network formation was only observed with the highlighted reaction parameters. Green highlights describe reaction parameters resulting in very crystalline framework structures, yellow highlights describe a starting crystallization of the framework with high amorphous amounts and non-highlighted parameters did not result in any framework structure.

Table 8.1: Overview of the tested reaction parameters for the synthesis of QP-COF.

Experiment	QPBA HHTP Molar ratio	Solvent1	Solvent2	Ratio	Time	Temp.	Vol.
MD276	3:2	Mesitylene	Dioxane	50:50	72h	150°C	1.0ml
MD278_1	3:2	Anisole	MeOH	90:10	20min	150°C	1.0ml
MD278_2	3:2	Anisole	MeOH	90:10	72h	150°C	1.0ml

MD288_1	3:2	Anisole	MeOH	90:10	20min	150°C	1.0ml
MD288_2	3:2	Anisole	MeOH	90:10	5min	150°C	1.0ml
MD288_3	3:2	Anisole	MeOH	90:10	20min	150°C	0.5ml
MD288_4	3:2	Anisole	MeOH	90:10	5min	150°C	0.5ml
MD283_3	3:2	Mesitylene	Dioxane	50:50	120h	100°C	1.0ml
MD283_5	3:2	Mesitylene	Dioxane	50:50	120h	150°C	1.0ml
MD283_6	3:2	Anisole	MeOH	90:10	120h	100°C	1.0ml
MD283_14	3:2	Anisole	MeOH	90:10	120h	150°C	1.0ml
MD286_6	3:2	Mesitylene	Dioxane	50:50	72h	150°C	1.0ml
MD286_14	3:2	Mesitylene	Dioxane	50:50	72h	150°C	1.0ml
MD289_1	3:2	Mesitylene	Dioxane	50:50	72h	150°C	0.5ml
MD289_2	3:2	Mesitylene	Dioxane	50:50	72h	150°C	1.0ml
MD289_3	3:2	Mesitylene	Dioxane	50:50	72h	150°C	1.5ml
MD289_4	3:3	Mesitylene	Dioxane	50:50	72h	150°C	1.0ml
MD289_5	2:1	Mesitylene	Dioxane	50:50	72h	150°C	1.0ml
MD289_6	3:0	Mesitylene	Dioxane	50:50	72h	150°C	1.0ml
MD289_7	3:2	Anisole	MeOH	95:5	72h	150°C	1.0ml
MD289_8	3:2	Mesitylene	Dioxane	90:10	72h	150°C	1.0ml
MD289_9	3:2	Mesitylene	Dioxane	85:15	72h	150°C	1.0ml
MD289_10	3:2	Mesitylene	Dioxane	80:20	72h	150°C	1.0ml
MD289_11	3:2	Mesitylene	Dioxane	100:0	72h	150°C	1.0ml
MD289_12	3:2	THF	MeOH	90:10	72h	150°C	1.0ml
MD293_1	3:0	Mesitylene	Dioxane	50:50	72h	150°C	1.0ml
MD293_2	3:2	Mesitylene	Dioxane	50:50	72h	150°C	1.4ml
MD293_3	3:2	Mesitylene	Dioxane	50:50	72h	150°C	1.4ml
MD297_1	1:1	Mesitylene	Dioxane	50:50	72h	150°C	1.5ml

MD297_2	2:3	Mesitylene	Dioxane	50:50	72h	150°C	1.5ml
MD321_1	3:2	Toluene	MeOH	95:05	72h	150°C	1.0ml
MD321_2	3:2	Toluene	MeOH	90:10	72h	150°C	1.0ml
MD321_3	3:2	Toluene	MeOH	85:15	72h	150°C	1.0ml
MD321_4	2:1	Toluene	MeOH	95:05	72h	150°C	1.0ml
MD321_5	2:1	Toluene	MeOH	90:10	72h	150°C	1.0ml
MD321_6	2:1	Toluene	MeOH	85:15	72h	150°C	1.0ml
MD321_7	3:2	Toluene	Acetone	95:05	72h	150°C	1.0ml
MD321_8	3:2	Toluene	Acetone	90:10	72h	150°C	1.0ml
MD321_9	3:2	Toluene	Acetone	85:15	72h	150°C	1.0ml
MD321_10	2:1	Toluene	Acetone	95:05	72h	150°C	1.0ml
MD321_11	2:1	Toluene	Acetone	90:10	72h	150°C	1.0ml
MD321_12	2:1	Toluene	Acetone	85:15	72h	150°C	1.0ml

8.1.3. Results and Discussion

Powder X-ray diffraction (PXRD) confirms the formation of a highly crystalline Covalent Organic Framework. In order to identify the new phase, possible structures were modelled with MS Studio.[119] Based on the calculated structures, the corresponding powder patterns were simulated and compared to the experimentally obtained data. As reported for previous COF structures, the potential stacking types of the hexagonal planar sheets were calculated.[30] In principle two distinct arrangements are viewed as most likely: (1) AA arrangement with adjacent sheets packed directly on top of each other or (2) AB arrangement, like in graphite with a staggered packing of the hexagonal sheets. The PXRD patterns for eclipsed and

staggered conformation were simulated and compared to the experimentally obtained data. As can be concluded from Figure 8.2, it is possible to crystallize QP-COF, however, comparison of the PXRD of the QP-COF (MD286_14) with the starting material QPBA shows a high content of starting material in the product. The additional high amorphous background makes it difficult to assign a eclipsed or staggered arrangement of the lattice. As mentioned above, extending the organic aromatic linkers to enlarge the topology and pore size is accompanied with a severe solubility loss. Extraction of the product with different solvents or at elevated temperatures under vacuum is not enough to eliminate the insoluble QPBA.

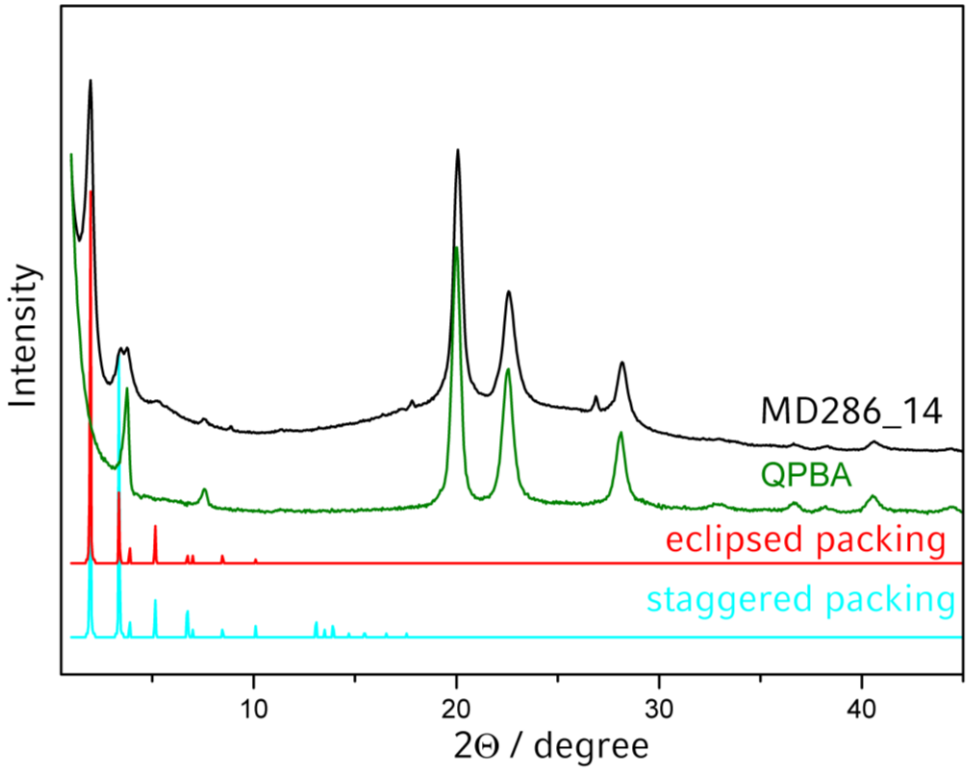

Figure 8.2: PXRD pattern of the experimentally observed QP-COF (MD286_14, in black) compared to the starting material QPBA (green) and the simulated patterns in an eclipsed (red) and staggered (cyan) conformation.

8.1.4. Conclusion

As indicated by the powder diffraction pattern the synthesis of a new mesostructured crystalline material with a large unit cell using the concept of reticular chemistry can be realized. However, the extraction of the starting material quaterphenyldiboronic acid was not successful yet. This once more shows the urgent need for a general efficient extraction procedure for COFs.

8.2. Prior to Synthesis modification of COFs

8.2.1. Decorating the Pores of AT-COF

As described in chapter 4, decoration of the inner surface of Covalent Organic Frameworks with functional moieties was carried out following a prior-to-synthesis approach. During this thesis several modified linkers were tested in the co-condensation reactions of COF-OMe, AT-COF and T-COF-H (Figure 8.3). The successful synthesis of an ortho-dimethoxy functionalized benzene diboronic acid is reported in my Diploma thesis: Pore Modification of Covalent Organic Frameworks.

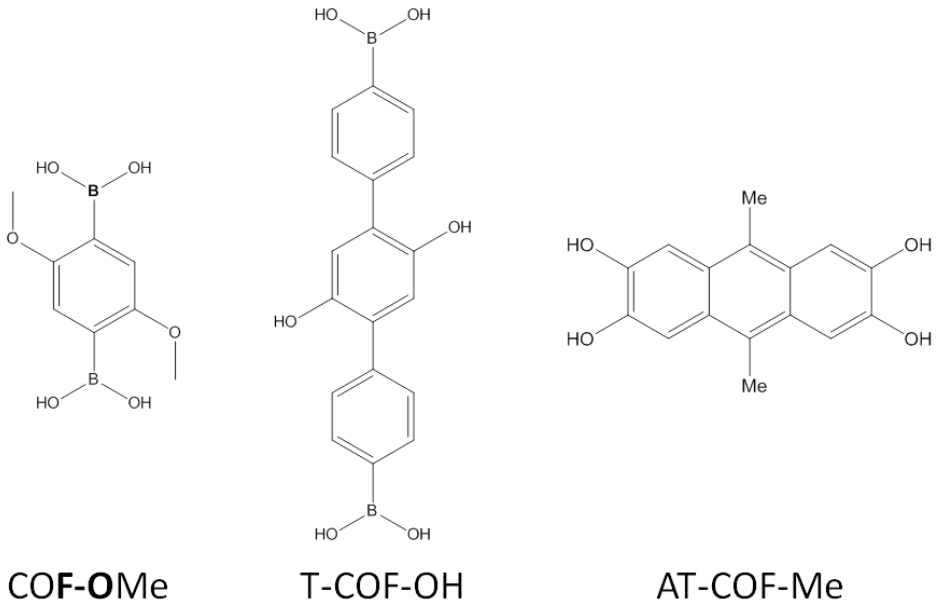

Figure 8.3: Modified linkers resulting in prior to synthesis functionalized COFs.

The co-condensation of a 9,10-dimethylanthracene tetraol with a triboronic acid results in a hexagonal crystalline framework with 2.3 nm open pores, as shown in chapter 4. In the following several strategies for a co-condensation of amino-functionalized tetrahydroxyanthracene linkers with triboronic acid are shown, however, for neither of the following linkers framework formation we observed.

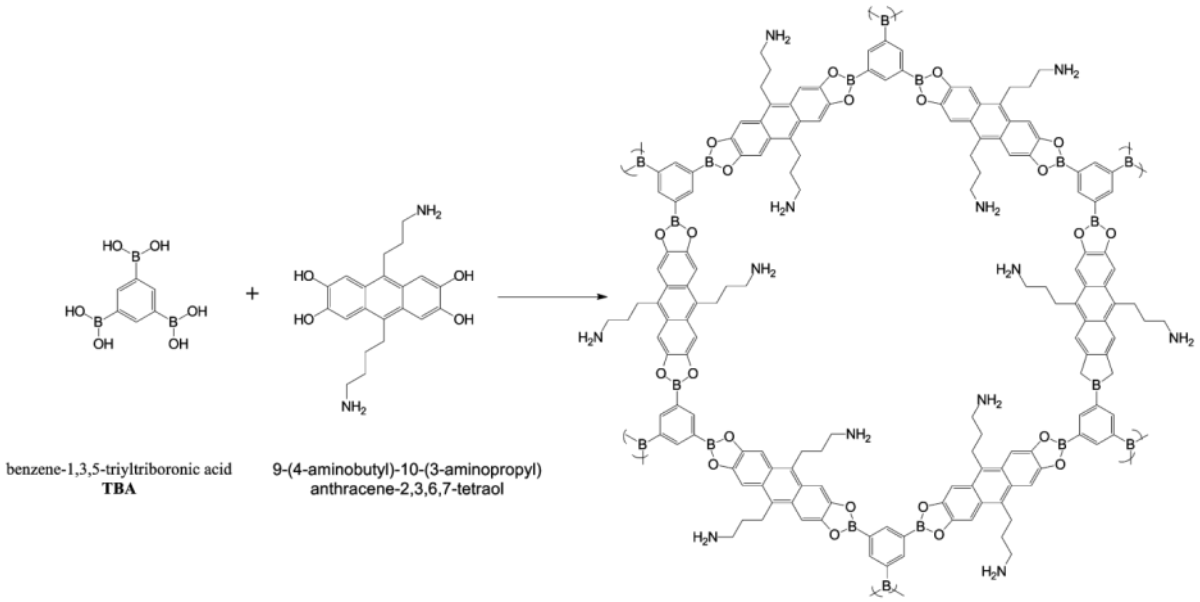

Figure 8.3: Reaction pathway for the synthesis of AT-COF-NH_2.

Experiment	Solvent1	Solvent2	Ratio	Time	Temp.	Volume	Additive
MD108_1	Anisole	MeOH	90:10	20min	120°C	1.5ml	
MD108_2	Anisole	Acetone	90:10	20min	120°C	1.5ml	
MD108_3	Anisole	Dioxane	50:50	20min	120°C	1.5ml	
MD108_4	Mesitylene	Dioxane	50:50	20min	120°C	1.5ml	
MD109_5	Mesitylene	Dioxane	50:50	20min	80°C	1.7ml	
MD109_6	Mesitylene	Dioxane	50:50	20min	100°C	1.7ml	
MD109_7	Mesitylene	Dioxane	50:50	20min	150°C	1.7ml	
MD109_8	Toluene	Dioxane	50:50	20min	80°C	1.7ml	
MD109_9	Toluene	Dioxane	50:50	20min	100°C	1.7ml	
MD109_10	Toluene	Dioxane	50:50	20min	120°C	1.7ml	
MD109_11	Toluene	Dioxane	50:50	20min	150°C	1.7ml	
MD111_1	Anisole	MeOH	95:05	72h	100°C	2.0ml	
MD111_2	Anisole	MeOH	95:05	72h	150°C	1.5ml	
MD113_1	Anisole	EtOH	98:02	20min	120°	1.7ml	
MD113_2	Anisole	EtOH	90:10	20min	120°	1.7ml	
MD113_3	Mesitylene	EtOH	90:10	20min	120°	1.7ml	
MD113_4	Mesitylene	EtOH	98:02	20min	120°	1.7ml	
MD113_5	THF	MeOH	95:05	20min	70°C	1.7ml	
MD113_6	THF	MeOH	95:05	20min	70°C	1.7ml	
MD113_7	DMF			20min	150°C	1.7ml	
MD113_8	DMF	Mesitylene	50:50	20min	150°C	1.7ml	
MD113_9	DMF	Anisole	50:50	20min	150°C	1.7ml	
MD113_10	Mesitylene	Dioxane	50:50	20min	85°C	1.7ml	
MD115_1	Anisole	Acetone	99:01	20min	120°	1.7ml	
MD115_2	Anisole	Acetone	98:02	20min	120°	1.7ml	

MD115_3	Anisole	Acetone	95:05	20min	120°	1.7ml	
MD115_4	DMF	Dioxane	50:50	20min	120°C	1.7ml	
MD115_5	THF	MeOH	99:01	20min	70°C	1.7ml	
MD115_6	THF	MeOH	98:02	20min	70°C	1.7ml	
MD115_7	THF	MeOH	90:10	20min	70°C	1.7ml	
MD115_8	THF	MeOH	95:05	20min	80°C	1.7ml	
MD120_1	DMF	MeOH	98:02	20min	150°C	1.5ml	
MD120_2	DMF	MeOH	95:05	20min	150°C	1.5ml	
MD120_3	DMF	MeOH	90:10	20min	150°C	1.5ml	
MD120_4	DCM			20min	35°C	1.5ml	
MD123_1	Anisole	MeOH	98:02	10min	100°	1.5ml	
MD123_2	Anisole	MeOH	98:02	10min	120°	1.5ml	
MD123_3	Anisole	MeOH	98:02	10min	150°	1.5ml	
MD123_4	Anisole	MeOH	95:05	20min	100°	1.5ml	
MD123_5	Anisole	MeOH	95:05	20min	120°	1.5ml	
MD123_6	Anisole	MeOH	95:05	20min	150°	1.5ml	
MD123_7	Anisole	MeOH	90:10	20min	100°	1.5ml	molec sieve
MD123_8	Anisole	MeOH	90:10	20min	120°	1.5ml	
MD123_9	Anisole	MeOH	90:10	20min	150°	1.5ml	
MD123_10	Anisole	MeOH	95:05	20min	120°	1.5ml	225µl HCl (1M)
MD124_1	Pentane	MeOH	98:02	20min	45°	1.5ml	
MD124_2	Pentane	MeOH	95:05	20min	45°	1.5ml	
MD124_3	Pentane	MeOH	90:10	20min	45°	1.5ml	
MD129_1	Anisole	MeOH	95:05	20min	120°	1.5ml	2µl HCl (conc.)
MD129_2	Anisole	MeOH	95:05	20min	120°	1.5ml	5µl HCl (conc.)
MD129_3	Anisole	MeOH	95:05	20min	120°	1.5ml	8µl HCl (conc.)
MD135_1	Anisole	MeOH	95:05	20min	120°	1.5ml	0.4mmol H_2SO_4 (1M)
MD135_2	Anisole	MeOH	95:05	20min	120°	1.5ml	0.8mmol H_2SO_4 (1M)
MD135_3	Anisole	MeOH	95:05	20min	120°	1.5ml	0.2mmol H_2SO_4 (1M)
MD145_5	Mesitylene	Dioxane	50:50	72h	100°C	2.0ml	80µl $HClO_4$
MD145_6	Anisole	MeOH	90:10	72h	150°C	2.0ml	80µl $HClO_4$
MD148_1	Anisole	MeOH	95:05	20min	100°C	1.0ml	4% HCl (conc.)
MD148_2	Anisole	MeOH	90:10	20min	100°C	1.0ml	4% HCl (conc.)
MD148_3	Anisole	MeOH	95:05	20min	120°C	1.0ml	4% HCl (conc.)
MD148_4	Anisole	MeOH	90:10	20min	120°C	1.0ml	4% HCl (conc.)
MD148_5	Anisole	MeOH	95:05	20min	150°C	1.0ml	4% HCl (conc.)
MD148_6	Anisole	MeOH	90:10	20min	150°C	1.0ml	4% HCl (conc.)

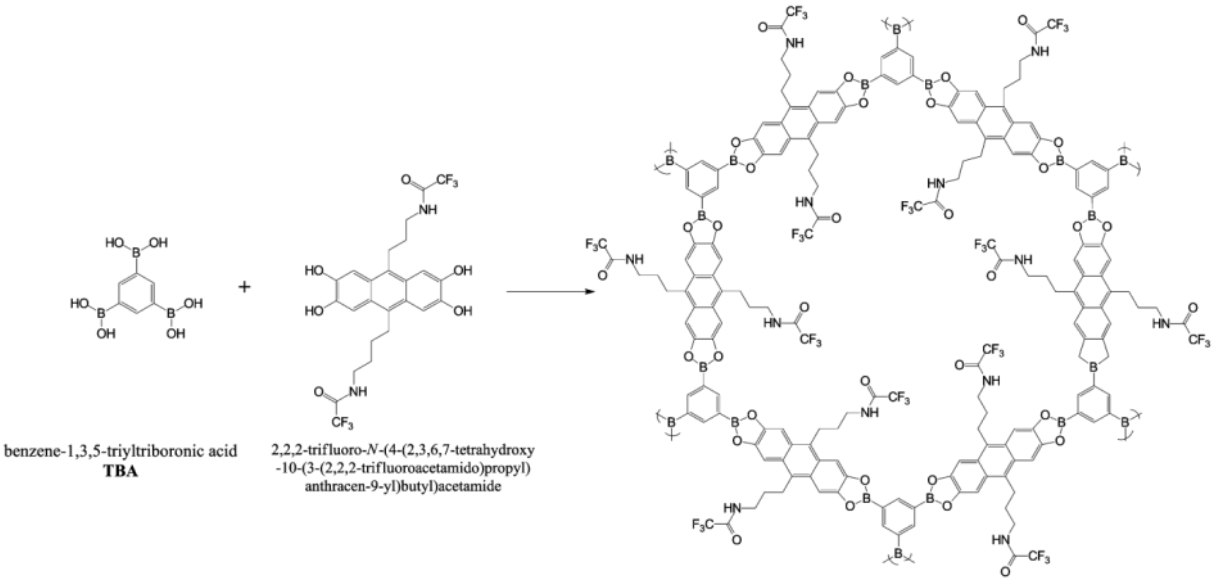

Figure 8.4: Reaction pathway for the synthesis of a trifluoroacetamide functionalized AT-COF.

Experiment	TBA: AT-CF_3	Solvent1	Solvent2	Ratio	Time	Temperature	Volume
HT_MD150							
A1	1:2.3	Mesitylene	Dioxane	50:50	72h	150°C	1.5ml
A2	1:2	Mesitylene	Dioxane	50:50	72h	150°C	1.5ml
A3	1:1	Mesitylene	Dioxane	50:50	72h	150°C	1.5ml
A4	1:2.3	Anisole	Dioxane	50:50	72h	150°C	1.5ml
A5	1:2	Anisole	Dioxane	50:50	72h	150°C	1.5ml
A6	1:1	Anisole	Dioxane	50:50	72h	150°C	1.5ml
B1	1:2	Anisole	MeOH	98:02	72h	150°C	1.5ml
B2	1:2	Anisole	MeOH	95:05	72h	150°C	1.5ml
B3	1:2	Anisole	MeOH	90:10	72h	150°C	1.5ml
B4	1:2	Anisole	Acetone	98:02	72h	150°C	1.5ml
B5	1:2	Anisole	Acetone	95:05	72h	150°C	1.5ml
B6	1:2	Anisole	Acetone	90:10	72h	150°C	1.5ml

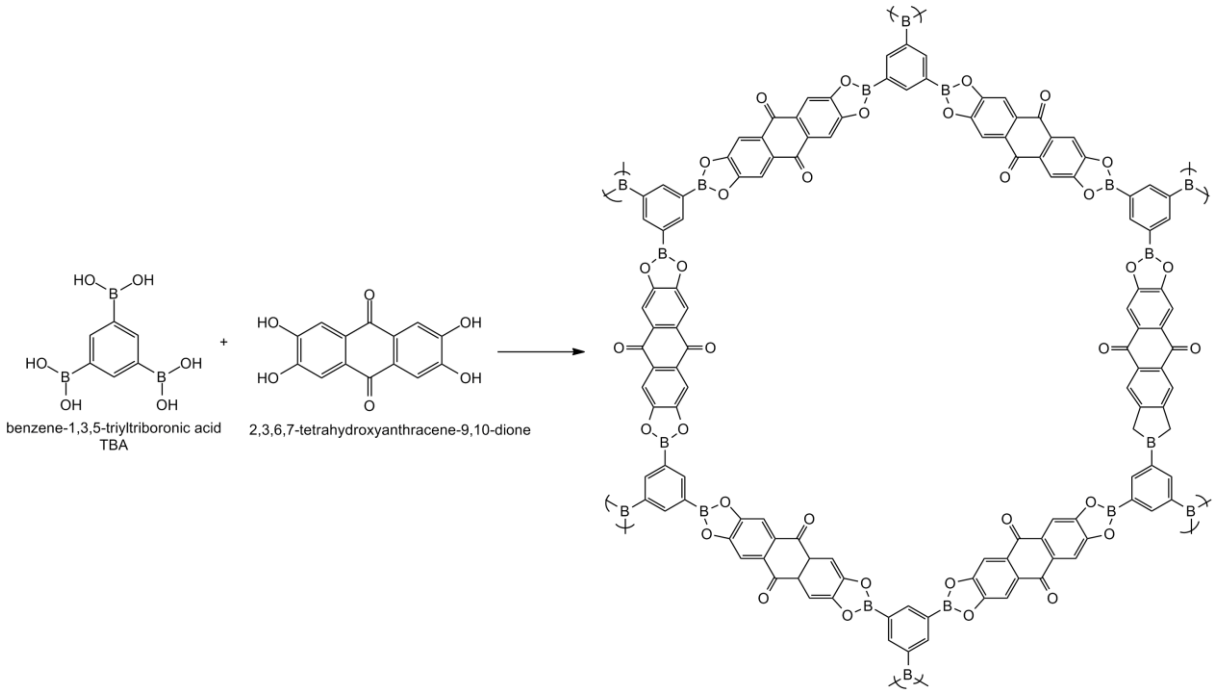

Figure 8.5: Synthesis for a chinone functionalized AT-COF.

Table 8.2: List of conducted experiments for a modified AT-COF.

Experiment	TBA: AT-ON	Solvent1	Solvent2	Ratio	Time	Temp.	Volume
HT_MD150							
D1	1:2	Mesitylene	Dioxane	50:50	72h	100°C	1.5ml
D2	1:2	Anisole	Dioxane	50:50	72h	100°C	1.5ml
D3	1:2	Anisole	MeOH	98:02	72h	100°C	1.5ml
D4	1:2	Anisole	MeOH	95:05	72h	100°C	1.5ml
D5	1:2	Anisole	MeOH	90:10	72h	100°C	1.5ml
D6	1:2	Anisole	MeOH	80:20	72h	100°C	1.5ml
HT_MD151							
C1	1:2.3	Mesitylene	Dioxane	50:50	72h	100°C	1.0ml
C2	1:2.3	Mesitylene	Dioxane	50:50	72h	100°C	1.0ml
C3	1:2.3	Anisole	Dioxane	50:50	72h	100°C	1.0ml
C4	1:2.3	Anisole	Dioxane	50:50	72h	100°C	1.0ml
C5	1:2.3	Toluene	Dioxane	50:50	72h	100°C	1.0ml
C6	1:2.3	Toluene	Dioxane	50:50	72h	100°C	1.0ml
D1	1:2.3	THF	MeOH	99:01	72h	100°C	1.0ml
D2	1:2.3	THF	MeOH	98:02	72h	100°C	1.0ml
D3	1:2.3	THF	MeOH	95:05	72h	100°C	1.0ml
D4	1:2.3	Anisole	MeOH	99:01	72h	100°C	1.0ml
D5	1:2.3	Anisole	MeOH	98:02	72h	100°C	1.0ml
D6	1:2.3	Anisole	MeOH	95:05	72h	100°C	1.0ml
MD152_3	1:2.3	Mesitylene	Dioxane	50:50	72h	150°C	2.0ml

MD152_5	1:2.3	Anisole	Dioxane	50:50	72h	150°C	2.0ml
MD152_6	1:2.3	Anisole	MeOH	99:01	72h	150°C	2.0ml
MD152_14	1:2.3	Anisole	MeOH	95:05	72h	150°C	2.0ml
MD154_1	1:2.3	Anisole	MeOH	98:02	20min	100°C	2.0ml
MD154_2	1:2.3	Anisole	MeOH	95:05	20min	100°C	2.0ml
MD159_1	1:2	Anisole	MeOH	95:05	72h	150°C	1.5ml
MD159_2	1:2	Anisole	MeOH	90:10	72h	150°C	1.5ml
MD159_3	1:2	Anisole	Dioxane	50:50	72h	150°C	1.5ml
MD159_4	1:2	THF	MeOH	95:05	72h	100°C	1.5ml
MD159_5	1:2	THF	MeOH	90:10	72h	100°C	1.5ml
MD163_1	1:2	Anisole	MeOH	95:05	72h	150°C	1.5ml
MD163_2	1:2	Anisole	MeOH	95:05	72h	150°C	1.5ml
MD163_3	1:2	Anisole	Dioxane	50:50	72h	150°C	1.5ml
MD163_4	1:2	Anisole	Dioxane	50:50	72h	150°C	1.5ml

One reason why we couldn't obtain a COF for the above shown linkers can be sterical hinderence of the pi-stack, due to big organic moieties hanging into the pore. To prevent sterical interference, a dilution with the methyl functionalized anthracene was carried out. The molar ratio of TBA and anthracene linker of 1 : 2.3 was kept constant and the ratio of methyl and chinone substituted tetrahydroxyanthracene was varied as followed (see Table 8.3). However in none of the reactions a crystalline COF was observed.

Table 8.3: Dilution with DMTHA linker

Experiment	Me: $NHCF_3$	Solvent1	Solvent2	Ratio	Time	Temp.	Volume
MD172_1	3:1	Anisole	MeOH	95:5	72h	150°C	1.7ml
MD172_2	1:1	Anisole	MeOH	95:5	72h	150°C	1.7ml
HT_MD175							
A1	1:1	Anisole	MeOH	95:5	72h	150°C	1.2ml
A2	2:1	Anisole	MeOH	95:5	72h	150°C	1.2ml
A3	3:1	Anisole	MeOH	95:5	72h	150°C	1.2ml
A4	1:1	Anisole	MeOH	95:5	72h	150°C	1.2ml
A5	2:1	Anisole	MeOH	95:5	72h	150°C	1.2ml
A6	3:1	Anisole	MeOH	95:5	72h	150°C	1.2ml

B1	1:1	Anisole	MeOH	98:02	72h	150°C	1.2ml
B2	2:1	Anisole	MeOH	98:02	72h	150°C	1.2ml
B3	3:1	Anisole	MeOH	98:02	72h	150°C	1.2ml
B4	1:1	Anisole	MeOH	90:10	72h	150°C	1.2ml
B5	2:1	Anisole	MeOH	90:10	72h	150°C	1.2ml
B6	3:1	Anisole	MeOH	90:10	72h	150°C	1.2ml
C1	1:1	Anisole	Acetone	98:02	72h	150°C	1.2ml
C2	2:1	Anisole	Acetone	98:02	72h	150°C	1.2ml
C3	3:1	Anisole	Acetone	98:02	72h	150°C	1.2ml
C4	1:1	Anisole	Acetone	95:05	72h	150°C	1.2ml
C5	2:1	Anisole	Acetone	95:05	72h	150°C	1.2ml
C6	3:1	Anisole	Acetone	95:05	72h	150°C	1.2ml
D1	1:1	Mesitylene	Dioxane	50:50	72h	150°C	1.2ml
D2	2:1	Mesitylene	Dioxane	50:50	72h	150°C	1.2ml
D3	3:1	Mesitylene	Dioxane	50:50	72h	150°C	1.2ml
D4	1:1	Anisole	Dioxane	50:50	72h	150°C	1.2ml
D5	2:1	Anisole	Dioxane	50:50	72h	150°C	1.2ml
D6	3:1	Anisole	Dioxane	50:50	72h	150°C	1.2ml

8.2.2. Decorating the Pores of T-COF:

The successful synthesis of a dihydroxy functionalized terphenyl diboronic acid is shown in chapter 4. Furthermore a terphenyl boronic acid with an attached carboxylic acid was tested. However up to now no framework formation was observed.

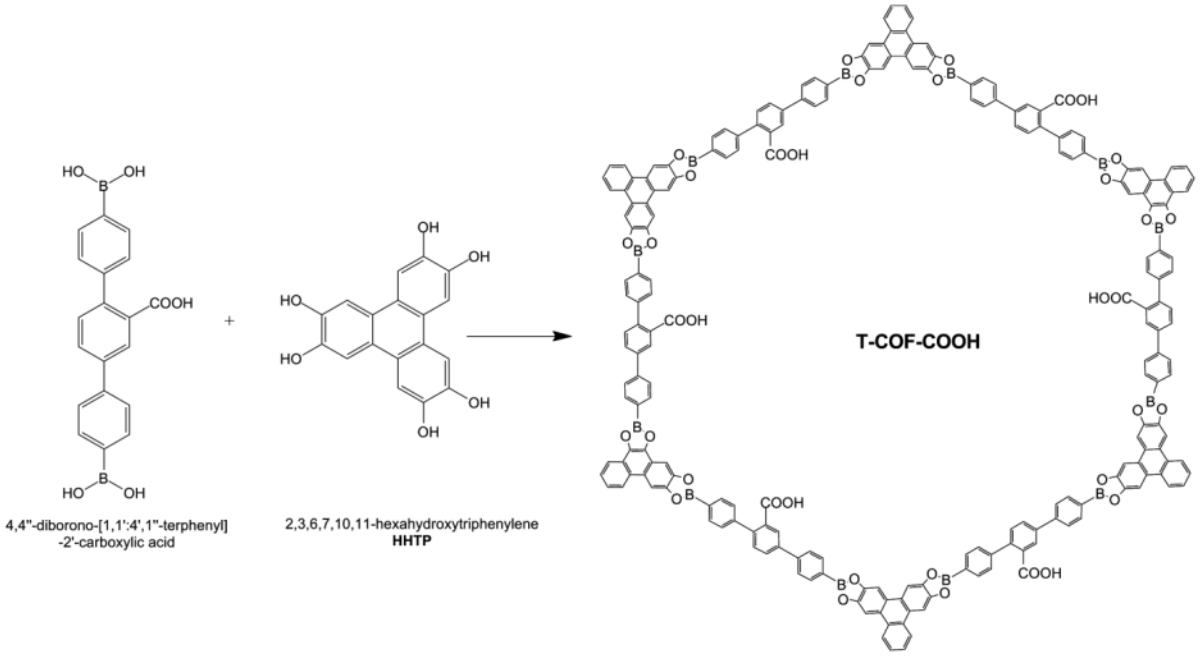

Figure 8.6: Illustration of the reaction pathway for T-COF-COOH.

Table 8.4: Conducted experiments with tested parameters for T-COF-COOH synthesis.

Experiment	CTBA HHTP	Solvent1	Solvent2	Ratio	Time	Temp.	Volume
MD330_1	3:2	Mesitylene	Dioxane	50:50	72h	150°C	1.5ml
MD330_2	3:2	Anisole	Dioxane	50:50	72h	150°C	1.5ml
MD330_3	3:2	Anisole	MeOH	95:05	72h	150°C	1.5ml
MD335_1	3:2	Mesitylene	Dioxane	50:50	72h	150°C	1.0ml
MD335_2	2:1	Mesitylene	Dioxane	50:50	72h	150°C	1.0ml
MD335_3	3:2	Anisole	Dioxane	50:50	72h	150°C	1.0ml
MD335_4	2:1	Anisole	Dioxane	50:50	72h	150°C	1.0ml
MD335_5	3:2	Toluene	Dioxane	50:50	72h	150°C	1.0ml
MD335_6	2:1	Toluene	Dioxane	50:50	72h	150°C	1.0ml
MD335_7	3:2	Anisole	MeOH	95:05	72h	150°C	1.0ml
MD335_8	3:2	Anisole	MeOH	90:10	72h	150°C	1.0ml
MD335_9	3:2	Anisole	MeOH	85:15	72h	150°C	1.0ml
MD335_10	3:2	Anisole	Acetone	95:05	72h	150°C	1.0ml
MD335_11	3:2	Anisole	Acetone	90:10	72h	150°C	1.0ml
MD335_12	3:2	Anisole	Acetone	85:15	72h	150°C	1.0ml
MD335_13	3:2	Toluene	MeOH	95:05	72h	150°C	1.0ml
MD335_14	3:2	Toluene	MeOH	90:10	72h	150°C	1.0ml
MD335_15	3:2	Toluene	MeOH	85:15	72h	150°C	1.0ml

MD335_16	3:2	Toluene	Acetone	95:05	72h	150°C	1.0ml
MD335_17	3:2	Toluene	Acetone	90:10	72h	150°C	1.0ml
MD335_18	3:2	Toluene	Acetone	85:15	72h	150°C	1.0ml
MD335_19	3:2	Toluene	MeOH	50:50	72h	150°C	1.0ml
MD335_20	3:2	Anisole	MeOH	50:50	72h	150°C	1.0ml
MD335_21	3:2	Mesitylene	MeOH	50:50	72h	150°C	1.0ml
MD335_22	3:2	Mesitylene	Acetone	95:05	72h	150°C	1.0ml
MD335_23	3:2	Mesitylene	Acetone	90:10	72h	150°C	1.0ml
MD335_24	3:2	Mesitylene	Acetone	85:15	72h	150°C	1.0ml
MD336_1	3:2	Toluene	MeOH	98:02	72h	150°C	2.0ml
MD336_2	3:2	Toluene	MeOH	98:02	72h	150°C	2.0ml
MD336_3	3:2	Toluene	Isoprop	95:05	72h	150°C	2.0ml
MD336_4	3:2	Toluene	THF	50:50	72h	150°C	2.0ml
MD339_1	3:2	Toluene	Acetone	99:01	72h	150°C	1.0ml
MD339_2	3:2	Toluene	Acetone	98:02	72h	150°C	1.0ml
MD339_3	3:2	Toluene	Acetone	95:05	72h	150°C	1.0ml

8.3. Post-Modification of T-COF-OH with FITC

It is well known from the polyurethane synthesis that isocyanate or isothiocyanate react easily with alcohols to form urethane or thiourethane (Figure 8.7).

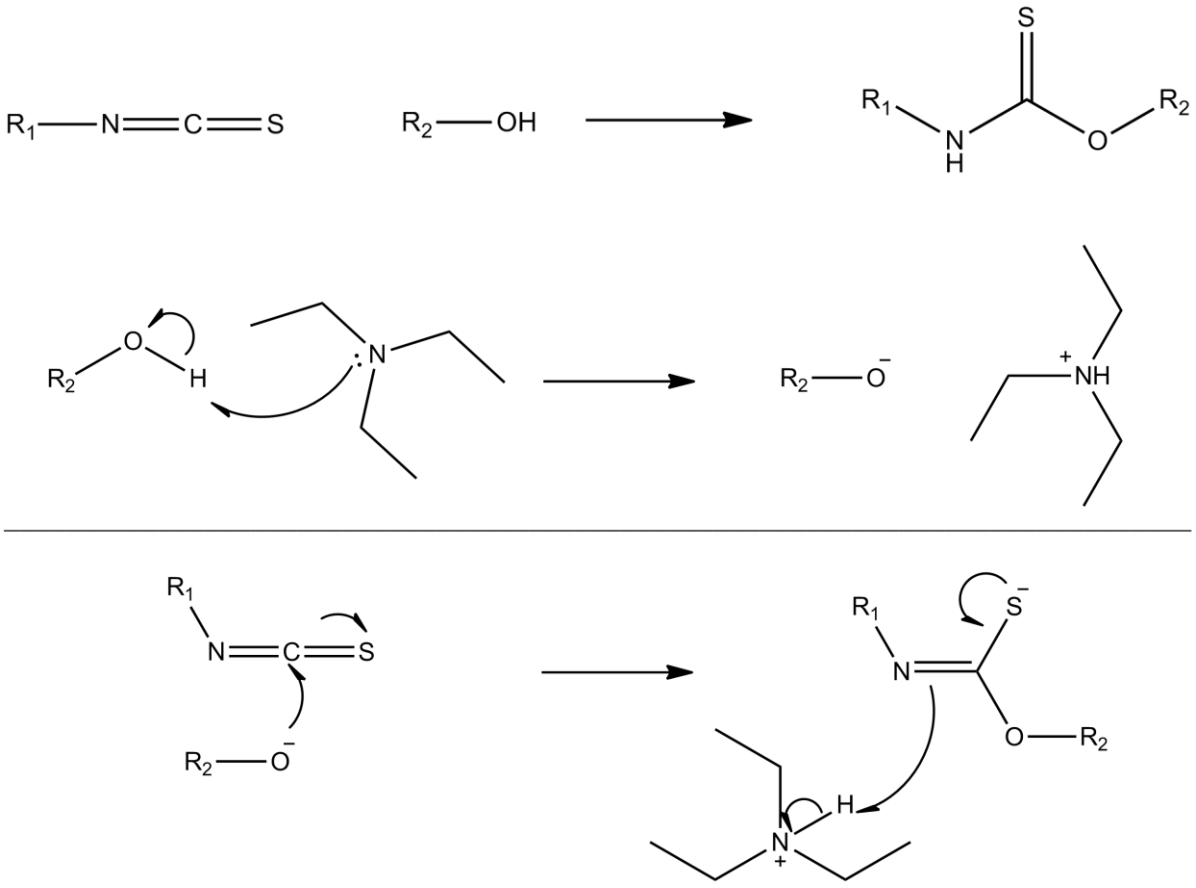

Figure 8.7: General reaction mechanism of isothiocyante with alcohol to thiourethane.

The carbon atom of the isothiocyanate moiety is (due to the electronegative nitrogen and sulfur) easily attacked by the nucleophilic oxygen of the alcohol. The reaction was carried out with fluorescein-isothiocyanate (FITC) and T-COF-OH. Labeling of porous solids with fluorescent dyes is a common procedure in materials chemistry. Using FITC as a functionalization reagent facilitates the characterization and broadens the spectrum of possible applications. The reaction conditions are

very mild, the used solvent is not harming the COFs, and reactions can be conducted at room temperature. A drawback of this reaction is the initial deprotonation of the hydroxyl group with a base, the base can also cleave the boronate ester and hence destroy the framework. Therefore the amount of base was kept as low as possible and a very sterically hindered base was examined in the reaction. With 10 % v. of triethylamine almost no degradation of the COF occurs and the crystallinity is preserved. The powder pattern of the T-COF-OFITC (Figure 8.8) agrees very well with a simulated powder pattern in which every third OH group was labeled with FITC and the calculations with the module Reflex were performed in P1 symmetry. The intensities of the 110 and 210 reflections increase and the 001 reflection shifts, due to bigger unit cell dimensions in c, from 26 to 25° 2θ. Unfortunately the amorphous background also increases after the functionalization with FITC, indicating either degradation of T-COF-OH by the added base or a lower x-ray contrast due to the FITC in the pores.

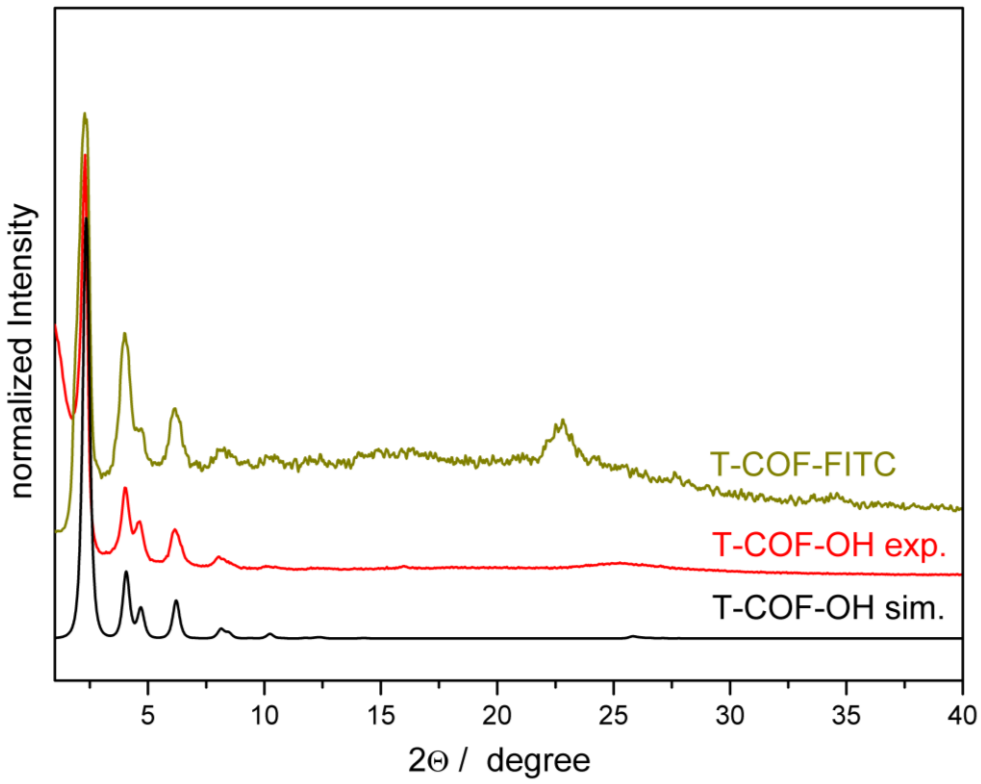

Figure 8.8: PXRD pattern of T-COFOFITC (dark yellow) compared to the experimental (red) and simulated pattern (black) of T-COF-OH, calculated and geometry optimized with three FITC molecules in the unit cell.

The ATR-IR spectrum (Figure 8.9) shows the presence of the FITC, however due to the large number of modes, especially in the aromatic C=C region between 1700 cm^{-1} and 1400 cm^{-1}, evaluation of the data is very difficult and does not prove the success of covalent linkage of FITC to the hydroxyl groups of the T-COF-OH.

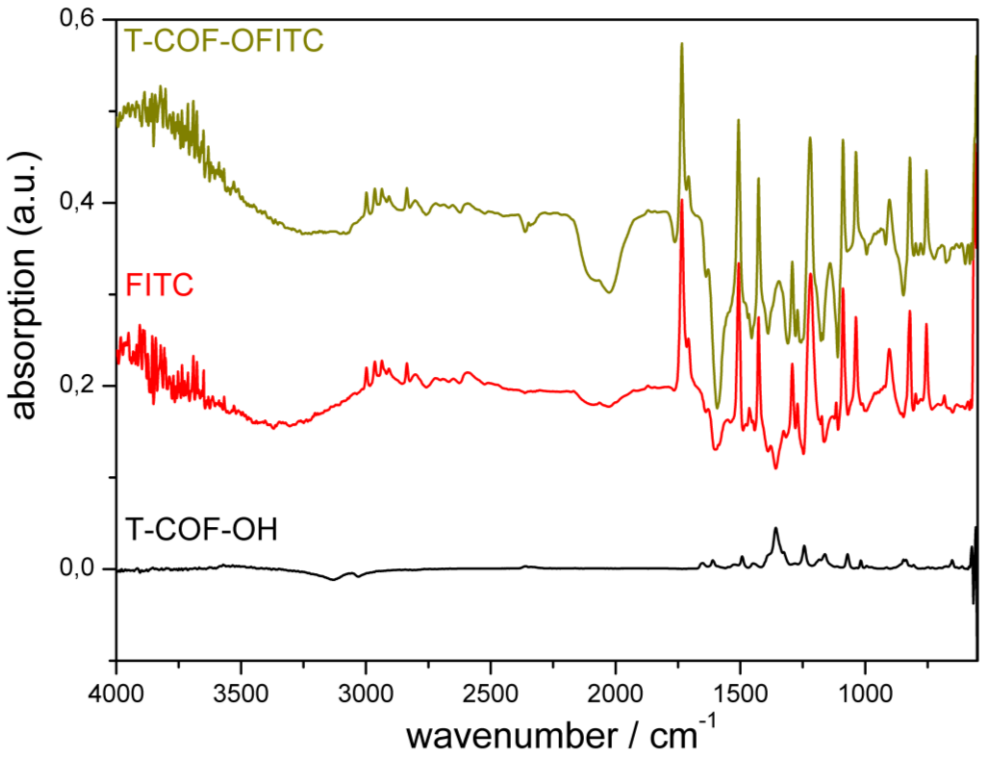

Figure 8.9: ATR-IR spectrum of T-COF-OH (black), T-COF-OFITC (dark yellow) and FITC (red).

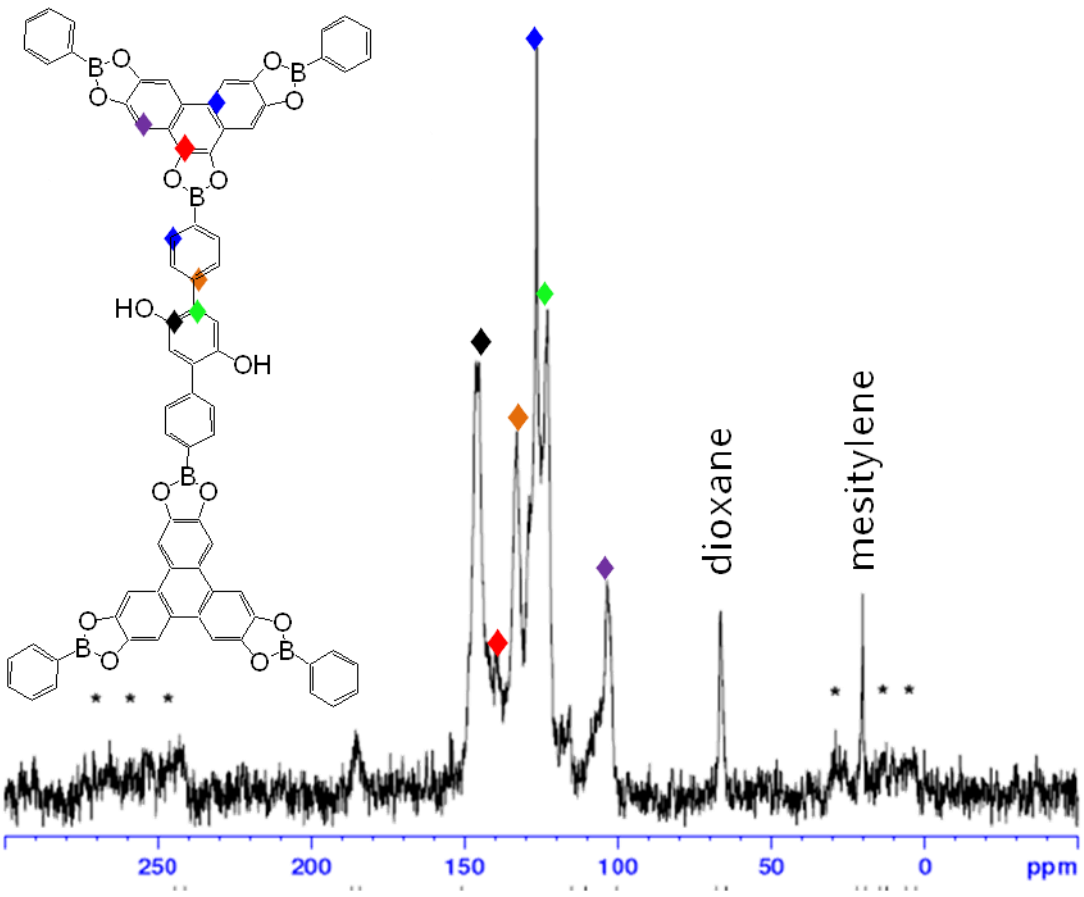

Figure 8.10: ^{13}C-CP-MAS Spectrum of T-COF-OH.* asterisk marked bands are rotational side bands.

.

8.4. Preparation of Spray-On Films of a Covalent Organic Framework by Steam Assisted Conversion

8.4.1. Introduction

Many technological devices, e.g. chemical sensors, catalytic and separation membranes and certain photovoltaic cells are based on the preparation of thin films of a porous crystalline material with tunable pore size and surface area.[108, 161-164] Zeolites,[126] ALPOs[165] and Metal-Organic Frameworks are the most common materials for these purposes.[166] Crystalline inorganic porous materials, of which zeolites are the most prominent, have many advantages due to their high chemical and thermal stability and their low production costs. However, a major drawback of this class of materials is the limited potential of functionalization.[14] Metal-Organic Frameworks (MOFs) offer a great variety of structural flexibility,[17-19] however most are in the microporous range thus have small windows for interactions with larger guest molecules.[26] More recently a new class of materials, the Covalent Organic Frameworks (COFs) have attracted the attention of scientists. The first COFs were formed by covalent bonds between diboronic acids and polyalcohols, and the resulting open pore framework exhibits great stability and a precisely tunable pore environment.[30, 36, 37, 39, 167] Although these materials exhibit great potential for several applications, e.g. photoconductivity, semiconductivity and high charge carrier mobilities[60, 63, 64], so far there has been little effort to synthesize films of COFs. Zwanevald et. al reported surface COFs (COF-1 and COF-5), with almost complete monolayer coverage by evaporation of the starting materials.[168] Gutzler et. al. reported the substrate-supported formation of a 2D COF through radical intermediates generated by cleavage of C-Br bonds.[169] For thin film preparations of

porous materials made from molecular building blocks different coating methods, e.g. growth from mother solutions (seeded growth, layer by layer method),[26, 170] or deposition of preformed nanocrystals (spin or dip coating)[26, 162] have been reported. Recently the fabrication of inorganic/organic films by simultaneous spray coating of interacting species (SSCIS) was demonstrated by Lefort et al.. With this method dense and homogeneous coatings can be created in a facile and controlled way.[171]

Here we report for the first time the preparation of a thin film of a new **B**enzo**t**hia**d**iazole Covalent Organic Framework (BTD-COF) (Figure 8.11) by spray coating of the starting materials followed by steam-assisted conversion (Figure 8.12). The substrate is totally covered with the desired material and the deposition can be realized on almost any solid support. This one-step deposition process can potentially be extended to other COF systems and would lead to a general method for the fabrication of thin organic crystalline porous films with ease of synthesis and a great variety of building blocks.

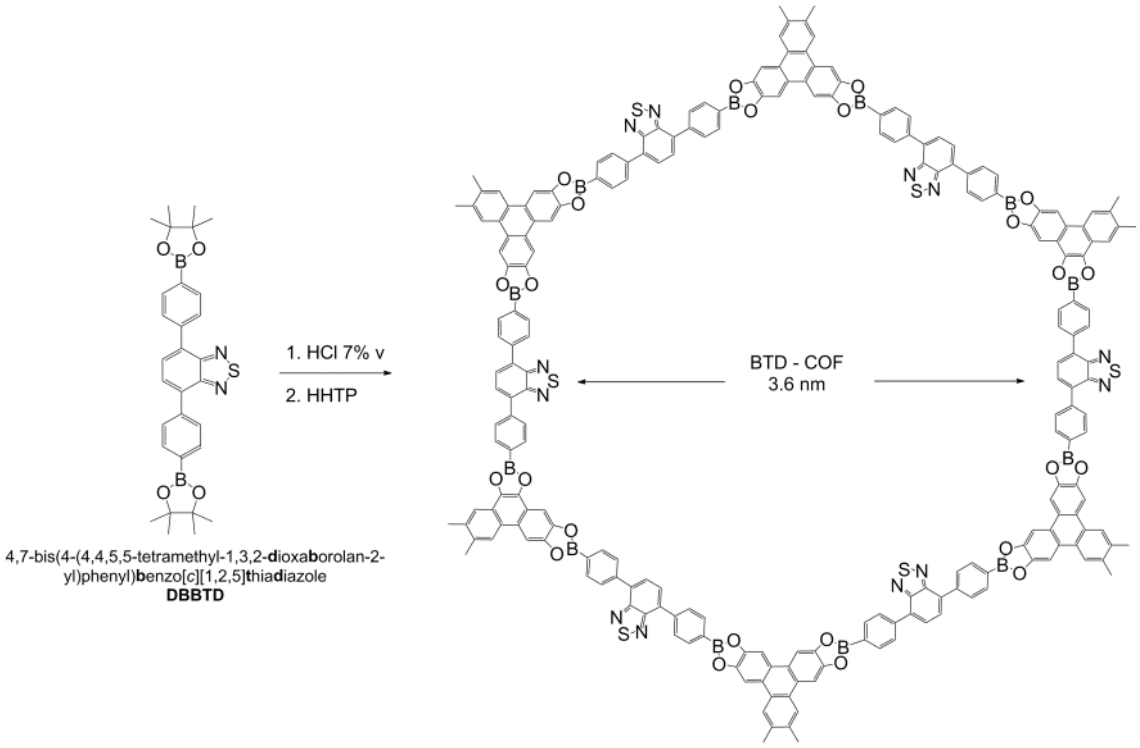

Figure 8.11: Reaction pathway for BTD-COF (see chapter 5).

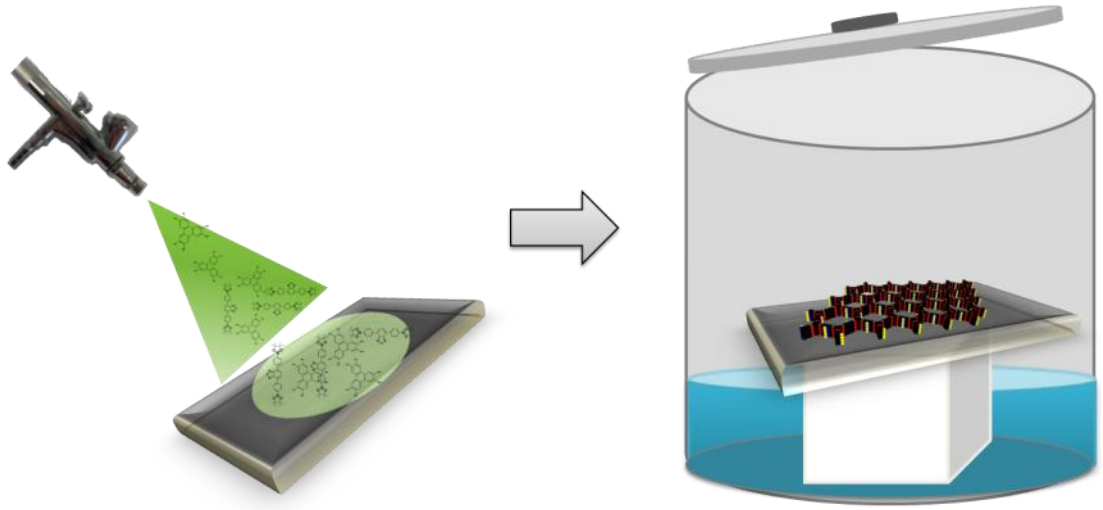

Figure 8.112: Schematic illustration of the spraycoating process with subsequent steam assisted conversion.

8.4.2. Experimental

For the synthesis of the BTD-COF film 0.1 mmol of DBBTD was hydrolyzed in 700 µL mesitylene : dioxane 1 : 1 v : v and 7 % v concentrated HCl. The reaction mixture was heated in the microwave oven for 10 min at 180 °C. The product was filtered off and dissolved with 0.06 mmol of HHTP in 7 mL ethanol : acetone 1 : 1. The clear solution was sprayed on the substrate. Prior to coating, the Si-wafer or glass substrates were cut in 1 x 1 cm rectangles and subsequently cleaned with piranha solution. The spray-coated supports were placed vertically in a teflon holder and inserted in a teflon-lined stainless steel autoclave containing 0.5 ml of a mixture of mesitylene and dioxane 1 : 1 and heated to 150 °C for 72 h. The synthesis of the bulk material was also carried out in two steps. After the first step described above the HHTP and the same amounts of solvents were added to the vial. The reaction solution was heated in the microwave for 60 min at 150 °C. The synthesis parameters for this new heterocyclic structure are described in chapter 5.

8.4.3. Results and Discussion

In Figure 8.13 A the XRD patterns of the bulk material and of the BTD-COF layer on the substrate are shown. The peak positions of the BTD-COF on silicon and in the bulk agree very well, hence the crystallization of the framework on a solid support via spray coating and steam assisted conversion technique is feasible. The full structure determination of the BTD-COF was performed as reported for previous COF structures[16] and is provided in chapter 5. The IR spectrum (Figure 8.13 B) shows the presence of the expected boronate ester functionality at 1354 cm^{-1} in both the bulk BTD-COF and the film BTD-COF, respectively.

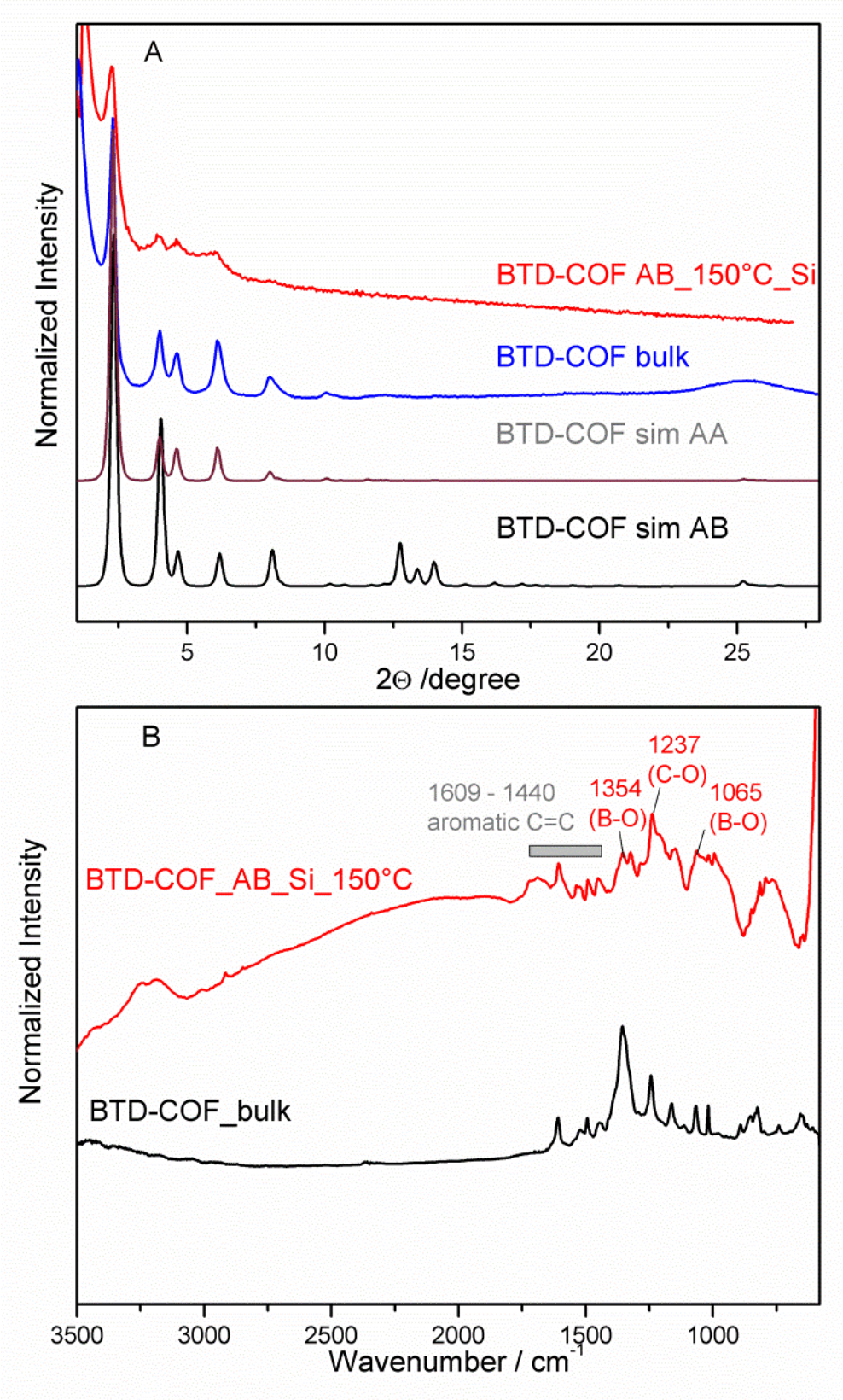

Figure 8.13: A) XRD patterns of BTD-COF bulk (blue) and on a silicon wafer by steam assisted conversion (red) compared to the simulated PXRD obtained by force

field calculations, B) IR spectrum of BTD-COF film and bulk show the boronate ester functionality.

The SEM images of the BTD-COF on the substrate show complete coverage and a film thickness of about 3 µm (Figure 8.14). The material doesn't consist of crystals with distinct morphologies as known from MOFs, but rather of 100 nm piles that are stuck together in partly spherical shape and partly random distribution. The thickness of the films can be easily varied by changing the concentration of the sprayed solution and or by the amount sprayed.

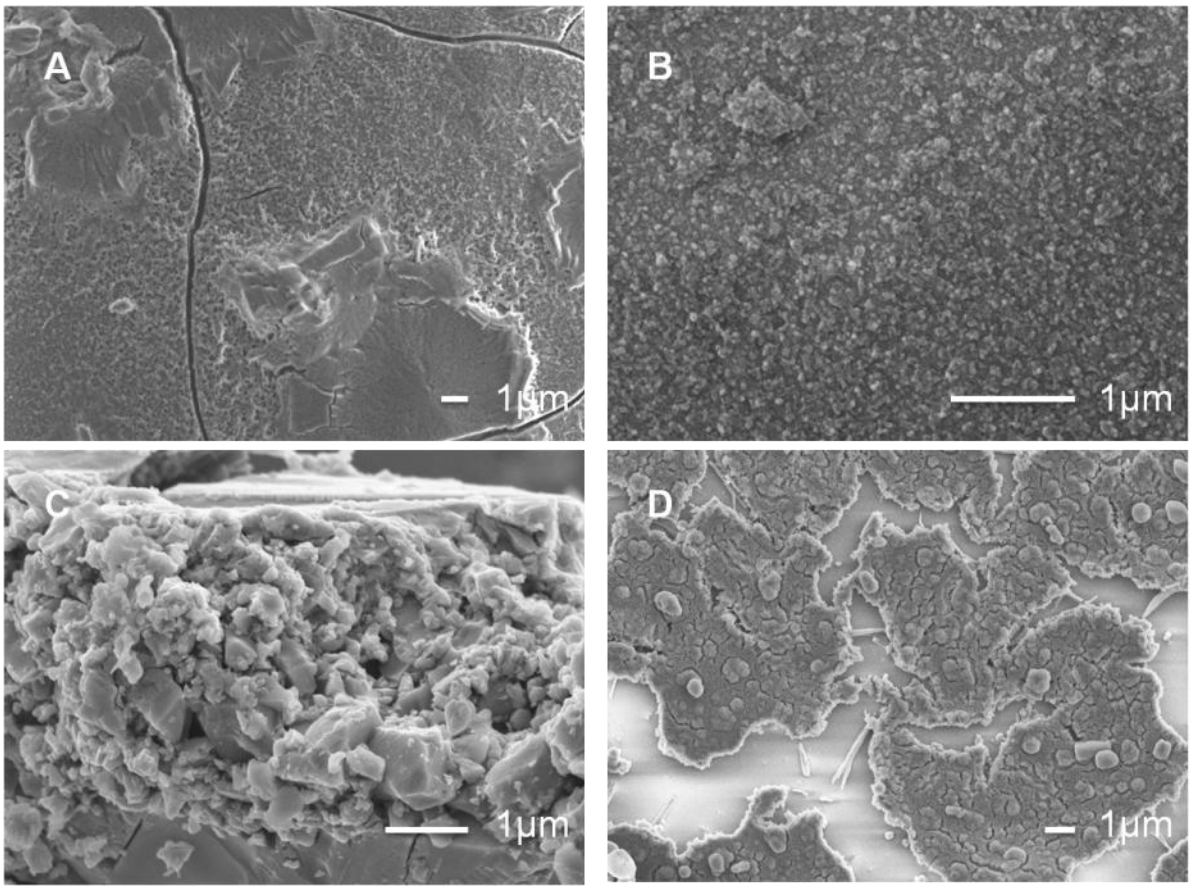

Figure 8.14: SEM images of A) silicon substrate spray-coated with reaction solution B) Top view of substrate after steam assisted conversion: BTD-COF C) Cross section of BTD-COF on silicon substrate, D) BTD-COF film synthesized in the reaction solution during solvothermal synthesis for 60 min at 150°C.

8.4.4. Conclusion

In summary we have demonstrated an easy method for the preparation of thickness-tunable Covalent Organic Framework films by spray coating followed by steam assisted conversion. The crystallization on the solid support is possible and yields total coverage of the support with the desired material. This can be essential for possible future applications of COFs, and can possibly accelerate research on the fabrication of electronic devices. The concepts of this work are currently extended to other COFs. Electronic and optoelectronic properties of these COF films are presently explored.

8.5. References

14. Ferey, G., *Chem. Soc. Rev.* **2008,** *37* (1), 191-214.

17. Yaghi, O. M.; O'Keeffe, M.; Ockwig, N. W.; Chae, H. K.; Eddaoudi, M.; Kim, J., *Nature* **2003,** *423* (6941), 705-714.

18. Kitagawa, S.; Kitaura, R.; Noro, S.-i., *Angew. Chem., Int. Ed.* **2004,** *43* (18), 2334-2375.

19. Serre, C.; Taulelle, F.; Ferey, G., *Chem. Commun.* **2003,** (22), 2755-2765.

26. Ranjan, R.; Tsapatsis, M., *Chem. Mater.* **2009,** *21* (20), 4920-4924.

30. Cote, A. P.; Benin, A. I.; Ockwig, N. W.; O'Keeffe, M.; Matzger, A. J.; Yaghi, O. M., *Science* **2005,** *310* (5751), 1166-1170.

36. Tilford, R. W.; Gemmill, W. R.; zur Loye, H.-C.; Lavigne, J. J., *Chem. Mater.* **2006,** *18* (22), 5296-5301.

37. Cote, A. P.; El-Kaderi, H. M.; Furukawa, H.; Hunt, J. R.; Yaghi, O. M., *J. Am. Chem. Soc.* **2007,** *129* (43), 12914-12915.

39. Tilford, R. W.; Mugavero, S. J., III; Pellechia, P. J.; Lavigne, J. J., *Adv. Mater.* **2008,** *20* (14), 2741-2746.

60. Wan, S.; Guo, J.; Kim, J.; Ihee, H.; Jiang, D., *Angew. Chem.* **2009,** *121* (18), 3253.

63. Wan, S.; Guo, J.; Kim, J.; Ihee, H.; Jiang, D., *Angew. Chem., Int. Ed.* **2009,** *48* (30), 5439-5442.

64. Ding, X.; Guo, J.; Feng, X.; Honsho, Y.; Guo, J.; Seki, S.; Maitarad, P.; Saeki, A.; Nagase, S.; Jiang, D., *Angew. Chem.* **2010**, n/a-n/a.

108. Seo, J. S.; Whang, D.; Lee, H.; Jun, S. I.; Oh, J.; Jeon, Y. J.; Kim, K., *Nature* **2000,** *404* (6781), 982-986.

117. *SWAVE*, Chemspeed Technologies: Augst.

119. *Accelrys MS Modeling 4.4*, 2008.

126. Yan, Y.; Bein, T., *J. Am. Chem. Soc.* **1995,** *117* (40), 9990-9994.

161. Gopel W., J. T. A., Kleitz M., Lundstrom J., Seiyama T, *Chemical and Biochemical Sensors*. 1. Edition ed.; New York, **1991**.

162. Bein, T.; Brown, K.; Frye, G. C.; Brinker, C. J., *J. Am. Chem. Soc.* **1989,** *111* (19), 7640-7641.

163. Chen, B.; Yang, Y.; Zapata, F.; Lin, G.; Qian, G.; Lobkovsky, E. B., *Adv. Mater.* **2007,** *19* (13), 1693-1696.

164. Krebs, F. C., *Sol. Energy Mater.* **2009,** *93* (4), 394-412.

165. Mintova, S.; Mo, S.; Bein, T., *Chem. Mater.* **1998,** *10* (12), 4030-4036.

166. Zacher, D.; Shekhah, O.; Woll, C.; Fischer, R. A., *Chem. Soc. Rev.* **2009,** *38* (5), 1418-1429.

167. Mastalerz, M., *Angew. Chem., Int. Ed.* **2008,** *47* (3), 445-447.

168. Zwaneveld, N. A. A.; Pawlak, R.; Abel, M.; Catalin, D.; Gigmes, D.; Bertin, D.; Porte, L., *J. Am. Chem. Soc.* **2008,** *130* (21), 6678-6679.

169. Gutzler, R.; Walch, H.; Eder, G.; Kloft, S.; Heckl, W. M.; Lackinger, M., *Chem. Commun.* **2009,** (29), 4456-4458.

170. Shekhah, O.; Wang, H.; Kowarik, S.; Schreiber, F.; Paulus, M.; Tolan, M.; Sternemann, C.; Evers, F.; Zacher, D.; Fischer, R. A.; Wöll, C., *J. Am. Chem. Soc.* **2007,** *129* (49), 15118-15119.

171. Lefort, M.; Popa, G.; Seyrek, E.; Szamocki, R.; Felix, O.; Hemmerlé, J.; Vidal, L.; Voegel, J.-C.; Boulmedais, F.; Decher, G.; Schaaf, P., *Angew. Chem., Int. Ed.* **2010,** *49* (52), 10110-10113.

9. Bibliography

1. Breck, D. W., *Zeolite molecular sieves: structure, chemistry, and use.* Wiley: New York, 1974.

2. Cundy, C. S.; Cox, P. A., *Chem. Rev.* **2003,** 103 (3), 663-702.

3. Corma, A., *J. Catal.* 216 (1-2), 298-312.

4. Wilson, S. T.; Lok, B. M.; Messina, C. A.; Cannan, T. R.; Flanigen, E. M., *J. Am. Chem. Soc.* **1982,** 104 (4), 1146-1147.

5. Huang, Q.; Ulutagay, M.; Michener, P. A.; Hwu, S.-J., *J. Am. Chem. Soc.* **1999,** 121 (44), 10323-10326.

6. Parise, J. B., *Inorg. Chem.* **1985,** 24 (25), 4312-4316.

7. Gier, T. E.; Stucky, G. D., Nature **1991,** 349 (6309), 508-510.

8. Wingenfelder, U.; Hansen, C.; Furrer, G.; Schulin, R., *Environ. Sci. Technol.* **2005,** 39 (12), 4606-4613.

9. Moreno, N.; Querol, X.; Ayora, C.; Pereira, C. F.; Janssen-Jurkovicová, M., *Environ. Sci. Technol.* **2001,** 35 (17), 3526-3534.

10. Clearfield, A., *Chem. Rev.* **1988,** 88 (1), 125-148.

11. Magee John, S., *Zeolite Cracking Catalysts?an Overview. In Molecular Sieves?*II, American Chemical Society: **1977**; Vol. 40, pp 650-668.

12. TatlIer, M.; Erdem-Senatalar, A., *Applied Thermal Engineering* **1999,** 19 (11), 1157-1172.

13. Fuel and Energy Abstracts **1997,** 38 (5), 348-348.

14. Ferey, G., *Chem. Soc. Rev.* **2008,** 37 (1), 191-214.

15. Budd, P. M., *Science* **2007,** 316 (5822), 210-211.

16. Rowsell, J. L. C.; Yaghi, O. M., *Microp. Mesop. Mat.* **2004,** 73 (1-2), 3-14.

17. Yaghi, O. M.; O'Keeffe, M.; Ockwig, N. W.; Chae, H. K.; Eddaoudi, M.; Kim, J., *Nature* **2003,** 423 (6941), 705-714.

18. Kitagawa, S.; Kitaura, R.; Noro, S.-i., *Angew. Chem., Int. Ed.* **2004,** 43 (18), 2334-2375.

19. Serre, C.; Taulelle, F.; Ferey, G., *Chem. Commun.* **2003,** (22), 2755-2765.

20. Eddaoudi, M.; Kim, J.; Rosi, N.; Vodak, D.; Wachter, J.; O'Keeffe, M.; Yaghi, O. M., *Science* **2002,** 295 (5554), 469-472.

21. Li, H.; Eddaoudi, M.; O'Keeffe, M.; Yaghi, O. M., *Nature* **1999,** 402 (6759), 276-279.

22. Song, Y.-F.; Cronin, L., *Angew. Chem., Int. Ed.* **2008,** 47 (25), 4635-4637.

23. Wang, Z.; Cohen, S. M., *J. Am. Chem. Soc.* **2007,** 129 (41), 12368-12369.

24. Burrows, A. D.; Frost, C. G.; Mahon, M. F.; Richardson, C., *Chem. Commun.* **2009,** (28), 4218-4220.

25. Wang, Z.; Cohen, S. M., *Chem. Soc. Rev.* **2009,** 38 (5), 1315-1329.

26. Ranjan, R.; Tsapatsis, M., *Chem. Mater.* **2009,** 21 (20), 4920-4924.

27. Sonnauer, A.; Hoffmann, F.; Fröba, M.; Kienle, L.; Duppel, V.; Thommes, M.; Serre, C.; Férey, G.; Stock, N., *Angew. Chem.* **2009,** 121 (21), 3849-3852.

28. Lorand, J. P.; Edwards, J. O., *J. Org. Chem.* **1959,** 24 (6), 769-774.

29. Niu, W.; O'Sullivan, C.; Rambo, B. M.; Smith, M. D.; Lavigne, J. J., *Chem. Commun.* **2005,** (34), 4342-4344.

30. Cote, A. P.; Benin, A. I.; Ockwig, N. W.; O'Keeffe, M.; Matzger, A. J.; Yaghi, O. M., *Science* **2005,** 310 (5751), 1166-1170.

31. El-Kaderi, H. M.; Hunt, J. R.; Mendoza-Cortes, J. L.; Cote, A. P.; Taylor, R. E.; O'Keeffe, M.; Yaghi, O. M., *Science* **2007,** 316 (5822), 268-272.

32. Hall, D. G., *Boronic Acids*. Wiley-VCH: Weinheim, **2005**.

33. Uribe-Romo, F. J.; Hunt, J. R.; Furukawa, H.; Klock, C.; O'Keeffe, M.; Yaghi, O. M., *J. Am. Chem. Soc*. **2009,** 131 (13), 4570-4571.

34. ndara, F.; Asano, A.; Furukawa, H.; Saeki, A.; Dey, S. K.; Liao, L.; Ambrogio, M. W.; Botros, Y. Y.; Duan, X.; Seki, S.; Stoddart, J. F.; Yaghi, O. M., *Chem. Mater*. **2011,** 23 (18), 4094-4097.

35. Uribe-Romo, F. J.; Doonan, C. J.; Furukawa, H.; Oisaki, K.; Yaghi, O. M., *J. Am. Chem. Soc*. **2011,** 133 (30), 11478-11481.

36. Tilford, R. W.; Gemmill, W. R.; zur Loye, H.-C.; Lavigne, J. J., *Chem. Mater*. **2006,** 18 (22), 5296-5301.

37. Cote, A. P.; El-Kaderi, H. M.; Furukawa, H.; Hunt, J. R.; Yaghi, O. M., *J. Am. Chem. Soc*. **2007,** 129 (43), 12914-12915.

38. Tilford, R. W.; Mugavero, S. J.; Pellechia, P. J.; Lavigne, J. J., *Adv. Mater*. **2008,** 20 (14), 2741-2746.

39. Tilford, R. W.; Mugavero, S. J., III; Pellechia, P. J.; Lavigne, J. J., *Adv. Mater*. **2008,** 20 (14), 2741-2746.

40. Dogru, M.; Sonnauer, A.; Gavryushin, A.; Knochel, P.; Bein, T., *Chem. Commun.* **2011,** 47 (6), 1707-1709.

41. Spitler, E. L.; Dichtel, W. R., *Nat. Chem*. **2010,** 2 (8), 672-677.

42. Ding, X.; Guo, J.; Feng, X.; Honsho, Y.; Guo, J.; Seki, S.; Maitarad, P.; Saeki, A.; Nagase, S.; Jiang, D., *Angew. Chem., Int. Ed.* **2011,** 50 (6), 1289-1293.

43. Feng, X.; Chen, L.; Dong, Y.; Jiang, D., *Chem. Commun*. **2011,** 47 (7), 1979-1981.

44. Chae, H. K.; Siberio-Perez, D. Y.; Kim, J.; Go, Y.; Eddaoudi, M.; Matzger, A. J.; O'Keeffe, M.; Yaghi, O. M., *Nature* **2004,** 427 (6974), 523-527.

45. Ferey, G.; Mellot-Draznieks, C.; Serre, C.; Millange, F.; Dutour, J.; Surble, S.; Margiolaki, I., *Science* **2005,** 309 (5743), 2040-2042.

46. Hunt Joseph, R.; Doonan Christian, J.; LeVangie James, D.; Cote Adrien, P.; Yaghi Omar, M., *J. Am. Chem. Soc*. **2008,** 130 (36), 11872-3.

47. http://www.mobilemag.com/2006/09/08/bmw-to-release-7-series-hydrogen-limousine-in-2007/.

48. Yang, J.; Sudik, A.; Wolverton, C.; Siegel, D. J., *Chem. Soc. Rev*. **2010,** 39 (2), 656-675.

49. http://en.wikipedia.org/wiki/Metal-organic_framework.

50. Furukawa, H.; Ko, N.; Go, Y. B.; Aratani, N.; Choi, S. B.; Choi, E.; Yazaydin, A. Ö.; Snurr, R. Q.; O'Keeffe, M.; Kim, J.; Yaghi, O. M., *Science* **2010,** 329 (5990), 424-428.

51. Klontzas, E.; Tylianakis, E.; Froudakis, G. E., *J. Phys. Chem. C* **2008,** 112 (24), 9095-9098.

52. Li, F.; Zhao, J.; Johansson, B.; Sun, L., *Int. J. Hydrogen Energ*. **2010,** 35 (1), 266-271.

53. Han, S. S.; Furukawa, H.; Yaghi, O. M.; Goddard, W. A., III, *J. Am. Chem. Soc*. **2008,** 130 (35), 11580-11581.

54. Cao, D.; Lan, J.; Wang, W.; Smit, B., *Angew. Chem., Int. Ed*. **2009,** 48 (26), 4730-4733, S4730/1-S4730/25.

55. Klontzas, E.; Tylianakis, E.; Froudakis, G. E., *Nano Lett*. **2010,** 10 (2), 452-454.

56. Furukawa, H.; Yaghi, O. M., *J. Am. Chem. Soc*. **2009,** 131 (25), 8875-8883.

57. Mulfort, K. L.; Hupp, J. T., *J. Am. Chem. Soc*. **2007,** 129 (31), 9604-9605.

58. Lan, J.; Cao, D.; Wang, W., *J. Phys. Chem. C* **2010,** 114 (7), 3108-3114.

59. Zou, X.; Zhou, G.; Duan, W.; Choi, K.; Ihm, J., *J. Phys. Chem. C* **2010,** 114 (31), 13402-13407.

60. Wan, S.; Guo, J.; Kim, J.; Ihee, H.; Jiang, D., *Angew. Chem.* **2009,** 121 (18), 3253.

61. Niu, W.; Smith, M. D.; Lavigne, J. J., *J. Am. Chem. Soc.* **2006,** 128 (51), 16466-16467.

62. Li, Y.; Ding, J.; Day, M.; Tao, Y.; Lu, J.; D'Iorio, M., *Chem. Mater.* **2003,** 15 (26), 4936-4943.

63. Wan, S.; Guo, J.; Kim, J.; Ihee, H.; Jiang, D., *Angew. Chem., Int. Ed.* **2009,** 48 (30), 5439-5442.

64. Ding, X.; Guo, J.; Feng, X.; Honsho, Y.; Guo, J.; Seki, S.; Maitarad, P.; Saeki, A.; Nagase, S.; Jiang, D., *Angew. Chem.* **2010**, n/a-n/a.

65. Ding, X.; Chen, L.; Honsho, Y.; Feng, X.; Saengsawang, O.; Guo, J.; Saeki, A.; Seki, S.; Irle, S.; Nagase, S.; Parasuk, V.; Jiang, D., *J. Am. Chem. Soc.* **2011,** 133 (37), 14510-14513.

66. Bain, C. D.; Troughton, E. B.; Tao, Y. T.; Evall, J.; Whitesides, G. M.; Nuzzo, R. G., *J. Am. Chem. Soc.* **1989,** 111 (1), 321-335.

67. Nuzzo, R. G.; Allara, D. L., *J. Am. Chem. Soc.* **1983,** 105 (13), 4481-4483.

68. Maoz, R.; Sagiv, J., *J. Colloid Interface Sci.* **1984,** 100 (2), 465-496.

69. Wasserman, S. R.; Tao, Y. T.; Whitesides, G. M., *Langmuir* **1989,** 5 (4), 1074-1087.

70. Chandekar, A.; Sengupta, S. K.; Whitten, *J. E., Appl. Surf. Sci.* **2010,** 256 (9), 2742-2749.

71. Kang, J.; Rowntree, P. A., *Langmuir* **2006,** 23 (2), 509-516.

72. Semaltianos, N. G.; Wilson, E. G., *Thin Solid Films* **2000,** 366 (1-2), 111-116.

73. Wanunu, M.; Vaskevich, A.; Rubinstein, I., *J. Am. Chem. Soc.* **2004,** 126 (17), 5569-5576.

74. Whitesides, G. M.; Laibinis, P. E., *Langmuir* **1990,** 6 (1), 87-96.

75. Ulman, A., *Chem. Rev.* **1996,** 96 (4), 1533-1554.

76. Barriet, D.; Yam, C. M.; Shmakova, O. E.; Jamison, A. C.; Lee, T. R., *Langmuir* **2007,** 23 (17), 8866-8875.

77. Onclin, S.; Ravoo, B. J.; Reinhoudt, D. N., *Angew. Chem., Int. Ed.* **2005,** 44 (39), 6282-6304.

78. Brunner, H.; Vallant, T.; Mayer, U.; Hoffmann, H., *J. Colloid Interface Sci.* **1999,** 212 (2), 545-552.

79. Ulman, A., *An introduction to ultrathin organic films from Langmuir-Blodgett to self-assembly*. Academic Press: Boston, **1991**.

80. Vickerman, J. C., *Surface analysis: the principal techniques*. Wiley: Chichester, **1997**.

81. Magonov, S. N.; Whangbo, M.-H., Frontmatter. *In Surface Analysis with STM and AFM*, Wiley-VCH Verlag GmbH: **2007**; pp I-XII.

82. Poirier, G. E., *Langmuir* **1997,** 13 (7), 2019-2026.

83. Camillone, N., *J. Chem. Phys.* **1993,** 98 (4), 3503.

84. Love, J. C.; Estroff, L. A.; Kriebel, J. K.; Nuzzo, R. G.; Whitesides, G. M., *Chem. Rev.* **2005,** 105 (4), 1103-1170.

85. Porter, M. D.; Bright, T. B.; Allara, D. L.; Chidsey, C. E. D., *J. Am. Chem. Soc.* **1987,** 109 (12), 3559-3568.

86. Feng, S.; Bein, T., *Nature* **1994,** 368 (6474), 834-836.

87. Hermes, S.; Schröder, F.; Chelmowski, R.; Wöll, C.; Fischer, R. A., *J. Am. Chem. Soc.* **2005,** 127 (40), 13744-13745.

88. Biemmi, E.; Scherb, C.; Bein, T., *J. Am. Chem. Soc*. **2007,** 129 (26), 8054-8055.

89. Colson, J. W.; Woll, A. R.; Mukherjee, A.; Levendorf, M. P.; Spitler, E. L.; Shields, V. B.; Spencer, M. G.; Park, J.; Dichtel, W. R., *Science* **2011,** 332 (6026), 228-231.

90. Mizoshita, N.; Ikai, M.; Tani, T.; Inagaki, S., *J. Am. Chem. Soc*. **2009,** 131 (40), 14225-14227.

91. Akporiaye, D. E.; Dahl, I. M.; Karlsson, A.; Wendelbo, R., *Angew. Chem*. **1998**, 110 (5), 629-631.

92. L. Smart, E. M., *Einführung in die Festkörperchemie.* Vieweg Verlag: **1997**.

93. Atkins, p., *Physikalische Chemie. 2.* Auflage ed.; VCH Weinheim: **1996**.

94. Massa, W., *Kristallstrukturbestimmung*. Teubner: **1996**.

95. http://en.wikipedia.org/wiki/Electron_microscope.

96. P. J. Goodhew, J. H., R. Beanland, *Electron microscopy and analysis*. 3 nd ed.; London, **1988**.

97. D. B. Williams, C. B. C., *Transmission electron microscopy: a textbook for material science: I: basics*. Plenum: New York, **1996**.

98. (http://barrett-group.mcgill.ca/teaching/nanotechnology/nano02.htm).

99. H. Nauner, W. H., *Untersuchungsmethoden in der Chemie*. Thieme Verlag: Stuttgart, **1997**.

100. http://www.niu.edu/ANALYTICALLAB/ftir/index.shtml.

101. M. Hesse, H. M., B. Zeeh, *Spektroskopische Methoden in der organischen Chemie*. 5. überarb. Auflage ed.; Georg Thieme Verlag: Stuttgart New York, **1995**.

102. Jacobson, N. E., *NMR Spectroscopy Explained*. Wiley Interscience: Hoboken, **2007**.

103. Macomber, R. S., A *Complete Introduction to Modern NMR Spectroscopy*. Wiley Interscience: New York, **1998**.

104. http://en.wikipedia.org/wiki/File:MagicAngleSpinning.svg.

105. http://web.uvic.ca/ail/techniques/epi-fluorescence.html.

106. Sing, K. S. W.; Everett, D. H.; Haul, R. A. W.; Moscou, L.; Pierotti, R. A.; Rouquerol, J.; Siemieniewska, T., *Pure Appl. Chem.* **1985,** 57 (4), 603-19.

107. Condon, J. B., *Surface Area and Porosity Determinatons by Physisorption - Measurements and Theory*. Elsevier: Amsterdam, **2006**.

108. Seo, J. S.; Whang, D.; Lee, H.; Jun, S. I.; Oh, J.; Jeon, Y. J.; Kim, K., *Nature* **2000,** 404 (6781), 982-986.

109. Kobler, J.; Lotsch, B. V.; Ozin, G. A.; Bein, T., *Acs Nano* **2009,** 3 (7), 1669-1676.

110. Frontmatter. *In Handbook of Porous Solids*, F. Schüth, K. S. W. S., J. Weitkamp, Ed. Wiley- VCH, Weinheim: **2008**.

111. Férey, G.; Serre, C.; Mellot-Draznieks, C.; Millange, F.; Surblé, S.; Dutour, J.; Margiolaki, I., *Angew. Chem.* **2004,** 116 (46), 6456-6461.

112. Klein, N.; Senkovska, I.; Gedrich, K.; Stoeck, U.; Henschel, A.; Mueller, U.; Kaskel, S., *Angew. Chem., Int. Ed.* **2009,** 48 (52), 9954-9957.

113. Y. Park; S.Choi; Kim, H.; Kim, K.; Won, B.; Choi, K.; Choi, J.; Ahn, W.; Won, N.; Kim, S.; Jung, D.; Choi, S. n.; G.Kim; Su.Cha; Jhon, Y.; J.Yang; Kim, J., *Angew. Chem.* **2007,** 119 (43), 8237.

114. Doonan, C. J.; Tranchemontagne, D. J.; Glover, T. G.; Hunt, J. R.; Yaghi, O. M., *Nat. Chem.* **2010,** 2 (3), 235-238.

115. Chung, Y.; Duerr, B. F.; McKelvey, T. A.; Nanjappan, P.; Czarnik, A. W., *J. Org. Chem.* **1989,** 54 (5), 1018-1032.

116. Huang, W.-H.; Jia, W.-L.; Wang, S., *Can. J. Chem.* **2006,** 84 (4), 477-485.

117. SWAVE, Chemspeed Technologies: Augst.

118. Campbell, N. L.; Clowes, R.; Ritchie, L. K.; Cooper, A. I., *Chem. Mater.* **2009,** 21 (2), 204-206.

119. Accelrys MS Modeling 4.4, **2008**.

120. Sichel, E. K.; Miller, R. E.; Abrahams, M. S.; Buiocchi, C. *J., Phys. Rev. B* **1976,** 13 (Copyright (C) 2009 The American Physical Society), 4607.

121. Leach, A. R., *Molecular Modelling: Principles and Applications*. 2nd ed.; Prentice Hall: Harlow, England, **2001**.

122. Connolly, M., *J. Appl. Crystallogr.* **1983,** 16 (5), 548-558.

123. Duren, T.; Millange, F.; Ferey, G.; Walton, K. S.; Snurr, R. Q., *J. Phys. Chem. C* **2007,** 111 (42), 15350-15356.

124. Assfour, B.; Seifert, G., *Microp. Mesop. Mat.* **2010,** 133 (1-3), 59-65.

125. E. F. Vansant, P. V. d. V., K.C. Vrancken, *Characterization and Chemical Modification of the Silica Surface*. Elsevier Science B. V.: Amsterdam, **1995**.

126. Yan, Y.; Bein, T.*, J. Am. Chem. Soc.* **1995,** 117 (40), 9990-9994.

127. Wada, Y.; Otsuka, K.; Morikawa, A., *J. Catal.* **1980,** 64 (2), 417-425.

128. Thijs, A.; Peeters, S.; Vansant, E. F.; Peeters, G.; Verhaert, I., *J. Chem. Soc.*, Faraday Transactions 1: Physical Chemistry in Condensed Phases **1986,** 82 (3), 963-975.

129. Kitaura, R.; Onoyama, G.; Sakamoto, H.; Matsuda, R.; Noro, S.-i.; Kitagawa, S., *Angew. Chem., Int. Ed.* **2004,** 43 (20), 2684-2687.

130. Kiang, Y. H.; Gardner, G. B.; Lee, S.; Xu, Z.; Lobkovsky, E. B., *J. Am. Chem. Soc.* **1999,** 121 (36), 8204-8215.

131. Ma, L.; Falkowski, J. M.; Abney, C.; Lin, W., *Nat. Chem.* **2010,** 2 (10), 838-846.

132. Wang, Z.; Cohen, S. M., *Angew. Chem., Int. Ed.* **2008,** 47 (25), 4699-4702.

133. Yamakawa, T.; Kagechika, H.; Kawachi, E.; Hashimoto, Y.; Shudo, K., *J. Med. Chem.* **1990,** 33 (5), 1430-1437.

134. Neises, B.; Steglich, W., *Angew. Chem. Int. .* **1978,** 17 (7), 522-524.

135. Tsubata, Y.; Suzuki, T.; Miyashi, T.; Yamashita, Y., *J. Org. Chem.***1992,** 57 (25), 6749-6755.

136. Pilgram, K.; Zupan, M.; Skiles, R., *J. Heterocycl. Chem.* **1970,** 7 (3), 629-633.

137. Yaghi, O. M.; Cote, A. P.; El-Kaderi, H. M.; Hunt, J. R. Crystalline 3d- and 2d-covalent organic frameworks. 2008-US518592008091976, 20080124., **2008**.

138. Spitler, E. L.; Colson, J. W.; Uribe-Romo, F. J.; Woll, A. R.; Giovino, M. R.; Saldivar, A.; Dichtel, W. R., *Angew. Chem.* **2012**, n/a-n/a.

139. Dennler, G.; Scharber, M. C.; Brabec, C. J., *Adv. Mater.* **2009,** 21 (13), 1323-1338.

140. Heeney, M.; Bailey, C.; Genevicius, K.; Shkunov, M.; Sparrowe, D.; Tierney, S.; McCulloch, I., *J. Am. Chem. Soc.* **2005,** *127* (4), 1078-1079.

141. Sariciftci, N. S.; Smilowitz, L.; Heeger, A. J.; Wudl, F., *Science* **1992,** *258* (5087), 1474-1476.

142. Savenije, T. J.; Grzegorczyk, W. J.; Heeney, M.; Tierney, S.; McCulloch, I.; Siebbeles, L. D. A., *J. Phys. Chem. C* **2010,** *114* (35), 15116-15120.

143. Xie, Q.; Perez-Cordero, E.; Echegoyen, L., *J. Am. Chem. Soc.* **1992,** *114* (10), 3978-3980.

144. Duche, D.*, et al. Sol. En. Mat* **2011**.95*, 18–25.*

145. McCulloch, I.; Heeney, M.; Bailey, C.; Genevicius, K.; MacDonald, I.; Shkunov, M.; Sparrowe, D.; Tierney, S.; Wagner, R.; Zhang, W.; Chabinyc, M. L.; Kline, R. J.; McGehee, M. D.; Toney, M. F., *Nat Mater* **2006,** *5* (4), 328-333.

146. Mann, S., *Nature* **1993,** 365 (6446), 499-505.

147. Addadi, L.; Weiner, S., *Angew. Chem.* **1992,** 104 (2), 159-176.

148. Heinz Adolf Lowenstam, S. W., *On biomineralization*. Oxford University Press: **1989**.

149. Song, R.-Q.; Colfen, H., *CrystEngComm* **2011,** 13 (5), 1249-1276.

150. Aizenberg, J., *Adv. Mater.* **2004,** 16 (15), 1295-1302.

151. Allara, D. L.; Nuzzo, R. G., *Langmuir* **1985,** 1 (1), 52-66.

152. Aizenberg, J.; Black, A. J.; Whitesides, G. M., *J. Am. Chem. Soc.* **1999,** 121 (18), 4500-4509.

153. Hsu, J. W. P.; Tian, Z. R.; Simmons, N. C.; Matzke, C. M.; Voigt, J. A.; Liu, J., *Nano Lett.* **2004,** 5 (1), 83-86.

154. Addadi, L.; Raz, S.; Weiner, S., *Adv. Mater.* **2003,** 15 (12), 959-970.

155. Zacher, D.; Baunemann, A.; Hermes, S.; Fischer, R. A., *J. Mater. Chem.* **2007,** 17 (27), 2785-2792.

156. Kitagawa, S.; Matsuda, R., *Coord. Chem. Rev.* **2007,** 251 (21-24), 2490-2509.

157. Otero, R.; Gallego, J. M.; de Parga, A. L. V.; Martín, N.; Miranda, R., *Adv. Mater.* **2011**, n/a-n/a.

158. Kanayama, N.; Kitano, H., *Langmuir* **1999,** 16 (2), 577-583.

159. Morgan, A. B.; Jurs, J. L.; Tour, J. M., *J. Appl. Polym. Sci.* **2000,** 76 (8), 1257-1268.

160. Coutts, I. G. C.; Goldschmid, H. R.; Musgrave, O. C., *J. Chem. Soc. C: Organic* **1970,** (3), 488-493.

161. Gopel W., J. T. A., Kleitz M., Lundstrom J., Seiyama T, *Chemical and Biochemical Sensors*. 1. ed.; New York, **1991**.

162. Bein, T.; Brown, K.; Frye, G. C.; Brinker, C. J., *J. Am. Chem. Soc*. **1989,** 111 (19), 7640-7641.

163. Chen, B.; Yang, Y.; Zapata, F.; Lin, G.; Qian, G.; Lobkovsky, E. B., *Adv. Mater.* **2007,** 19 (13), 1693-1696.

164. Krebs, F. C., *Sol. Energy Mater*. **2009,** 93 (4), 394-412.

165. Mintova, S.; Mo, S.; Bein, T., *Chem. Mater*. **1998,** 10 (12), 4030-4036.

166. Zacher, D.; Shekhah, O.; Woll, C.; Fischer, R. A., *Chem. Soc. Rev.* **2009,** 38 (5), 1418-1429.

167. Mastalerz, M., *Angew. Chem., Int. Ed*. **2008,** 47 (3), 445-447.

168. Zwaneveld, N. A. A.; Pawlak, R.; Abel, M.; Catalin, D.; Gigmes, D.; Bertin, D.; Porte, L., *J. Am. Chem. Soc*. **2008,** 130 (21), 6678-6679.

169. Gutzler, R.; Walch, H.; Eder, G.; Kloft, S.; Heckl, W. M.; Lackinger, M., *Chem. Commun.* **2009,** (29), 4456-4458.

170. Shekhah, O.; Wang, H.; Kowarik, S.; Schreiber, F.; Paulus, M.; Tolan, M.; Sternemann, C.; Evers, F.; Zacher, D.; Fischer, R. A.; Wöll, C*., J. Am. Chem. Soc*. **2007,** 129 (49), 15118-15119.

171. Lefort, M.; Popa, G.; Seyrek, E.; Szamocki, R.; Felix, O.; Hemmerlé, J.; Vidal, L.; Voegel, J.-C.; Boulmedais, F.; Decher, G.; Schaaf, P*., Angew. Chem., Int. Ed.* **2010,** 49 (52), 10110-10113.

11. Publications and Presentations

PUBLICATIONS

1. Dogru, M.; Sonnauer, A.; Gavryushin, A.; Knochel, P.; Bein, T., A Covalent Organic Framework with 4 nm open pores, *Chem. Commun.* **2011,** *47* (6), 1707-1709.

2. Dogru, M.; Bein, T., Honeycomb on graphene, *Nat Nano* **2011,** *6* (6), 333-335.;,

3. Dogru, M.; Handloser M.; Kunz, T.; Hartschuh, A.; Knochel, P.; Bein, T.; A photoconductive thienothiophene-based Covalent Organic Framework showing charge transfer to PCBM, submitted to Nature Nanotechnology.

4. Dogru M., Gavryushin, A.; Knochel P., Bein, T., Covalent functionalization of Covalent Organic Frameworks, manuscript in preparation

5. Dogru, M. Medina, D., Kunz, T., Knoche, P. Bein, T., Oriented growth of Covalent Organic Framworks, manuscript in preparation

PRESENTATIONS

Mirjam Dogru, Andrei Gavryshin, Monika Plabst, Markus Döblinger, Paul Knochel and Thomas Bein, Pore modification of Covalent Organic Frameworks, 21. Deutsche Zeolith-Tagung, Kiel, Germany, 04.-06.03.2009

Mirjam Dogru, Andreas Sonnauer, Andrei Gavryshin, Paul Knochel and Thomas Bein, Pore modification of Covalent Organic Frameworks, MOF08, Augsburg, Germany, 08.-10.10.2010

Mirjam Dogru, Andreas Sonnauer, Andrei Gavryshin, Markus Döblinger, Paul Knochel and Thomas Bein, Tuning the Pores in Covalent Organic Frameworks, 22. Deutsche Zeolith-Tagung, Munich, Germany, 03.-05.03.2010.

Mirjam Dogru, Andreas Sonnauer, Andrei Gavryshin, Paul Knochel and Thomas Bein, Pore Modification of Covalent Organic Frameworks, 16th International Zeolite Conference/7th International Mesostructured Materials Symposium, 04.-09.07.2010, Sorrento, Italy

Mirjam Dogru, Andreas Sonnauer, Andrei Gavryshin, Markus Döblinger, Paul Knochel and Thomas Bein, Pore Modification of Covalent Organic Frameworks, 2nd International Conference on Metal-Organic Frameworks and Open Framework Compunds, 05.09-08.09.2010, Marseille, France.

Mirjam Dogru, Kun Hou, Silvia Zimdars, Andreas Sonnauer, Markus Döblinger, Paul Knochel and Thomas Bein, Porous Electroactive Organic Frameworks, CeNS Winterschool, St. Christoph, Austria. 2011